

See discussions, stats, and author profiles for this publication at: <https://www.researchgate.net/publication/48410628>

Characterization and performance optimization of radiation monitoring sensors for high energy physics experiments at the CERN LHC and Super-LHC

Article · January 2009

Source: OAI

CITATIONS

3

READS

594

2 authors, including:



J. Mekki

CERN

53 PUBLICATIONS 502 CITATIONS

SEE PROFILE

Académie de Montpellier

UNIVERSITE MONTPELLIER II
SCIENCES ET TECHNIQUES DU LANGUEDOC

T H E S E

pour obtenir le grade de

DOCTEUR DE L'UNIVERSITE MONTPELLIER II

Discipline : Electronique

Formation Doctorale : Electronique – composants et systèmes

Ecole Doctorale : Information, Structures et Systèmes

Présentée par

Julien Mekki

**Characterization and performance optimization of
radiation monitoring sensors for high energy physics
experiments at the CERN LHC and Super-LHC**

Soutenue publiquement le 27 novembre 2009 devant le jury composé de :

Mr. L. Dusseau	Professeur, IES, Université Montpellier II	Directeur de thèse
Mr. G. Sarabayrouse	Directeur de Recherche, CNRS-LAAS, Toulouse	Rapporteur
Mr. B. Barelaud	Professeur, XLIM, Université de Limoges	Rapporteur
Mr. E. Tournié	Professeur, IES, Université Montpellier II	Examinateur
Mr. F. Wrobel	Maître de conférence, IES, Université Montpellier II	Examinateur
Mme. M. G. Pia	Directeur de Recherche, INFN, Genova, Italie	Examinateur
Mr. M. Moll	Docteur, CERN, Genève, Suisse	Examinateur

Préparée au :

Centre Européen de Recherche Nucléaire (CERN)

Genève 23, CH-1211, Suisse

Académie de Montpellier

UNIVERSITE MONTPELLIER II
SCIENCES ET TECHNIQUES DU LANGUEDOC

T H E S E

pour obtenir le grade de

DOCTEUR DE L'UNIVERSITE MONTPELLIER II

Discipline : Electronique

Formation Doctorale : Electronique – composants et systèmes

Ecole Doctorale : Information, Structures et Systèmes

Présentée par

Julien Mekki

Caractérisation et optimization des performances de capteurs
pour la métrologie du rayonnement dans les expériences de
physique des hautes énergies des futurs accélérateurs LHC et
Super-LHC du CERN

Soutenue publiquement le 27 novembre 2009 devant le jury composé de :

Mr. L. Dusseau	Professeur, IES, Université Montpellier II	Directeur de thèse
Mr. G. Sarrabayrouse	Directeur de Recherche, CNRS-LAAS, Toulouse	Rapporteur
Mr. B. Barelaud	Professeur, XLIM, Université de Limoges	Rapporteur
Mr. E. Tournié	Professeur, IES, Université Montpellier II	Examinateur
Mr. F. Wrobel	Maître de conférence, IES, Université Montpellier II	Examinateur
Mme. M. G. Pia	Directeur de Recherche, INFN, Genova, Italie	Examinateur
Mr. M. Moll	Docteur, CERN, Genève, Suisse	Examinateur

Préparée au :

Centre Européen de Recherche Nucléaire (CERN)

Genève 23, CH-1211, Suisse

« Science sans conscience n'est que ruine de l'âme. »

Rabelais, « Pantagruel »

A la mémoire de mon père ...

Résumé

De nos jours, afin de vérifier les théories fondamentales telles que le “Modèle Standard” des particules élémentaires qui permettraient d’expliquer et de comprendre la nature et la constitution de la matière, les physiciens des hautes énergies ont besoin de construire de nouvelles expériences.

Le Centre Européen pour la Recherche Nucléaire (CERN) a été fondé dans ce but en 1954, à Genève (Suisse). Ce centre de recherche a vu le jour grâce à un effort européen commun, dont l’objectif était de construire de nouveaux accélérateurs de particules pour étudier les constituants fondamentaux de la matière et leurs interactions mutuelles. Cette organisation compte aujourd’hui parmi les plus importants centres scientifiques de la planète. Vingt états européens ainsi que 65 pays sont impliqués, avec la participation d’environ 9000 scientifiques provenant de 600 instituts et universités.

Dans le monde, plusieurs accélérateurs de particules et des expériences de physique des hautes énergies ont été construits dans le but de répondre à ces questions fondamentales : de quoi est constituée la matière de l’univers ? Qu’est ce que la matière et l’énergie noire ? Quels étaient les constituants fondamentaux de la matière juste après le « Big Bang » ? etc...

Au CERN, l’accélérateur de particules SPS (Super Proton Synchrotron) et le LEP (Large Electron Positron) ont déjà permis la découverte d’un grand nombre de particules et d’interactions, aujourd’hui incluses dans la théorie existante. Néanmoins, beaucoup de questions restent encore sans réponse et les particules prédictes par la théorie non pas encore été toutes détectées. L’exemple le plus connu de ces particules est sans doute le fameux « boson de Higgs », particule prédicta par la théorie, mais jamais encore mise en évidence avec les moyens disponibles dans la génération précédente d’expériences. Le LEP par exemple, ne mettait pas en jeu des énergies suffisantes pour libérer ce type de particule. Le boson de Higgs étant relativement massif, il nécessite d’avoir recours à des accélérateurs en capacité de délivrer une énergie plus importante, et par conséquent d’augmenter la vitesse des particules accélérées.

Dans l’intention de répondre à toutes ces questions, un nouvel accélérateur de particules a été développé au CERN : un accélérateur circulaire baptisé LHC pour « Large Hadron

Collider ». Le LHC permettra d'accélérer des hadrons (dans ce cas précis, il sera question de collision proton-proton ou bien ion-ion). Grâce à ce nouvel instrument, il sera possible d'étudier la matière telle qu'elle existait quelques instants après le « Big-Bang ». Une telle expérience devrait permettre d'atteindre des grandeurs physiques jamais obtenues par le passé, telles que le nombre de collisions de particules par seconde et par cm² à l'intérieur des expériences, jusqu'à 10³⁴ (10³⁵ pour le Super-LHC) et une énergie des particules accélérées pouvant atteindre les 7 TeV. Cinq expériences de physique des hautes énergies (ATLAS (A Toroidal LHC ApparatuS), CMS (Compact Muon Solenoid), LHCb (Large Hadron Collider beauty experiment), ALICE (A Large Ion Collider Experiment) et TOTEM (TOTal and Elastic Measurement) sont situées en différents points de l'accélérateur (aux endroits où les 2 faisceaux de particules vont rentrer en collision).

Afin d'identifier, de compter et de suivre les particules libérées lors de la collision d'hadrons, des détecteurs de particules ont été disposés tout autour des points d'interactions. Un détecteur est généralement constitué d'un ensemble de sous-détecteurs, ainsi que d'une électronique de lecture qui communique avec un système d'analyse et de reconstruction d'événements.

A l'intérieur de chaque expérience, le champ de radiation engendré par les collisions de protons sera composé d'une multitude de particules possédant une grande diversité d'énergies. Ce champ de particules aura une conséquence fondamentale sur les composants environnant les points d'interactions, puisque non seulement les détecteurs, mais aussi toute l'électronique qui les constituent pourront être endommagés.

Dans le but d'assurer une qualité de mesure sur toute la durée de fonctionnement de l'accélérateur, ce champ radiatif doit être précisément contrôlé et caractérisé. Pour cette raison, des capteurs pour la métrologie des rayonnements ont été caractérisés et installés dans les expériences du LHC ainsi que dans le tunnel.

A l'intérieur des expériences, ces capteurs peuvent être installés en deux types d'emplacements. Proche du point d'interaction, le champ de radiation très intense sera dominé par les hadrons chargés provenant directement de la collision de particules. La dose totale est estimée à près de 1×10⁵ Gy et la fluence équivalente silicium (Φ_{eq}) attendue supérieure à 1×10¹⁴ n_{eq}/cm². Plus loin du point d'interaction, au contraire, le champ de radiation sera principalement composé de particules secondaires telles que les neutrons, les électrons et les photons résultant de l'interaction des hadrons chargés avec les sous détecteurs. Il est donc important que les

capteurs utilisés puissent résister à un environnement radiatif très hostile, mais soient aussi sensibles à des champs moins intenses. En fonction de leur localisation à l'intérieur de l'expérience, certains capteurs peuvent aussi n'être exposés qu'à une dose totale de quelques Gy seulement et à une fluence équivalente de l'ordre de $1 \times 10^8 \text{ n}_{\text{eq}}/\text{cm}^2$.

Dans une étude précédente [Rav06], un système complet pour la métrologie du rayonnement à l'intérieur des expériences du LHC a été développé. Il est constitué de RadFETs (Radiation-sensing Field Effect Transistors) pour la mesure de la dose ionisante (TID), ainsi que de diodes PIN pour contrôler la fluence équivalente. Ces deux types de composants sont utilisés pour quantifier le champ de radiation du LHC durant toute sa durée de fonctionnement.

Afin de permettre un maniement simple, de protéger les capteurs inclus dans ce système et dans le but de fournir une connectique standard pour la lecture de ces capteurs, un support en PCB (Printed Circuit Board) ainsi que son boîtier ont été spécialement conçus et produits au CERN. Les RadFETs, les diodes PIN ainsi qu'un capteur de température sont montés sur ce support. Ce dernier permet la mesure de la température ambiante durant la lecture des capteurs.

La mesure de la dose ionisante totale (TID) effectuée à l'aide des capteurs RadFETs peut être influencée par ces mêmes supports et boîtiers qui, selon leurs matériaux et leurs géométries, peuvent induire des erreurs dans la mesure de dose ionisante.

L'environnement radiatif du LHC et ceux de ces 5 expériences seront détaillés dans le chapitre 2 de cette thèse ainsi que les effets que cet environnement pourra avoir sur l'électronique et les détecteurs présents dans ce champ de particules. Afin d'obtenir une meilleure compréhension des effets des radiations sur les composants et matériaux utilisés durant cette thèse, une brève description de l'interaction des principales particules présentent dans le LHC avec la matière sera présentée dans le chapitre 3.

Comme mentionné ci-dessus, le support ainsi que le boîtier du système pour la métrologie des radiations pourront influencer la mesure de dose ionisante effectuée avec des dosimètres RadFETs. Une étude complète menée à l'aide de l'outil Geant4 (outil permettant de simuler l'interaction des particules avec la matière) a été réalisée afin d'évaluer cette influence et sera présentée dans le chapitre 4.

Les diodes PIN utilisées dans ce système avaient été caractérisées dans une étude précédente [Rav06] pour une utilisation dans le LHC. Néanmoins, dans le but de les utiliser

aussi pour le Super-LHC (même accélérateur que le LHC, sauf que la luminosité atteindra 10^{35} $\text{cm}^{-2} \cdot \text{s}^{-1}$ à l'intérieur du Super-LHC), où le niveau de radiation sera multiplié par un facteur 10 et où la fluence équivalente pourra atteindre une valeur de l'ordre de $10^{16} \text{ n}_{\text{eq}}/\text{cm}^2$ (dans les zones proches du point d'interaction), une étude complète sur la réponse aux radiations de ces diodes jusqu'à très hautes fluences a été réalisée. Celle-ci sera présentée dans le chapitre 5. Elle est basée sur une meilleure compréhension des phénomènes physiques entrant en jeu dans la diode irradiée à de telles fluences. Ceci permettra d'obtenir une formule de prédiction de la réponse aux radiations de la diode jusqu'à des fluences très élevées comme il est prévu d'atteindre lors du fonctionnement du Super-LHC.

Le chapitre 6 est dédié aux perspectives découlant de ce travail de thèse. L'objectif étant de réaliser dans l'avenir notre propre dosimètre pour la mesure de fluence équivalente, des détecteurs silicium fabriqués avec différents types de matériaux et géométries, ainsi que d'autres types de diodes silicium ont été testés. L'objectif est ici de donner quelques pistes et suggestions pour le futur au sujet des principaux paramètres clés de l'optimisation de la réponse aux radiations des diodes silicium.

Le « Large Hadron Collider »

Le champ de radiation à l'intérieur du LHC différera complètement de celui rencontré dans le monde de la dosimétrie comme par exemple pour les applications médicales. Il sera composé d'une grande diversité de particules et d'énergies provenant directement de la collision entre les deux faisceaux de protons, ou bien indirectement suite à l'interaction des particules créées par cette collision avec les sous détecteurs qui entourent le point d'interaction. Ce champ radiatif a été simulé pour les différentes expériences du LHC, à l'aide d'outils de simulation utilisant le code Monte Carlo lors de précédentes études [Daw00], [Huh95]. Ces simulations ont montré que l'intensité du champ radiatif peut varier de 5 ou 6 ordres de grandeurs selon la localisation à l'intérieur de l'expérience.

Le LHC est un « collisionneur » de protons (ou bien d'ions) qui a été construit dans le tunnel du LEP, d'une longueur de 26.6 km situé 100 mètres sous terre. Avant d'être injectées, les particules sont accélérées par l'intermédiaire de deux accélérateurs plus petits, le « Proton Synchrotron »(PS) et le « Super Proton Synchrotron » (SPS). Lorsque que dans le SPS, les protons atteignent une énergie de 450 GeV, ils sont injectés dans le LHC, où ils atteignent une énergie de 7 TeV avant la collision des 2 faisceaux. Lors du fonctionnement du LHC, 10^{34}

collisions de protons se produiront par cm^2 et seconde. Cette grandeur caractérise la « luminosité » de l'accélérateur. Lors de l'augmentation de la puissance du LHC (le Super-LHC), la luminosité ainsi que le niveau de radiation de l'accélérateur seront multipliés par un facteur 10, soit une luminosité de $10^{35} \text{ cm}^{-2} \cdot \text{s}^{-1}$. Comme décrit dans l'introduction, les collisions des deux faisceaux de particules auront lieu dans 5 expériences toutes conçues selon le même modèle, mais dont chacune offrira la possibilité d'étudier un sujet différent de la physique des particules.

Les détecteurs permettant de retracer le trajet des particules émergeantes de la collision et ainsi de déterminer leur type, sont situés dans la région centrale entourant le point d'interaction et sont donc exposés à un champ de radiation très intense. Cette région est suivie par 2 types de calorimètres permettant de stopper les particules émergeantes et ainsi de mesurer leur énergie initiale. Les particules supposées ne pas être stoppées dans les calorimètres sont les muons et les neutrinos. Un troisième sous détecteurs est donc rajouté dans l'expérience à la suite des calorimètres, la « chambre à muon » permettant de détecter les muons. Quand aux neutrinos, puisque qu'ils n'interagissent pas avec la matière et ne peuvent donc pas être détectés, ils seront évalués comme énergie manquante lors de l'analyse des données.

La luminosité prévue pour les expériences ATLAS et CMS du LHC est de $10^{34} \text{ cm}^{-2} \cdot \text{s}^{-1}$, alors que pour ALICE et LHCb elle sera plus faible, comprise entre $10^{27} \text{ cm}^{-2} \cdot \text{s}^{-1}$ et $10^{30} \text{ cm}^{-2} \cdot \text{s}^{-1}$ pour ALICE et $2 \times 10^{32} \text{ cm}^{-2} \cdot \text{s}^{-1}$ pour LHCb. Cependant, certaines parties de ces dernières expériences pourraient être tout de même soumises à un champ radiatif intense.

Le champ de radiation des différentes expériences est susceptible d'affecter les composants électroniques et ce de différentes manières : les effets de dépôt de dose ionisante (TID) créent des phénomènes de piégeage et d'interface au niveau des isolants; les effets de déplacements sont liés à la création de défauts à l'intérieur de structures cristallines suite à l'interaction de neutrons et de particules chargées avec celles-ci. Enfin, les effets singuliers apparaissant lors de l'interaction d'une particule unique avec un circuit digital, pouvant engendrer la perte d'information numérique ou même la destruction totale du circuit.

L'influence du boîtier des capteurs sur la mesure de dose ionisante

L'un des capteurs utilisés durant cette thèse est le transistor de type MOSFET optimisé pour la mesure de dose ionisante, le « *RadFET* ». A la différence du transistor MOSFET conventionnel, celui-ci possède un oxyde épais, le rendant plus sensible aux radiations. La tension de seuil du RadFET varie à mesure que celui-ci est irradié. La mesure de cette tension devient donc un paramètre d'évaluation de la dose ionisante déposée dans l'oxyde de grille.

Comme décrit dans la section précédente, l'environnement radiatif de chaque expérience a été simulé à l'aide de codes Monte Carlo. Même si celui-ci est suffisamment bien prédit, il n'en reste pas moins que la dose déposée par différent types de particules dans les dosimètres, n'est pas connue. Il est clair qu'il n'est pas possible d'évaluer expérimentalement l'impact des radiations sur les dosimètres ainsi que sur leur boîtier pour tous les types de particules et toutes les énergies présentes dans le LHC. Pour cela il est nécessaire d'effectuer d'autres simulations. De plus, l'influence du boîtier sur la mesure de dose déposée dans les dosimètres introduit une difficulté supplémentaire. En effet, lors du passage des particules à travers le boîtier, différents mécanismes physiques tels que la création de particules secondaires ou l'absorption totale de la particule incidente conduisant à la perte d'informations peuvent se produire. Pour toutes ces raisons, il est donc important de comprendre l'influence du boîtier sur cette mesure afin de l'optimiser.

Dans ce travail de thèse, la réponse aux radiations des dosimètres RadFETs dans un tel environnement radiatif a été étudiée à l'aide de l'outil de simulation d'interactions particules-matière « *Geant4* ». Une application a été spécialement développée pour cette étude, décrivant la géométrie et le matériau des dosimètres ainsi que ceux du boîtier.

Dans ce chapitre, l'outil de simulation Geant4 est présenté, suivi par une description détaillée des dosimètres RadFETs ainsi que de leur support et boîtier. Les résultats obtenus lors d'une précédente étude [Rav06] au cours de laquelle les RadFETs et le boîtier ont été irradiés au moyen de neutrons rapides et de protons d'énergie de 254 MeV sont alors présentés. Sont aussi présentées dans cette partie, les simulations évaluant l'impact du boîtier sur la mesure de dose pour différents types de particules et d'énergies, puis finalement, l'influence que

possèdera ce support et boîtier dans un champ de particules rencontré dans une typique expérience du LHC, l'expérience « *ATLAS* ».

L'influence du support et du boîtier sur la mesure de dose des RadFETs a été évaluée en deux endroits de l'expérience *ATLAS*, l'un dans la région centrale de l'expérience où le champ de particules est dominé par des hadrons chargés, résultant directement de la collision des deux faisceaux de protons, le « *Inner detector* ». Puis l'autre dans une région plus éloignée du point d'interaction, le « *Liquid Argon calorimeter* », où le champ est plutôt dominé par des particules secondaires telles que les électrons, qui proviennent de l'interaction des hadrons chargés avec les sous-détecteurs. Pour ces simulations, un couvercle de boîtier en Alumine (ou céramique (Al_2O_3)), d'une épaisseur de 260 μm a été utilisé, puisque cette configuration avait été sélectionnée pour l'utilisation des dosimètres dans le LHC.

Ces simulations ont montré que l'utilisation de ce couvercle pouvait conduire à une augmentation de la dose mesurée pouvant aller jusqu'à 25 %. Cette augmentation dépend de l'emplacement où les dosimètres seront installés à l'intérieur de l'expérience. L'influence de ce couvercle sur la mesure de dose et certainement moins importante que la précision de mesure des RadFETs dans un tel environnement radiatif, cependant celle-ci n'est pas négligeable puisque la différence de mesure entre des dosimètres protégés et non protégés par ce couvercle peut différer de 25 %. La sélection d'un support et boîtier approprié est donc une question importante pour la mesure de dose ionisante dans le cadre d'expériences pour la physique des hautes énergies.

Les diodes PIN utilisées comme dosimètres

Comme discuté dans la partie précédente le système de métrologie des radiations à l'intérieur des expériences du LHC, effectue la mesure de dose ionisante au moyen de dosimètres RadFETs. Les défauts de déplacements que les différents types de rayonnements peuvent engendrer à l'intérieur du silicium conduisent à considérer une fluence équivalente mesurée à l'aide de diodes PIN polarisées en direct. Ce type de composants a déjà été caractérisé dans des études précédentes [Pro89], [Sop91], [Ros03], principalement pour de la dosimétrie dans le domaine médical et militaire.

A l'intérieur du LHC, la fluence équivalente pourra être comprise entre $10^8 - 10^{10}$ et $10^{14} - 10^{15}$ $\text{n}_{\text{eq}}/\text{cm}^2$, en fonction de la localisation à l'intérieur des expériences. Lors de l'augmentation de la puissance, le LHC devenant le Super-LHC, le niveau de radiation sera amplifié d'un

facteur 10, en raison de l'augmentation de $10^{34} \text{ cm}^{-2} \cdot \text{s}^{-1}$ à $10^{35} \text{ cm}^{-2} \cdot \text{s}^{-1}$ de la luminosité. Dans la partie centrale de l'expérience, proche du point d'interaction, les détecteurs pourront alors être exposés à une fluence équivalente pouvant atteindre $10^{16} \text{ n}_{\text{eq}}/\text{cm}^2$.

Les diodes PIN silicium commerciales *BPW34FS* utilisées pour cette étude sont produites par la société OSRAM. Ce type de diode PIN a déjà été caractérisé au CERN lors de précédentes études [Mal92], [Rav06], [Rav08b]. Pour la mesure de radiations, la diode PIN est polarisée en mode direct. La tension est mesurée en injectant un courant constant dans la diode et ce pendant une courte durée afin d'éviter les effets d'échauffements. Grâce à cette méthode, la variation de la tension directe en fonction de la fluence donne une information sur la fluence équivalente reçue.

Ces précédentes études ont montré qu'un courant direct de 1 mA injecté dans la diode pendant une durée de 700 ms est un bon choix pour une utilisation dans les expériences du LHC. Dans cette configuration, la diode BPW34FS présente une sensibilité aux radiations dans une gamme de fluence qui s'étend de $2 \times 10^{12} \text{ n}_{\text{eq}}/\text{cm}^2$ à $4 \times 10^{14} \text{ n}_{\text{eq}}/\text{cm}^2$.

Cependant, pour mesurer des niveaux de radiations comme ceux prévus lors du fonctionnement du Super-LHC, où la fluence équivalente pourra atteindre jusqu'à $10^{16} \text{ n}_{\text{eq}}/\text{cm}^2$ en certains endroits, il est nécessaire de trouver une nouvelle solution permettant d'étendre la mesure de la diode à de plus hautes fluences.

Pour répondre à cette question, dans ce chapitre sera présentée une évaluation détaillée de la réponse aux radiations de ce type de diode PIN exposée à un faisceau de proton de très haute énergie (24 GeV/c). Tout d'abord une étude préliminaire sera présentée, basée sur la réponse aux radiations des diodes lorsque celles-ci seront alimentés par un courant direct entre 10 µA et 25 mA avec une durée d'injection égale à 50 ms. Celle-ci montrera que la diode doit être mesurée avec un courant de lecture faible, afin d'éviter les effets d'échauffements lors de la lecture. De plus, cette étude révèle, qu'il est aussi possible d'éviter que la diode ne se comporte comme un thyristor [Rav06], [Rav08b] lorsque celle-ci est fortement irradiée et mesurée avec un courant de lecture élevé.

Ensuite, une nouvelle approche permettant de prédire la réponse aux radiations de cette diode jusqu'à de très hautes fluences est proposée. Celle-ci est basée sur la théorie de la « relaxation des matériaux » qui sera aussi décrite dans ce chapitre. Celle-ci permet d'obtenir

une meilleure compréhension du comportement de la diode PIN, lorsque celle-ci est fortement irradiée.

A partir de cette théorie, il est possible d'obtenir une fonction permettant de décrire les courbes expérimentales courant-tension (I-V) de la diode, pour toutes les fluences équivalentes $\Phi_{\text{eq}} \geq 1 \times 10^{13} \text{ n}_{\text{eq}}/\text{cm}^2$ et pour tous les courants de lecture $I_F \leq 1 \text{ mA}$. L'évaluation des ajustements des différentes courbes I-V a permis d'obtenir un nouveau modèle de prédiction de la variation de la tension directe de la diode en fonction de la fluence équivalente. Cette nouvelle approche permet d'étendre la mesure de radiations jusqu'à des fluences très élevées comme celles attendues lors du fonctionnement du Super-LHC (pour cette étude les diodes ont été irradiées jusqu'à une fluence de $6.3 \times 10^{15} \text{ n}_{\text{eq}}/\text{cm}^2$, ce qui représente 60 % de la fluence maximum du Super-LHC). Elle offre aussi la possibilité de prédire la réponse aux radiations des diodes PIN, pour des mesures effectuées avec tous les courants de lecture $I_F \leq 1 \text{ mA}$.

Pour conclure cette étude, afin d'être en mesure de donner quelques suggestions sur la température optimale lors de l'utilisation de ces dosimètres pour le Super-LHC, l'influence de la température sur la mesure a été qualitativement évaluée et sera présentée à la fin de ce chapitre. Cette étude révèle que la sensibilité de la diode peut être étendue à de plus hautes fluences, si celles-ci sont mesurées à basse température.

Perspectives de travail

Sur la durée de fonctionnement du LHC, en fonction de la localisation à l'intérieur des expériences, la fluence équivalente sera comprise entre 10^9 - 10^{10} et 10^{14} - $10^{15} \text{ n}_{\text{eq}}/\text{cm}^2$ ($10^{16} \text{ n}_{\text{eq}}/\text{cm}^2$ pour le Super-LHC). Grâce à la nouvelle approche présentée dans cette thèse, les diodes PIN BPW34FS permettent de mesurer une large gamme de fluences équivalentes jusqu'à des valeurs supérieures à $10^{15} \text{ n}_{\text{eq}}/\text{cm}^2$. Néanmoins ce type de diode n'est pas sensible pour des fluences plus faibles que $2 \times 10^{12} \text{ n}_{\text{eq}}/\text{cm}^2$. Bien qu'il soit possible de mesurer des faibles fluences soit en pré-irradiant la diode (avec cette méthode il est possible de mesurer de fluences à partir d'environ $8 \times 10^9 \text{ n}_{\text{eq}}/\text{cm}^2$), soit en utilisant un autre type de diode (dans le cas de cette application il est question de la diode CMRP, mais celle-ci coûte relativement cher), d'autres composants ont été testés durant cette thèse.

Dans l'intention de développer notre propre dosimètre, une étude a été dirigée sur des détecteurs silicium possédant une haute résistivité, fabriqués à partir de différentes techniques

de croissance du silicium et différentes géométries ainsi que sur un autre type de diode dont l'épaisseur est plus élevée que celle des BPW34FS.

L'étude menée sur les détecteurs silicium et sur l'autre type de diode silicium a été effectuée en irradiant les pièces avec un faisceau de proton d'énergie 24 GeV/c pour des fluences allant de $\Phi_{eq} \approx 10^9 n_{eq}/cm^2$ à quelques $10^{14} n_{eq}/cm^2$. Dans ce chapitre, les différentes techniques de croissance du silicium sont brièvement présentées. De plus, les résultats sur l'étude de la réponse aux radiations de ces différents détecteurs en fonction du matériau utilisé, de l'épaisseur et de la surface sensible de la diode ainsi que ceux des diodes LBSD sont présentés et discutés.

Le résultat de cette étude montre que le paramètre qui influence principalement la réponse du dosimètre aux radiations est l'épaisseur du composant. Les composants les plus épais présentent des seuils de détection plus faibles et montrent une sensibilité augmentée d'un facteur 25. L'utilisation de dosimètres épais dans le LHC pour mesurer de faibles fluences se révèle donc être une bonne solution.

Pour la mesure de très haute fluences, il serait judicieux dans l'avenir de mener sur ce type de composants une étude complète, similaire à celle menée sur les BPW34FS et de caractériser leur réponse aux radiations avec la nouvelle approche présentée dans ce travail de thèse.

Dans ce chapitre, une solution est proposée dans le but de mesurer la gamme complète des fluences rencontrées dans le LHC. Elle consiste en l'utilisation de détecteurs silicium épais pour la mesure de faibles fluences et de détecteurs plus fins pour les hautes fluences. De plus une pré-irradiation de ces composants pourra aussi être effectuée afin de détecter des fluences encore plus faibles. Il serait enfin intéressant de tester des détecteurs encore plus fins que ceux présentés dans cette thèse, pour étudier leur comportement à très haute fluences, comme celles prévues lors du fonctionnement du Super-LHC.

Contents

CHAPTER 1	INTRODUCTION.....	1
CHAPTER 2	LHC RADIATION ENVIRONMENT AND ITS EFFECTS ON ELECTRONIC DEVICES	5
2.1	THE LARGE HADRON COLLIDER (LHC)	6
2.2	THE EXPERIMENTS.....	10
2.2.1	<i>The radiation environment of the two biggest experiments: ATLAS and CMS.....</i>	10
2.2.2	<i>The radiation environment of two low luminosity experiments: ALICE and LHCb.....</i>	15
2.3	RADIATION ENVIRONMENT EFFECTS ON ELECTRONIC DEVICES.....	16
2.3.1	<i>Total Ionizing Dose effects (TID).....</i>	16
2.3.2	<i>Displacement damage effects</i>	17
2.3.3	<i>Single Event effects.....</i>	19
2.4	CONCLUSION	20
CHAPTER 3	PARTICLE INTERACTIONS WITH MATTER.....	21
3.1	INTERACTION OF CHARGED PARTICLES WITH MATTER.....	22
3.1.1	<i>Charged hadrons</i>	22
3.1.2	<i>Charged leptons</i>	26
3.2	INTERACTION OF PHOTONS WITH MATTER.....	30
3.2.1	<i>The photoelectric effect.....</i>	31
3.2.2	<i>Compton effect.....</i>	32
3.2.3	<i>Pair production effect.....</i>	34
3.3	INTERACTION OF NEUTRONS WITH MATTER	36
3.4	CONCLUSION	36
CHAPTER 4	PACKAGING EFFECTS ON RADFET SENSORS FOR THE RADIATION MONITORING PROJECT	39
4.1	WHAT IS THE GEANT4 TOOLKIT?	41
4.1.1	<i>Geant4 properties</i>	41
4.1.2	<i>User action classes</i>	42
4.2	DESCRIPTION OF THE SYSTEM FOR TOTAL IONIZING DOSE MEASUREMENTS AT THE LHC EXPERIMENTS.....	46
4.3	PREVIOUS EXPERIMENTAL STUDIES	49
4.4	GEANT4 APPLICATION	50
4.4.1	<i>Simulation geometry</i>	51
4.4.2	<i>Physics processes.....</i>	53
4.5	RADFET PACKAGING EFFECTS EVALUATED USING GEANT4 SIMULATIONS	55

4.5.1	<i>Results for charged hadron simulations</i>	55
4.5.2	<i>Results for charged lepton simulations</i>	65
4.5.3	<i>Results for photon simulations</i>	70
4.5.4	<i>Results for neutrons simulations</i>	74
4.6	RADFET SENSORS IN THE ATLAS DETECTOR	75
4.6.1	<i>Simulation of dose measurements in the ATLAS Detector</i>	75
4.6.2	<i>Refined simulations assuming a smaller sensitive volume</i>	81
4.7	CONCLUSION	86
CHAPTER 5 FORWARD BIASED PIN DIODES USED AS DOSIMETERS		87
5.1	THE COMMERCIAL OSRAM BPW34FS SILICON PIN DIODE	89
5.2	SUMMARY OF PREVIOUS EXPERIMENTAL STUDIES	90
5.2.1	<i>First study aiming at using BPW34F as neutron sensor</i>	90
5.2.2	<i>Characterization and calibration of the BPW34F PIN diode for the LHC experiment</i>	91
5.3	SILICON PIN DIODE MEASUREMENT SETUP.....	96
5.4	PRELIMINARY STUDY OF THE BPW34FS RADIATION RESPONSE.....	99
5.4.1	<i>New Readout protocol</i>	99
5.4.2	<i>BPW34FS radiation response</i>	101
5.4.3	<i>Self-heating effect</i>	104
5.5	NEW APPROACH IN PREDICTING THE RADIATION RESPONSE OF PIN DIODES UP TO VERY HIGH FLUENCES.....	108
5.5.1	<i>Measurement method and equipment</i>	109
5.5.2	<i>Experimental results</i>	111
5.5.3	<i>Analysis of the Current-Voltage characteristics</i>	113
5.5.4	<i>Qualitative evaluation of the temperature dependence</i>	123
5.6	CONCLUSION	129
CHAPTER 6 PERSPECTIVES AND OUTLOOK ON FUTURE STUDIES		131
6.1	SILICON DETECTORS.....	132
6.1.1	<i>Silicon growth method</i>	132
6.1.2	<i>Investigated silicon detectors</i>	134
6.1.3	<i>Comparison between MCz and FZ silicon detectors</i>	135
6.1.4	<i>Influence of the detector thickness</i>	137
6.1.5	<i>Influence of the active area</i>	139
6.2	LBSD SILICON PIN DIODES	141
6.3	CONCLUSION	144
CHAPTER 7 SUMMARY AND CONCLUSIONS.....		147
APPENDIX A VALUE SPECIFICATIONS OF THE ENERGY DEPOSITED IN THE RADFET SENSORS		151
LIST OF PUBLICATIONS		158
ACKNOWLEDGEMENTS		160
BIBLIOGRAPHY		162

Chapter 1

Introduction

Particle physicists aim at confirming existing theories such as the Standard Model of elementary particle (SM) [Gla61], [Wei67], and [Sva68]. Understanding the nature and the consistency of matter originating from the universe requires the building of large equipments to run high energy physics experiments.

For this reason, the European Organization for Nuclear Research (CERN) was founded in 1954 in Geneva (Switzerland) as a joint European effort for the purpose of building new particle accelerators in order to study the fundamental constituents of matter and their mutual interactions. This organization is today one of the world's largest and most successful scientific laboratories. 20 European member states and 65 countries are involved in the CERN international collaboration, with around 9000 scientists from 600 institutes and universities all over the world.

Several particle accelerators and high energy physics experiments have been built around the world for the purpose of discovering fundaments of the matter. At CERN the Super Proton Synchrotron (SPS) and the LEP (Large Electron Positron) collider allowed to discover a whole set of new particles and particle interactions which are well predicted by the existing theories. Nevertheless, questions remain open and not all the particles predicted by the theory have been detected yet, as for example the most famous one nowadays: "the Higgs Boson". This particle is clearly predicted by the existing theory, but never appeared yet up to the highest energies reached in LEP collisions. For releasing such a massive particle, colliding particles

used in the experiments need more energy and consequently more speed than the one currently provided by the existing accelerators.

With the intention of answering to all these questions, a new large circular particle accelerator has been built at CERN, the “Large Hadron Collider” (LHC). It is a new experiment which will serve to study matter and sub-nuclear scale by colliding protons or ions. Such experiment will reach unprecedented luminosity ($10^{34} \text{ cm}^{-2} \cdot \text{s}^{-1}$) and center of mass (14 TeV due to the collision of 7 TeV proton beams) to verify the existence of the Higgs boson and other particles. Five large experiments are attached to the LHC as: ATLAS, CMS, LHCb, ALICE and TOTEM.

With the aim to identify, count and trace particles moving outwards from the interaction point, the result of a collision has to be observed through experimental devices called “*detectors*”. A detector is usually composed by many sub-detectors, and all of them are connected to readout electronic and computer system for analyzing and reconstructing events.

Inside all experiments, the complex radiation field caused by the proton-proton collision will be composed by different particles types and energies. In this particle field, not only the detectors but also all the equipment for reading and measuring them can be affected by radiation damage. In order to ensure reliability of the measurements over time, this radiation field has to be precisely characterized and monitored. For this purpose, radiation monitoring sensors have been characterized and installed in four of the five LHC experiments as in the various sub-detectors which compose these experiments. Some of them are also installed in the LHC tunnel and experimental areas cavern walls.

The Radiation Monitoring equipment can be installed either close to the interaction point where the radiation field will be very intense; dominated by charged hadrons originating from the proton-proton collision and where the Total Ionizing Dose (TID)¹ will be of about $1 \times 10^5 \text{ Gy}$ and the 1-MeV neutron equivalent fluence (Φ_{eq}) of more than $1 \times 10^{14} \text{ n}_{\text{eq}}/\text{cm}^2$, or in the outer region of the experiments. Contrary to the innermost region, in the outer region the radiation field is mainly composed by secondary particles, such as neutrons and photons, resulting from the interaction of charged hadrons with sub-detectors. Since the intensity and composition of the radiation field can significantly vary depending on the location of the radiation monitoring equipment, the sensors used have to withstand a high intensity radiation field, but also have to be sensitive to lower intensity field where the TID is some Gy and the Φ_{eq} is around $1 \times 10^8 \text{ cm}^{-2}$.

In previous study [Rav06], a complete radiation monitoring equipment has been developed for this purpose. It includes Radiation-sensing Metal Oxide Semiconductor sensors

¹ Definition of TID and Φ_{eq} are given in Chapter 2

(RadFETs) for measuring the TID and commercial silicon PIN diodes for monitoring the 1-MeV equivalent neutron fluences. Both kind of devices used as radiation monitoring sensors are employed for quantifying the radiation field over a full LHC lifetime.

In addition, to allow easy handling and to provide a standard connectivity for reading sensors, an integrated PCB carrier as the conception of a dedicated packaging suitable for the installation into LHC experiments were designed and produced at CERN. It allows carrying RadFET sensors, PIN diodes and temperature sensors. The latter one being used for recording the temperature during measurement, since such devices are very sensitive to temperature variation.

However, especially for RadFET sensors this custom-made packaging may influence the measure of ionizing dose, since the use of inappropriate material and geometry close to or around them can modify their radiation response inducing errors in the measured dose.

In this thesis, a description of the LHC radiation environment and its five experiments (ATLAS, CMS, LHCb, ALICE and TOTEM) is given in Chapter 2 . This environment's possible effects on the electronic devices and particle detectors are also presented. For a deeper understanding on how radiations transport and lose their energy in materials, an analysis of the particle interactions with matter for the main particles present in the radiation field of the LHC is given in Chapter 3.

Since the packaging surrounding the RadFET sensors might influence their TID measurement, a complete investigation on its influence on the measured ionizing dose has been carried out using the GEANT4 Monte Carlo simulation code and presented in Chapter 4. After a detailed assessment on the influence of each particle present in the complex radiation field of LHC experiments, a study for evaluating the packaging effects on RadFET sensors in two specific locations of the ATLAS experiments has been carried out.

Furthermore, in order to monitor equivalent fluences as expected for the upgrade of the LHC, the Super-LHC, where the luminosity will be increased by a factor of 10 ($10^{35} \text{ cm}^{-2} \cdot \text{s}^{-1}$) and where the innermost detectors could be exposed to equivalent fluences up to $1 \times 10^{16} \text{ n}_{\text{eq}}/\text{cm}^2$, a complete study on the commercial PIN diode already employed in the Radiation Monitoring equipment has been performed in view to optimize their utilization for the next generation of high energy physics experiments. This study, presented in Chapter 5, is based on a comprehensive analysis of the diode's radiation response, which allows predicting their response up to very high fluences as expected for the Super-LHC.

Finally, Chapter 6 is entirely dedicated to the future and perspectives of this thesis work. With the intention to produce our specific custom-made radiation sensors for monitoring

equivalent fluences, the radiation response of several silicon detectors and silicon PIN diodes, made from diverse producers, with different materials and geometries have been evaluated in order to give some suggestions about the main parameters which influence their radiation response.

In addition, it should be mentioned that the devices presented in both latter chapters have been characterized and irradiated with proton irradiations performed at CERN, which allow reproducing the displacement damage effects which will potentially affect the detector performance in LHC experiments. These proton irradiations have been carried out at the CERN Proton Synchrotron (PS) accelerator in the irradiation facility IRRAD1 [Gla08].

Chapter 2

LHC radiation environment and its effects on electronic devices

With the intention to push the limits in understanding and discovering the fundamental constituents of matter, and to answer the questions of the Standard Model and beyond, experiments for high energy particle collisions are required. For this reason, in 1994 the construction of a new accelerator which will be the world's largest particle collider was approved: the Large Hadron Collider (LHC). Following this decision, the existing Large Electron Positron Collider (LEP) used at CERN which allowed colliding particles with a center of mass energy of 200 GeV was dismantled in the year 2000. This collider was limited to 200 GeV due to the energy loss by synchrotron radiation. Since charged particles are submitted to synchrotron radiation when they are accelerated in circular trajectories and that at a certain velocity the energy loss per turn is equal to the input energy, no further acceleration is possible. The only way to achieve higher energies is to increase either the radius of the collider or the mass of the colliding particles.

In LHC, the radiation field will differ strongly from the radiation environment that can be encountered where dosimeters are typically used as for instance for space applications, radiation protection, medicine etc... This complex radiation field will be composed of charged hadrons and leptons², neutrons and photons and was simulated by Monte Carlo codes [Daw00], [Huh95]. The mixed field present in the large collider is due to the emergent particles from the

² The definition of charged hadrons and charged leptons are given in Chapter 3.

high energetic proton-proton collisions and also from the interactions of these particles with the sub-detectors and materials of the experiments themselves. As it has been mentioned in [Rav06], the proportion of the different particle types in the radiation field will depend on the distance and on the angle with respect to the interaction point (i.e. the radiation environment will be unique in each sub-detector composing the experiments). For example, in the EndCap modules of the electromagnetic calorimeter of the CMS Experiment [CMS94], the Total Ionizing Dose (TID) over a 10-year LHC run is estimated to reach 100 kGy and the fast hadron fluence is expected to be within 10^{14} - 10^{15} particles/cm². These radiation levels are much lower if one considers instead the muon chamber location at the ATLAS Experiment [ATL97]. Cumulated radiation doses of some tens of mGy and hadron fluences of 10^8 particles/cm² are expected there.

In LHC experiments, all the electronic devices and systems present in this radiation field can be affected unintentionally by radiation damage. By interacting with electronic equipments, particles present within this field can release their energy into them, so that their operating characteristics can be modified. The energy deposition due to ionization, can be responsible of a charge accumulation in insulator material as for example the silicon dioxide (SiO₂) present in many electronic devices and can be responsible of the aging of MosFET transistors, optical fibers, scintillators etc... In addition, particles can create defects in the crystalline structure of semiconductor devices, which induce a modification of their properties such as the loss of performance of the silicon detectors present in LHC experiments used for tracking the emergent particles from the proton-proton collisions. Finally, the high amount of energy released by fast hadrons can be responsible for the occurrence of Single Event Effects (SEE) phenomena, which may induce digital errors in circuits and systems such as memories, microprocessor and other digital devices.

In this chapter a short description of the LHC and its High Energy Physics (HEP) experiments radiation environments is given. With the intention to give an overview to the reader about the radiation effects on electronic devices present in the collider, a short description of the different radiation damages is also introduced there.

2.1 The Large Hadron Collider (LHC)

The challenge in the modern particle physics research field is to build accelerator that can provide high energy as possible, either because the constituents to be discovered appear at very high energies, or because they are tied in complex aggregates and can be released only at

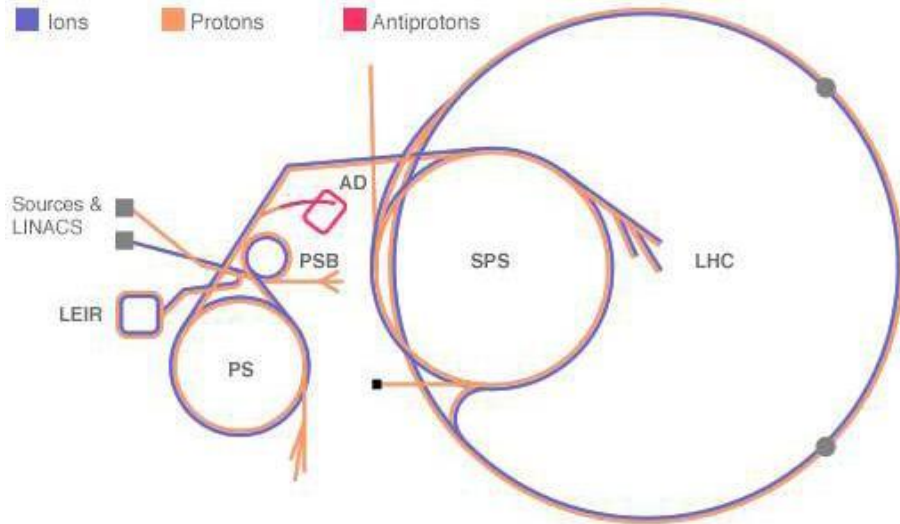


Figure 2.1: Plan of the accelerators at CERN. Before being injected in the LHC, protons are accelerated through the PS and the SPS up to 450 GeV.

such very high energies. The two main parameters for a particle accelerator are the “luminosity” and the “energy”.

The luminosity is defined as the measurement of the number of events per second generated by the collision of two particle beams and is expressed in unit of $\text{cm}^{-2} \cdot \text{s}^{-1}$. For large collider such as LHC, physical effects for which physicists are looking for, occur very rarely and are typically covered by the background produced by other effects which have larger cross-sections. As a consequence, large statistics is necessary to distinguish desired events from the background signal.

The energy of the particles is the second important factor. Most events searched by high energy physicists appear if the colliding particle energy is high enough for producing them. The LHC is the first accelerator in which the accelerated particle will exceed the border of the TeV. However, the more the energy is increased, the more the collision produces particles, which makes the discrimination between background and searched events even more difficult.

The LHC is a proton-proton (and also ion-ion) collider which has been built into the existing 26.6 kilometers LEP tunnel [CER04] at 100 m underground, with the earth shielding its radiation. As it is illustrated in Figure 2.1, before being injected into the LHC accelerator, protons are successively accelerated through the Proton Synchrotron (PS) and through the Super Proton

Synchrotron (SPS) until reaching a kinetic energy of 450 GeV. The proton having a mass 1836 times heavier than the electron, the LHC allows to achieve a center of mass energy of 14 TeV (collision of two 7 TeV proton beams). LHC is also designed to accelerate heavy ions, as for example lead. Pb-Pb collisions allow to reach a center of mass energy of 1148 TeV (or 5.5 TeV per participating nucleon) [Gou95], but it will only be happens in the future planned schedule of LHC.

In the LHC, for proton-proton collisions a luminosity of about $10^{34} \text{ cm}^{-2}\text{s}^{-1}$ ($10^{35} \text{ cm}^{-2}\text{s}^{-1}$) for the upgrade of the LHC where the radiation level will be multiplied by a factor of 10: the Super-LHC (SLHC)) can be achieved. For ion-ion collision, the luminosity can reach up to $10^{27} \text{ cm}^{-2}\text{s}^{-1}$ ($10^{28} \text{ cm}^{-2}\text{s}^{-1}$ for SLHC). Possible candidates for ion are lead, tin, krypton, argon and oxygen.

In circular particle colliders such as the LHC, intense magnetic fields keep the particles in circular trajectory. To allow the circulation of the two 7 TeV proton beams, the machine uses a magnetic system composed of 1232 dipoles that employed superconducting magnets operating at 11.2 kA with a nominal field of 8.33 T, which are located all along the ring to bend the beams. To achieve superconductivity at these strong magnetic fields, the magnets must be cooled at $\approx 1.9 \text{ K}$ (at atmospheric pressure) by using superfluid helium which has a lower viscosity and a higher heat transmission capacity than liquid helium. The two proton beams will also be segmented in 2865 bunches (when the LHC is fully filled) of up to about 10^{11} protons per bunch every 24.95 ns (as the nominal speed collision frequency is equal to 40.08 MHz) which corresponds to a distance between each bunch of around 7 meters. At LHC luminosity, in one bunch collision, about 20 proton-proton collisions occur.

Contrary to the LEP, where the two electron and positron beams were circulating in the same beam pipe, for the LHC two particle beams are accelerated by radio frequency (RF) cavities in opposite direction and brought to head-on collision in the center of four points in the ring called “Interaction Points” (IPs) in where the five experiments are located as it is shown in Figure 2.2. The five LHC experiments are:

- ATLAS (A Toroidal LHC ApparatuS)
- CMS (Compact Muon Solenoid)
- LHCb (Large Hadron Collider beauty experiment)
- ALICE (A Large Ion Collider Experiment)

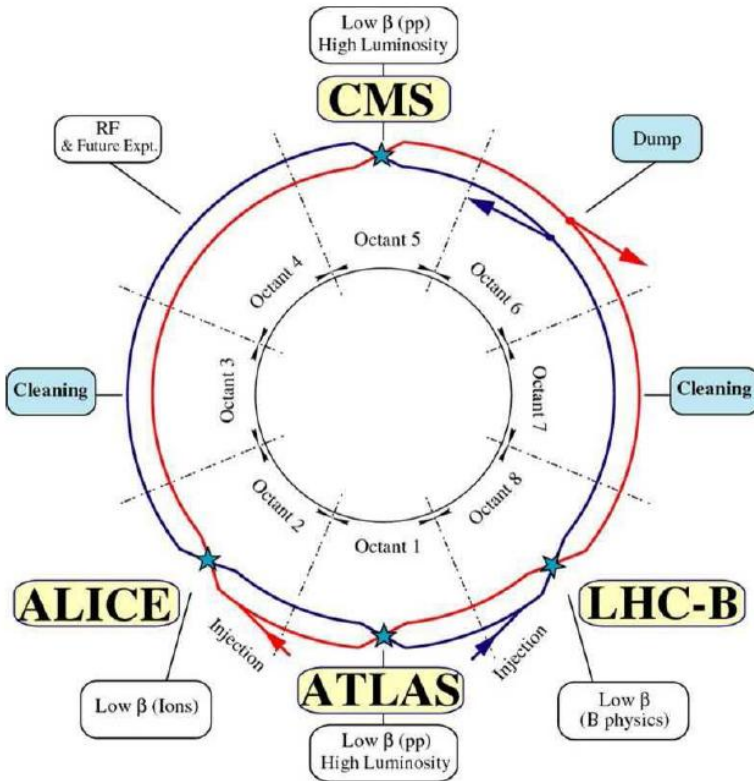


Figure 2.2: Layout of the LHC accelerator. The four large LHC experiments (ATLAS, CMS, ALICE, LHCb) are illustrated, where the two particle beams collide.

- TOTEM (TOTal and Elastic Measurement)

The two biggest ones are ATLAS [ATL97] and CMS [CMS94]. The main issues of ATLAS and CMS experiments are to discover the Higgs boson and study rare events occurring with high energetic particles collisions. Detectors present in both experiments are optimized for the operation of the LHC at high luminosity pp runs. In addition, LHC has two low luminosity experiments, the LHCb [LHC98] experiment is dedicated to the physics of B-meson and the TOTEM experiment [TOT99] is made for the detection of protons from elastic scattering at small angles with respect to the direction of the incoming particle beams (TOTEM is located in the same place than CMS). Finally, the ALICE experiment is designed to explore the heavy ion (Pb-Pb) collisions e. g. the quark gluon plasma. In the following section, the LHC experiments as their radiation environments are briefly described.

2.2 The experiments

Each LHC experiment offers the possibility to detect different physics topics and set of properties for a define particle type. As a general design principle, they are made up from different detectors layers which are called “sub-detectors”. The tracking devices are located in the inner region, and are exposed to the most harsh radiation environment. For this reason, for some designs, devices are expected to be exchanged after a certain LHC running time. They operate in a strong particle field allowing to measure points on the bent particle trajectories. Due to the Lorentz force, the trajectory of a charged particle moving in a particle field is a helix with a radius of curvature (R). By reconstructing the track of particles, it is possible to determine their charge (q) as their momentum (p).

The inner tracking detectors are followed by the calorimeters, where particles deposite their energy. There are two types of calorimeter, the electromagnetic and hadronic ones. The first one is used for measuring the energy of particles interacting via electromagnetic processes³. In the electromagnetic calorimeter, high energetic electrons and photons are completely stopped, while hadrons are stopped in the hadronic calorimeter.

For this reason, hadrons (such as for example neutron) energy is measured in the hadronic calorimeter and added to their deposited energy in the electromagnetic calorimeter. The only particles which are supposed to escape both calorimeters are the neutrinos and muons since their cross-section are very low. Muons are detected in an outer muon gas chamber after traversing all sub-detectors whereas neutrino cannot be identified since they don't interact with matter. For evaluating the amount of neutrino, they are referred as the missing energy in the analysis. The radiation environment for the different LHC environment has already been well described in [Rav06] and presented in this section.

2.2.1 The radiation environment of the two biggest experiments:

ATLAS and CMS

The radiation environment close to the Interaction Points (IPs) of ATLAS and CMS is expected to be extremely hostile. The LHC will produce around 8×10^8 pp inelastic events per second, at luminosity of $10^{34} \text{ cm}^{-2}\text{s}^{-1}$ and for a total cross section of 80 mb⁴.

³ The definition of the different particle types and interaction processes are given in Chapter 3.

⁴ The unit mb is the millibarn, which is a unit of area; 1 mb corresponds to 10^{-31} m^2 and 10^{-27} m^2 .

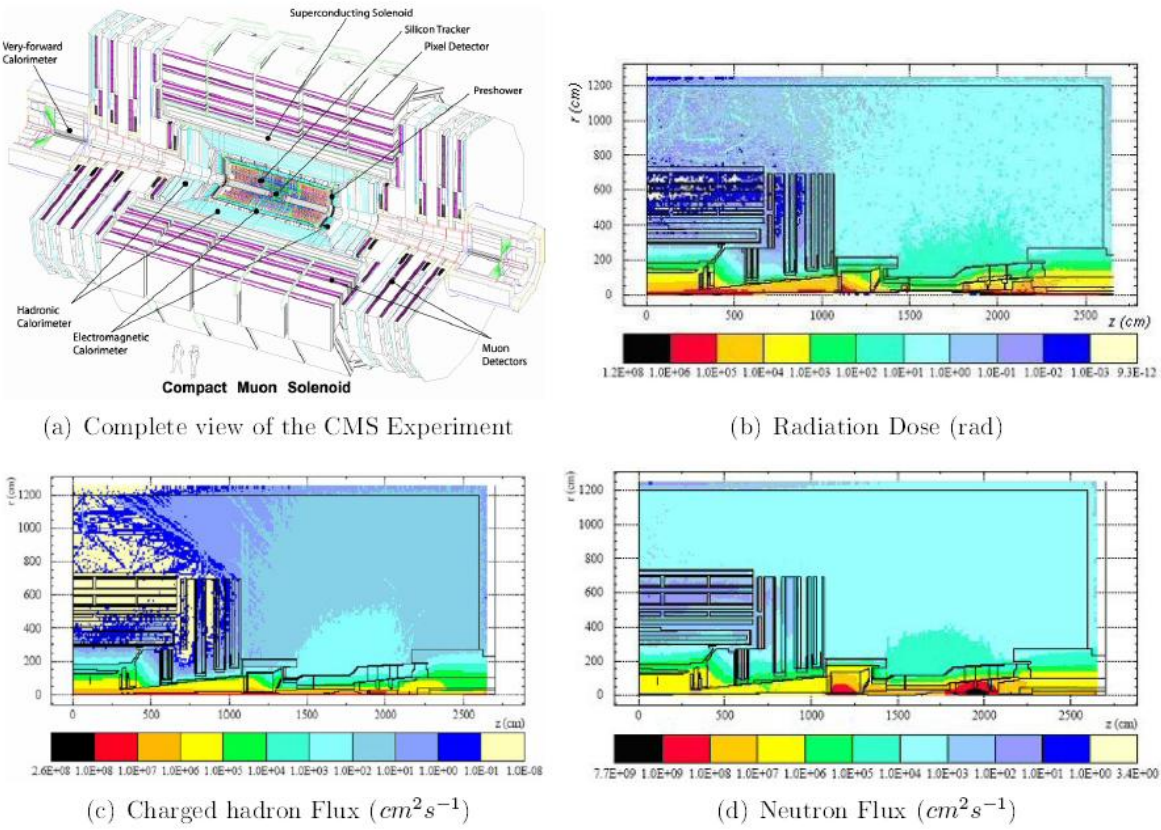


Figure 2.3: Radiation Field inside the CMS Experiment. A complete view of the CMS experiment is illustrated in (a). The dose map (b) has been determined for 10 years operation of the machine while charged hadrons (c) and neutron (d) fluxes have been calculated for normal operational conditions (see text) [Huh02].

From the interaction point a high amount of secondary particles and collision products will be generated. Then the detector front end electronics has to stand this huge amount of high energetic radiation, especially in the inner part of the experiment. Radiations will deposit their energy in the material surrounding the interaction point by ionization or will create displacement damages (see section 2.3) in the bulk material.

Fluka Monte Carlo simulations [Huh95] have been performed in order to evaluate the Total Ionizing Dose (TID) and the time-integrated particle flux per unit surface also called the particle fluence⁵.

As it has been mentioned in [Rav06], to obtain year-averages for radiation studies the recommended assumption [Pot95] is that during the first year LHC would reach 1/10 of the

⁵ Both definitions of the TID and particle fluence are given in section 2.3.

Position	Dose/y [Gy]	Dose rate [Gy/sec.]	Dose/run [Gy]	Neut. Φ/y [n/cm ²]	Ch. Had. Φ/y [p/cm ²]
Pixel	1×10^5	2×10^{-2}	8.6×10^2	2×10^{13}	2×10^{14}
Tracker	1×10^4	2×10^{-3}	8.6×10^1	1×10^{13}	5×10^{13}
ECAL EB/EE	1×10^3	2×10^{-4}	8.6	$10^{12}/10^{13}$	negligible
HCAL HB/HE	1×10^1	2×10^{-6}	8.6×10^{-2}	$10^{13}/10^{14}$	$<10^{12}/10^{13}$
MB	1×10^{-2}	2×10^{-9}	8.6×10^{-5}	$10^{10}/10^{11}$	$10^8/10^9$
Cavern Side	1×10^{-3}	2×10^{-10}	8.6×10^{-6}	$<10^{10}$	negligible
Cavern End	1	2×10^{-7}	8.6×10^{-3}	$<10^{10}$	negligible

Table 2.1: Maximum dose and particle fluence estimation in the different sub-detectors of CMS. ECAL and HCAL stand for Electromagnetic CALorimeter and Hadron CALorimeter respectively. EB and EE identify the Barrel and the EndCap part of the ECAL sub-detector. The same apply for the HCAL (HB/HE). MB stands for MUON Barrel sub-detector.

design luminosity and in the two following years 1/3 and 2/3, respectively. From the fourth year onwards LHC would operate at full luminosity. For the above calculations the assumed annual operation time of LHC was fixed to 1.5×10^7 s (≈ 220 days). Integrated luminosity, which is the best measurement for the time required to obtain physics discovery can be expressed in terms of inverse femtobarn (fb^{-1}). The standard LHC physics program is then based on 500 fb^{-1} , which corresponds to 5×10^7 s at peak luminosity. The quoted numbers are equivalent to roughly 10 years of LHC operation.

In the case of the Compact muon Solenoid (CMS) experiments, Figure 2.3(b) gives the dose map after 500 fb^{-1} while in Figure 2.3(c) and (d) the expected fast charged hadron and neutron fluxes are plotted respectively. The central region of the experiment is exposed directly to the particle flux coming from the interaction region and to neutron albedo (backsplash from the surfaces of the calorimeters) emerging from the electromagnetic calorimeters. Moving in the outer layers of the experiments, this second contribution becomes dominant.

Table 2.1 details, for the different CMS sub-detectors, the doses expected over a year of normal operation, the calculate dose-rate and the dose expected during a 12 hour physics run. In the same table, the annual neutron and charged hadron fluences are reported. It has to be noted here that the fluence and dose can vary by several orders of magnitude when moving

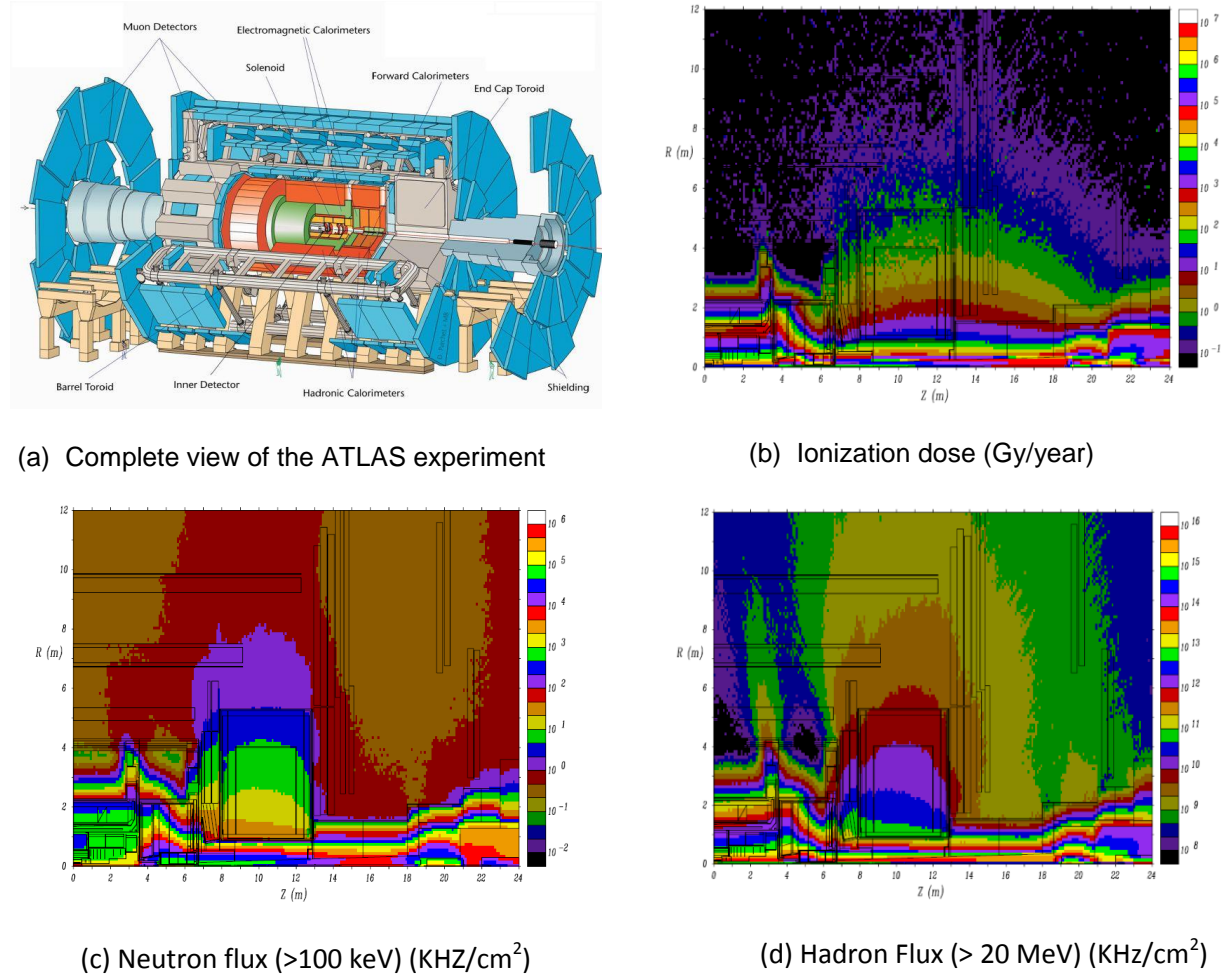


Figure 2.4: Radiation Field inside the ATLAS Experiment. A complete view of the ATLAS experiment is illustrated in (a). The annual dose map (b), annual neutron and hadron flux respectively (c) and (d) are shown here [Bar05].

along the radial component (r) with respect to the IP. Moving along the z direction in the central part of the experiment (e.g. along the beam axis) those values are almost constant [Her04].

The radiation field for the ATLAS experiment [Bar05] is shown in Figure 2.4. In the inner detector region, charged hadrons are dominated by charged pions originating from the proton-proton collisions. This particle type constitutes the most serious background for the innermost layers of the inner detector. Some neutrons are originating from the pp collision, as secondaries from the beampipe, but as for the CMS experiment most neutron come from albedo. Albedo particles are predominantly thermal and low energy neutrons. The other feature of this region is

Position	Dose [kGy]	Neutron Φ [1 MeV _{eq} n/cm ⁻²]	Ch. Hadron Φ [1 MeV _{eq} n/cm ⁻²]
Pixel (ID)	17-160	$1-5 \times 10^{13}$	$2-20 \times 10^{13}$
SCT (ID)	4-8	1×10^{13}	$4-8 \times 10^{12}$
TRT (ID)	1-5	$4-15 \times 10^{12}$	$0.5-4 \times 10^{12}$
LAr	$0.6-5 \times 10^{-3}$	$10^{10}-10^{11}$	$4-40 \times 10^9$
TILE	1×10^{-5}	$5-30 \times 10^9$	10^8-10^9
FCAL	2.3	$>10^{15}$	-
MUON	$3-20 \times 10^{-5}$	10^9-10^{11}	10^8-10^{10}

Table 2.2: Annual dose and particle fluence estimations in the different ATLAS sub-detectors at full luminosity. The Pixel, SCT and TRT tracking sub-detectors of ATLAS constitute the innermost detector of the experiment. LAr stands for Liquid Argon calorimeter. Both TILE and FCAL are hadronic calorimeters installed in different ATLAS locations. MUON is the acronym to identify the muon system.

the services gap between the barrel and EndCap calorimeters, which can potentially allow radiations in the inner detector to escape into the barrel muon system. However in this experiment, most of the energy from primary protons is dumped in the outer regions of the detector such TAS collimator, the forward calorimeter and the beamline which are a strong source of secondary radiation.

The TAS collimator and the forward calorimeter are self-shielding with surrounding massive materials to reduce their radiation emissions. Finally the beam pipe which spans over the length of the detector, creates a long line source of secondary radiation since it is not self-shielding. Primary particles from the interaction point strike the beam pipe at very shallow angles, so the projected material is large, and by this mechanism the beam pipe becomes a line radiation source producing secondary radiation which interact with the interior of the forward cavity. Studies have shown that the radiation contribution from the beam line are not only the main background in the forward region, they also create most of the radiation background in the muon system [Bar05]. Simulation results for the most important ATLAS sub-detectors are reported in Table 2.2.

2.2.2 The radiation environment of two low luminosity experiments: ALICE and LHCb

Monte Carlo simulations to predict the radiation environment of the ALICE experiment at LHC were carried out using the following source terms [Pas02]:

- Particle production at the interaction points during a typical running scenario with protons, Calcium and Lead ions according with the experimental Technical Design Report [ALI95].
- Beam loss due to beam misinjection (ALICE experiment is located near the injection point from the SPS).
- Beam gas interactions.

Simulations made for predicting the radiation environment of the LHCb experiment was performed assuming an average luminosity of $2 \times 10^{32} \text{ cm}^{-2}\text{s}^{-1}$ and a cross section for inelastic and diffracting proton events of 80 mb, therefore 1.6×10^7 interaction/s and 10^7 seconds of data per year have been simulated.

Results for both experiments are reported in Table 2.3 taken from [Tav05] and [Cor03]. It can be mentioned that the predicted dose and fluence values for both experiments are much lower than the ones for the two biggest experiments ATLAS and CMS. This is due to the fact that the luminosity in ALICE and LHCb will be much lower going from $10^{27} \text{ cm}^{-2}\text{s}^{-1}$ to $10^{30} \text{ cm}^{-2}\text{s}^{-1}$ for ALICE and $2 \times 10^{32} \text{ cm}^{-2}\text{s}^{-1}$ for LHCb.

Even if the radiation level is less intense in both low luminosity experiments, some sub-detectors are located very close to the beam (few mm) and so exposed to an intense radiation environment. For this reason, it is expected that the sub-detectors present in these locations will be exchanged after few years of LHC running [Gou05].

As all electronic equipments present within this field can be affected by radiation damage, in the next section, the three different effects of the LHC radiation environment on electronic devices are described.

Position in ALICE	Dose / year [Gy]	Φ_{TOT} / year [cm $^{-2}$]	Position in LHCb	Dose / year [Gy]	Φ_{eq} / year [cm $^{-2}$]
SPD1	200	3x10 ¹¹	VELO	5x10 ⁴	2.4x10 ¹⁴
SPD2	26	2x10 ¹⁰	Si TRACK	4.8x10 ³	5x10 ¹²
TPC	10	1x10 ¹¹	RICH	2x10 ³	2x10 ¹¹
TDR+TOF	0.1	3x10 ⁹	CAL	200-300	9x10 ¹⁰
MUON	0.5	6x10 ¹⁰	MUON	60-300	1-5x10 ¹⁰
Cavern	0.001	7x10 ⁶	Cavern	0.06	-

Table 2.3: Annual dose and equivalent fluence (Φ_{eq}) in the different sub-detectors of ALICE and LHCb experiments.

2.3 Radiation environment effects on electronic devices

In the previous sections, the radiation environments of the LHC particle accelerator and its experiments have been described. It is then clear that detectors and electronic devices present in this particle field will also be irradiated by different particle types and energy in the range from the eV to GeV.

Since this thesis work is based on the study of sensors for monitoring this complex radiation field, it is then necessary to give to the reader an overview of the three major effects induced by radiation damage in electronic devices which are the Total Ionizing Dose effects, the displacement damage effects and the Single Event effects.

2.3.1 Total Ionizing Dose effects (TID)

When a charged particle will pass through electronic devices, it will interact with the atomic electrons by coulomb interactions so that it will lose its energy by ionizing the atoms along the track. The terms of “dose”, “Total Ionizing Dose” or “IEL” (Ionizing Energy Loss) are used when many particles over time cross the material and deposit their energy inside it, which means that the TID is a cumulative effect. The dose is defined as the energy imparted to matter

per unit of mass. It is expressed in Grays (Gy). 1 Gy corresponds to the energy of 1 joule released in 1 kg of matter.

The ionizing dose is responsible for the surface and interface effects in silicon devices such as MOS⁶ or bipolar devices, as well as inducing gas detector aging effects [Hol02], [Bar05].

2.3.2 Displacement damage effects

Neutrons and charged particles (protons, pions, high energetic electron and others) can produce bulk damage in silicon devices by interacting with the atoms of crystalline materials as silicon. For instance, at low energy charge hadrons mainly interact with matter via the electromagnetic interaction. However, at all energies neutral and charged particles have large elastic scattering cross sections on nuclei. Particles colliding with the atoms of crystalline material lose a part of their energy by displacing a primary atom out of its lattice site resulting in a silicon interstitial and left over vacancy (Frenkel Pair). The incident particle and the recoil nucleus can migrate through the material and may finally provide the building block for extended defects [Mol99]. As an example, the neutron energy threshold (by elastic collisions) for displacement damage in silicon is about 100 keV.

Bulk damage can induce performance degradations in many electronic devices, such as silicon particle detectors, solar cells etc... [Hol02]. The displacement damage is proportional to the total number of particles hitting the devices per unit surface. This quantity is called the “particle fluence” and is expressed in unit of inverse area. Fluence is the time integral of the fluence rate, or flux and is indicated with the symbol Φ and measured in unit of particles/cm².

It should be also taken into account that neutrons interact only with the nucleus by transfer momentum to atoms (elastic scattering) and for energy higher than 1.8 MeV also nuclear reactions occur [Lin80]. Therefore, the question arises how to scale the radiation damage produced by different particle types and energies with respect to the radiation induced changes observed in the material. The answer is found in the so-called *Non Ionizing Energy Loss (NIEL)* hypothesis as explained in [Mol99].

The basic assumption of the NIEL hypothesis is that any displacement damage induced change in the material scales linearly with the amount of energy imparted in displacing collisions, without taking into account the spatial distribution of the introduced displacement defects and the various annealing sequences taking place after the initial damage event. In this way the NIEL can be calculated and is expressed by the displacement damage cross section $D(E)$ which is illustrated in Figure 2.5 for neutrons, protons, pions and electrons. With the help of the

⁶ MOS : Metal Oxide Semiconductor.

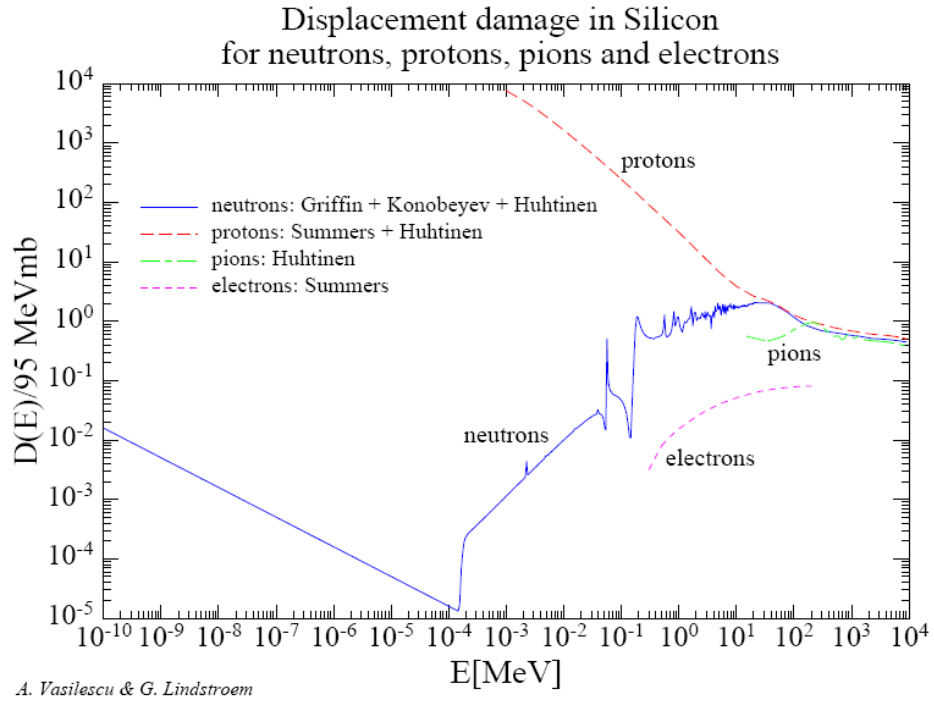


Figure 2.5.: Displacement damage functions $D(E)$ normalized to 95 MeVmb for neutrons (10⁻²⁰ to 20 MeV [Gri96], 20 to 400 MeV [Kon92], 805 MeV to 9 GeV [Huh93b]), protons [Huh93b], [Sum93], [Huh93a]), pions [Huh93b] and electrons [Sum93]. Due to the normalization to 95 MeVmb the ordinate represents the damage equivalent to 1 MeV neutrons (see text).

displacement damage cross section $D(E)$, it is finally possible to define a hardness factor k allowing to compare the damage efficiency of different radiation sources with different particles and individual energy spectra $\phi(E)$. It is common practice to define *the hardness factor k* in such a way that it compares the damage produced by a specific irradiation to the damage which would have been produced by monoenergetic neutrons of 1 MeV and the same fluence:

$$k = \frac{\int D(E)\phi(E)dE}{D(E_n = 1\text{MeV}) \cdot \int \phi(E)dE} \quad (2.1)$$

Here, $D(E_n = 1\text{MeV})$ is set to 95 MeVmb [AST94]. The equivalent 1 MeV neutron fluence Φ_{eq} can thus be calculated by:

$$\phi_{eq} = k\phi = k \int \phi(E)dE \quad (2.2)$$

which can be either measured in 1-MeV neutron equivalent particles/cm² or in cm⁻².

2.3.3 Single Event effects

Some types of single event effects are described in this section. The first one is the Single Event Upset (SEU), which is the change of state of a bistable element caused by the impact of an energetic particle. The effect is non-destructive and may be corrected by “rewriting” the affected element. An SEU is the result of ionization by a single energetic particle, or the nuclear reaction products of an energetic charged hadron [Hol02].

Contrary to SEU, another single event effect may occur which is a destructive one: the Single Event Latchup (SEL). When a particle crosses a PNP or NPN transistor structure (as in CMOS structures), it can reduce its impedance by creating free carriers due to the ionization, leading to the conduction of a parasitic transistor structure. If the current passing through this structure cannot be limited, the conduction of such parasitic structure can evolve in a destructive effect called Single Event Burnout (SEB), as it has been observed in power MOSFET⁷ transistors. In the case of the LHC experiments, hadronic showers that consist mainly of charged and neutral hadrons may induce nuclear reactions if their energies are high enough. Spallation processes can afterwards break the nuclei in large fragments with high Z that are slowed down on a short length in dense materials. This kind of events lead to the large amount of deposited energy in a small volume as required to generate SEUs. In such conditions, it has been shown [Huh00] that the SEE rate in the LHC environment will be dominated by hadrons with a kinetic energy greater than 20 MeV.

Another type of SEE can be observed on power MOSFETs transistors. The Single Event Gate Rupture (SEGR) is characterized by heavy ions going through the gate-to-drain overlap region of the device (neck region) producing sufficient accumulation of charges at the silicon to silicon-dioxyde interface to exceed the breakdown voltage of the oxide, resulting in localized dielectric breakdown. This effect can induce catastrophic failure and leads to the lost of device functionality. This phenomenon was modeled for the first time by Wrobel [Wro87], as being the result of creating a charge column into the oxide, drawing away a short-circuit between the gate and the substrate. The energy stored on the capacity would be dissipated across the insulator causing the dielectric rupture. Later, the model evolved for taking into account the variation of different parameters, as the incident angle, the substrate resistivity, the channel type, the pre-irradiation, the temperature, the multiple impacts assumption and so on [Mou94], [Tit95], [Tit96], [Sex98], [Pey08].

⁷ Metal Oxide Semiconductor Field Effect Transistor : MOSFET

2.4 Conclusion

The radiation environment of LHC experiments will be composed of different particle types and energies. In this chapter, simulations performed using Monte Carlo codes have been presented and revealed that depending on the location inside the experiments or even depending on the experiment itself, radiation levels can vary over a range of 5-6 orders of magnitude. In any cases this complex radiation field will have an important impact on electronic devices present in experiments. The major radiation effects which can affect the electronic components present within such a field have been described. Particles can deposit energy in matter either by Ionizing Energy Loss (IEL) process or by Non Ionizing Energy Loss (NIEL) process. Due to the large amount of energy deposit by particles, electronic components can be strongly damaged and can lead to an accelerated aging of the experimental equipments.

For deeper understanding on how radiations can interact and deposite their energy in electronic devices, the following chapter introduces the different principles of radiation interactions with matter, for the main particles that can be encountered in LHC experiments.

Chapter 3

Particle interactions with matter

When a particle passes through a medium, which can be usually either a gas or a solid matter, it will deposit a part or the totality of its energy (expressed in MeV), by interacting with nuclei and atomic electrons. For this reason, it is important to know the different effects governing the travel of particles through a medium since the comprehension of radiation effects on devices needs a well understanding of the fundamental particle interactions with matter.

Two different particle families can be distinguished; charged particles as charged hadrons and electrons, which are directly ionizing and non-charged particles as neutrons and photons.

Depending on the mass and charge of the incident particle, the particle interaction can be subjected to different processes. In the case of charged particles, the energy is lost throughout the travel of the particle across the medium, by successively transferring their energy to the atomic electrons (excitation or ionization). In addition light charged particles such as electrons, can be deviated from their trajectory close to nuclei as their deceleration can produce a X-ray photon (Bremsstrahlung effect).

In contrast, the neutral particle can cross a medium over a long distance without interacting with it and give all or a part of their energy to the atoms in only one interaction by

photoelectric absorption, Compton scattering or pair production effects in the case of gamma interactions, or by directly interacting with the nuclei which will ionize the medium.

The complex radiation field encountered in LHC experiments is mainly constituted by charged hadrons, electrons, muons, photons and neutrons. In order to give a general idea to the reader on how all the components and devices present in this radiation field can be potentially affected by radiation damage, a short summary of the interactions of these different particle types with matter is presented in this chapter.

3.1 Interaction of charged particles with matter

Charged particles can interact with the medium through three different forces, the electromagnetic, the weak and the strong forces⁸. While the weak interaction plays an important role in the detection of mysterious particle such as neutrino, the strong interaction usually only concern the detection of neutrons, more particularly the nuclear reaction which produce charged particle from an interaction with an incident neutron. The electromagnetic force is the most probable that can be encountered and thus will be detailed in this section. The coulomb interaction may induce two different phenomena, the excitation and the ionization of the atoms. On the one hand, an incident particle can excite an atom if the energy transferred to the atom is lower than its ionization potential (I) (energy necessary to eject an electron from its atom). In this case, excitation can induce the emission of an electron or a photon by de-exciting process. On the other hand, an incident charged particle can ionize the medium by transferring its energy to the atoms and then creating electron-hole pairs along its track. In this case the incident particle loses a small fraction of its energy for each interaction and therefore will traverse the matter over a long distance. Any electrons produced by one of the two interaction processes defined above are named secondary electrons or particles, which can also produced other secondaries if they acquire additional energy (e.g. in the presence of an electric field).

3.1.1 Charged hadrons

Charged hadrons are all the subatomic particles which are constituted by quarks and then can interact via the strong force. In LHC experiments the most probable charged hadrons which can be encountered in terms of quantities are protons, pions and kaons. Except for protons, which are with neutrons the elements of the nucleus, all the other charged hadrons such as charged pions (π^+ , π^-) and kaons (k^+ , k^-), are produced by high energetic particle

⁸ Electromagnetic, weak and strong forces are three of the fundamental interactions of nature. The fourth one is the gravitation force.

	Proton	Kaon	Pion	Electron
Particle Mass (MeV/c ²)	938.3	493.7	139.6	0.511

Table 3.1: List of charged hadrons and electron masses

collisions and have a short lifetime. Charged hadrons can interact with matter via the electromagnetic force and then can ionize the medium by coulomb interactions.

At low energies, interactions with atomic electrons dominate while for high energies interactions with the atomic nuclei become more significant. The mass of charged hadrons is higher than the one for electrons, they are usually not subjected to deflection and normally they follow straight paths in the medium.

In order to give some orders of magnitude, the mass for charged hadrons and electrons are reported in Table 3.1. As example, proton is 1836 times heavier than electron, which induce that this particle type is not strongly deviated by its interaction with atomic electrons. However the probability that they can interact with atomic nuclei is not negligible at high energy. Nonetheless, charged hadrons can lose their total energy rapidly, even if they cross a thin thickness of shielding (depending on the atomic density of the target material). As discussed previously, in the case of ionization process the kinetic energy of charged hadrons decreases after each interaction and particle will interact more strongly with atomic electrons as its energy becomes lower. For this reason, the energy deposit in the material increases with the travelled distance until proton loses all its energy (Bragg peak). A schematic representation of this phenomenon is illustrated in Figure 3.1.

When a charged hadron interacts with matter by coulomb interaction, its kinetic energy decreases due to ionization and excitation of the atomic electrons. This energy loss by the incident particle is named “Stopping Power”. The mean rate of energy loss (or stopping power) is given by the Bethe-Bloch equation as referenced in [Bic06]:

$$\left| \frac{dE}{dx} \right| = kz^2 \frac{Z}{A} \frac{1}{\beta^2} \left[\frac{1}{2} \ln \frac{2m_e c^2 \beta^2 \gamma^2 T_{\max}}{I} - \beta^2 - \frac{\delta(\beta\gamma)}{2} \right] \quad (3.1)$$

Where $|dE/dx|$: mean rate of energy loss by proton along the track; unity: MeV.cm⁻².g⁻¹

z : charge of incident particle. For protons z is equal to 1

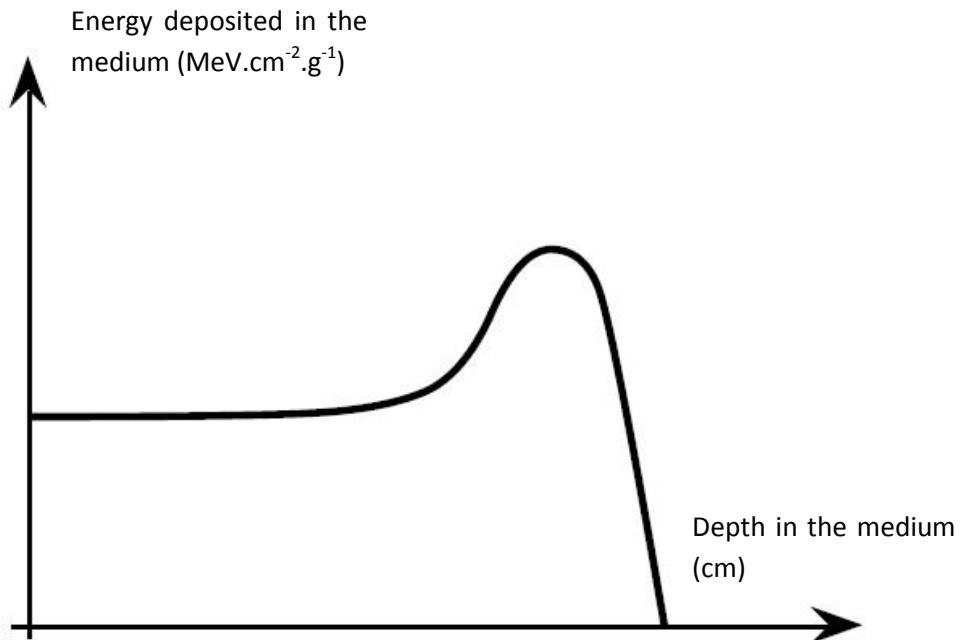


Figure 3.1: Schematic representation of the energy deposited by charged hadrons as a function of distance travelled by the particle in the medium (Bragg peak).

Z: Atomic number of absorber

A: Atomic mass of absorber

$\beta = v/c$, where v is the speed of the proton in m/s

c is the celerity and is equal to 3×10^8 m/s

m_e : electron mass $\times c^2$ which is equal to 0,511 MeV/c²

I: Mean excitation energy (eV). It stands for the average excitation and ionization potential of the medium. For example for SiO₂ $I \approx 139$ eV

$$\gamma = \frac{1}{(1 - \beta^2)} \quad (3.2)$$

$$k \text{ is a constant coefficient equal to: } k = 4\pi N_A r_e^2 m_e c \quad (3.3)$$

Where N_A is the Avogadro's number $\approx 6.0221414 \times 10^{23}$ mol⁻¹

r_e is the classical electron radius ≈ 2.817940325 fm

$\delta(\beta\gamma)$ is the density effect to ionization energy loss

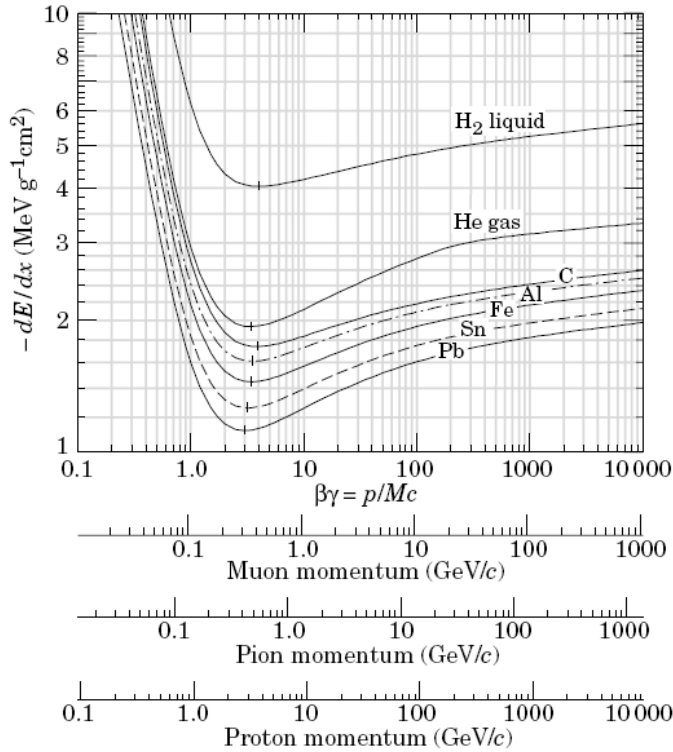


Figure 3.2: Mean Energy loss rate in liquid (bubble chamber) hydrogen, gaseous helium, carbon, aluminium, iron, tin, and lead. Radiative effects, relevant for muons and pions are not included. These become significant for muons in iron for $\beta\gamma \geq 1000$, and at lower momenta for muons in higher-Z absorbers [Bic06].

In the Bethe-Bloch equation, T_{\max} is the maximum kinetic energy which can be imparted to a free electron in a single collision.

For an incident particle of mass M , T_{\max} is given by the following formula in unit of MeV:

$$T_{\max} = \frac{2m_e c^2 \beta^2 \gamma^2}{1 + 2\gamma m_e / M + (m_e / M)^2} \quad (3.4)$$

Where M is the mass of the incident particle in unit of MeV/c^2 . The only difference for computing the energy lost by protons, kaons or pions is their divergence in term of mass. Figure 3.2 shows the mean rate of energy loss along the track by different particle types as a function of their momentum. Particles which possess a momentum corresponding to the region where the energy loss is at minimum are called “*Minimum Ionizing Particles*” (MIP’s).

As discussed previously, electromagnetic interactions can induce either ionization or excitation mechanism. The latter one occurs when the transferred energy is not high enough to eject the atomic electron from its atom. In this case, the atom becomes excited and unstable. By recovering its stable state, the de-excitation process produces an emission of a X-ray photon or an Auger electron [Mor99].

As described above, electromagnetic interactions manifest themselves in many ways, such as ionization and excitation of the medium. The energy loss by the particle subjected to such interactions is called the “*Ionizing Energy Loss (IEL)*”.

In addition charged hadrons can interact with the medium via hadronic (or nuclear) interactions, also called strong interactions. A charged hadron subjected to it, interact directly with the nucleus which will ionize itself the medium. As a consequence the energy deposited in the medium is called the “*Non-Ionizing Energy Loss*”.

However, as the goal of this chapter is to give some indications to the reader about the analytical calculations and physics involved in Chapter 4, in which a study is carried out for evaluating the Total Ionizing Dose deposited in our dosimeters, a general and detailed description of hadronic interactions goes beyond the limit of this thesis. For more details of this type of interaction, the reader is referred to [Ler04]. In the next section, the description of the interaction of another type of charged particles: the “*charged leptons*”, also present in the LHC radiation field is given.

3.1.2 Charged leptons

The lepton family is a class which includes electron, muon, tau and neutrino as their antiparticles. Leptons are the lightest particles having a nonzero rest mass and which are not subjected to the strong interaction. In the LHC environment, the main charged leptons which can be encountered are the electrons and the muons. Both types of particle are almost identical except from their mass, which are $0.511 \text{ MeV}/c^2$ and $105.7 \text{ MeV}/c^2$ for electrons and muons respectively.

Electrons interact with the matter via two main processes, ionization interaction and Bremsstrahlung production. Transport of electrons through matter is relatively complex [Hol02]. Electrons can be considered as light particles which mainly interact at the atomic level. At low energy, electrons primarily lose energy by collision as heavy particles (e.g. charged hadrons). At high energies the Bremsstrahlung effect becomes dominant due to their small mass so that the main energy loss is caused by radiative emission. Electrons are easily scattered and complete “back scattering” can be significant especially in high-Z materials.

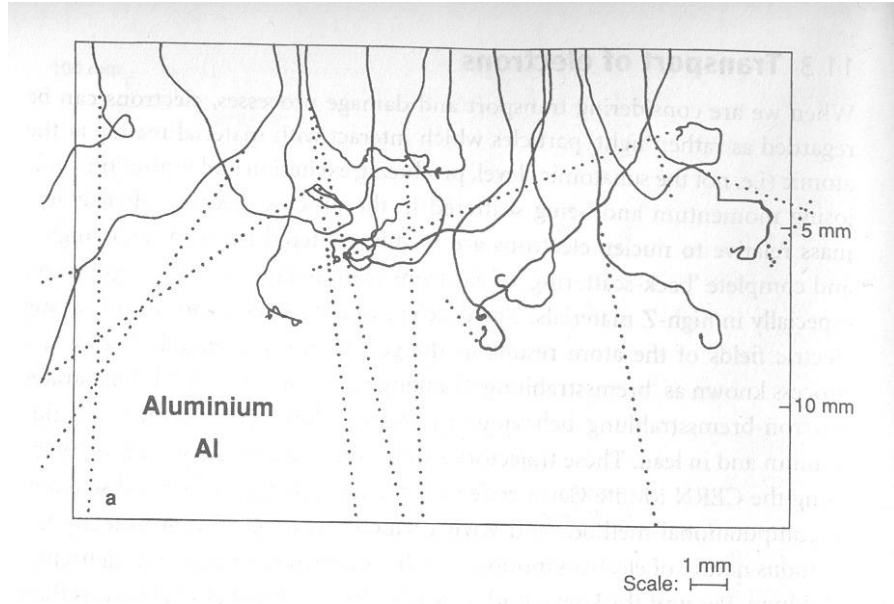


Figure 3.3: Trajectories of 5MeV electrons in Aluminium computed with the Geant Monte Carlo code, electrons are injected from above. Dotted lines represent the paths of bremsstrahlung photons induced by the electrons [Hol02].

They do not travel in a straight path (which is the case for heavy particles) through a material and electron scattering induces that both the energy and the flux of the particle are reduced (see the Number Transmission Coefficient (NTC) in section 4.5.2.1). As it can be observed in Figure 3.3, electrons traversing Aluminium absorber do not cross the material in a straight path. In addition, the emergent particle energy spectrum shifts towards smaller value than the incident energy caused by the electron trajectories within matter [Hol02]. Particles of low energies, (e. g. with range less than the medium thickness) may be completely stopped in the material, while for higher energies the flux is reduced. As a result, it is more complex to calculate the energy deposited in matter by electrons compared to the one calculated for charged hadrons.

For electrons in the energy range from a few tens of electron volts to few MeV, the stopping power is governed by collision and can be written as [Roh54]:

$$-\frac{dE}{dx} = N \times Z \times \alpha \times \left[\ln\left(\frac{T^2}{I^2} \times \frac{\gamma+1}{2}\right) + f^-(\gamma) \right] \quad (3.5)$$

Where T: Kinetic energy of the electron in MeV, $T = (\gamma - 1)mc^2$ (3.6)

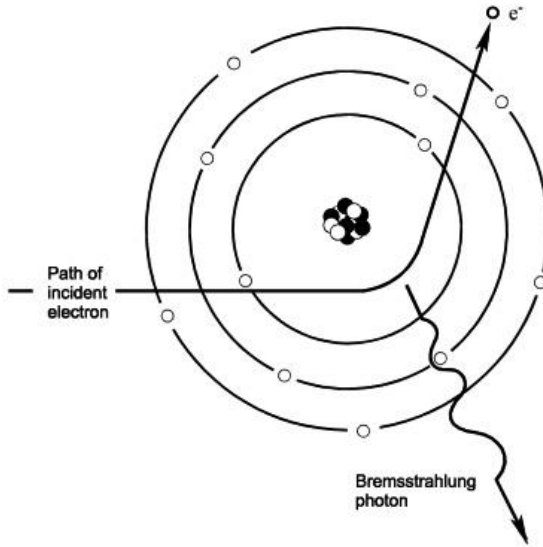


Figure 3.4: Interaction of electron with matter. The photon is emitted by Bremsstrahlung effect.

N: Number of atoms per unit volume

Z: Atomic number of absorber

$$\alpha = \frac{2\pi e^4}{mv^2} = \frac{2\pi r_0 mc^2}{\beta^2} \quad (3.7)$$

$$\text{with } r_0 = \frac{e^2}{mc^2} \quad (3.8)$$

$$f^-(\gamma) = 1 - \beta^2 - \frac{2\gamma - 1}{\gamma^2} \ln 2 + \frac{1}{8} \left(\frac{\gamma - 1}{\gamma} \right)^2 \quad (3.9)$$

However as described previously, in contrast with the calculation of the mean energy loss by charged hadrons, this formulation cannot be directly taken for calculating the energy deposited by electrons as they are easily scattered in materials. In addition, when an electron passes close to a nucleus, it can be deviated from its trajectory due to the electric field of the nucleus. The incident electron can be then accelerated or decelerated, so that its momentum changes inducing the emission of a photon to conserve momentum as it is schematically illustrated in Figure 3.4

High energetic electrons predominantly lose energy in matter by Bremsstrahlung interaction [Bic06]. The characteristic amount of matter traversed for these related interaction is called the “*radiation length*”, it is indicated with the symbol X_0 and measured in g.cm⁻². It is

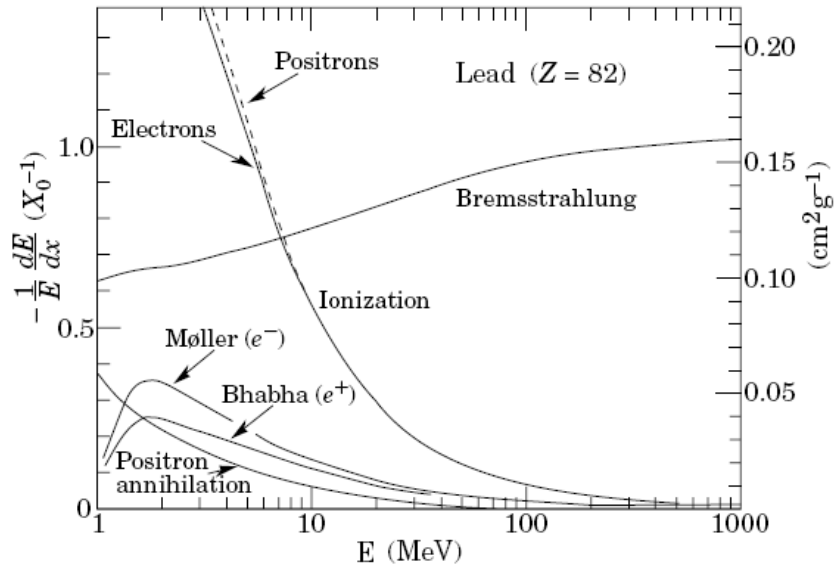


Figure 3.5: Fractional energy loss per radiation length in lead as a function of electron energy. Electron scattering is considered as ionization when the energy loss per collision is below 0.255 MeV [Bic06].

defined by the average distance in which the energy of a high energetic electron is reduced by a factor of $1/e$ (≈ 0.368). Figure 3.5 illustrates the energy loss by incident electron in Lead per radiation length versus electron energy. The Møller scattering which is the scattering of electrons by electrons is not addressed in this thesis. As it can be observed in this figure, the interactions of electrons with matter are governing by ionization processes at low energy, while the Bremsstrahlung effect dominates for high energetic particles.

Due to their low mass, electrons are easily scattered by atomic electrons when they cross matter compare to muons which are heavier. The name of lepton comes from the Greek name “Lepton” which means light. However, muons are heavy leptons which can ionize matter as charged hadrons since both are heavy charged particles. Figure 3.6 shows the stopping power for positive muons in copper based on the Bethe-Bloch formulation presented in Equation (3.1).

In the next chapter, a complete investigation on the radiation response of our dosimeters located in two different locations of the ATLAS detector is presented. In both locations the muon energy range does not exceed 10 GeV.

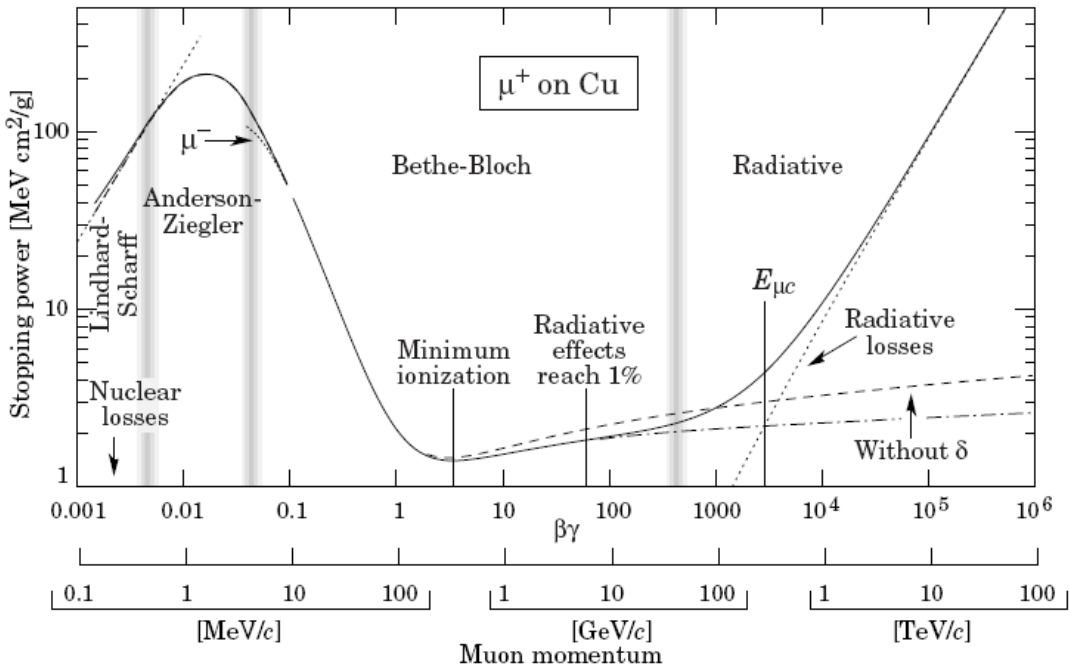


Figure 3.6: Stopping power for positive muons in copper as a function of muon momentum. Solid curves indicate the total stopping power [Bic06].

Therefore in the energy range of interest the mean rate energy loss by a muon across the medium is mainly governed by the same Bethe-Bloch formulation as for charged hadrons [Bic06]. For high energetic muons ($E_{\text{muon}} >$ some hundreds GeV) radiative processes become more important than ionization. Since our dosimeters are exposed to a maximum of 10 GeV incident muon energy (see section 4.5.2.2), this effect is not developed in this thesis. Nevertheless, their transport through matter is not limited to ionization process as they can interact with matter also via Bremsstrahlung (not very significant since muons are heavy particles) and direct electron pair production effects as well as by nuclear interactions and other contribution to the energy loss. For more details about the transport of muons through matter, the reader is referred to [Loh85] and [Fas90].

3.2 Interaction of photons with matter

The photon is a neutral particle which therefore interacts differently than the charged particles described above as it indirectly ionizes the medium when it travels through it. Contrary to charged particles which transfer energy to the atomic electron successively along the track, photons lose all of a part of their energy in only one interaction. From their interaction with the

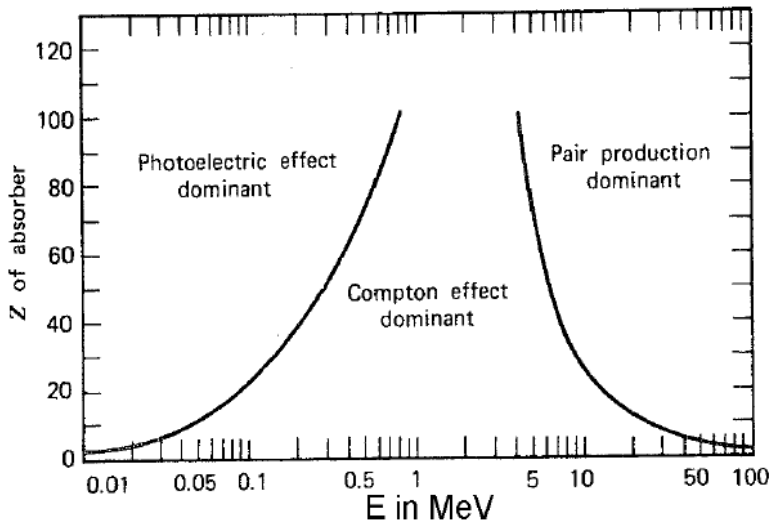


Figure 3.7: Relative importance of the three principal modes of interaction as a function of photon energy and atomic number of absorber [Hen92].

medium, photons generate secondary particles which are mainly secondary electrons. Three fundamentals processes can govern the photon interaction with matter, the photoelectric, the Compton and the pair-production effect. These three effects govern the transport of photon through matter, but however the occurrence probability of each of them is depending on the atomic number of the crossed material and the photon energy as it is shown in Figure 3.7. These three different effects are detailed in the next sections.

3.2.1 The photoelectric effect

The photoelectric effect is the predominant effect at lower energies. The incident photon crosses the material without interacting with it until colliding with an atomic electron of one of the atom inner shell. By this, the incident photon transfers its total energy to the electron and so disappears in only one interaction. Since a free electron cannot absorb a photon, the photoelectric absorption probability is larger for more tightly bound electrons, i. e. for K-shell [Ler04]. As is illustrated in Figure 3.8, from this interaction a secondary photoelectron is created and ejected from the inner shell. This process can occur only if the energy of the incident photon (E_γ) is higher than the bound energy of the electron (E_e), where:

$$E_\gamma = h\nu \quad (3.10)$$

h is the Planck constant equal to $4.13566733(10) \times 10^{-15}$ eV.s

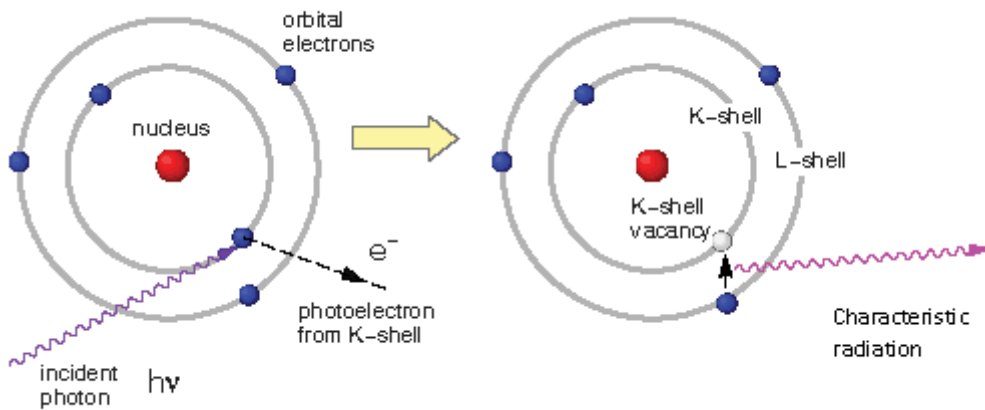


Figure 3.8: The two processes of the photoelectric effect. On the left-hand side an incident electron of energy $E=h\nu$ is absorbed by an electron of one of the inner shell of the atom. This process induces the ejection of a photoelectron. On the right-hand side, the vacancy left by the photoelectron is filled by another electron which produces the emission of characteristic radiation.

v is its associated electromagnetic wave in s^{-1} .

In this case, the energy of the ejected photoelectron is given in unit of MeV as:

$$E_{\text{photoelectron}} = E_\gamma - E_e \quad (3.11)$$

It leaves an ionized atom and the vacancy produced by this process is quickly filled by an electron from the other atom shells or by capture of a free electron. Both of these phenomena induce that the atom is on an excited state and by de-excitation a characteristic radiation is emitted, which can be either a X-ray photon or an Auger electron. The process of emitting a characteristic X-ray photon is called “fluorescence yield”.

3.2.2 Compton effect

The Compton effect takes place at higher energies than the photoelectric effect (see Figure 3.7). It describes the interaction between an incident photon and an electron which is assumed to be initially free and at rest (the electron energy bound is lower than the energy of the incident photon). For this type of interaction, the incident photon is deflected through an angle θ from its original direction and transfers a fraction of its energy to the electron which recoils.

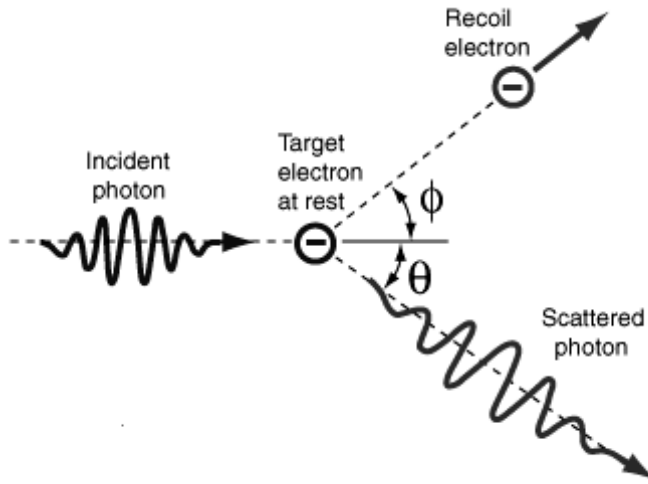


Figure 3.9: Compton effect between an incident photon and an electron. The incident photon is scattered through an angle θ .

Figure 3.9 illustrates this effect. The energy of the scattered photon in unit of MeV is given by the following formula:

$$E_{\gamma'} = \frac{E_{\gamma}}{1 + \frac{E_{\gamma}}{m_e c^2} (1 - \cos(\theta))} \quad (3.12)$$

The angular distribution of the scattered photon is predicted by the Klein-Nishina formula for the differential cross section as:

$$\frac{d\sigma}{d\Omega} = Zr_0^2 \left(\frac{1}{1 + \alpha(1 - \cos(\theta))} \right)^2 \left(\frac{1 + \cos^2(\theta)}{2} \right) \left(1 + \frac{\alpha^2(1 - \cos(\theta))^2}{(1 - \cos^2(\theta))[1 + \alpha(1 - \cos(\theta))] } \right) \quad (3.13)$$

$$\text{Where } \alpha = \frac{E_{\gamma}}{m_e c^2} \quad (3.14)$$

and r_0 is the classical radius of electron.

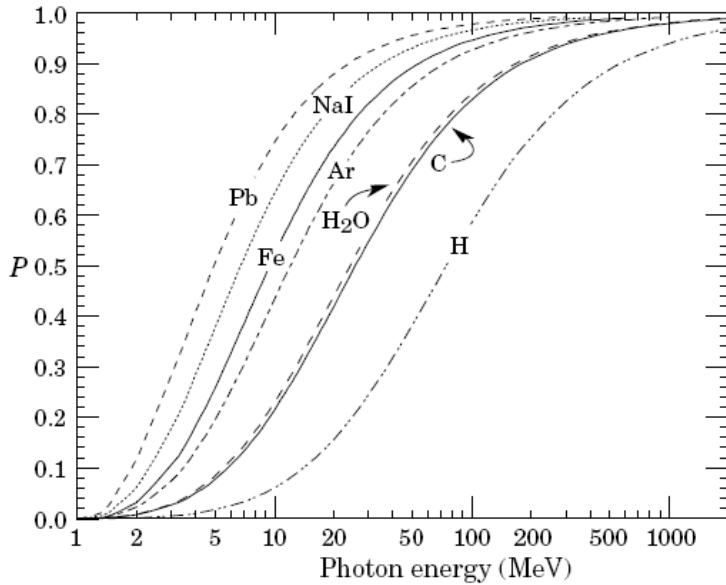


Figure 3.10: Probability P of the electron-positron pair production as a function of the incident photon energy for different materials [Bic06].

3.2.3 Pair production effect

The pair production effect can be only observed if the energy of the incident photon exceeds twice the rest mass energy of an electron ($2 \times 0.511 \text{ MeV} = 1.022 \text{ MeV}$). However, even if this condition is fulfilled, the probability of occurrence of the phenomenon is still quite low at energy of several MeV and increases as the photon energy becomes higher, as it is shown in Figure 3.10.

When the interaction of photon with matter is dominated by this process, the photon is converted in an electron-positron pair. This phenomenon can occur for both typical cases, when an incident photon is influenced by the coulomb field either of the nucleus or of the atomic electrons. In the case on interaction with the nucleus, the incident photon transfers only a small amount of recoil energy to the nucleus and is converted to an electron-positron pair as is it shown in Figure 3.11(a).

In the case of interaction with an atomic electron, the recoiling electron can receive a sufficient amount of energy to emerge as an additional (to the produced positron and electron pair) fast electron from the interaction [Ler04], as it is illustrated in Figure 3.11(b). This phenomenon is called the “triplet production”, due to the three emerging particles from this process and appears at an energy threshold of $4 \times 0.511 \text{ MeV} = 2.044 \text{ MeV}$.

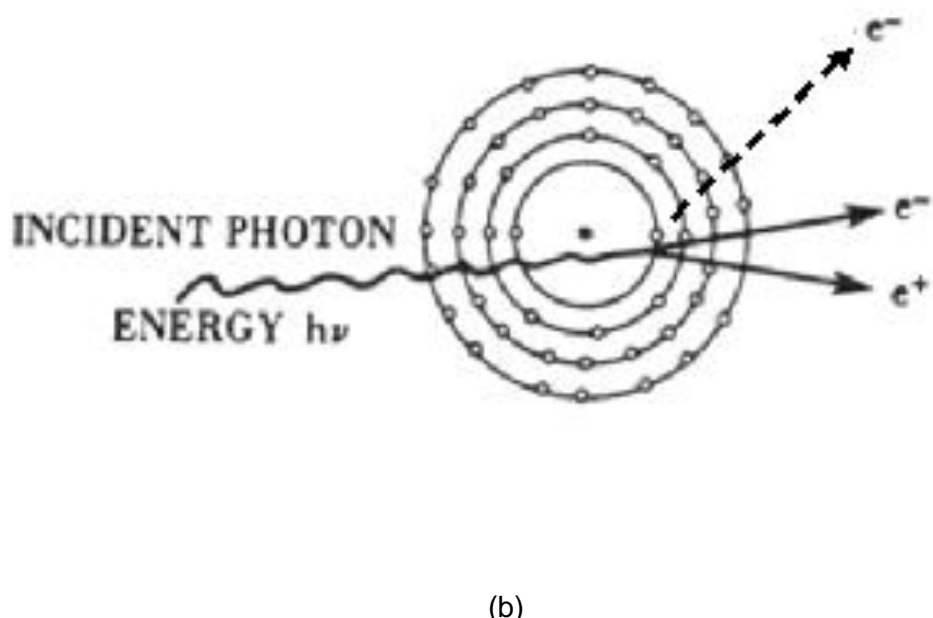
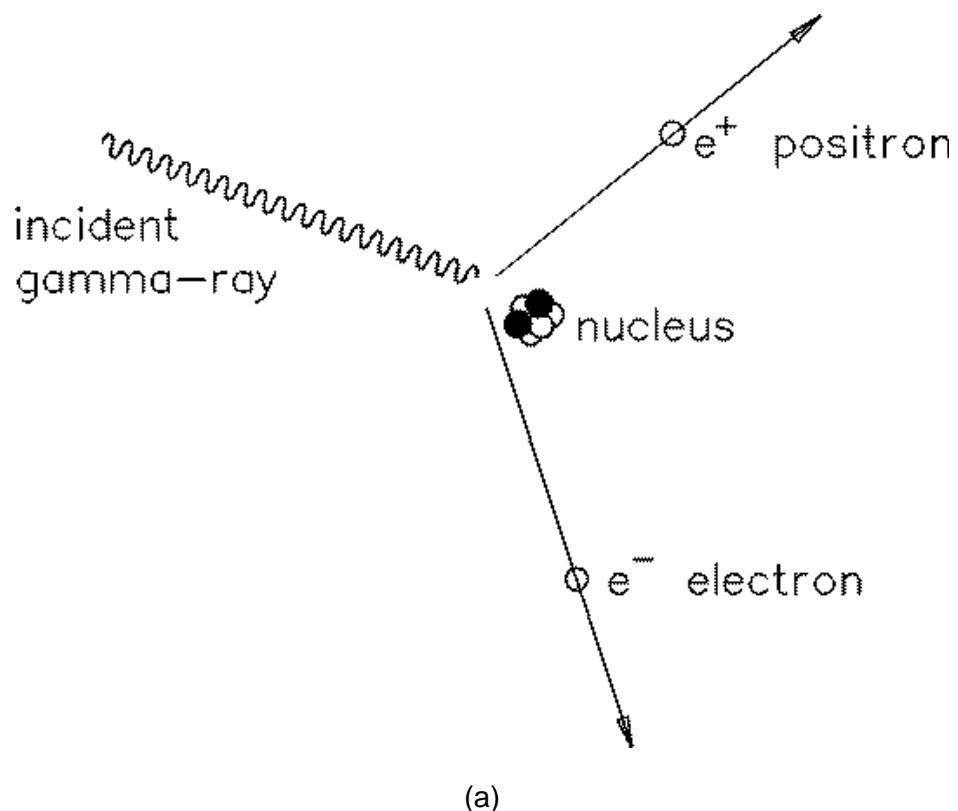


Figure 3.11: Schematic illustration of the electron-positron pair production effect when the incident photon interacts (a) with the nucleus and (b) with an atomic electron. This latter interaction is called the “triplet interaction”.

The electron and positron are rapidly slowed down by the medium absorber, and after losing all of its energy, annihilation between the positron and an atomic electron can occur, which releases two gamma rays of energy 0.511 MeV.

3.3 Interaction of neutrons with matter

The neutron interacts with the nuclei of atoms, and so can penetrate matter deeply due to its low interaction probability. Neutron interacts with atomic nuclei so that it is the nucleus recoil and the secondary particles released by it which are responsible of the ionization of the medium.

As it is illustrated in Figure 3.12, the interaction of neutron with matter can occur via two different processes, elastic scattering and inelastic scattering, which dominate its transport [Wro05].

The elastic scattering is defined as a reaction which does not modify the nature and the excitation energy of the initial particles. Initially the nucleus is at rest and only the incident neutron has a kinetic energy. After the interaction, the initial kinetic energy is shared between the scattered neutron and the target nucleus. In other words, the kinetic energy is conserved.

When a neutron passes close to a nucleus, it can be scattered by its nuclear field and can transfer a part of its energy to the recoil nucleus which will ionize the medium (shape elastic scattering), as an interaction of an ion with matter. It can also be captured by the nucleus, which by de-excitation process emits a neutron of the same energy (compound elastic scattering).

The inelastic process occurs if the energy of the incident neutron is high enough so that the recoil nucleus is excited to another energy state during the collision. Then, by de-excitation the recoil nucleus can emit neutrons, gamma rays and/or charged particles, which will ionize the medium. In this case the kinetic energy is not conserved since a part of the incident energy is used to break up the nucleus. In addition to the scattered neutron and the recoil nucleus, the inelastic scattering induces the generation of secondary particles which will be able to ionize the medium.

3.4 Conclusion

In addition with the description given in section 2.3 of the radiation damage effects, in this chapter a short review on the particle interactions with matter as relevant for this thesis is given.

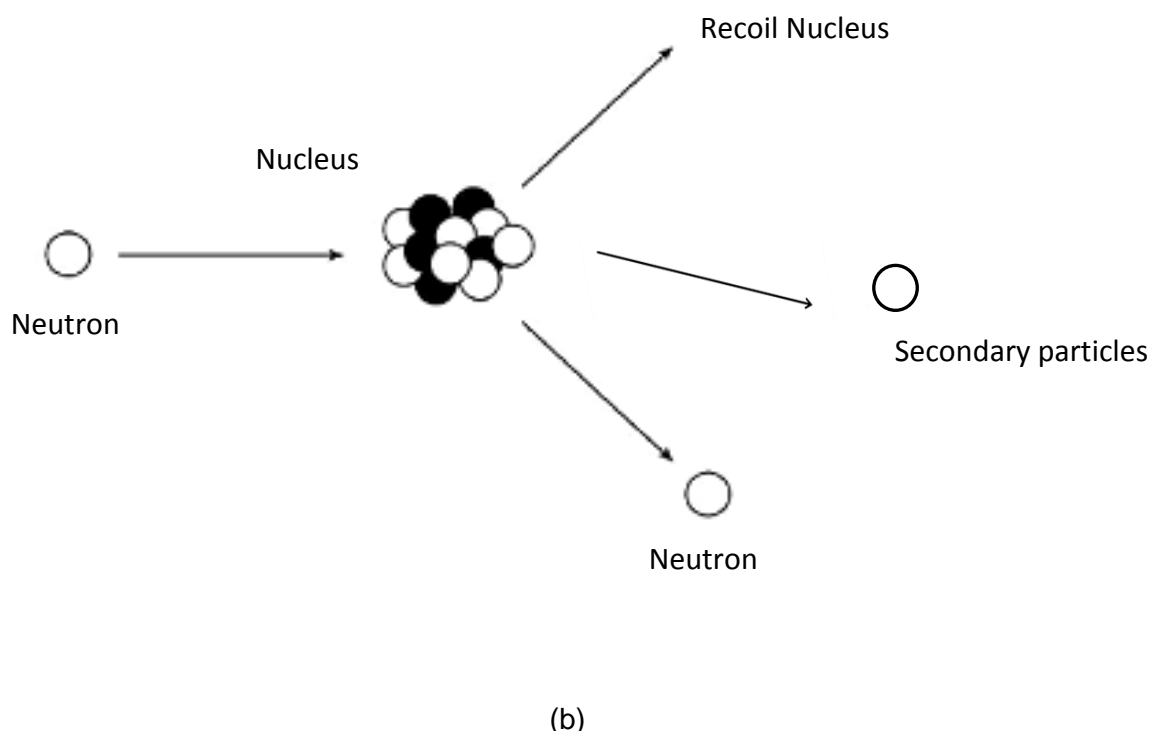
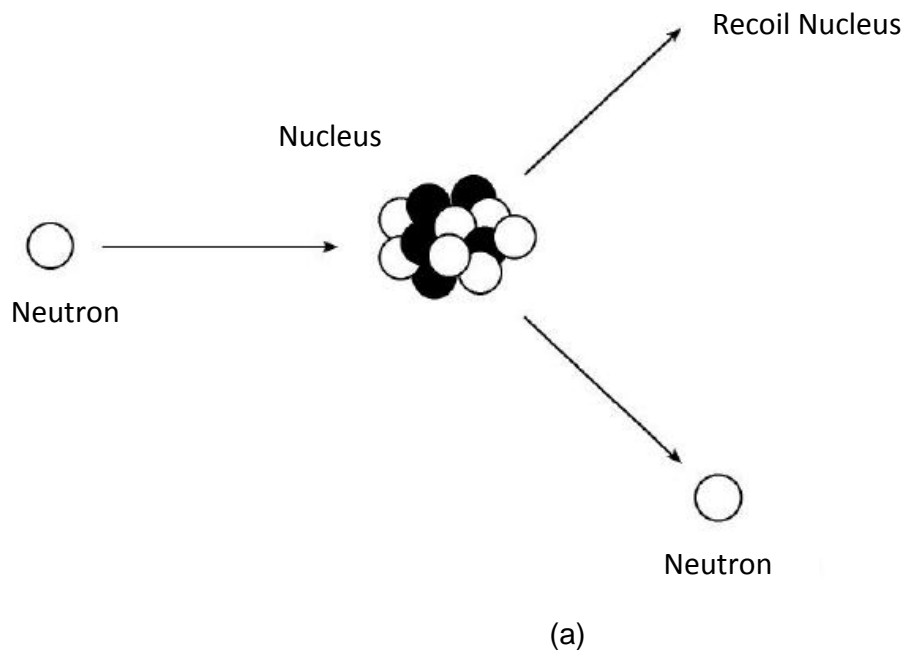


Figure 3.12: Schematic illustration of the interaction of a fast neutron with the nucleus. (a) represents the elastic scattering with the recoil nucleus and the scattered neutron and (b) represents the inelastic scattering interaction, which induces the emission of other particles from the nucleus.

The fundamental interactions with matter of the main particles present in the complex LHC radiation field are described in order to have a deeper understanding on their potential effects on the electronic components installed in the experiments.

For this reason a complete radiation monitoring equipment has been developed at CERN in previous study [Rav06]. However the packaging of this radiation monitoring equipment itself can influence the measure of the Total Ionizing Dose since particles also interact with it before depositing dose in the radiation sensors. Incident particles can generate secondaries (e.g. secondary electrons) by interacting with the atoms of the package, which might influence the measure of the sensors. Furthermore, information might be missed, since primary particles can be totally stopped (e.g. charged particles) inside the package without depositing dose in the sensors.

In the next chapter, a study using the Geant4 toolkit has been carried out aiming at evaluating the packaging effect on RadFET sensors for each particle type and energy present inside the collider.

In this chapter, it has been described that incident particles travelling through materials can either cross over all the material or being totally stopped in it. For both cases, secondary particles will be created along the tracks of primaries. Depending on the particle type and energy, interactions with matter can occur via different processes such as direct or indirect ionization, excitation, elastic and inelastic scattering etc... In any cases, the incident particle lose all or a part of its energy by interacting either with the atomic electrons, or with the nuclei.

As described in the introduction of this thesis, the behavior and the characteristics of the readout electronic and devices present within this field will be clearly influenced by this radiation field.

Chapter 4

Packaging effects on RadFET sensors for the radiation monitoring project

At the Large Hadron Collider (LHC), the complex radiation environment will be composed of charged hadrons, neutrons, electrons and photons [Daw00], [Huh95]. All detectors and electronic components present in this particle field are potentially affected by radiation damage [Hol02]. For this reason, the radiation fields in the LHC have to be precisely characterized and monitored.

In the framework of the RADMON project several radiation sensors have been evaluated for this purpose [Rav05a]. Finally, integrated sensor boards including RadFETs (Radiation-sensing Field-Effect Transistors) for Total Ionizing Dose (TID) measurements, p-i-n diodes to record the equivalent particle fluence and temperature sensors have been developed [Rav07], produced and installed in the LHC experiments ALICE, ATLAS [Man07], LHCb [Wie07] and TOTEM [Rav08a].

RadFETs are p-channel MOSFET Transistors optimized for dose measurement [Hol02]. The radiation sensitivity of these FETs is achieved by a thicker gate oxide compared to conventional MOSFETs. Radiation induced charge trapping at the Si/SiO₂ interface causes a variation of the threshold voltage (V_{th}), which is measured at a constant source-drain current. V_{th} is then a measure for the dose deposited in the gate oxide.

Even assuming that the particle spectrum in the experiments is sufficiently well predicted by Monte Carlo simulations, the question remains how much dose is deposited by different

particles with different energies in the RadFETs. As not all particles and particle energies can be evaluated experimentally, simulations are needed for converting the particle fluence to measured dose for all particle types and particle energies.

A further complication in interpretation of the measured dose values is arising from the packaging of the RadFETs. The package can alter the measured dose by various mechanisms (absorption, attenuation, creation of secondary particles, etc...). A clear understanding of the influence of the package in the particular radiation field of interest is therefore crucial to optimize the package or at least understand its impact on the measurement.

Only few experimental works have been reported on this topic. For example, the increase of the dose measured with RadFETs exposed to fast neutrons and covered with Polyethylene slabs of different thickness was investigated in [Rav05b]. In addition, RadFETs exposed to a Co-60 source and to monoenergetic low energy protons, covered or not covered by a lid were investigated in [Kea03].

For MOSFET devices exposed to low-energy photons an increase of the measured TID due to the packaging has been reported in [Ros95], [Bru95].

In this thesis work, the expected response of RadFETs in the complex radiation fields of the LHC experiments has been studied using the Geant4 toolkit [Ago03], [All06], [Col07]. A Geant4 application was developed describing the geometry and material of the RadFET sensors and the surrounding package in great detail. An assessment on the validity of the physics models used for the application was performed to evaluate the reliability of the performed simulations for various particles and particle energies being present in High Energy Physics experiments radiation fields. Finally, the application was used to optimize the package of the RadFETs. To our best knowledge a similar approach for the packaging optimization of a FET based dosimeter has been performed only once. However, the work described in [Kea03] is aiming for space applications and is limited to low energy protons, while our study spans over a multitude of particles and a wide particle energy range up to 100 GeV.

In this chapter, a presentation of the Geant4 toolkit is given, followed by a detailed description of the RadFETs and their package. Furthermore, experimental data from previous studies [Rav06], obtained with fast neutrons and 254 MeV protons using the RadFETs and the type of packaging under consideration in this work are presented. In addition, the Geant4 application and its validity is described and discussed. Simulations describing package impact on the dose measurement for various particles are also presented and finally, the influence of the packaging on the RadFETs response in typical LHC experiment radiation fields is presented and discussed.

4.1 What is the Geant4 toolkit?

The Geant4 toolkit [Ago03] , [All06] and [Col07] is a well established general purpose Monte Carlo particle transport toolkit for simulation of particle interactions with matter. It has been developed by a large international collaboration named RD44 between 1994 and 1998 and based on different institutes and universities including also CERN and ESA. This software is free and can be download directly from the Geant4 website [Gea].

This particle transport toolkit is the latest of a Geant-series emanating from a high energy physics community created by the CERN collaboration. The abbreviation of Geant means “Geometry and Tracking”, representing the two main functions of a detailed transport calculation. The previous version named Geant3 based on FORTRAN was mainly used for the LEP (Large Electron-Positron Collider) at CERN. RD44 investigated the adoption of the object oriented technology and nowadays the software is coded in C++ and it is used for space application, high energy physics as well as medical physics.

It can be considered that Geant4 is one of the software that allow to study the next generation of HEP detectors for the LHC and for the future Super-LHC (SLHC) using the object-oriented C++. For instance ATLAS is a member of the Geant4 collaboration. For this experiment, scientists and engineers used Geant4 in order to optimize the geometry of the detector and to validate electro-magnetic and hadronic physics.

In addition to be able to track particles through matter, it is also necessary to calculate the interaction probabilities with atoms and nucleus. Moreover, it provides advanced functionality typically for detector simulation such as geometry and material modeling, description of particle properties, physics processes, tracking, event, and run management, total energy deposited calculation, user interface and visualization.

4.1.1 Geant4 properties

This software is based on the Monte-Carlo method which refers to a distribution based on the generation of probability statistics and random numbers [Dup02]. In the case of Geant4, the Monte-Carlo Method can be used to sample the different variables from this distribution. In this way, it's possible to quantify these variables as for instance traveled distance by a particle prior to interaction point, called “step”, as well as the type of interaction, the number and types of interaction products or the recoil and energy of the interaction products.

Geant4 allows constructing any sort of geometry by placing “Constructed Solid Geometry” (CSG) geometry primitives, such as boxes or cylinders with associated material

information as the density and the chemical composition. The geometry includes some volumes, like a tree architecture originating from a “world volume”. It is possible to combine the different created volumes with Boolean operations.

With this tool, developers can model interactions inside complex target geometries and material compositions. Moreover, all aspects of the simulation are included in the toolkit, such as the generation of primary event, the tracking of the particles through materials and electromagnetic fields. In addition, Geant4 allows the user to visualize particle trajectories through the geometry and the emergence of secondary particles resulting from the interactions between primary particle and material as well as the physic processes governing the particle interaction with matter. This process is defined in a macro build with the C++ code of a user application and named “*Physics list*”. In this way, processes can be assigned to particles and the software can manage the trajectory of all of them for all interaction and particle type which have been defined in the code.

Such processes modify considerably the particle energy and thus the cross-section, during a step. However, a limitation of the step size has to be implemented. But the problem is that if the step size is reduced, the limit has not to be so small that computation time is greatly increased.

Applications are developed in C++ programming, using different classes. The collaboration provides some examples with the Geant4 package allowing the novice as well as the expert developers to build their own application. The following section describes the different classes which can be implemented in a Geant4 program.

4.1.2 User action classes

Geant4 is not an automatic program; users need to build their own applications. The simulation includes Geant4 classes and users can define their own classes that inherit from base classes provided by the software. There are at least three classes which must be developed to write an application. The “*detector construction*” class which details all volumes and materials used. The definition of how primary and secondary particles interact with the material is given by the “*physics list*” class and the type of incident particle, initial energy and beam position by the “*primary generator action*” class.

4.1.2.1 Detector construction class

In Geant4 this class is named “*G4VUserDetectorConstruction*”. The detector construction is based on the definition of geometrical elements, materials and chemical properties as well as

the visualization and user defined properties. This concept can be separated in two parts, the logical and the physical volume.

A logical volume describes the properties such as the material, sensitive detector, electro-magnetic field, shape (called Solid) which may contain other volumes. The material description includes elements which exist as isotopes. Solids may be of simple shape, like rectilinear boxes, cylinders, trapezoids, spherical and cylindrical sections. Another way to construct solids is to use Boolean operation with other solids as intersection, union and subtraction.

The role of the physical volume is to place the logical volume in the geometry; it represents the spatial positioning of a detector element with a specific shape. As a consequence, the detector geometry may contain several volumes included in other volumes as a hierarchical tree structure.

In addition, Geant4 allows modeling the particle transport in an electric, magnetic as well as an electromagnetic field. It provides the ability to monitor a snapshot of the particle interaction or an accumulation of interactions of a “track” or “tracks” named “hits” within the sensitive volume. Thanks to the *hits*, it is possible to record several information such as energy deposition along the track, particle characteristics (energy, mass ...) and information relating to the geometry as the spatial coordinates of the *hit*.

Moreover, it exists another term called “digit” representing a detector output. It is created by one or more hits and/or other digits.

4.1.2.2 Physics list class

Within this class, the user defines which particles will be considered during the simulation, the range cuts parameters and how to model the physics interactions (physics processes). It inherits from “*G4VUSERPhysicList*” base class and allows users to use all existing particles with seven major sub-categories of processes such as electromagnetic, hadronic, decay, photolepton-hadron, optical, parameterization and transportation. Moreover, the Geant4 toolkit offers a wide range of energies for all types of interactions.

When a particle crosses a material with an electromagnetic process, it might generate infrared divergence. To avoid that, users should define a threshold (range cut-off), which is converted to an energy. In this case, if a particle is regenerated with a residual range less high than this cut value, it will not be tracked in the material and the energy is assumed to be deposited at the point of generation.

In flight, particles are submitted to various processes and each of them is treated in the same manner from the tracking point of view. This allows the user to create a process and assign it to a particle. Thanks to this openness, it should be possible to create specific and customized applications for individual users. As a result, it is important for the collaboration to update the software with results collected from real experiments. In other words, a wide number of physics processes have been compared between simulated data and reference for extending the experimental validation of Geant4.

4.1.2.3 Primary Generator Action Class

The primary beam definition in terms of position, direction, particle and energy is described by the “*G4VUSERPrimaryGeneratorAction*” class. From here, the “*G4ParticleGun*” class is invoked and it may be used to define a particle, its momentum and momentum direction, its energy, the particle time, position and polarization, and the number of primaries. According to the required simulation, users can generate one or more primaries. The randomization of the energy, the momentum and the position is possible. There are many modules used in Geant4 to handle random numbers such as the “*HEPRandom*” module for instance which allows implementing different random distributions in a simulation.

For running a simple example in Geant4, without scoring any information about the particle interaction with detectors, the user needs to build the first three classes presented above. In order to optimize the simulation, other optional classes might be included and are described in the following sections.

4.1.2.4 Run Action class

This class contains three virtual methods. The first one is called “*GenerateRun()*” which is invoked with the command line “*BeamOn*”. The two other ones named “*BeginOfRunAction()*” and “*EndofRunAction()*” are respectively invoked before that the simulation enter into an event loop and is executed at the very end of the run processing. A run consists of a sequence of events. During the run, no parameters can be modified.

4.1.2.5 Event Action Class

An event starts when a primary particle is generated and tracked through the geometry and finishes when all secondaries have no more energy. Two virtual methods are invoked at the beginning and at the end of each event. The “*beginofEventAction()*” is invoked just before converting the primary particles to *G4track* objects. A typical use of this method is to initialize histograms for a particular event. The “*endofEventAction()*” is invoked at the end of event

processing. This method is often used for analyzing “*hits*” when particles pass through the sensitive region, in order to collect some information such as the energy deposition.

4.1.2.6 Stepping action class

This class is normally used if the user wants to visualize trajectories in a sensitive volume. A step describes the transport of a particle between two points in space. When a particle passes through the sensitive volume, the “*G4Step*” is invoked and provides information on the particle interaction as the energy lost along the step.

4.1.2.7 Sensitive detector class

As described in the previous section, a simulation can provide results as energy deposited in a sensitive volume. For that, users have to create a detector class that inherits behavior from the “*G4VUserSensitiveDetector*” base class. The main purpose of a sensitive volume is to extract useful information from the simulation like for instance scored dose when a particle steps in the sensitive volume. This class gives access to “*G4Step*” information of particles that cross the detector.

This class invokes three virtual methods such as the “*ProcessHits()*” method called when a step is created in a sensitive volume. The “*endOfEventAction()*” defined previously (see 4.1.2.5). Variables used to score the desired information as a dose variable should be initialized at the beginning of each event and which is done by the “*Initialize()*” method.

4.1.2.8 Visualization and user interface commands

In order to visualize detectors components and many aspects of the simulation as geometry, trajectories of the particles, hits, tracking steps, texts etc..., Geant4 provides visualization drivers and external interfaces. The most commonly used on a Linux platform is the “*OpenGL driver*”. It is a standard Linux system component. This driver is considered as the best for visualizing the generation of primary events and the tracking of particles through the detector. To change parameters such as parameters concerning the physics, the geometry, the primary beam or the number of events, users can use a base class named “*G4UIMessenger*”. Thus, commands can be used interactively with the system from a macro file (Batch mode) or with the interactive mode. Depending on the user requirements, it’s useful to have both modes.

The iterative mode is useful for visualizing simulation running or for debugging geometry, but it is slow. With the “Batch mode”, no visualization is used, interface commands are implemented in a macro file so that simulation parameters may be modified between runs.

Once the definition of the toolkit including the Geant4 user classes is established, in the next section the real geometry of the chip carrier for RadFET sensors used for monitoring the radiation field in LHC experiments will be described in detail.

4.2 Description of the system for total ionizing dose measurements at the LHC experiments

Actually, the system for monitoring the ionizing energy deposition (i.e. the creation of electron-hole pairs in a semiconductor material) in LHC experiments includes two types of RadFET sensors: The REM TOT-501C supplied by the REM Oxford Ltd, UK and the LAAS 1600 manufactured by the Laboratory of Analysis and Architecture of System of CNRS in France. They have an oxide thickness of 250 nm and 1600 nm and a size of $0.95 \times 0.95 \text{ mm}^2$ and $1.9 \times 1.9 \text{ mm}^2$, respectively.

The selection of these two types of dosimeters was carried out in a previous study [Rav06]. From it, the device REM TOT-501C appeared to be the best device for monitoring the most hostile environments of the LHC experiments.

On the other hand as it has been explained in these previous works, with thin-oxide devices the minimum achievable sensitivity is limited so that a unique device cannot be sufficient for LHC applications.

However, the locations at the LHC experiments where high sensitivity measurement (mGy) is required are generally far away from the interaction regions. The radiation field expected in these locations will be composed mainly of neutrons and γ -rays, while charged particles constitute a small background. Therefore, the TID cumulated there rarely exceed the tens of Gy over 10 years of LHC operation. The monitoring of this environment can be so performed with a thick oxide. From measurements carried out in this previous work, the RadFET LAAS 1600 is therefore the best device as it combines a high-sensitivity together with a high stability over time.

As explained in the introduction of this chapter, the package of RadFET dosimeters can alter their radiation responses inducing errors in the TID measurement. Moreover, in terms of dimension and materials, the commercial packaging provided for these dosimeters could not satisfy the requirements for using it in LHC experiments [Rav06].

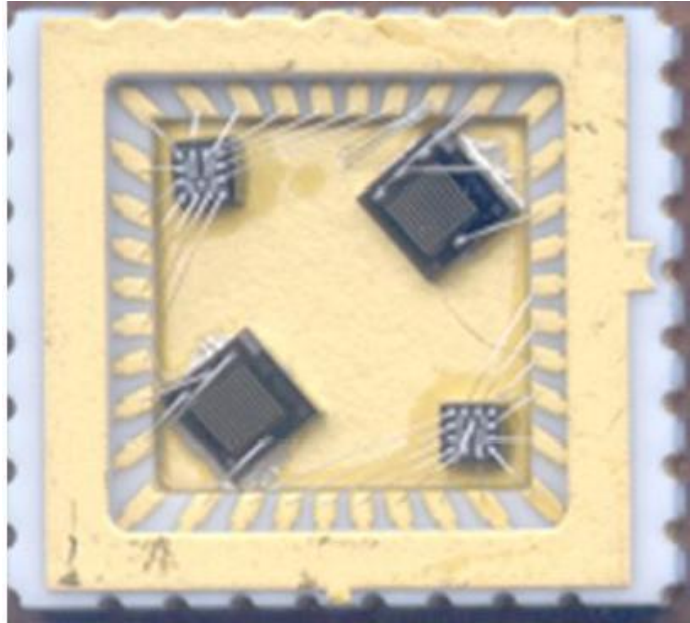


Figure 4.1: Chip carrier used for the LHC experiments. Four RadFETs of 2 different types are mounted and wire-bonded on it ($2 \times$ “REM-TOT-501C” and $2 \times$ “LAAS 1600”).

Therefore, design studies of the chip carrier for RadFET dosimeters were also performed [Rav06] by the CERN Physics Department in order to find the best suitable package for RadFET dosimeters to be used in the LHC experiments [Rad]. The selected package is an Alumina (Al_2O_3) chip carrier with a size of $1 \times 1 \text{ cm}^2$ and a thickness of 1.3 mm. It allows mounting of up to 4 RadFETs inside the carrier as illustrated in Figure 4.1.

The RadFETs are wire-bonded and connected via an Au/W metallization (backplane and bond pads) of about 3 μm thickness. The number of sensors in the carrier supplied to the LHC experiments varies from 1 to 4 according to the specific needs of the experiments [Rav06].

For this reason the connection layout for all pins of the carrier and the dosimeters has been standardized [Rad].

Having fixed the type of carrier and its connection scheme for the development of the read-out electronics and the carrier mounting in the experiments, the only freedom remaining in the design of the package is the chip carrier cover.

It will protect the RadFETs against dust and mechanical damage. However, like the chip carrier itself, it has also an impact on the TID measurement which is evaluated in this thesis.

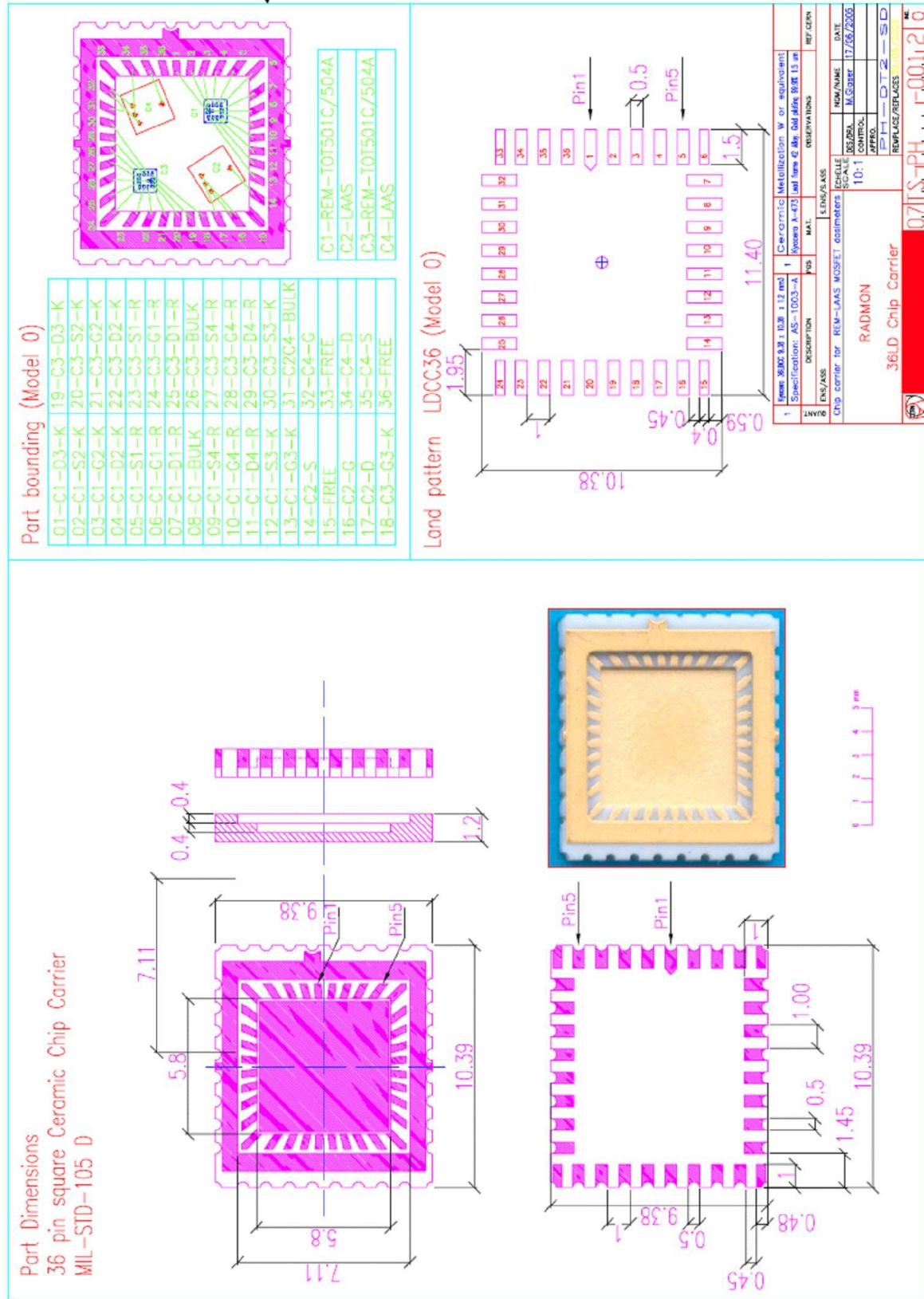


Figure 4.2: Detailed connection layout for the chip carrier for the RadFET sensors used at the LHC experiments [Rav06].

This detailed connection layout for the RadFETs chip carrier is illustrated in Figure 4.2. In addition, all the dimensions of the chip carrier are represented in it and the Geant4 geometry description was based on this layout.

4.3 Previous experimental studies

Previous experimental studies [Rav06] were carried out in two irradiation fields; one with protons at the High Energy Proton Facility (HE-PIF) of the Paul Scherrer Institute (PSI) in Villigen, Switzerland [Haj02] and the other one with neutrons at the Reactor Research Center (Triga Mark II reactor) of the Joseph Stephan Institute (JSI) in Ljubljana, Slovenia.

At JSI, the neutron irradiations were performed in a reactor of type TRIGA [Rav03]. The neutron spectrum available in this facility ranges from thermal to fast neutrons of about 1 MeV. Moreover, the RadFET sensors were also exposed to a significant γ -rays component. The RadFET carriers were irradiated by placing them into the reactor core through an irradiation tube that occupies a fuel rod position.

At PIF the carriers were irradiated perpendicularly to the beam-axis with 254 MeV protons at an average flux of about 1.0×10^8 proton/sec/cm².

The type of RadFET used for carrying out in these experiments was the REM-TOT-501C. In order to evaluate the influence of the chip carrier cover on the dose measurement, irradiations at both facilities were performed by increasing the fluence in steps and by covering the chip carrier with different thicknesses of different materials during the various irradiation steps.

The materials used for evaluating the cover influence on the TID measurement were Alumina (or Ceramic), Aluminium, FR4 (e.g. Epoxy-glass, the common printed-circuit board material) and Kapton.

Furthermore, measurements on bare RadFETs were also performed in order to be consistent with the theoretical RadFET calibration curve.

The results are presented in Figure 4.3 where the materials and thicknesses of the covers are indicated for each irradiation step. Results showed that for 254 MeV protons, the different covers had no effect on the TID measured. Results show that all data points are contained in the 5% error due to the measurement of the proton fluence. Even irradiating the RadFET sensors from the backside (see filled triangular marker), no packaging effect can be observed with this proton energy.

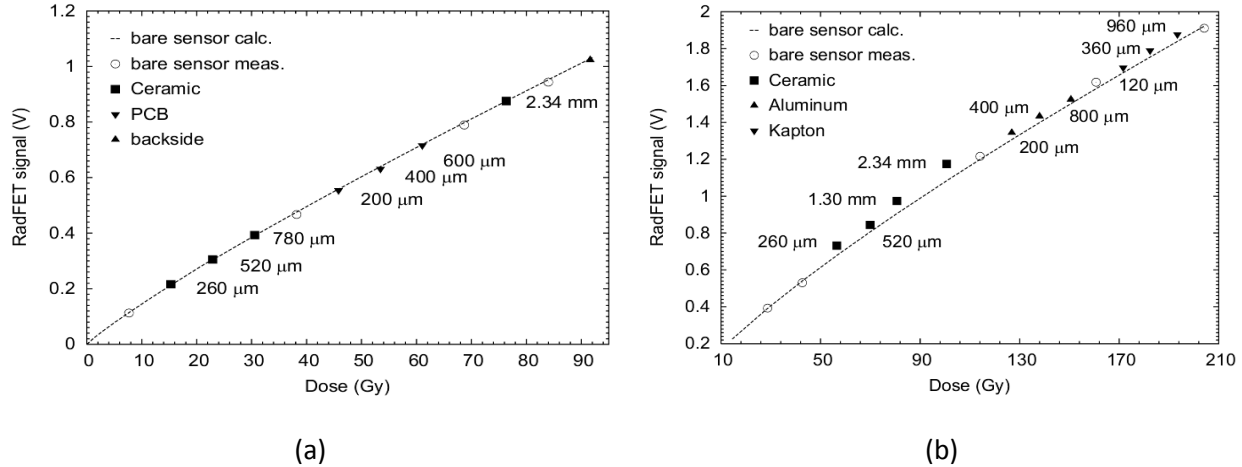


Figure 4.3 : Experimental results of the REM-TOT-501C obtained (a) at PSI with 254 MeV protons. (b) Experimental results obtained at JSI during neutron irradiation. Error bars are smaller than the symbol size.

The experiment at the nuclear reactor revealed that most of the used covers are transparent to neutrons. Only for Alumina covers exceeding a thickness of 1 mm a slight increase of the TID was observed. A more detailed description of the experiments is given in [Rav06], [Gla06].

A brief comparison with simulation results is described in 4.5.1.1.

4.4 Geant4 application

The RadFET sensors will measure the dose (or more precisely the ionization energy) deposited in the Silicon oxide layer of the FET. An interpretation of this value in a complex radiation field can only be achieved if the full particle spectrum is known. As mentioned in the introduction of this chapter, as not all particles and particle energies can be evaluated experimentally, simulations are needed to get a more conclusive picture for estimating the packaging dependence on TID measurement as well as the deposited dose in the RadFET sensors present in the LHC radiation environment.

For this purpose, a simulation application was developed specifically for this study in collaboration with the Geant4 group of the Istituto Nazionale di Fisica Nuclear (INFN) of Genova in Italy, exploiting the Geant4 toolkit. It models the detector with various packaging options and the radiation field it is exposed to, it configures the selection of Geant4 physics to be activated in

Device	x (mm)	y (mm)	z (mm)	Oxide (nm)
REM-TOT-500	0.95	0.95	0.405	250
LAAS-1600	1.9	1.9	0.405	1600

Table 4.1: Geometry of the four dies representing the RadFET Sensors in the Geant4 Application.

order to approach the complex radiation environment which is present in the LHC experiments, and it scores the energy deposited in the sensor.

4.4.1 Simulation geometry

The detector model in the simulation is based on a detailed description of the geometry and materials of the RadFET sensors and the chip carrier.

Figure 4.4 shows the 3-dimensional model of the detector geometry. The four RadFETs are represented by four dies placed on an Alumina chip carrier with a size of $1 \times 1 \text{ cm}^2$ and a total thickness of 1.3 mm. The die sizes and oxide thicknesses are given in Table 4.1. The Front view of the chip carrier with and without cover is illustrated in Figure 4.5. In a first set of simulations, discussed in section 4.5, a preliminary model was adopted: the full dies, assumed to consist of Epoxy-glass, are taken as sensitive volume, where the total energy deposited in the four dies deriving from the interaction of primary and secondary particles with the target volume is scored. Although this first set of simulations will not match the real geometry of the RadFET sensors, they provide a good overview on the detector response according to the cover thickness used. This geometry also holds for simulation presented in section 4.6.1.

The simulations presented in section 4.6.2 were performed with a more detailed detector model: the sensitive volume was reduced to represent only the thin oxide layer (SiO_2) of the RadFETs as the sensitive part of the device is the oxide layer. The two geometry models were verified to produce consistent results, as discussed in section 4.6.2.

The radiation environment is modeled as a monochromatic beam orthogonally incident on the chip carrier.



Figure 4.4: 3 -dimensional view of the Geant4 model representing the chip carrier for RadFET dosimeters installed at the LHC experiments.

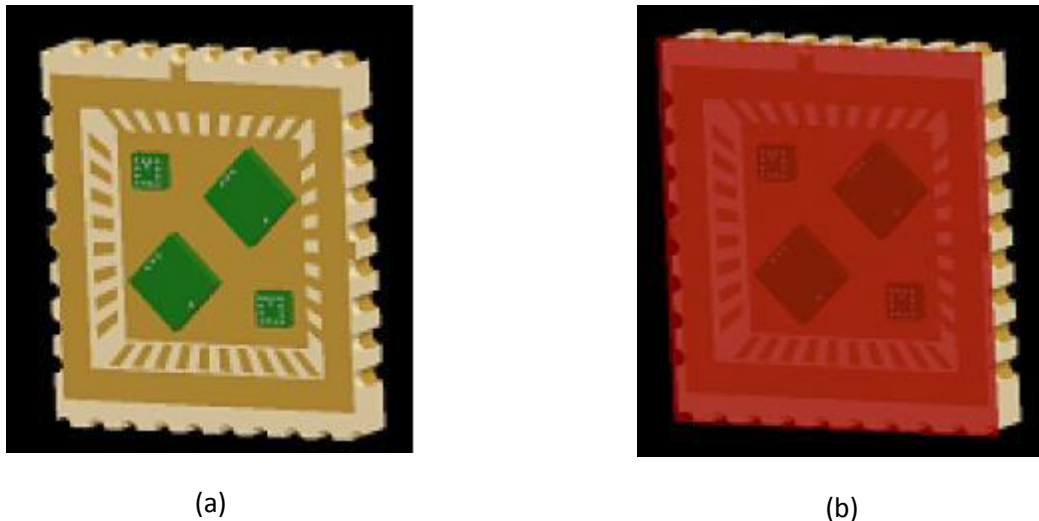


Figure 4.5: Front view of the chip carrier hosting the RadFETs (a) without and (b) with Alumina cover.

Complex radiation environments were studied as a superposition of results from different simulations with monochromatic beams, each one characterized by a given energy and particle type. The particle beam size was $1.2 \times 1.2 \text{ cm}^2$, which is slightly bigger than the $1 \times 1 \text{ cm}^2$ chip carrier; the larger transversal beam section was meant to exclude border effects.

4.4.2 Physics processes

A Geant4-based simulation requires that all the particle species involved are instantiated, and their interaction processes are specified [Ago03]; for many physics processes Geant4 offers the option to choose among different models. Both electromagnetic and hadronic physics processes were activated in the Geant4 application, to describe the interactions of the incident particle, and of all the secondary particles produced.

The electromagnetic processes activated in the simulation encompassed ionization and multiple scattering for all charged particles, Bremsstrahlung for electrons, photoelectric effect, Compton and Rayleigh scattering, and pair production for photons. The Low Energy [Cha01], [Cha04] model based [Gia99] on the ICRU49 [Icr93] parameterizations was selected for hadron ionization.

The models for electrons and photons in the Low Energy or in the Standard [Bur05] Electromagnetic packages were alternatively activated in the simulation; specifically, among the low energy ones [Apo99], those based on the EEDL [Per97] and EPDL97 [Cul97] data libraries, The Rayleigh scattering was activated only in connection with the usage of the Low Energy Electromagnetic package, since this process is not implemented in the Standard Electromagnetic package.

The selection of the models used in the simulation is supported by documented validation.

The above mentioned electromagnetic models have been compared [Ama05] to the authoritative NIST Physical Reference Data [Nis09]; both the Standard and Low Energy ones were demonstrated to be in agreement against the reference. Validation results of Low Energy electromagnetic models against precision measurements of energy deposited by low energy incident electrons are documented in [Lec09]. Various models of proton ionization are available in the Geant4 Low Energy package, respectively based on parameterizations in [Icr93], [And77], [Zie85], Wro87; they exhibit different behavior [Lec08] in the low energy domain (below 2 MeV). Their differences amount to a few percent at most with respect to the NIST Reference Data; the one chosen in the application is equivalent to the NIST Reference data at the 90% confidence level. Such differences are not critical to the study presented in this thesis.

Muon interactions are simulated through the processes in the Geant4 Standard muon package [Bog06].

The multiple scattering process [Urb05] was activated according to its default configuration. Recent studies [Lec09] have documented its contribution to the accuracy of dosimetry simulations.

Hadronic elastic and inelastic processes were activated in the simulation; they were articulated through different models according to the energy range and particle type. The fission and capture processes were active for neutrons. The design of Geant4 hadronic physics package allows the user to select different cross section and final state models associated with a given process.

Hadronic elastic scattering is treated according to the Low Energy Parameterized model, which is based on original parameterizations from GHEISHA [Fes85].

Default inelastic cross sections were used in the simulation.

Several models were selected to generate hadronic inelastic final states in different energy ranges; their activation ranges partly overlapped to ensure a smooth transition between different simulation regimes.

The binary cascade model [Fol04] was active in the lower energy range (up to 10 GeV) for protons, neutrons and pions; it encompasses models for intranuclear transport, pre-equilibrium phase and nuclear de-excitation. At intermediate energies (8-25 GeV) the Parameterized models, originally derived from GHEISHA [Fes85], were activated. The highest energy range (20 GeV – 100 TeV) was covered by the Quark Gluon String model [Fol03].

The inelastic hadronic scattering of deuteron, triton and α particles was modeled with the Low Energy Parameterized model up to 25 GeV and the Binary Light Ion model up to 10 GeV/nucleon; Tripathi [Tri96], [Tri97], [Tri99a], [Tri99b] and Shen [She89] cross sections were selected. The Binary Ion Model was active for ions.

The validation of the hadronic interaction models used in the simulation is documented in [Iva03], [Wel03], [Ers04] and [Wri06]; it is worth remarking, however, that while the validity of the Geant4 electromagnetic models used is well established, the validation of the hadronic ones is still in progress, due to the complexity of the physics domain.

A Geant4-based simulation requires that the user defines a threshold for the production of secondary particles from processes affected by infrared divergence [Ago03]; the secondary production threshold is expressed in terms of range. The secondary production threshold affects the precision of the energy deposit distribution; its setting should be consistent with the desired precision and the geometrical characteristics of the simulated experimental set-up. The

production threshold of secondary particles was fixed to 1 μm for the simulations in section 4.5 and section 4.6.1, and 0.2 μm for simulations in section 4.6.2; in both cases these settings were significantly smaller than the thickness of the sensitive volume associated with the detector model, thus ensuring the accuracy of the spatial distribution of the energy deposit in the simulation.

The energy deposited in the four dies (respectively oxide layers for simulations in section 4.6.2) is scored as a result of the simulation; it accounts for the interactions of primary and secondary particles with the target volume. The average energy deposited per incident primary particle per unit area is calculated by scaling this value by the number of primary particles hitting the chip carrier and its area.

It should be mentioned that the simulations presented in this thesis were performed with Geant4 version 8.0.

4.5 RadFET packaging effects evaluated using Geant4 simulations

For the following simulations, the packaging effect was investigated by studying the energy deposited by primary and secondary particles in the sensitive volume which in this case is the four full dies, using different thicknesses of the chip carrier lids: 260 μm , 780 μm , 2340 μm and without any lid. One of the issues under study is the contribution of secondary particles to possible dose enhancements.

The following sections report the results of the analysis for various kinds of primary particles which are present in LHC experiments; when the error bars are not explicitly reported in the figures, the statistical uncertainties of the simulation results are smaller than the size of the symbols.

In addition, comparisons between results from simulations and analytical calculations were carried out for different particle types, in the following sections. The aim is not to verify the validity of Geant4 simulations, because all the particle transport theories are already implemented in the toolkit, but rather to give an idea on the validity of our approach to use Geant4 as it was a new simulation toolkit used by our scientific group.

4.5.1 Results for charged hadron simulations

The energy deposit resulting from incident protons (p^+), negatively or positively charged kaons (k^+, k^-) and pions (π^+, π^-) were investigated in the following simulations. Since the

particles carry the same charge and nuclear reactions play only a minor role for the total energy deposit in the RadFET, the main difference in terms of our application for charged hadrons is their particle mass: 938,3 MeV/c² for protons, 493,7 MeV/c² for kaons and 139,6 MeV/c² for pions. The heaviest particle being the more ionizing, for the same kinetic energy protons deposite more energy in the material than kaons and pions.

4.5.1.1 Proton simulations

In this section, results from simulations using five different proton energies of 20, 50, 100, 150 and 254 MeV are discussed. The latter energy is the energy of the protons used to obtain experimental results at PSI presented in section 4.3 (254 MeV protons). With the intention of comparing the experimental data with the Geant4 model, this proton energy was also employed in Geant4 simulations.

Figure 4.6 represents the ratio between the deposited energy on the four full dies simulating the RadFET sensors with cover (pack. + lid) and without any cover (pack. Bare) according to its thickness for few proton energies. As expected the simulation shows that the energy deposited in the sensitive volume for low energy protons depends strongly on the cover thickness.

For example RadFET sensors with an Al₂O₃ cover of 1.2 mm thickness exposed to 20 MeV protons will get a two times higher dose than RadFET sensors without any cover. In addition, for 50 MeV protons, the dose enhancement by the package can be even more significant than for 20 MeV.

On the other hand, the TID measured in sensors covered by a 6.7mm thick ceramic slab can reach a factor of about 4. For higher energy protons the dose enhancement by the cover becomes less significant. For example, for 100 MeV protons the influence of the same 6.7 mm thick ceramic slab is around 13% only, while for even higher proton energies of e.g. 150 MeV and 254 MeV the dose enhancement becomes almost negligible.

It can be mentioned that 20 MeV protons interact more strongly with the atomic electrons compared to 50 MeV protons due to their lower energies [Hol02]. Therefore the deposited energy on uncovered RadFET sensors by 20 MeV proton energies is more important than the one deposited by 50 MeV proton energies. For this reason, the difference of the energy deposited between RadFET sensors covered and uncovered is more important for 50 MeV protons than for 20 MeV. These effects can clearly be understood using the Bethe-Bloch formulation⁹ [Bic06] which was used to perform the analytical calculations given in Figure 4.6.

⁹ Bethe Bloch formulation described in section 3.1.1.

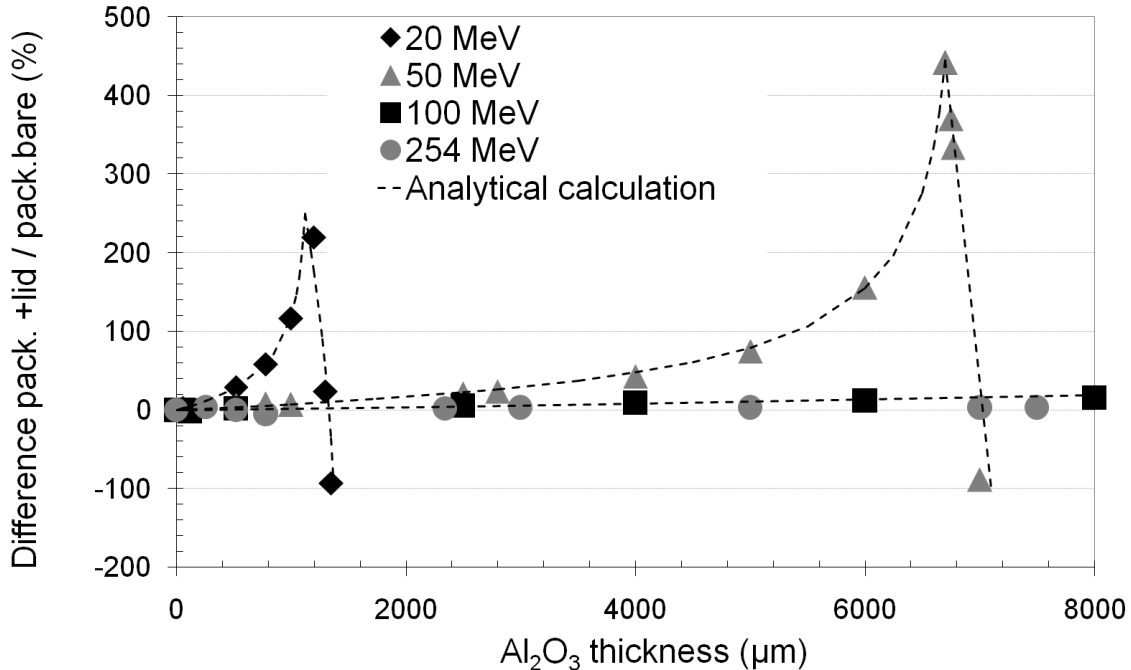


Figure 4.6: Difference of energy deposited (dose enhancement) in the four RadFET sensors between chip carriers with and without ceramic cover in dependence of the cover thickness. The points and dashed lines represent the Geant4 simulation results and analytical calculations based on the Bethe-Bloch formulation, respectively.

Rough calculations involving the transport of proton through the packaging and the RadFET sensors was performed. The calculations were performed considering a 405 μm thick die, as referenced in Table 4.1, covered by an Alumina layer with variable thickness.

As discussed in section 3.1.1, when a proton interacts with matter, its kinetic energy decreases due to the generation of holes-electrons pairs which is named the ionization energy loss (IEL), along the track and atomic excitation.

For comparing simulation with analytical calculation, the mean rate energy loss $\left| \frac{dE}{dx} \right|$

(named stopping power) by protons crossing the RadFET sensors was calculated for various proton energies and cover thicknesses using the Bethe-Bloch equation presented in section 3.1.1.

At high energy ($E_p > 1\text{GeV}/c$) the qualitative difference in stopping power behavior between a gas (He) and other materials is due to the density effect correction¹⁰. Since proton energies in simulations presented in this section do not exceed 1 GeV, the density effect correction is not taken into account in the analytical calculations. Once the stopping power is calculated for the cover material and for the RadFET sensor material used in the Geant4 simulation, the mean energy rate loss is respectively integrated over their layer thicknesses.

The difference between the energy deposited by a proton in the sensor with and without an Alumina cover is then given in [%] and expressed by the following formula:

$$Ratio(\%) = \frac{\int_0^{RadFET \text{ thickness}} \left(\frac{dE_i}{dx} \right)_{lid} dx - \int_0^{RadFET \text{ thickness}} \left(\frac{dE_p}{dx} \right)_{bare} dx}{\int_0^{RadFET \text{ thickness}} \left(\frac{dE_p}{dx} \right)_{bare} dx} \times 100 \quad (4.1)$$

Where

$$\int_0^{RadFET \text{ thickness}} \left(\frac{dE_p}{dx} \right)_{bare} dx \quad (4.2)$$

is the energy deposited in the 0.405 mm thick RadFET die without any cover by a proton of energy E_p .

The other term represents the energy deposited in the RadFET sensor by a proton of energy E_p after having travelled through the Al_2O_3 cover, which is named E_i :

$$E_i = E_p - \int_0^{Cover \text{ thickness}} \left(\frac{dE_p}{dx} \right).dx \quad (4.3)$$

Where

$$\int_0^{Cover \text{ thickness}} \left(\frac{dE_p}{dx} \right).dx \quad (4.4)$$

represents the mean energy loss in the Al_2O_3 cover.

¹⁰ See Bethe –Bloch formulation presented in section 3.1.1..

Therefore, the energy deposited in the covered RadFET sensor is equal to:

$$\int_0^{\text{RadFET thickness}} \left(\frac{dE_i}{dx} \right)_{\text{lid}} dx \quad (4.5)$$

As illustrated in Figure 4.6, analytical calculations are in good agreement with the data arising from the Geant4 simulations. The results confirm that 20 MeV protons can penetrate an Alumina thickness of about 1400 μm as well as 50 MeV protons can cross a cover of approximately 7 mm before losing all their energy. For all other analytical calculations with proton energies higher than 50 MeV, the packaging effect on the dose measured by the RadFET sensors is negligible. The cover thicknesses causing the highest dose enhancement for certain proton energies are clearly related to ‘Bragg peaks’.

One reason to perform Geant4 simulations instead of analytical calculations was to understand the impact of secondary particles generated in the package surrounding the RadFET, as they could potentially cause a dose enhancement [Jak06].

However, as the analytical calculations match very well the Geant4 simulations, no significant dose contribution from secondaries created by protons in the cover is expected.

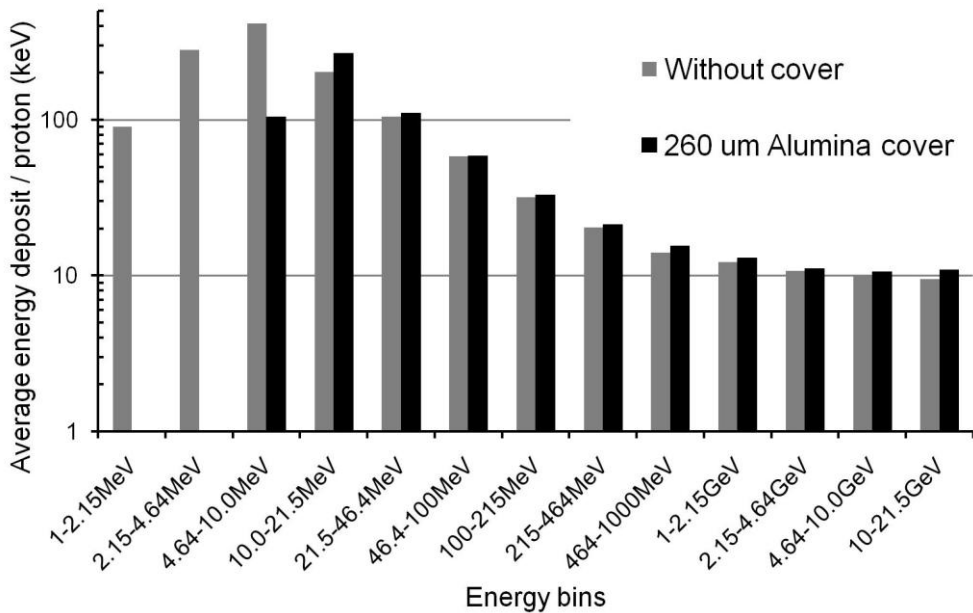


Figure 4.7: Average energy deposited in the four RadFET sensors per incident particle for protons. Simulations were performed with or without Alumina cover thickness of 260 μm . The energy bins correspond to a realistic proton energy spectrum present in LHC experiments.

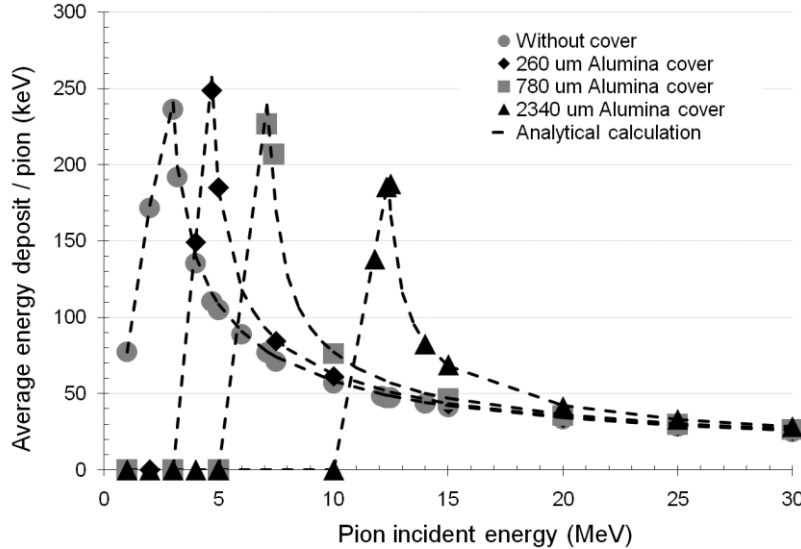


Figure 4.8: Average energy deposited in the four RadFET sensors per incident particle for pions. Simulations were performed with or without Alumina cover of the thickness indicated in the figure. Dashed lines represent analytical calculations.

Finally it has to be mentioned that simulations have been performed simulating the 254 MeV proton experiment described in the previous section. The simulations predict, as observed in the experiment, that no dose enhancement for the used cover materials and thicknesses is expected. Furthermore, the average deposited energy on the four RadFETs covered and uncovered by a 260 μm Alumina lid was evaluated as a function of proton energies over energy bins corresponding to a realistic proton energy spectrum expected in the LHC experiments. More precisely, the y-axis corresponds to the average energy deposited per proton of certain energy as a function of incident proton energy bins (x-axis), which here span over energies binning resulting from simulations made for the ATLAS detector [Shu03]. As it can be notified in Figure 4.7, low energy protons are absorbed in the cover and which induces that no energy is deposited in the RadFET sensors. The same evaluation has been done for pions and kaons and is discussed in more detail in the next section.

4.5.1.2 Pion and Kaon simulations

Like protons, kaons and pions are charged hadrons¹¹. Figure 4.8 presents pion simulations performed with the Geant4 application indicating how the energy deposit in the RadFETs depends on the cover thickness and the pion energy.

¹¹ Definition of charged hadrons given in chapter 3, concerning the interactions of particle with matter

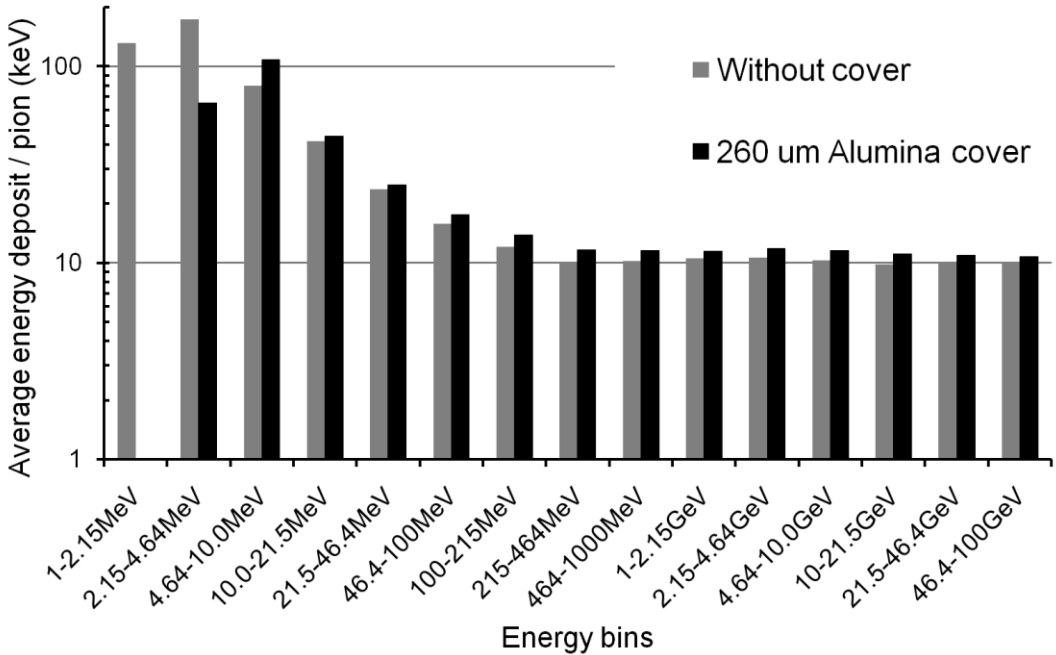


Figure 4.9: Average energy deposited in the four RadFET sensors per incident particle for pions. Simulations were performed with or without Alumina cover thickness of 260 μm .

The amount of material in the lid modulates the fraction of lower energy primary particles which are absorbed in the cover and the creation of secondary particles, which in turn contribute to the energy deposit observed in the sensitive volume.

This effect is illustrated in Figure 4.9 and Figure 4.10, which compares the average deposited energy on the four RadFETs covered by a 260 μm Alumina lid and without any cover as a function of pion and kaon energies respectively. As for Figure 4.7, for both figures, the energy bins correspond to a realistic radiation spectrum expected in the LHC experiments [Shu03].

For both particle types, at lower energies, charged hadrons are totally absorbed in the cover. As the mass of kaons is heavier than the one for pions, they interact more strongly with matter.

It is observable here, as kaons need more energy for passing through the cover and deposit energy in the RadFET sensors. The dose enhancement at higher energies due to the cover is of the order of 10%.

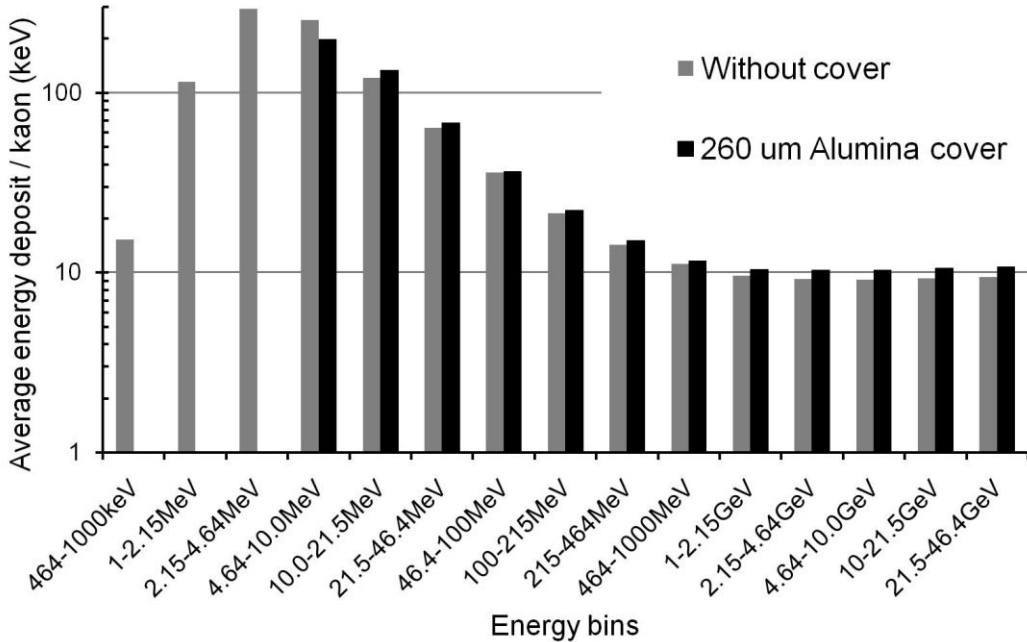


Figure 4.10: Average energy deposited in the four RadFET sensors per incident particle for kaons. Simulations were performed with or without Alumina cover thickness of 260 μm .

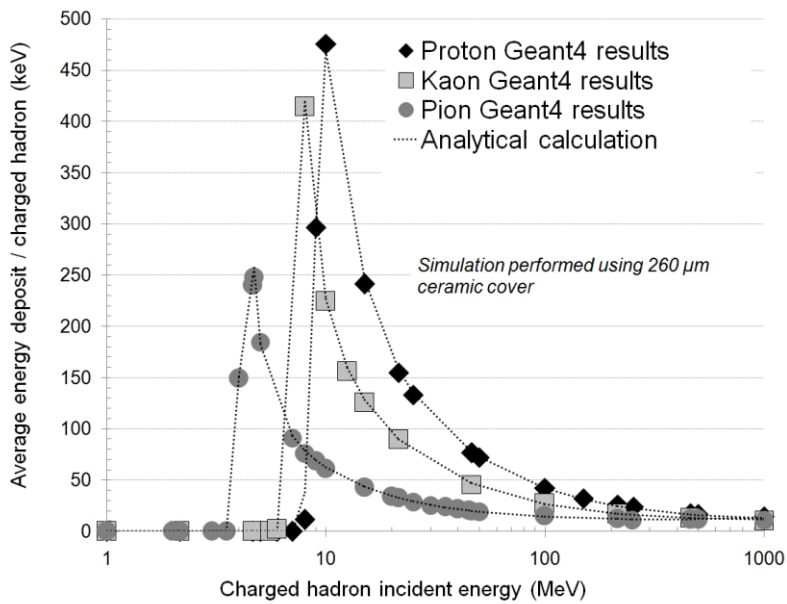


Figure 4.11: Average energy deposited in the four RadFET sensors per incident particle. Simulations were performed with Alumina cover of the thickness indicated in the figure. Dashed lines represent analytical calculations.

Figure 4.11 gives a comparison of results for protons, kaons and pions. For the same kinetic energy protons deposit more energy in the sensitive volume than kaons and pions. This is due to the higher proton mass which is leading to a higher ionization density in the traversed material.

Protons are therefore absorbed in the cover up to higher energies. In summary the argumentations given previously for protons can thus be generalized to all charged hadrons: Low energetic hadrons are absorbed in the Alumina cover and depending on the mass of the particle, the energy necessary for passing through it is higher for the heavier ones.

Since the Bethe-Bloch formulation can be applied to all charged hadrons, in figures presented in this section, the dashed lines represent analytical calculations based on the same method as described in section 4.5.1.1. The only changed parameter in the calculation is the mass of the particle.

As the analytical calculations match quite well the simulations, as for protons no significant contribution of secondary particles to the deposited dose in the RadFET is expected for our packaging geometry.

4.5.1.3 Comparison between electromagnetic and hadronic interactions

For the three types of charged hadrons presented here, the contribution to the energy deposit in the four RadFET sensors, deriving from electromagnetic and hadronic interactions was evaluated by comparing simulations where both types of processes were activated, to those where electromagnetic interactions only were active in the Geant4-based application.

Hadronic interactions can modify the energy deposited in the sensitive volume through different effects. In the case of elastic scattering, it affects the particle direction of the particle, therefore the path traverses in the detector and the resulting energy loss can be modified. On the other hand, inelastic interactions affect the energy loss through the possible suppression of the primary particle and the creation of secondary ones, whose energy deposit may differ significantly from the one due to the electromagnetic interactions of the primary particle only [Lec08]. The results are shown in Figure 4.12 for protons, pions and kaons; they concern an energy range similar to what is expected in realistic operation conditions at LHC.

In the previous sections, analytical calculations based on the Beth-Bloch formation have been made for comparison with simulations. Since calculations match quit well the Geant4 simulations, it means that electromagnetic interactions mainly contribute to the energy deposited on the RadFET.

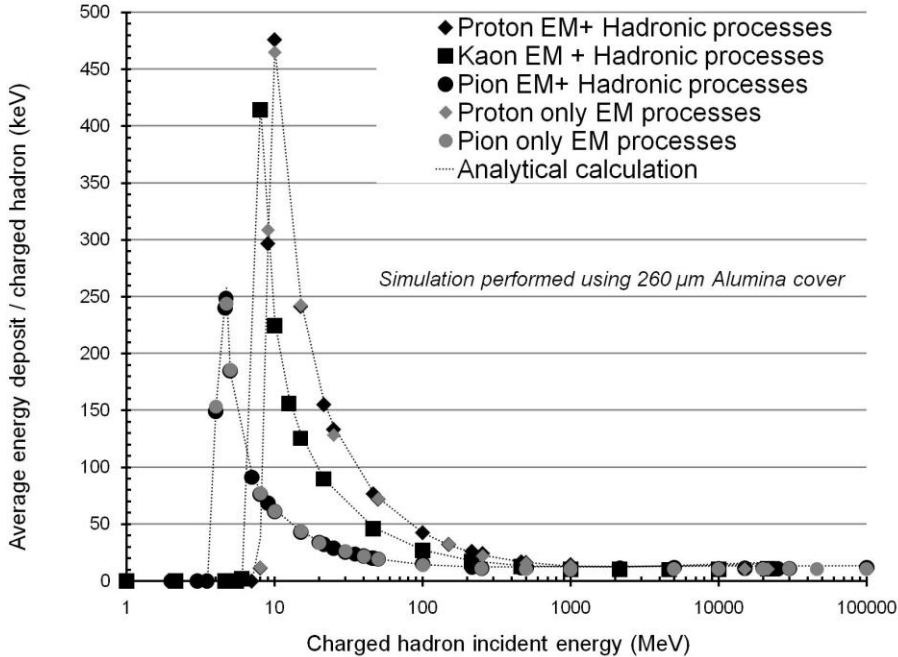


Figure 4.12: Average energy deposited in the four RadFET sensors per incident particle for charged hadrons resulting from electromagnetic (EM) interactions only and by both electromagnetic and hadronic ones. Simulations were performed with an Alumina cover thickness of 260 μm . Dashed lines represent analytical calculations.

For confirming that, in order to estimate the influence of hadronic interactions on charged hadron simulations presented in this section, a statistical analysis has been performed. It evaluates the degree of compatibility of the energy deposit distributions deriving from simulations where only electromagnetic interactions were active with respect to simulations accounting for both electromagnetic and hadronic interactions.

Without entering in the detail of the calculation, the Kolmogorov-Smirnov goodness-of-fit test, which is well documented in [Kol33], [Smi39] was applied to compare the two distributions respectively for protons and pions shown in Figure 4.12; the null hypothesis stated their compatibility. A confidence level of 0.1 was set to define the critical region determining the rejection of the null hypothesis; the p-value resulting from the test was 0.589 and 0.937 respectively for protons and pions, thus failing to reject the null hypothesis in both cases. In addition, similar behavior was also verified with kaons.

This result demonstrates that the energy deposited by charged hadrons in the RadFET sensors is mostly due to electromagnetic interactions, while hadronic processes contribute to a lesser degree.

Furthermore the accuracy of the results presented in this thesis is dominated by the accuracy of the Geant4 electromagnetic processes used in the simulation, which is discussed in section 4.4.2.

This gives confidence into the predictive capabilities of the simulation as the validity of the Geant4 electromagnetic processes is well established. This result also shows that no significant dose contribution from secondary particles created by nuclear interactions of charged hadrons in the cover is expected.

With the analytical calculation matching quite well the simulation results, a negligible dependence on the energy deposit by secondary particles resulting from electromagnetic interactions of the incident charged hadron with the cover is also considered here.

4.5.2 Results for charged lepton simulations

4.5.2.1 Electron simulations

Electrons are classified as leptons¹² and have a mass of $0,511 \text{ MeV}/c^2$. The energy deposited in matter is smaller than for hadrons of same kinetic energy. One of the reasons is their mass, which is lighter than the mass of charged hadrons; therefore electrons are less ionizing than protons, kaons, or pions.

In addition, the transport of MeV electrons through material is much more complex [Hol02], as they are easily scattered or even “back scattered”. Their path in the material does not follow a straight line and the scattering reduces the energy and the flux of the electrons.

For our specific case this means that all or a significant fraction of the electrons up to several MeV kinetic energy is absorbed in the Alumina cover. Particles of low energy, i.e. with range less than the ceramic thickness may be completely stopped in the material, while for higher energies the flux is reduced. As a consequence a smaller fraction of the incident particles contribute to the energy deposited in the sensors than for charged hadrons for which the cover reduces the energy of the particles but not their flux, unless they are completely stopped in the cover.

The Number Transmission Coefficient (NTC) describes the ratio between incident particle fluence and particle fluence after an absorber as in our case the Alumina cover. Figure 4.13

¹² Definition is given in chapter 3, concerning particle interactions with matter.

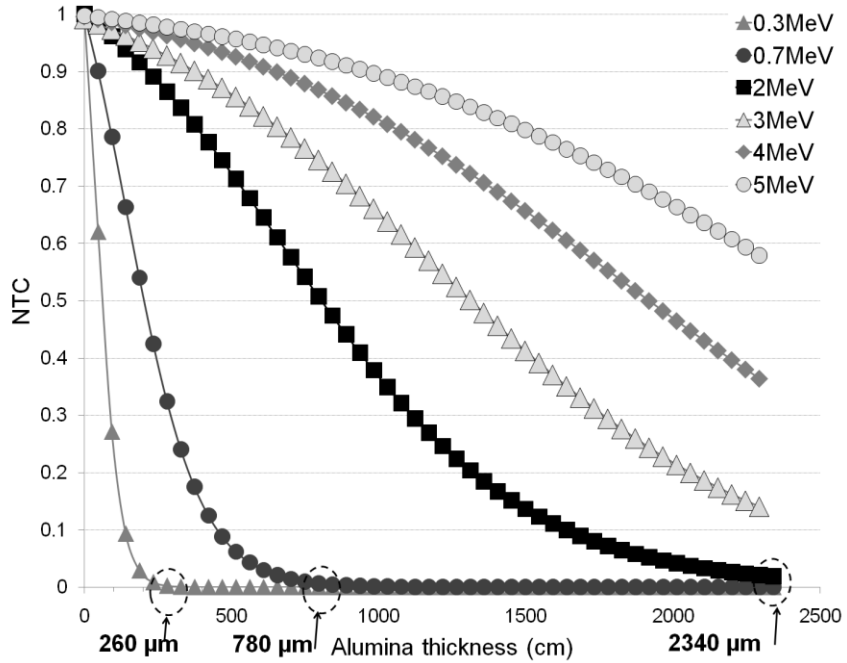


Figure 4.13: Calculated transmission coefficients (NTC) for different incident electron energies in dependence of Alumina absorber thickness.

shows the NTC for electrons passing through Alumina according to the formulations given in [Ebe69], [Tab75].

In order to understand the results given by Geant4 simulations, the number of transmitted electrons by the Alumina slab as well as the emergent electron energy spectra has to be considered.

The number of electron transmitted through a slab absorber for monoenergetic electrons is a function of the thickness and the incident kinetic energy and is given by the following formula:

$$NTC = \frac{[1 + \exp(-s_0)]}{\left\{ 1 + \exp \left[(s_0 + 2) \left(\frac{x}{R_{ex}} \right) - s_0 \right] \right\}} \quad (4.6)$$

Where x : Thickness of the ceramic cover in cm.

R_{ex} : Extrapolated range of the electron in cm referenced in [Tab72].

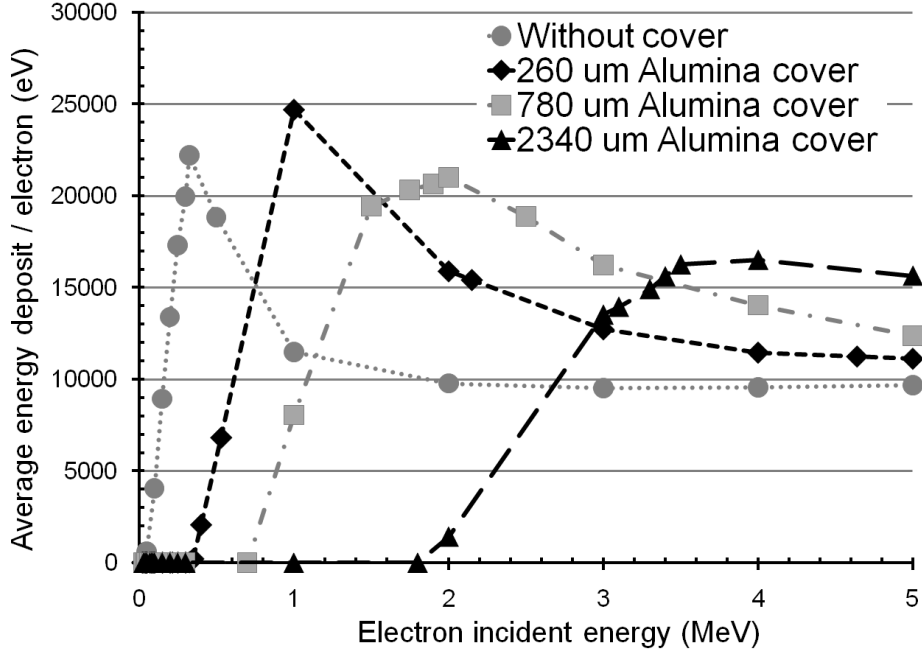


Figure 4.14: Average energy deposit per incident electron in the four RadFET sensors covered or not covered by Alumina slabs of different thicknesses.

$$s_0 = a_1 \exp \left[\frac{-a_2}{1 + a_3 \tau_0^{a_4}} \right] \quad (4.7)$$

where a ($i=1, 2, 3, 4$) is a constant for a given absorber and τ_0 represent the incident energy E_i on the rest energy mc^2 of the electron:

$$\tau_0 = \frac{E_i}{mc^2} \quad (4.8)$$

Figure 4.14 shows simulations for the average energy deposition in the RadFET by electrons of up to 5 MeV kinetic energy assuming different Alumina thicknesses used to cover the RadFET sensors. The simulations reveal that for RadFETs covered with a 2340 μm ceramic slab, the energy cut-off appears around incident electron energies of 2 MeV. This is in good agreement with the NTC data shown in Figure 4.13 indicating that 2 MeV electrons are almost totally absorbed in a 2340 μm Alumina slab. The same comparison can be done for 260 μm and 780 μm Alumina thicknesses for which the ‘electron-cut off energy’ is about 300 keV and 700 keV, respectively.

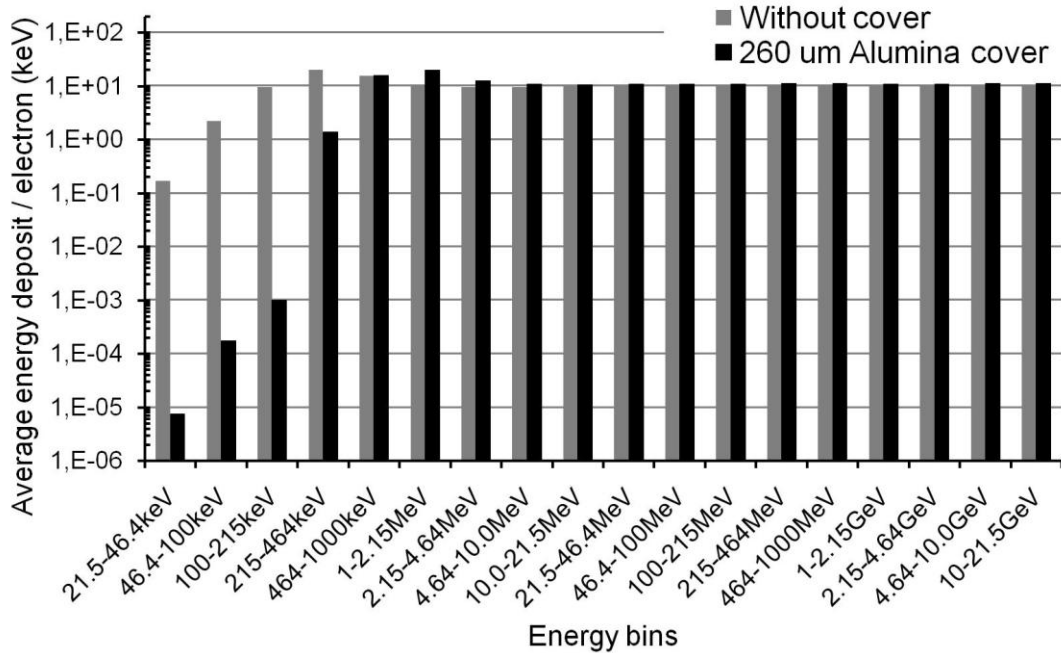


Figure 4.15: Average energy deposited in the four RadFET sensors per incident particle for electrons. Simulations were performed with or without Alumina cover thickness of 260 μm .

It should be mentioned that contrary to the charged hadron case, the deposited dose in the RadFET could not have been easily calculated in an analytical way. This is clearly one of the reasons why a Monte Carlo Simulation has been used for this work. The same holds for photons which are discussed in the section concerning photon simulations (see section 4.5.3).

As for charged hadrons, the energy deposited in the four RadFETs has been evaluated over a realistic LHC energy spectrum. Results of RadFETs uncovered and covered by a 260 μm Alumina slab are illustrated in Figure 4.15. It is more difficult for this particle type to clearly distinguish the bin where the energy deposit is at maximum, i.e. the ‘‘Bragg peak’’.

As electrons are light particles, even when they are totally stopped in the RadFET sensors so that they deposit all their energy inside it, the energy scored is only a factor of about 2 higher than the energy deposit in the RadFETs when high energetic electrons pass totally through the sensors.

For comparison, in the case of pion simulations presented in section which are the lightest type of charged hadron evaluated in this thesis, the ratio between the energy deposited in the sensor at maximum (i.e. when the particle is totally absorbed in RadFETs) and the energy deposited when energetic pions cross totally the RadFET sensors is of about 20.

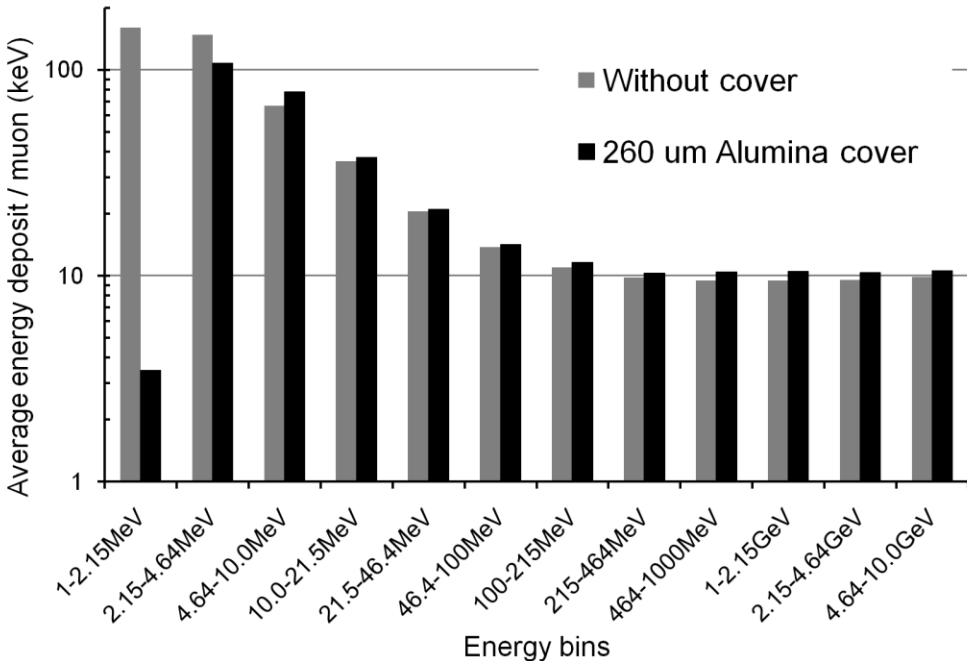


Figure 4.16: Average energy deposited in the four RadFET sensors per incident particle for muons. Simulations were performed with or without Alumina cover thickness of 260 μm .

For this reason it is easier to observe the Bragg peak for charged hadrons but it does not mean that it does not exist for electrons. It is just a matter of difference on the energy deposited in the sensors due to different particle masses.

The same observation can be done with muon simulations presented in the following section.

4.5.2.2 Muon simulations

As for all particle types presented in previous simulations, the cover material has the effect of stopping low energy muons, while some effect of dose enhancement is observed at higher energies, as documented in Figure 4.16. This simulation derives from a primary muon spectrum as expected in realistic operation conditions in the LHC experiments.

Even if the interaction of muons with matter can be considered as similar as the one for electrons, their mass ($105.7 \text{ MeV}/c^2$ for muons) differ. It implies that muons deposit more energy in the sensors than electrons. This can clearly be observed in Figure 4.16 where the “Bragg peak” is easily noticeable compared in the case of electron. The difference between the energy deposited at maximum when the particle is totally absorbed in the sensor and the energy deposited when energetic muon cross all the sensitive volume is of the order of 15.

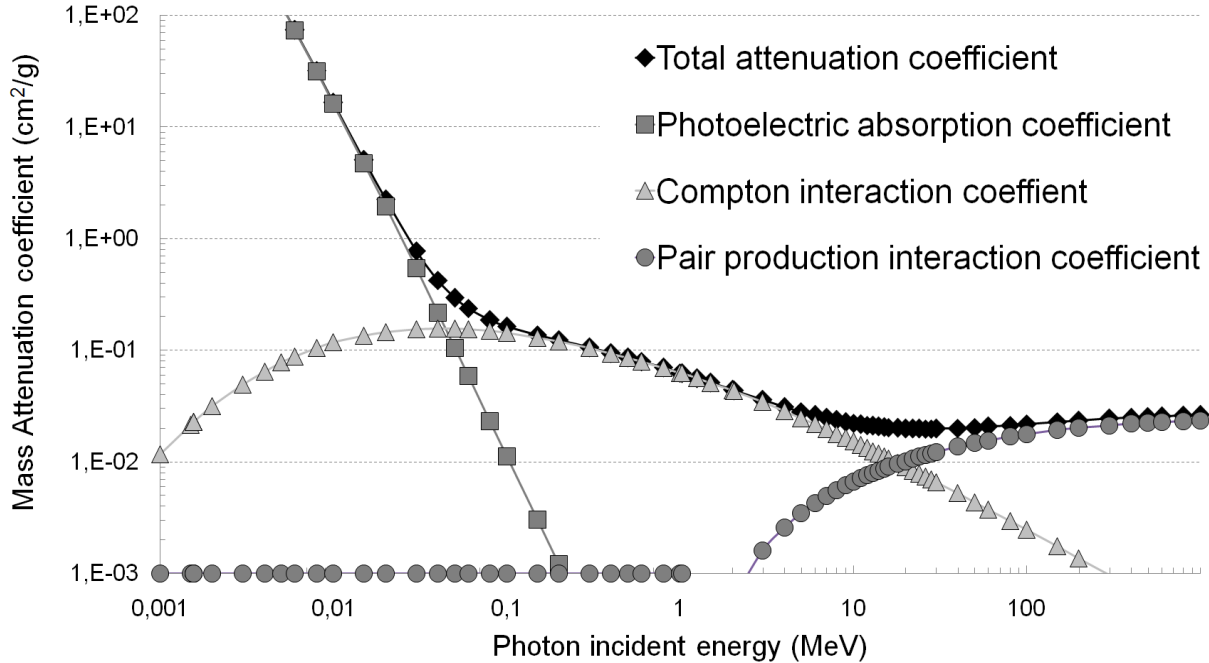


Figure 4.17: Mass attenuation coefficient in Al_2O_3 as a function of photon energy calculated from the NIST-XCOM reference data.

In summary, we can state that electrons are less ionizing than charged hadrons and muons mainly due to their lower mass, but other effect can be also considered but not discussed in detail in this thesis as it was not the principal aim of the work. For instance, it is known, that muons are more penetrating than electrons because in the case of muon interactions the probability of having Bremsstrahlung radiation is rather low, due to their greater mass.

4.5.3 Results for photon simulations

The total mass attenuation coefficient in Alumina for photons of up to 10 MeV is shown in Figure 4.17 (NIST-XCOM [Ber99]). It is composed of contributions arising from the photoelectric effect, the Compton effect and pair production which are also indicated¹³.

At low photon energies up to about 40 keV the interaction with matter is dominated by the photo-electric effect. The photons lose their entire energy in one interaction with a bound atomic electron and cease to exist. A part of the energy is used to overcome the electron binding energy and the rest is transmitted to the free electron.

¹³ Definitions of the different effects are given in chapter 3, concerning the interactions of particles with matter.

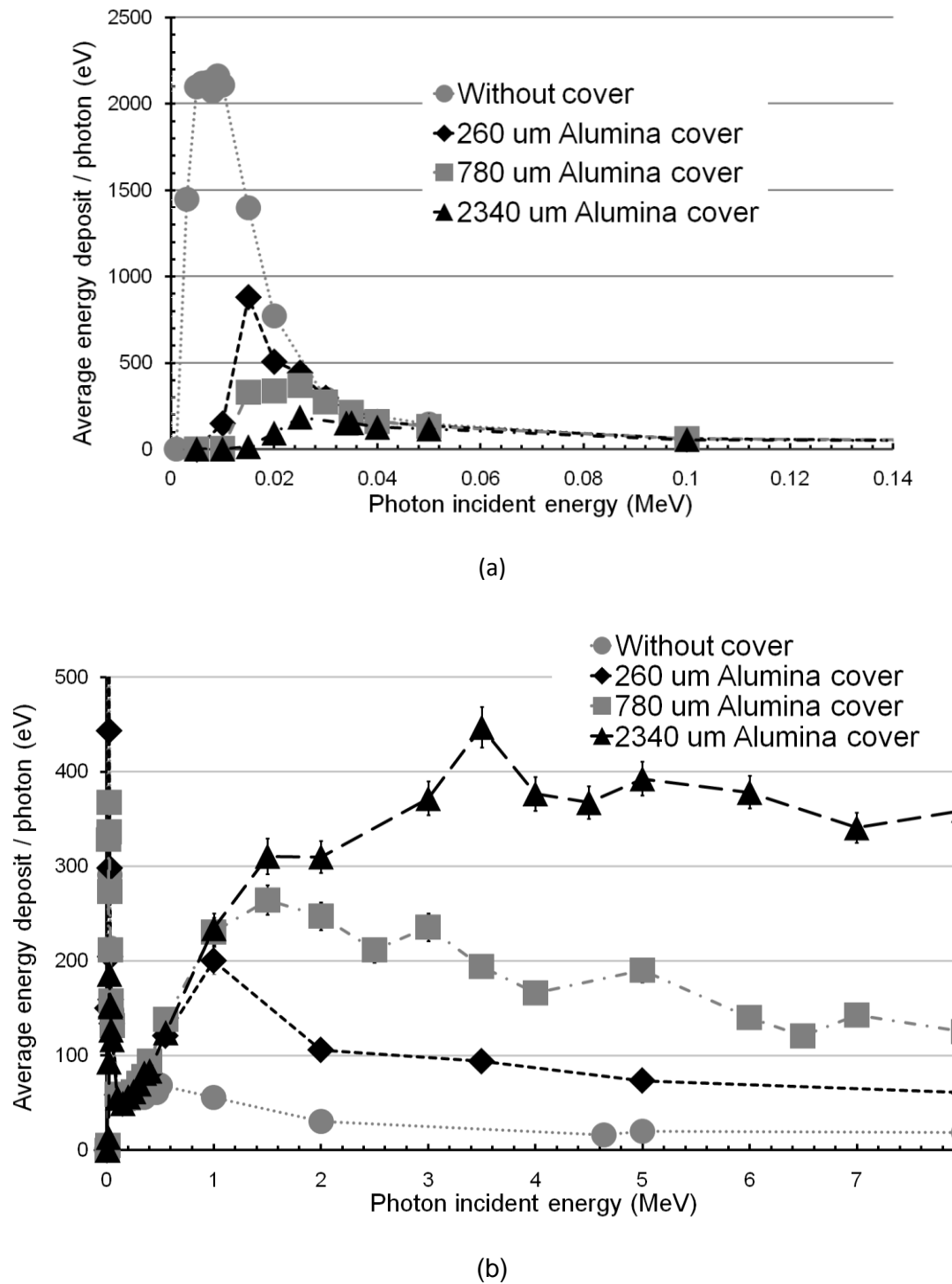


Figure 4.18: Simulation results for average energy deposit per event in the sensitive volume using three different Alumina thicknesses. (a) Zoom to the average energy deposit at low energy photons. (b) Over a photon energy range up to 8 MeV

The average energy deposit in the RadFETs for photons of up to 150 keV is shown in Figure 4.18 (a). Due to the strong photo-electric effect the photons are quickly absorbed even in thin layers of Alumina resulting in a strong difference in the deposited dose between Alumina covered and non covered RadFETs for photons of up to 40 keV.

A peak in the average energy deposit is observed since at low energies up to about 20 keV the photons are almost completely absorbed in the cover and the RadFET, while above about 20 to 40 keV the photons start to traverse the cover and the RadFET.

As can be seen from Figure 4.17, at photon energies higher than 40 keV the Compton effects start to dominate.

The second peak in the average energy deposit of the RadFETs shown in Figure 4.18 (b) is arising from Compton electrons created outside the sensitive volume which means in our case outside the RadFET sensors. The peak itself reflects the rising and falling of the Compton effect mass attenuation coefficient shown in Figure 4.17 as well as the decrease of energy deposition for electrons with rising energy (see e.g. Figure 4.14).

When the incident photon energies increases, the secondary Compton electrons created in the cover become more energetic and crosses totally the RadFET sensors without being absorbed. As it is shown in the figure concerning primary incident electrons, the energy deposited in the RadFET sensors decreases with increasing electron energies.

With increasing thickness of the cover more secondaries are created. Therefore, more energy is deposited in RadFETs with thicker covers. This can be interpreted as an increasing “dose enhancement” with increasing cover thickness.

For the energy range of the simulations presented in this section, up to 8 MeV, the contribution of the pair production effect is negligible (e.g. see Figure 4.17) compared to the two other effects discussed above. Nevertheless at higher energies this effect becomes predominant. For this reason, a more detailed discussion on the contribution of secondary particles created in the cover to the average energy deposition as well as some quantitative investigations on the role of pair-production at very high photon energies is given in section 4.6.2.

As it is shown in Figure 4.18, the dose enhancement is more important for sensors covered by thick ceramic lids due to the more significant number of secondary particles generated within the thicker package.

Photon energy (keV)	Mass attenuation coefficient (cm ² /g)	Difference of absorbed energy (%) (260μm/780μm)	Difference I/I ₀ (%) (260μm/780μm)	Difference of absorbed energy (%) (260μm/2340μm)	Difference I/I ₀ (%) (260μm/2340μm)
10	1.67E+01	96.7	96.8	100	100
15	5.07E+00	62.7	64.9	98.5	98.5
20	2.23E+00	33.7	36.9	81.6	84.1

Table 4.2: Comparison between differences of energy deposited in the RadFET for different Alumina thicknesses calculated from simulation results and gamma rays transmission at energy lower than 20 keV. At such energies the transport of photons inside Al₂O₃ is governed by the photo-electric absorption.

Furthermore, when gamma rays of intensity I₀ travels though a shielding materials of thickness (L), they are submitted to an attenuation so that the intensity transmitted (I) by the absorber is given by the following formula:

$$I = I_0 e^{(-\mu \rho L)} \quad (4.9)$$

Where I: Intensity transmitted by the absorber

I₀: Initial intensity of gamma radiation

μ: Total attenuation coefficient of the absorber

P: Mass density of the absorber

L: Thickness of the absorber

The ratio I/I₀ is called the gamma ray transmission.

Since at low energies, the energy deposited in the target volume is mainly due to primary particles and not to secondary Compton electrons, once the total attenuation coefficient extracted from the NIST-XCOM reference data, it was possible to compare gamma ray transmission calculations and Geant4 simulations. Results are summarized in Table 4.2.

The difference (%) indicates the difference in percent between the energy deposited in the sensor covered by 260 μm Alumina lid and other lid configurations used for the simulation results, while the I/I₀(%) represents the difference of gamma ray transmission between two different packaging configurations.

$$Difference \left(\frac{I}{I_0} \right) (\%) = \frac{\left(\frac{I}{I_0} \right)_{260\mu m} - \left(\frac{I}{I_0} \right)_{780\mu m \text{ or } 2340\mu m}}{\left(\frac{I}{I_0} \right)_{260\mu m}} \times 100 \quad (4.10)$$

For instance, for 15 keV proton energies, the difference between the energy deposit on sensors covered by Alumina lid of 260 µm and by a lid of 780 µm or 2340 µm is of 62.7% and 98.5% respectively. Calculating the gamma ray transmission for the three cover configurations presented in Table 4.2, the difference between 260 µm Alumina cover and the two other configurations was calculated and represented by the difference $I/I_0(\%)$ in this table.

Results show a good correlation between the difference on gamma rays transmission and the difference of the energy deposited on RadFETs resulting from Geant4 simulations. It can be interpreted as the energy deposit in the sensors is obviously correlated to the number of photons passing through the Alumina cover (e.g. the gamma-ray transmission coefficient). Since it is reduced when the cover thickness is increased (caused by the absorption of incident photons due to the photo-electric effect) the energy deposited on the sensor is also reduced. This proves that the energy deposited by low energy photon when photo-electric effect dominates, is directly linked to the transmission coefficient of photon passing through the cover.

4.5.4 Results for neutrons simulations

A preliminary evaluation has been performed concerning incident neutrons. Their effect is illustrated in Figure 4.19, which compares the average energy deposit with a 260 µm Alumina lid and without any cover as a function of neutron energy corresponding to a realistic radiation spectrum in the LHC environment, as for the charged hadrons and leptons, a dose enhancement is observed at higher energies.

A more detailed appraisal of the effect of neutrons would require dedicated simulations with the specialized “High Precision” models for neutron interactions available in the Geant4 Toolkit; it should be noted, however, that, according to the preliminary results, in the realistic operation environment described in section 4.6.2, neutrons contribute by approximately 10% at maximum to the energy deposit in the sensitive part of the RadFETs, while they represent a major component in the radiation spectrum. For this reason and also because the main aim of this work was not to compare the different physic models included in the Geant4 toolkit, the investigation of the specialized “High Precision” models have not been done in this thesis.

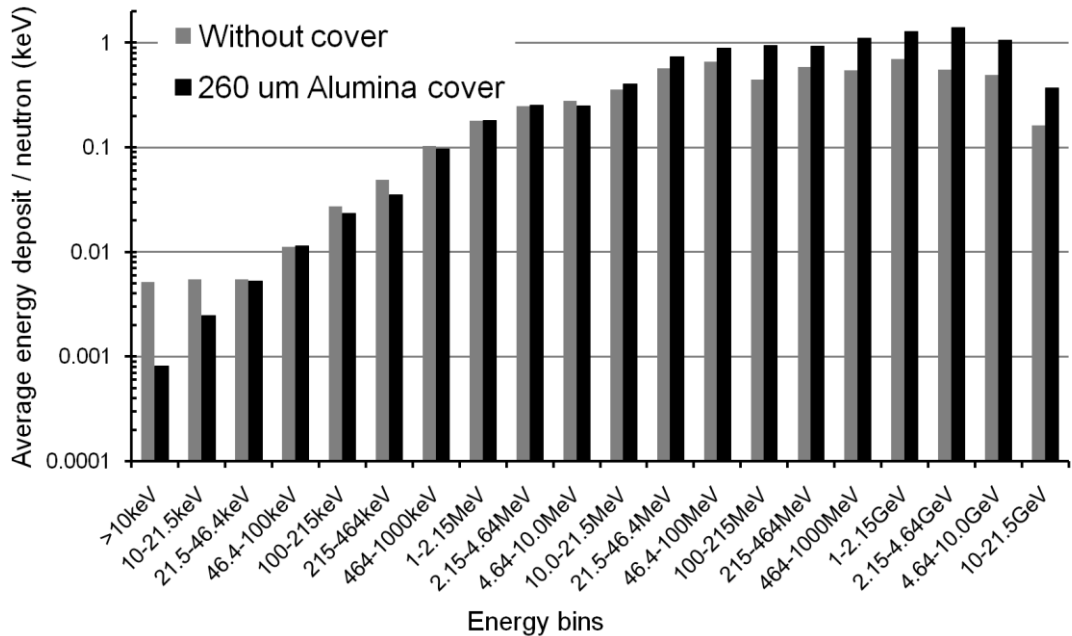


Figure 4.19: Average energy deposited in the four RadFET sensors per incident particle for neutrons. Simulations were performed with or without Alumina cover thickness of 260 μm .

4.6 RadFET sensors in the ATLAS detector

4.6.1 Simulation of dose measurements in the ATLAS Detector

The RadFET sensors described in this work will provide online information about the TID at various locations inside the LHC experiments. One LHC experiment in which the RadFETs are already installed is the ATLAS experiment [Man07]. The radiation fields in two specific locations of ATLAS are therefore taken here as an example to understand the influence of the package on the measured dose in typical LHC experiment spectra.

Figure 4.20 represents the full ATLAS detector of the LHC in which both specific locations are clearly specified. Data taken from these locations are tabulated by zones in unit of centimeters (cm) as the minimum and maximum Z and the minimum and maximum radius, respectively ZLO, ZHI, RLO and RHI.

The first location, labeled "SCTB1" whose zone (0, 75, 30, 30), is situated inside the inner detector (more precisely inside the SCT Tracker, from Figure 4.20) which is very close to the interaction point, where charged hadrons are dominated by charged pions from the proton-

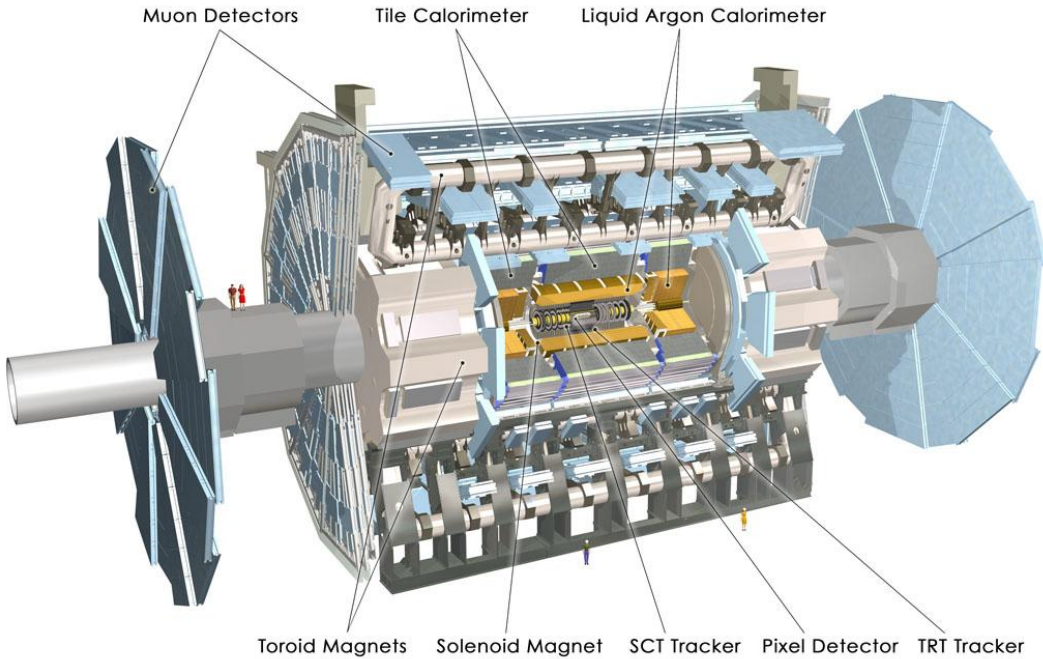


Figure 4.20: Representation of the complete ATLAS detector. The 2 specific locations where the RadFET sensors have been simulated are illustrated here: the “*SCT Tracker*” for the one labeled “*SCTB1*” and the “*Liquid Argon Calorimeter*”.

proton interaction and constitute the most serious ionizing background for the innermost layers of the inner detector [Bar05].

The second one, labeled “*LAR Barrel*” whose zone (300, 350, 290, 340), is located in the liquid argon calorimeter which is situated far away from the interaction point and where the amount of neutrons is more significant than in the inner detector.

The photon and pion spectra for the inner detector as the neutron and proton spectra for the liquid argon calorimeter are illustrated in Figure 4.21 and Figure 4.22 respectively. It clearly shows that for the amount of photons in the case of the “*SCTB1*” location and neutrons for the liquid argon calorimeter are more significant than charged hadrons (pions and protons respectively).

In order to compare their respective amount in both locations, charged hadron spectra for the inner detector and for the liquid argon calorimeter have been plotted in Figure 4.23.

As discussed in section 4.5, charged hadrons are the most ionizing type of particle in the full particle spectrum of the LHC experiments. Thus, the energy deposit in materials and in detectors strongly depends on their amount. The selection of both locations were made

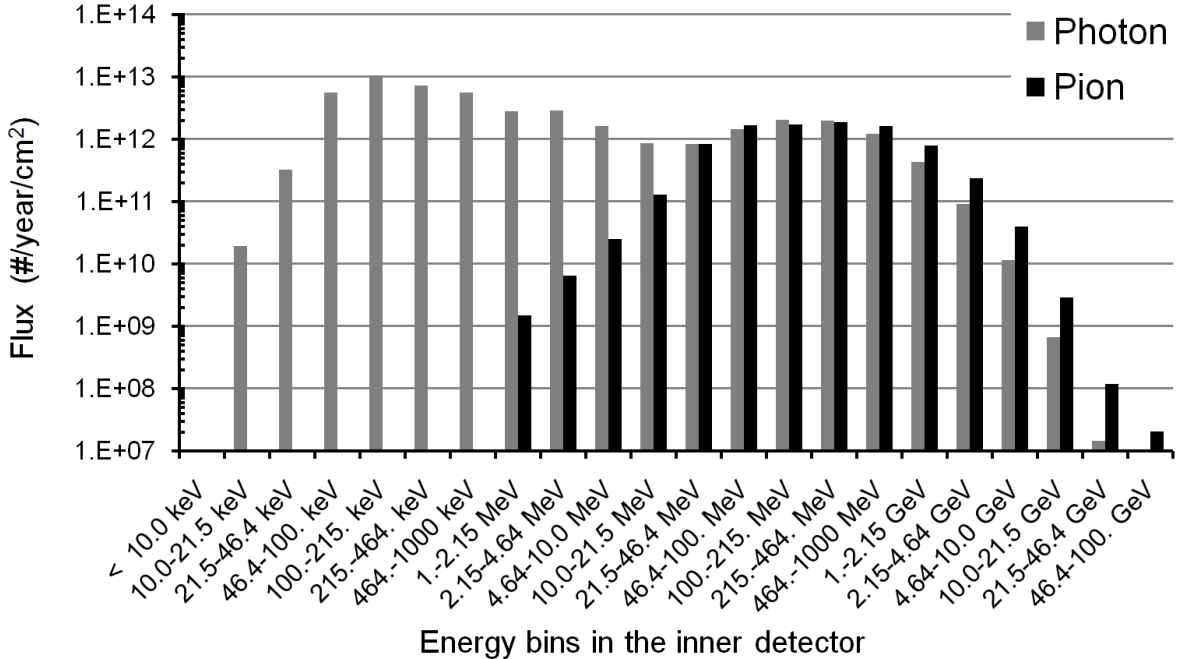


Figure 4.21: Photon and pion spectra for ATLAS inner detector (SCTB1).

according to this parameter, so that in one case the energy deposited is mainly due to the interaction of charged hadrons with the sensors and in the other case the amount of charged hadrons being less important, the contribution of other types of particle such as electrons will no longer be negligible.

The number of charged hadrons arising from the inner detector is about 5×10^3 times higher than in the “LAR Barrel” inducing a major role of this particle type in the inner detector of the ATLAS experiment.

The spectra were provided by the ATLAS radiation task force [Shu03] and give the number of expected particles per year and cm^2 per energy bin assuming “annual predictions” for 10^7 seconds at high luminosity ($10^{34} \text{ cm}^{-2}\text{s}^{-1}$) ; they derive from Monte Carlo simulations based on FLUKA [Fer05], [Fas03] and GCalor [Zei94].

Statistical uncertainties for the total flux values of each particle type are less than 3% for the “SCTB1” location while they are lower than 7% for the “LAR Barrel” position.

To estimate the contribution of each particle type to the total energy deposited in the RadFETs as well as the corresponding packaging effects a Geant4 simulation for each particle type (protons, photons, electrons, pions, neutrons, muons) and energy bin has been performed.

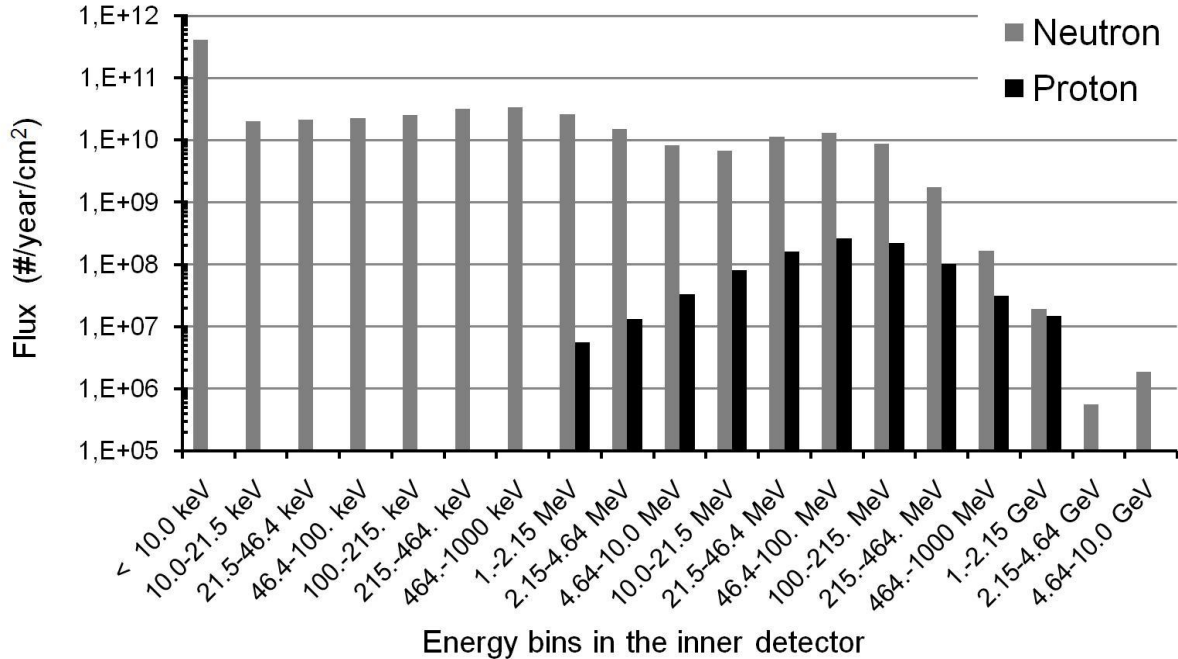


Figure 4.22: Neutron and proton spectra for the Liquid Argon Calorimeter of the ATLAS experiment (LAR Barrel).

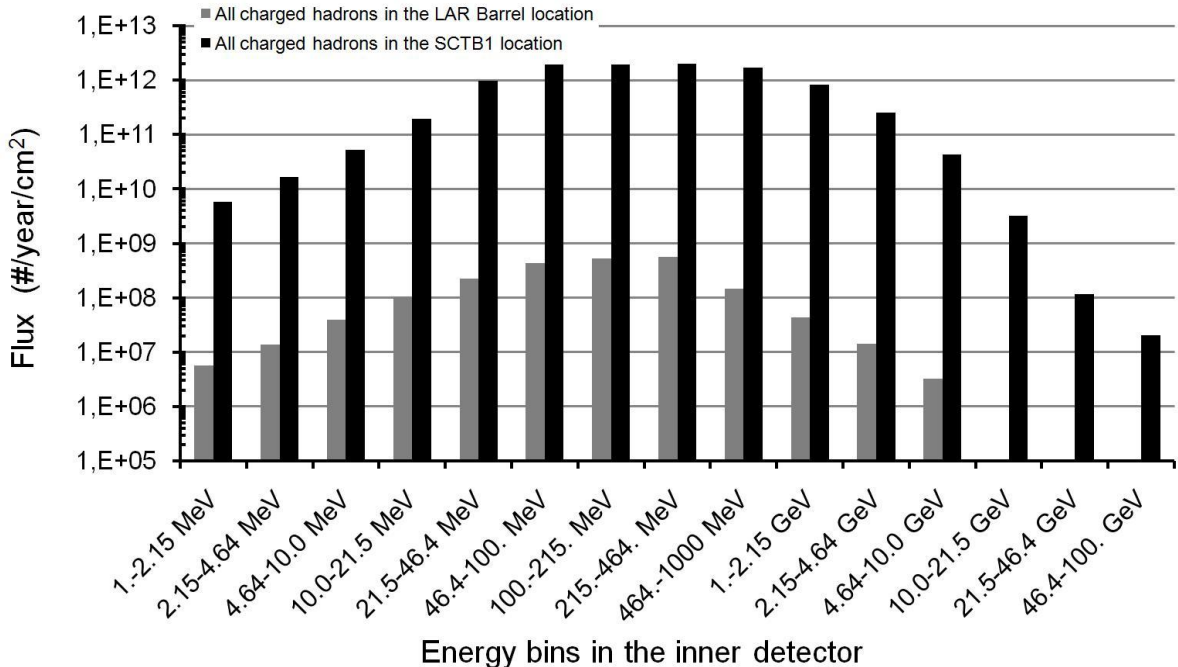


Figure 4.23.: Comparison between the amount of charged hadrons present in the inner detector, and the one in the liquid argon calorimeter.

	% of the total number of particles	Annual dose without cover in units of kGy/year (contribution %)	Annual dose with cover in units of kGy/year (contribution %)	Dose enhancement (%)
Protons	1.2	1.68×10^0 (25)	1.53×10^0 (21.5)	-8.9
Photons	54.9	6.37×10^{-2} (0.9)	1.07×10^{-1} (1.5)	68.8
Electrons	5.9	1.18×10^0 (17.6)	1.35×10^0 (19)	15
Pions	10.8	2.98×10^0 (44.6)	3.29×10^0 (46.4)	10.3
Neutrons	25.2	4.67×10^{-2} (0.7)	5.74×10^{-2} (0.8)	23
Muons	1.9	7.46×10^{-1} (11.1)	7.51×10^{-1} (10.6)	0.8
Total	100	6.7	7.1	5.9

Table 4.3 Summary of simulations made for the inner detector (SCTB1 position).

The same geometry and Geant4 model as presented in the previous sections has been used for these simulations meaning that the four full RadFET sensors have been considered as sensitive volume. The calculations were performed with an Alumina lid of 260 μm thickness, which has tentatively been defined as the cover to be used in the LHC experiments.

The results for the “SCTB1” as for the “LAR Barrel” positions are given in Table 4.3 and Table 4.4 respectively.

The first column indicates for each particle type its fraction in the full ATLAS spectrum.

In the second and third column the total annual dose in kGy/year and Gy/year for the inner detector and for the LAR barrel locations respectively, as well as the percent contribution to the overall annual deposited dose in the RadFETs is given for each particle type using RadFETs with and without cover, respectively.

	% of the total number of particles	Annual dose without cover in units of Gy/year (contribution %)	Annual dose with cover in units of Gy/year (contribution %)	Dose enhancement (%)
Protons	0.08	1.86×10^0 (32.6)	1.67×10^0 (24.9)	-10.3
Photons	42.3	6.69×10^{-1} (11.7)	1.09×10^0 (16.3)	63.7
Electrons	0.6	1.66×10^0 (29.2)	2.19×10^0 (32.7)	31.8
Pions	0.1	3.83×10^{-2} (6.7)	4.28×10^{-2} (6.4)	11.8
Neutrons	57	1×10^0 (17.5)	1.19×10^0 (17.8)	19.1
Muons	0.03	1.25×10^{-1} (2.2)	1.27×10^{-1} (1.9)	1.9
Total	100	5.7	6.7	17.6

 Table 4.4 Summary of simulations made for the liquid argon calorimeter (*LAR Barrel* position).

In the last column the dose enhancement in percent which represents the ratio of the expected measured dose with and without cover is given for each particle type.

For the “SCTB1” position, although neutrons represent a quarter of all particles, their total energy deposited is less than 1% of the overall deposited energy. This is understandable as they are non-charged hadrons and thus their interaction probability with the sensor material is low.

Photons represent about half of all particles but deposit less than 2% of the overall energy. However, a significant dose enhancement is observed when a cover is put on the RadFET, as expected from the results discussed in section 4.5.3. Placing the cover enhances the dose deposited by photons in the RadFET by about 70%.

The main contribution to the deposited energy in the inner detector is delivered by the pions (about 45%), while they represent only about 10% of all particles present in the full ATLAS spectrum. As discussed in the previous section, this is due to the important ionizing energy loss (IEL) of charged hadrons.

The total dose enhancement expected in the “SCTB1” spectrum by placing a cover on the RadFET is (5.9 ± 0.9) %. The annual TID expected to be measured is (6.7 ± 0.04) kGy/year without cover and (7.1 ± 0.04) kGy/year with cover, indicating that only a small and most probably not measurable influence of the RadFET cover is expected in this specific location.

Detailed results for the liquid argon calorimeter are presented in Table 4.4. The spectrum significantly differs from the one in the inner detector. First of all the absolute number of particles per unit area and time is around 70 times less than for the inner detector position. Furthermore, the spectrum is composed almost only of photons and neutrons. The annual TID expected on the 4 RadFETs located in the liquid argon calorimeter is (5.7 ± 0.08) Gy/year without cover and (6.7 ± 0.1) Gy/year with cover. This corresponds to a dose enhancement of (17.6 ± 2.3) % when the cover is placed on the RadFET which can be interpreted as a not negligible increase of measured dose.

4.6.2 Refined simulations assuming a smaller sensitive volume

A more detailed geometrical model of the detector was implemented for these simulations. In the simulations presented in the previous chapters the total volume of the RadFET dies was taken as sensitive volume. This allowed for the relative comparison of the measured energy deposition using different packaging solutions.

However, only the charge deposited in the oxide layer of the FET on the RadFET die actually contributes to the RadFET signal; this very thin oxide layer is located close to the surface of the RadFET die. For the simulations presented in this section therefore a new RadFET geometry composed of 3 different layers was used: a 1600 nm SiO₂ layer, representing the sensitive volume, sandwiched between a 0.5 μm Chrome layer on the top and a 400 μm Silicon layer below. This detailed geometrical model allows one to understand possible thickness effects of the sensitive volume on the dose measurement, and to improve the precision of the absolute dose values predicted by the simulations.

The energy deposit scored in the detailed geometrical model is largely equivalent to the one where the full RadFETs die represents the sensitive volume, with the exception of the low energy range, in which the particles are either completely stopped or are still close to the energy region of the Bragg peak. If, for example, the pion energy is completely deposited in the first

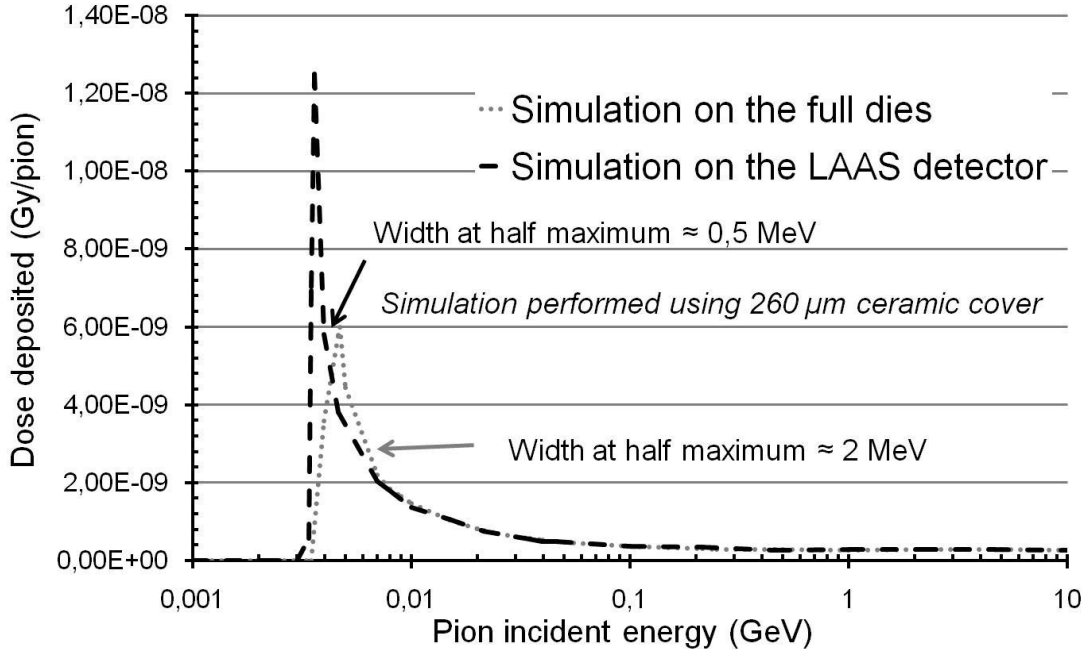


Figure 4.24: Geant4 simulations of the average deposited dose per pion. The results in both detector geometries used in this work are compared.

1600nm (in the oxide layer), the difference in the deposited dose is only a normalization effect arising from the different sizes of the sensitive volumes.

For higher energies, when the dE/dx can be regarded as constant over the full thickness of the sensitive volume, no difference is observed any more. An example is illustrated in Figure 4.24, which gives a comparison between the average deposited dose in unit of Gy/pion for the two geometries. In both cases the RadFET is assumed to be covered with a lid (260 μ m ceramic).

The different behavior of the two geometries would become relevant only in the case when a significant part of the pion spectrum in the operation environment would fall into the low energy range below 10 MeV identified in Figure 4.24; this is not the case expected in the LHC radiation field. No significant difference appears to be associated to the different materials (epoxy-glass and silicon oxide) considered in the two simulation models; the only visible difference at low energy is due to the different thicknesses in the two geometries.

Therefore the results discussed in the previous section, deriving from a simplified geometrical model, hold their validity also when a more detailed geometry is applied.

Simulations with the thin oxide layer as sensitive volume were performed with all particles in the same way as described in the previous section.

	% of the total number of particles	Annual dose without cover in units of kGy/year (contribution %)	Annual dose with cover in units of kGy/year (contribution %)	Dose enhancement (%)
Protons	1.2	1.73 (26.7)	1.65 (22.8)	-4.3
Photons	54.9	2.46×10^{-2} (0.4)	8.29×10^{-2} (1.1)	237.1
Electrons	5.9	1.13 (17.4)	1.34 (18.5)	19.4
Pions	10.8	2.89 (44.7)	3.39 (46.7)	17.2
Neutrons	25.2	3.17×10^{-2} (0.5)	3.72×10^{-2} (0.5)	17.2
Muons	1.9	6.66×10^{-1} (10.3)	7.42×10^{-1} (10.2)	11.5
Total	100	6.47	7.25	12.1

Table 4.5: Summary of simulations made for the inner detector.

The details of the simulations with the refined RadFET geometry are shown in Table 4.5 and Table 4.6 for the two different locations used in this work.

The total dose enhancement expected in the “SCTB1” spectrum by placing a cover on the RadFET is (12.1 ± 1) %. The annual TID expected to be measured is (6.47 ± 0.04) kGy/year without cover and (7.25 ± 0.05) kGy/year with cover.

For the liquid argon calorimeter, the annual TID expected is around (4.95 ± 0.08) Gy/year without cover and (6.12 ± 0.09) Gy/year with cover: this corresponds to a dose enhancement of (23.6 ± 2.4) %. As for the simulations made on a simpler geometry which are discussed in the previous section, at the liquid argon calorimeter, the increase of the deposited dose on covered RadFETs is not negligible, as it reaches more than 20 %.

	% of the total number of particles	Annual dose without cover in units of Gy/year (contribution %)	Annual dose with cover in units of Gy/year (contribution %)	Dose enhancement (%)
Protons	0.08	1.96 (39.5)	1.81 (29.6)	-7.4
Photons	42.3	2.47×10^{-1} (5)	8.62×10^{-1} (14)	248.9
Electrons	0.6	1.65 (33.3)	2.16 (35.3)	30.9
Pions	0.1	3.73×10^{-1} (7.5)	4.47×10^{-1} (7.3)	19.9
Neutrons	57	6.1×10^{-1} (12.3)	7.1×10^{-1} (11.6)	16.3
Muons	0.03	1.14×10^{-1} (2.3)	1.27×10^{-1} (2.1)	11.5
Total	100	4.95	6.12	23.6

Table 4.6: Summary of simulations made for the liquid argon calorimeter.

Looking at the data presented in Table 4.5 and Table 4.6 a very significant dose enhancement of about 200 % is observed for photons which deserves some discussions here, although their contribution to the total deposited energy is small .

The average deposited energy for photons in RadFETs with and without cover is shown in Figure 4.25. The dose enhancement observed with cover is typically due to secondary electrons and positrons generated by the Compton and pair production effect in the cover. For energies up to 1 MeV the enhancement is only due to Compton electrons while for energies above about 5 MeV, also secondary electrons and positrons created by the pair effect contribute to the average energy deposit.

Two data points at 22 and 464 MeV show a strong deviation from the data points surrounding them. In addition to the secondary electrons and positrons generated by the

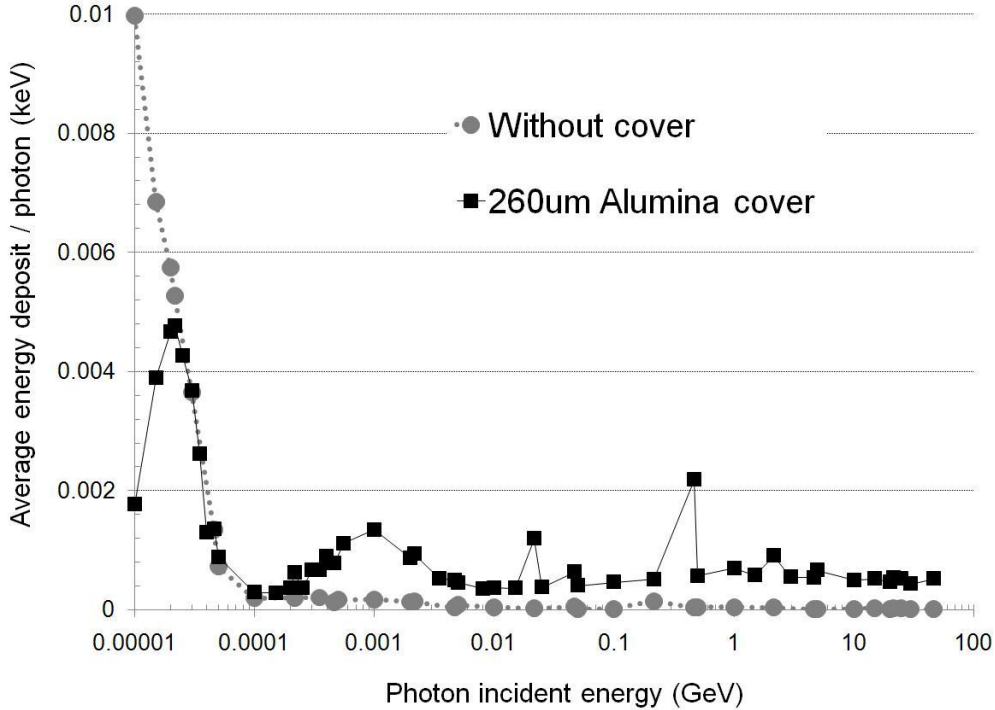


Figure 4.25: Geant4 simulations for photons of up to 50 GeV incident energy.

interaction of the photons with matter, the reason for this deviation at 22 MeV is found in the photonuclear production of protons from Al for which the cross section is peaking at an energy of around 24MeV [Ler04]. The statistical significance here is however very low as only 5 events where observed in the overall run of 10^6 events.

The fluctuation at 464 MeV is due to the production of alpha particles in one photonuclear absorption process, together with the production of secondary protons. This information is given directly by the Geant4 software, indicating which type of secondary particles are produced; deriving from which kind of physic processes implemented in the Geant4 application as discussed in section 4.4.2.

In summary, for energies above about 5 MeV, also secondary electrons and positrons created by the pair effect contribute to the energy deposit. Finally, for even higher energies photonuclear absorption processes occur [Ler04]. Although their total cross sections are small, they could contribute to the dose enhancement in the high energy range, as the resulting protons or alpha particles deposit a significant amount of energy in the sensitive RadFET layer.

The physics configuration in the simulation application accounts for this kind of processes through the models mentioned in section 4.4.2. Geant4 includes physics models [Kos02], [Deg00] specifically meant to handle photonuclear processes in detail; however, such a study

goes beyond the scope of this thesis and would be addressed in a dedicated project. In the present study the production of α particles contributing significantly to the dose released in the RadFETs appears with a frequency of the order of one event per million primary photons. In general the dose enhancement is more important for sensors covered by thick Alumina lids due to the more significant number of secondary particles generated within the thicker package.

Finally, it should be mentioned that the TID values obtained here without cover are consistent with the values evaluated by the ATLAS Radiation Background Task Force [Shu03], that states an annual dose of 7.5 kGy/year and 4.8 Gy/year for the TID respectively deposited in Silicon devices for the “SCTB1” and liquid Argon calorimeter position. The compatibility of the two sets of results is remarkable, considering the different simulation tools and configurations in the two studies.

4.7 Conclusion

A Geant4 application to simulate the impact of packaging on the dose measurements of RadFET dosimeters to be used in the LHC Experiments at CERN has been developed. The application was used to understand the dose enhancement produced by the package inside the complex radiation fields of the LHC experiments. The dose enhancement for electrons, muons, photons, neutrons, pions, protons in dependence of the particle energy was simulated.

Based on a detailed study on the validity of the physics models used for simulation, it was verified that the Geant4 application made specifically for this study is an adequate and reliable tool to investigate the packaging impact in the complex LHC radiation fields.

For two specific locations inside the ATLAS Experiment the TID was calculated for two different packaging options. It was demonstrated that the effect of placing or not placing a 260 μ m thick Alumina cover over the RadFETs can alter the predicted measured dose up to 25% in some locations of the LHC Experiments.

This relative dose enhancement between covered and uncovered RadFETs is certainly smaller than the absolute accuracy of RadFET dose measurements in LHC experiments. It is not due to the precision of RadFETs dosimeters which performed accurate measurements, but rather caused by the complex radiation field of the LHC Experiments. However, it represents a significant shift in the measured value as covered and uncovered RadFETs could indicate dose values that differ by 25%. The choice of RadFET packages is thus an important issue for measuring the TID in High Energy Physics Experiments.

Chapter 5

Forward biased PIN diodes used as dosimeters

As shown in the previous chapter, a complete system for monitoring the LHC radiation environment has to include RadFET sensors for total ionizing dose (TID) measurements. In addition, informations about the cumulative displacement damage are required for monitoring the 1-MeV equivalent neutron fluences. In our case this is performed by measuring the radiation response of forward biased silicon PIN diodes.

Silicon p-i-n diodes are important devices for radiation monitoring in high energy physics experiments in very harsh radiation conditions, such as the Large Hadron Collider (LHC) experiments at CERN [CER04]. This type of devices have been characterized and developed in previous works [Pro89], [Sop91], [Ros03]; mainly for medical and military topics in order to use them as dosimeters.

As presented in Chapter 2 the equivalent fluence Φ_{eq} which the detectors are exposed to, covers a wide range of more than five orders of magnitude from 10^8 - 10^{10} to 10^{14} - 10^{15} n_{eq}/cm^2 , depending on the location in the LHC experiments.

For the future upgrade of the LHC experiment (the Super-LHC [Rug02], [Gia05]), the radiation level will be multiplied by a factor 10 due to the increase of the luminosity from 10^{34} to $10^{35} cm^{-2}s^{-1}$. For the innermost detectors, the radiation sensors will be exposed to fluences up to $10^{16} cm^{-2}$ 1-MeV equivalent neutrons.

For the purpose of this study, the investigated device is the commercial OSRAM BPW34FS silicon p-i-n diode [Bpw]. This type of diode was already characterized at CERN in

earlier studies [Mal92], [Rav04], [Rav06], [Rav08b], in order to use them as radiation monitoring sensors for the LHC experiments and are summarized in section 5.2.

For monitoring such high fluences, p-i-n diodes are used in forward bias mode by applying a constant readout current of short duration pulse to avoid self-heating effects. Using this method, sensitivity to fast hadrons has been observed up to high fluences by measuring the variation of the forward voltage versus equivalent fluences.

These previous works showed that the commercial p-i-n diode powered at 1 mA in forward bias operation with a pulse duration of 700 ms was a valuable choice for the LHC experiments. It revealed a hadron sensitivity range between $2 \times 10^{12} \text{ n}_{\text{eq}}/\text{cm}^2$ and $4 \times 10^{14} \text{ n}_{\text{eq}}/\text{cm}^2$. Since the upper-limit of the LHC fluence range is within 10^{14} - $10^{15} \text{ n}_{\text{eq}}/\text{cm}^2$ and that only innermost detectors could be exposed to Φ_{eq} up to $10^{15} \text{ n}_{\text{eq}}/\text{cm}^2$, as our dosimeter is not supposed to be located very close to the interaction point, where the equivalent fluence is at maximum, its sensitivity range is sufficient for monitoring the radiation levels as expected for the location where it should be used. These results will be detailed in section 5.2.2, concerning the previous study carried out at CERN by Ravotti [Rav06], with the aim to develop the readout protocol which is employed nowadays in the collider.

However, for monitoring even higher radiation levels as expected for the next generation of high energy physics experiments, where the particle fluence will reach up to $10^{16} \text{ n}_{\text{eq}}/\text{cm}^2$, a solution for expanding the fluence measurement to very high fluences has to be found.

In this chapter, a detailed investigation into the response of BPW34FS silicon p-i-n diode exposed to very high energy proton fluences is presented.

In section 5.4, preliminary studies on the radiation response when diodes are operated at forward readout current from 10 μA to 25 mA with 50 ms pulse duration are presented.

In addition, based on the relaxation material theory (described in section 5.5.3.1), a new approach to parameterize the diode forward voltage response as function of particle fluence and injection current is proposed. It allows for the extension of the measurement range of the diodes up to about $6.3 \times 10^{15} \text{ n}_{\text{eq}}/\text{cm}^2$ and offers the possibility to predict the forward voltage response for any injection current $I_F \leq 1 \text{ mA}$.

The latter feature allows optimizing the injection current for the fluence range of interest.

Finally, the temperature dependence of irradiated diode has been qualitatively evaluated in section 5.5.4, with the intention to give some suggestions about the optimal temperature in which the diode should be used for monitoring radiation as expected for the future Super-LHC. However, the temperature is imposed by the experiments since detectors have to be measured at a certain temperature which is not defined yet for the Super-LHC. Therefore, one just gives

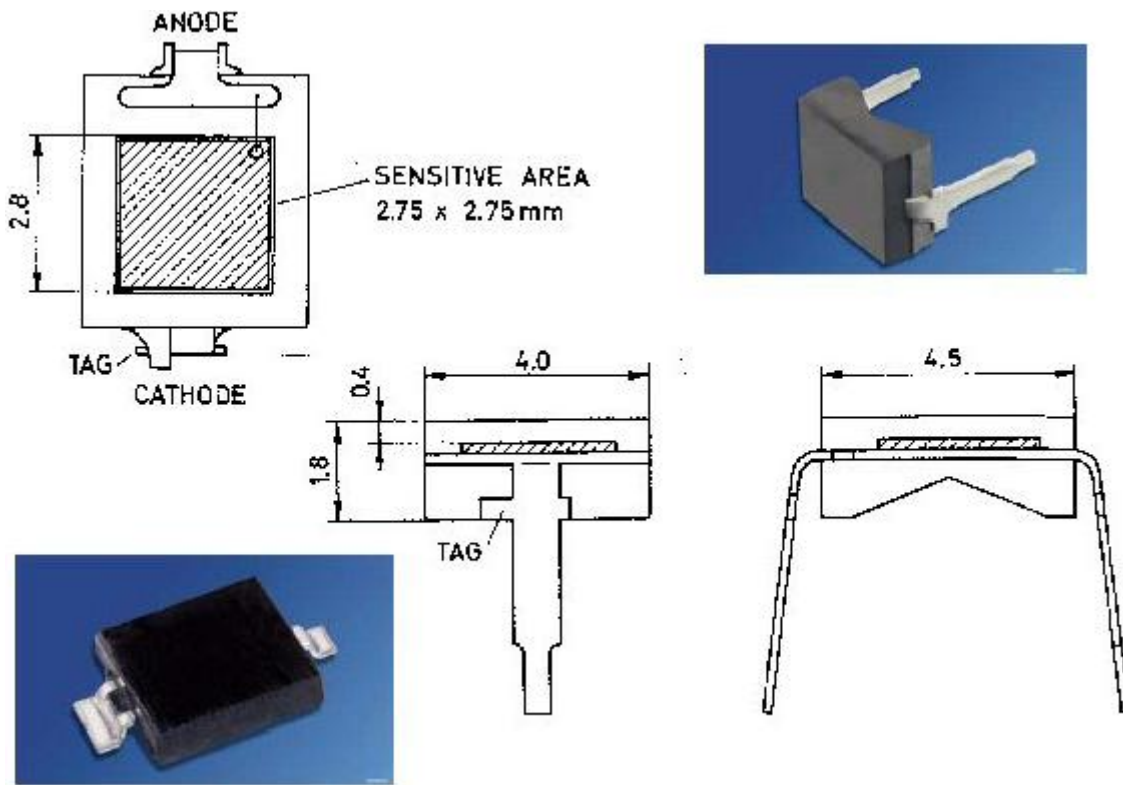


Figure 5.1 The commercial OSRAM BPW34FS silicon PIN diode, supplied in DIL (top right-hand corner) and SMD packages (bottom left-hand corner).

some suggestions concerning the optimized temperature that should be used for reading our dosimeter.

In the following section, a detailed description of the device used is given.

5.1 The commercial OSRAM BPW34FS silicon PIN diode

The BPW34FS silicon PIN diodes are produced by several semiconductor companies like for instance OSRAM, SIEMENS, TELEFUNKEN, etc. Their applications are mainly in the domain of photo-interrupters and IR remote controls. A list of typical electrical and optical characteristics for this device can be found in [Bpw]. According to the electronic nomenclature, the part number "BPW34" means the following: B is the material used for the active region of the diode (B = silicon), P indicates the circuit function (P = radiation sensitive diode) and W34 is the serial number [Tel97].

The fact that this kind of commercial Silicon PIN diodes is very unexpensive, between 1 and 2 € per piece, makes their use attractive in the large amount as radiation dosimeter for the LHC experiment.

As illustrated in Figure 5.1, the device can be provided with three different packaging configurations:

- BPW34: Transparent plastic DIL packaging that allows the device to be sensitive to light from 400 nm to 1100 nm.
- BPW34F: Plastic packaging DIL with a daylight filter that limits the light sensitivity of the device to about 950 nm to 1100 nm (see right-hand side of Figure 5.1).

While for their characterization in the previous study [Rav06] (which is summarized in the next section), the diodes were packaged with the configuration of type BPW34F, another packaging configuration was employed for the study presented here. This configuration is the BPW34FS which is identical to the BPW34F, but the diode is encapsulated in a SMD plastic packaging (see left-hand side of Figure 5.1) which is more compact and adequate for higher integrated PCB board. The diode has a $2.65 \times 2.65 \text{ mm}^2$ sensitive area.

5.2 Summary of previous experimental studies

5.2.1 First study aiming at using BPW34F as neutron sensor

The first study of the BPW34F PIN diode as radiation dosimeters was addressed at CERN in 1992. The main results from irradiation tests performed in the neutron field of the PSAIF facility [Tav91] at CERN were summarized in a CERN report [Mal92] and in a thesis [Rav06] following the few points presented below:

- The devices are reported to have a base thickness (W), which is the intrinsic part of the diode, of 210 μm , and a resistivity of $2.5 \text{ k}\Omega\cdot\text{cm}$.
- The diode were measured in condition of intermediate forward current injection ($I_F = 1\text{mA}$) after radiation exposure.
- The BPW34F neutron response was sometimes far from linear, the sensitivity to neutrons with energy higher than 140 keV were of about $35\text{-}50 \text{ mV}/10^{12} \text{ cm}^2$. The lower particle

fluence measured in this study was around 10^{12} cm^{-2} . No clear information about fluence measurement lower than 10^{12} cm^{-2} was given in this report.

- γ -ray irradiations were carried out on these devices, and their sensitivity was found very low compare to the neutron response. When the diode was irradiated with an ionizing dose of 100 kGy, the voltage shift measured was of about 100 mV. This value corresponds to a neutron exposition of about $2 \times 10^{12} \text{ cm}^2$.
- The room temperature annealing was evaluated after neutron irradiation exposure of $\Phi_{(>140\text{keV})} = 2.5 \times 10^{13} \text{ cm}^2$. It revealed that the forward voltage V_F decreases of about 0.5 % after 21 days.

5.2.2 Characterization and calibration of the BPW34F PIN diode for the LHC experiment

With the intention of using this device as radiation monitoring sensor for the LHC experiment, from 2002 several irradiations campaigns [Rav06], [Rav08b] were performed to characterize the BPW34 Silicon PIN diode. For this purpose, two different radiation environments were used: the 24GeV/c proton beam from the IRRAD1 facility and the neutron environment of the IRRAD2 facility at CERN [Gla08].

5.2.2.1 Characterization of the BPW34F PIN diode

The characterization of the Silicon PIN diode was carried out by measuring the forward I-V curves of the device after or during the radiation exposure. Measurements were performed using a test-bench based on a stand-alone Keithley 2400 and by placing the PIN diode in a light-tight box since the BPW34F diode is light sensitive. The injected forward current was of 100 ms-wide current pulse and the forward voltage V_F was measured across the device terminal.

Forward I-V characteristics after 24GeV/c proton irradiations for different Φ_{eq} values are shown in Figure 5.2. The proton fluence was converted into 1-MeV neutron equivalent fluence (Φ_{eq}) by the experimental hardness factor (k) of 0.62 [Mol02].

Two different régimes can be observed in this figure, for $\Phi_{\text{eq}} < 1 \times 10^{13} \text{ n}_{\text{eq}}/\text{cm}^2$ the analysis of the forward I-V curves reveals a shift in the positive direction of the characteristics with increasing particle fluence. On the other hand, for $\Phi_{\text{eq}} > 1 \times 10^{13} \text{ n}_{\text{eq}}/\text{cm}^2$, it can be observed that the I-V characteristics starts to bend back to lower V_F when the forward current I_F reaches a value of around 100 mA. From this observation and by comparing these results with the

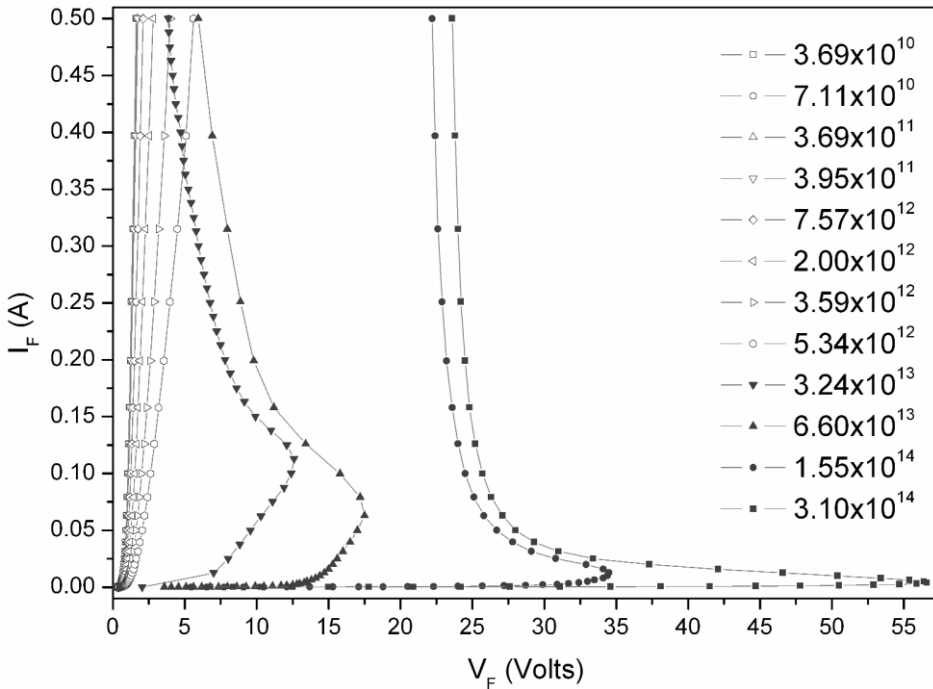


Figure 5.2: Forward I-V curves after 24 GeV/c proton irradiations (linear scale). In the y-axis the current (A) upon 100 ms wide forward voltage bias pulses is plotted. Each curve corresponds to a different Φ_{eq} as indicated in the legend. [Rav06], [Rav08b]

literature, it was assumed that PIN diodes irradiated with high fluences behave like a thyristor [Rav08b], since the forward voltage tends to lower values as the readout current increases. The set of devices irradiated with neutrons in IRRAD2 confirms the results presented in Figure 5.2; the I-V curves show a “thyristor-like” behavior for $\Phi_{eq} > 1 \times 10^{13} n_{eq}/cm^2$. From a practical point of view, thanks to these observations the upper limit for using the BPW34F as hadron dosimeter, before entering in a thyristor régime was defined at 25 mA.

In order to evaluate the BPW34F silicon PIN diode hadron sensitivity, diodes were powered with three different forward readout currents. The selected currents were 1 mA as it was the usual readout current, during the previous study presented in section 5.2.1; 25 mA as this value is the maximum level allowed from the observation of the I-V curves and 10 mA. This value has been intentionally selected in between both previous ones. Following the theoretical indications in [Swa66], the radiation response of forward biased silicon PIN diodes to particle irradiation is expected to be improved at higher injection levels. For this reason, in this previous study, no forward currents lower than 1 mA were selected.

For $\Phi_{\text{eq}} < 1 \times 10^{12} \text{ n}_{\text{eq}}/\text{cm}^2$, the radiation response of the BPW34F does not reveal any hadron sensitivity for and it is not depending on the injected forward current.

On the other hand, for $\Phi_{\text{eq}} > 1 \times 10^{12} \text{ n}_{\text{eq}}/\text{cm}^2$, V_F measured at constant readout current starts to increase with increasing particle fluence. In this régime, the sensitivity to fast hadrons as the upper limit of the linear fluence range depends on the injected I_F . Results show that when I_F is decreased, the diode sensitivity is also decreased while when I_F increases, the fluence range is reduced.

The purpose of this study was to select the optimum forward readout current I_F , to be used for operating the BPW34F silicon PIN diode in the LHC experiment as radiation dosimeter. Finally it appeared that an injected current of 1 mA remained the best compromise between the hadron sensitivity and the measurable fluence range.

Once the readout current was defined, the duration of the current pulse was also to be evaluated. This parameter can lead to diode self-heating, if the current injection duration is too long. The conclusion of this study was that the user should operate the BPW34F PIN diode with a pulse duration shorter than 1 second as it is detailed in [Rav06].

Finally, considering all the restrictions on the readout current and the pulse duration parameters presented and discussed above, the readout protocol defined and used in the LHC experiments was set to 1mA during an injection of 700 ms pulse duration.

Furthermore, from CV-IV measurement the evaluation of the base thickness and the material resistivity has been performed. A base thickness of about 300 μm and a material resistivity of 2.7 $\text{k}\Omega\cdot\text{cm}$ were estimated. Details of these calculations can be found in [Rav06].

5.2.2.2 Calibration of the BPW34F in different hadron fields

With the aim to use the BPW34F silicon PIN diode for measuring the particle fluence in different locations of LHC experiments, the PIN diode calibration was carried out in different particle beams and radiation fields. Figure 5.3 summarizes all the different proton irradiation runs in the IRRAD1 facility and the neutron irradiation made in the IRRAD2 facility at CERN. In the same plot the sensitivity to γ -rays is also plotted, for more detailed on the γ -rays irradiation refer to [Rav06]. In addition, irradiations were performed with 0.8 MeV neutrons [Wij05] and in the neutron spectrum of the TRIGA reactor at JSI [Kra04].

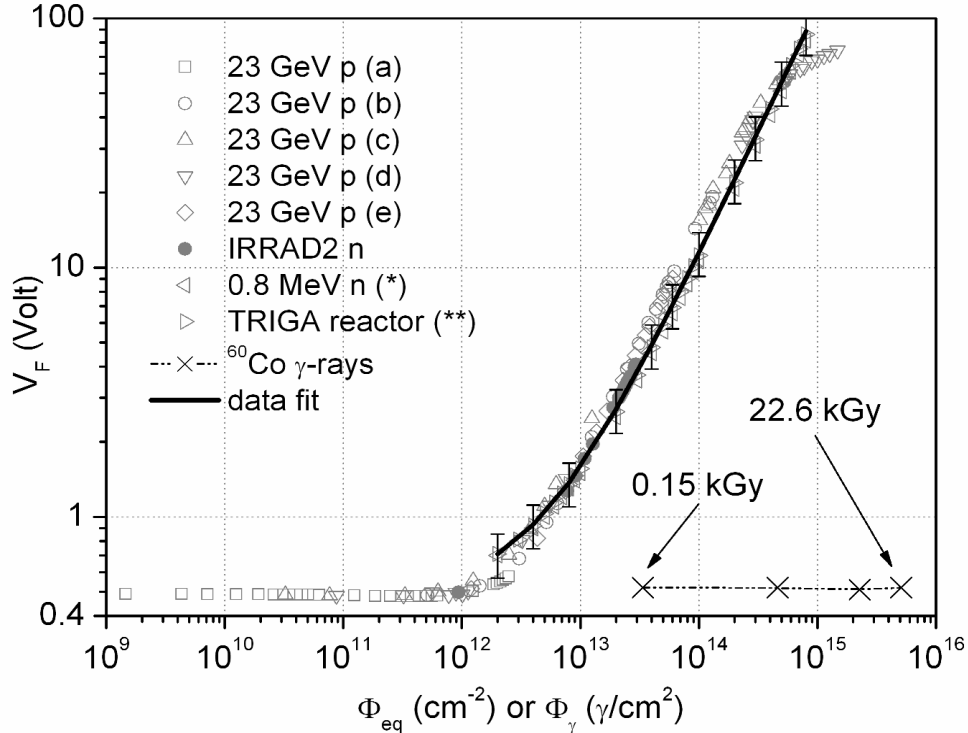


Figure 5.3: Radiation response of BPW34F diodes at room temperature. The diode's forward voltage at 1 mA is plotted versus the Φ_{eq} . The width of the readout current pulse was of 700 ms. The experimental data taken in IRRAD1 at CERN has been recorded at different proton rates: (a) $2.4 \times 10^{11} \text{ cm}^{-2} \cdot \text{h}^{-1}$, (b) $3.7 \times 10^{12} \text{ cm}^{-2} \cdot \text{h}^{-1}$, (c) $8.1 \times 10^{12} \text{ cm}^{-2} \cdot \text{h}^{-1}$, (d) $2.0 \times 10^{13} \text{ cm}^{-2} \cdot \text{h}^{-1}$, (e) $2.5 \times 10^{13} \text{ cm}^{-2} \cdot \text{h}^{-1}$. In the same pictures data from [Wij05], [Kra04] respectively noted with (*) and (**), and following exposure to γ -rays have been also reported. For the photon data, the x-axis corresponds to the number of photons per square centimeters. Error bars of $\pm 20\%$ have been reported to show the accuracy of the data best-fit. [Rav06], [Rav08b].

By fitting experimental data, the calibration factor $1/c$ which represents the growth of the forward voltage (ΔV_F) versus the 1-MeV equivalent fluence was determined as:

$$\Delta V_F = c \times k \times \phi = c \times \phi_{eq} \Leftrightarrow \frac{1}{c} = 9.1 \times 10^9 \text{ cm}^{-2} / \text{mV} \quad (5.1)$$

By injecting a readout current $I_F = 1 \text{ mA}$ during a 700 ms pulse duration, the maximum fluence measurable in the linear part of the calibration curve (before reaching the saturation phenomena observed at high fluence) is around $4 \times 10^{14} \text{ n}_{eq}/\text{cm}^2$.

Long term annealing and temperature dependence have been studied in this previous work, but the evaluation of these parameters will not be described in this thesis. More informations on this topic can be found in [Rav06].

Using the readout protocol presented above, users of the BPW34F silicon PIN diode as radiation monitoring sensor, do not have the choice to operate the diode with another readout current. For this reason, one of the objectives of the study presented in this thesis was to extend the possibilities of operating the PIN diode with different readout currents.

In addition it can be notified that in LHC experiments the expected fluence range from 10^8 - 10^{10} to 10^{14} - 10^{15} particles/cm². Operating the BPW34F Silicon PIN diode with the readout protocol presented above, the upper-limit of the measurable fluence range is of about 4×10^{14} n_{eq}/cm² which is in a good agreement with the maximum radiation level reached in LHC.

While this readout protocol allows monitoring radiation level for LHC experiments, for the Super-LHC, this readout protocol will become obsolete depending on the location where the dosimeters will be used. In the Super-LHC, the luminosity will be increased by a factor of 10 and the expected maximum 1-MeV equivalent fluence will be of the order of 10^{16} n_{eq}/cm² in the inner part of the experiments. For this reason, a new approach to use the BPW34 Silicon PIN diode has to be found. As a consequence, different questions which are presented below will be discussed in the next sections of this chapter:

- Why a saturation of the forward voltage V_F is observed at very high fluences?
- Can a new readout protocol be used for monitoring 1-MeV equivalent fluences for the Super-LHC?
- Can the existing protocol be extended by increasing the possibilities of readout current for operating the BPW34 silicon PIN diode?

In order to answer to these questions, a new readout system for PIN diode measurement has been developed at CERN as it is presented in the next section.

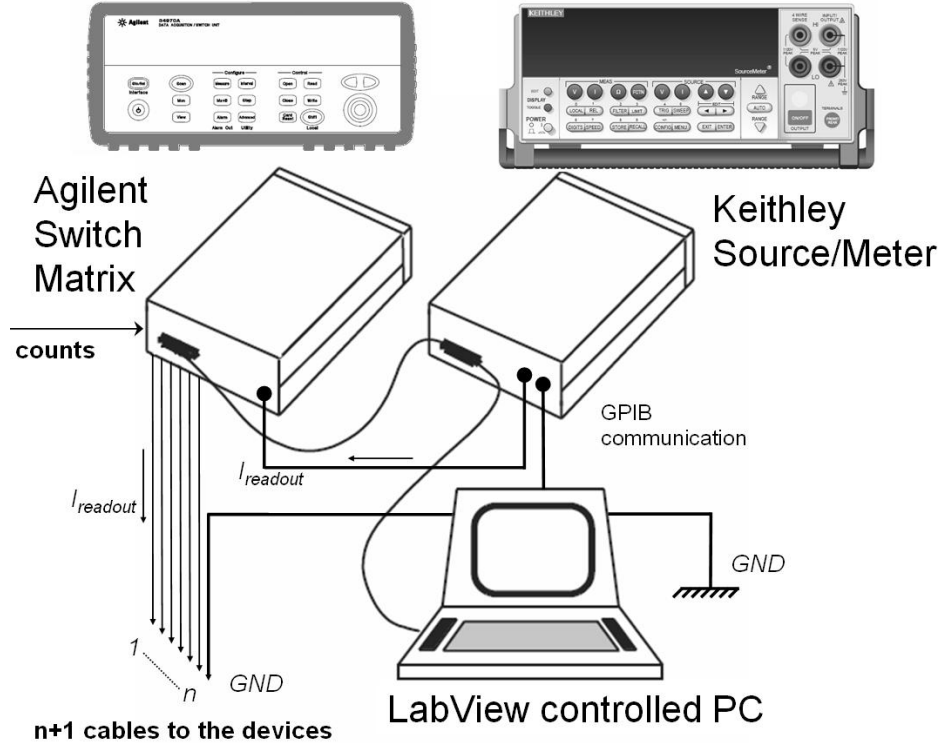


Figure 5.4: Setup for the silicon PIN diode dosimeters. The Agilent switch matrix is connected to the setup only if several dosimeters have to be measured one after the others.

5.3 Silicon PIN diode measurement setup

The measurement setup for PIN diodes presented in this section was already used in a previous study [Rav06], but it has been improved in order to satisfy the new requirements presented above.

Figure 5.4 schematically illustrated the system used to readout PIN diodes for all the measurements performed during the previous study presented in section 5.2.2.2, for the preliminary study presented in section 5.4 and for the temperature dependence evaluation presented in section 5.5.4.

The system consists of one Keithley 2400 source meter (or Keithley 2410 source meter) and an Agilent 34907A Switch Unit equipped with one (or two) switch module card (34903A) that allow to connect a maximum of 20 (or 40) devices. The Agilent Switch Unit was connected to the system only when it was necessary to measure several silicon PIN diodes sequentially one after the other. For instance, it was the case during the temperature study described in section 5.5.4,

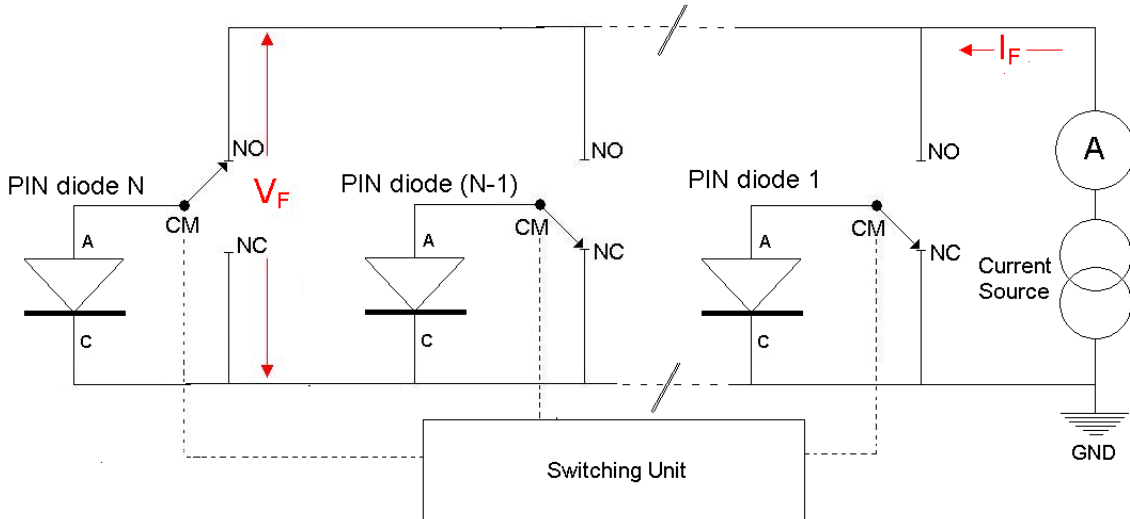


Figure 5.5: Schematic representation of the electrical setup when Silicon PIN diodes are measured one after the others using the Agilent 34907A Switch Unit. For any channels, the dosimeters are connected between the common (CM) and the “normally closed” (NC) terminals of the switch matrix. In the figure, the PIN diode (N) is readout as its terminals are connected between the “normally open” (NO) and the CM terminals. This configuration allows injecting a forward current I_F throughout the dosimeters.

when the temperature dependence of several irradiated BPW34 silicon PIN diodes was evaluated by placing and measuring them in a climate chamber at different temperatures.

In this case, the readout time of the whole dosimeter batch is therefore variable depending on the number of operated detectors connected to the system and in the time required to read all of them individually. For specific cases, like for instance for on-line radiation monitoring the Agilent 34907A Switch Unit can also host another module, which allows to acquire a counter value that may be converted to an 1-MeV equivalent fluence (Φ_{eq}) during an irradiation run.

A more detailed scheme of the PIN diode connections with the 34907A Switch Unit is given in Figure 5.5. The dosimeters are connected in a way that makes possible to read a single device and keep all the others shorted to ground to avoid self biasing phenomena.

The Keithley source meter as the Agilent Switch Unit are connected to a PC via IEEE-488 (GPIB) bus interface and were driven by a Labview Software.

Source Meter type	Keithley 2400	Keithley 2410
Source Voltage	5 µV to 210 V	5 µV to 1100 V
Measure Voltage	1 µV to 210 V	1 µV to 1100 V
Source Current	50 pA to 1.05 A	50 pA to 1.05 A
Measure Current	10 pA to 1.055 A	10 pA to 1.055 A

Table 5.1: Source and measurement ranges for both source meters used in this thesis work; Keithley 2400 and Keithley 2410. For both of them, the maximum source power is 22 W.

In this thesis work, in order to extend the existing protocol to a multitude of readout current options, a new software was developed with Labview to drive several detectors and operate them with different readout currents. As for the Labview program developed for the previous study summarized in section 5.2.2.2, the Labview control panel allows to set up all the acquisition parameters as the for instance the number of channels, time delays, repetition time, etc...

The previous software version made only possible to record a single I-V measurement point of the PIN diode characteristics. It is important to note that the new version makes now possible to record full I-V curves by forcing an increasing current step by step into the silicon PIN diode (not the case in section 5.2.2.2).

With this new software it is also possible to select the readout current pulse duration and cutting-off the readout current between two measurements for reducing the temperature inside the detector if there is a self-heating effect (not the case in section 5.2.2.1).

The selection of the readout currents that can be injected in the silicon PIN diode is not limited by the software performance but only by the range of currents provided by the Source meter. Table 5.1 illustrates the source and measurement ranges which can be achieved by the performance of both source meters used in this work.

The Keithley 2410 has the same characteristics than the model 2400, but allows operating the detector with a maximum voltage of 1100 V [Kei]. The possibility of measuring very

high voltages will be useful for characterizing heavily irradiated PIN diodes operate at high injection currents, as it will be shown in next sections.

As discussed in the previous section, the self-heating effect can be avoided by shorting the current pulse duration. This parameter can also be modified as for both instruments the minimum pulse duration is of about 1 ms.

5.4 Preliminary study of the BPW34FS radiation response

For this preliminary study, OSRAM BPW34FS (SMD plastic packaging) Silicon PIN diodes were exposed to the 24 GeV/c proton beam of the IRRAD1 facility at CERN. Irradiations were carried out at room temperature with a fluence accuracy within $\pm 7\%$.

The off-line proton data were obtained by measuring Silicon PIN diodes before and after being exposed to the proton beam. As this batch of irradiated silicon PIN diodes has been measured off-line, devices were not shorted to the ground during irradiations (see section 5.3 for on-line measurements). Immediately after the irradiation exposure, PIN diodes were stored until measurements in a freezer at a temperature below -20 °C in order to avoid room temperature annealing.

As for the previous work presented in section 5.2.2, the proton fluence was converted into 1-MeV equivalent neutron fluences (Φ_{eq}) by the experimentally obtained hardness factor $k = 0.62$ [Mol02].

5.4.1 New Readout protocol

In this preliminary study, instead of applying only one readout current to the device (as in section 5.2.2), silicon PIN diodes were operated by injecting forward current ranging from 10 μ A to 25 mA with 50 ms pulse duration.

More in detail, a new readout protocol was developed. It is driven by the new Labview Software presented in the previous section, in order to performed PIN diode I-V characterizations based on few measurement points (10 μ A, 100 μ A, 1 mA, 5 mA, 10 mA, 15 mA, 20 mA and 25 mA) with short current injection pulses. With the intention to avoid self-heating effect, the pulse duration was shorted to 50 ms and between each measurement, 10 μ A \times 50 ms current pulses were applied to the device as shown in Figure 5.6. This value has also been taken with the intention of monitoring the temperature enhancement inside the diode

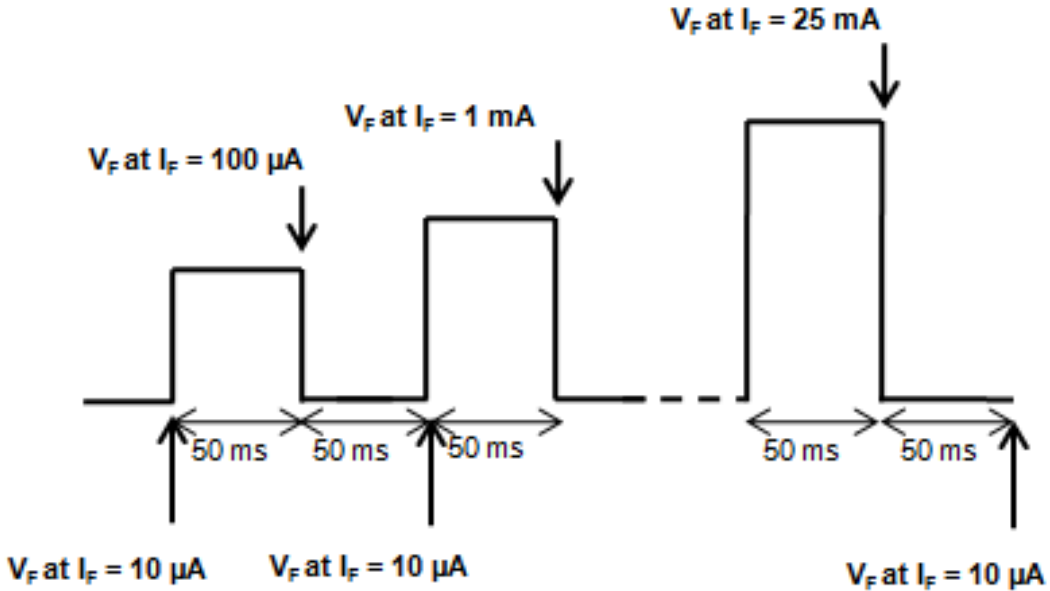


Figure 5.6: Schematic representation of the new readout protocol. The Labview Software developed for this study allows supplying the PIN diode with a custom list of forward currents. In this study, currents used were: 10 μA , 100 μA , 1 mA, 5 mA, 10 mA, 15 mA, 20 mA and 25 mA, with a pulse duration of 50 ms. Between each measurement the forward current is set to 10 μA to limit the self heating effect and monitor the temperature enhancement inside the diode during measurement.

during measurement, by measuring the difference of both current values taken with a 10 μA readout current before and after applying a higher readout current pulse. Since silicon has a negative temperature coefficient, if the diode is self-heated by a high current passing through it, the value of V_F measured at 10 μA after the injection of a higher current level would be lower than the one measured before. Using the new readout protocol presented here, the self-heating effect should be reduced in comparison with the previous I-V curves study presented in Figure 5.2. In this previous case a significant self-heating effect has been expected, since silicon PIN diodes were supplied by a wide range of forward currents, from low to very high values (500 mA) with long time injection. The lower and upper current level injection limits of the new readout protocol were defined taking into account the observations given in [Rav06] and summarized in section 5.2.2. From this previous study, it is considered that the maximum injected forward current by which the silicon PIN diode can be used as a dosimeter is 25 mA.

For this reason, this value was set to be the upper limit of the forward current injected in the BPW34F in this thesis work. In addition, since the radiation response is expected to be improved at high injection level, the lower limit of the forward current was set to 10 μ A.

5.4.2 BPW34FS radiation response

As described in the previous section, OSRAM BPW34FS Silicon PIN diodes have been measured with several readout currents. Figure 5.7 shows the radiation response of the BPW34FS Silicon PIN diode versus Φ_{eq} operated at (a) 10 μ A, 100 μ A, 1 mA and (b) 1mA, 10 mA, 20 mA. All measurements presented in this figure have been performed with 50 ms pulse duration.

It can be notified in Figure 5.7 that the flat region up to $\approx 2 \times 10^{12} n_{eq}/cm^2$ where the device is not sensitive to proton irradiations, does not depends on the readout current.

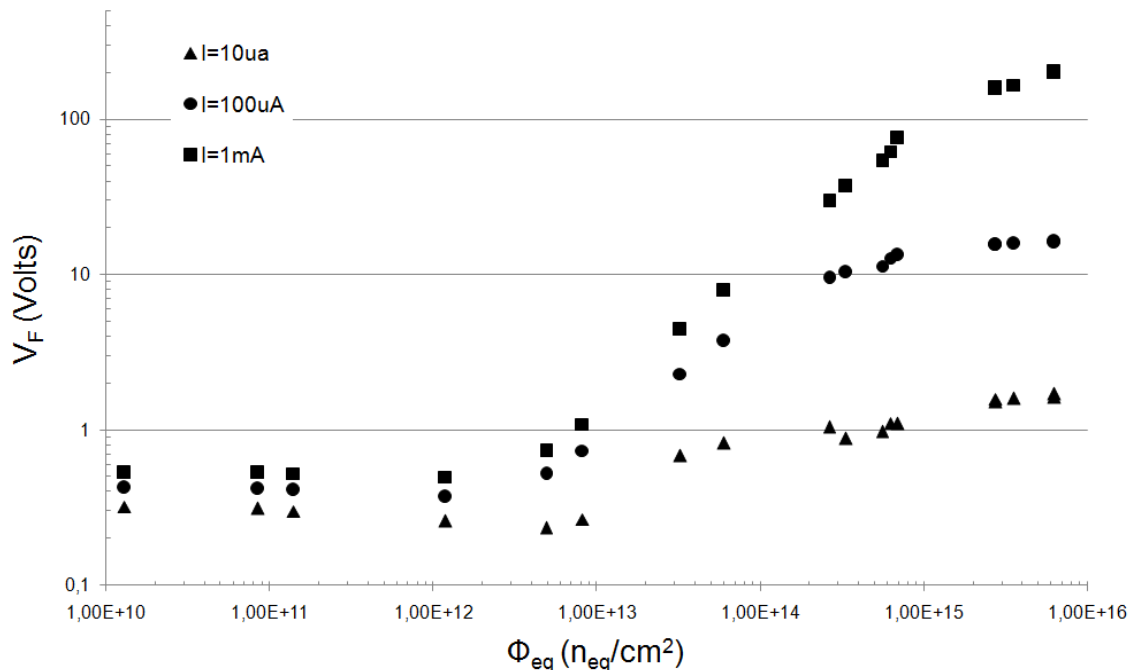
By contrast, for $\Phi_{eq} > 2 \times 10^{12} n_{eq}/cm^2$, the radiation response curves indicate that the BPW34FS PIN diode becomes sensitive to radiations up to around $5 \times 10^{14} n_{eq}/cm^2$ as it was described in section 5.2.2.

Other remarks can be made here; the upper-limit of the fluence measurement range (the linear part of the curve) is also not depending on the injected readout current, since at $\Phi_{eq} > 1 \times 10^{15} n_{eq}/cm^2$ a “saturation” of the radiation sensitivity is observed for all injected current values (see discussion below). Moreover, a comparison can be done between Figure 5.7(a) and (b) as the increase of the PIN diode radiation sensitivity (the slope of the linear part of the curve) is more significant between 10 μ A and 1 mA than between 1 mA and 20 mA.

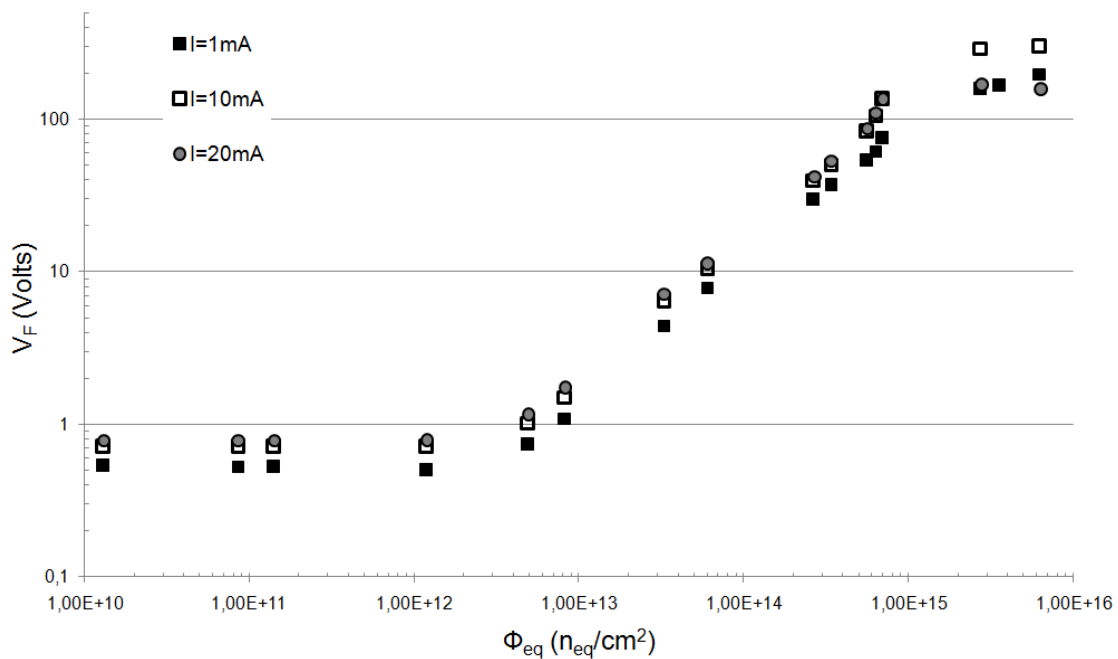
At Φ_{eq} higher than about $1 \times 10^{15} n_{eq}/cm^2$, a “saturation” of the measured forward voltage can be observed for all curves presented in this figure. In this regime, the linear equation (see Equation (5.1) which links the growth of the forward voltage (ΔV_F) with Φ_{eq}) does not fit anymore with the radiation response curves.

Data presented in Figure 5.7(b) revealed that in this regime, the forward voltage measured at $I_F = 20$ mA is lower than the measure performed at 10 mA. The phenomenon can be explained thanks to the theory developed in [Rav08b], in which it is assumed that the PIN diode has a ‘thyristor-like’ behavior. Moreover, this observation is confirmed by the current-voltage characteristic analysis presented below.

Each I-V curve presented in Figure 5.8 corresponds to a measurement performed with the new readout protocol, at a certain Φ_{eq} . By analyzing the data illustrated in this figure, same remarks can be done as for Figure 5.2.



(a)



(b)

Figure 5.7: Radiation response of the BPW34FS after 24 GeV/c proton irradiations. The diode's forward voltages (a) measured with a 50 ms readout current at $10\ \mu A$, $100\ \mu A$, $1\ mA$ and (b) $1\ mA$, $10\ mA$, $20\ mA$ are plotted versus Φ_{eq} .

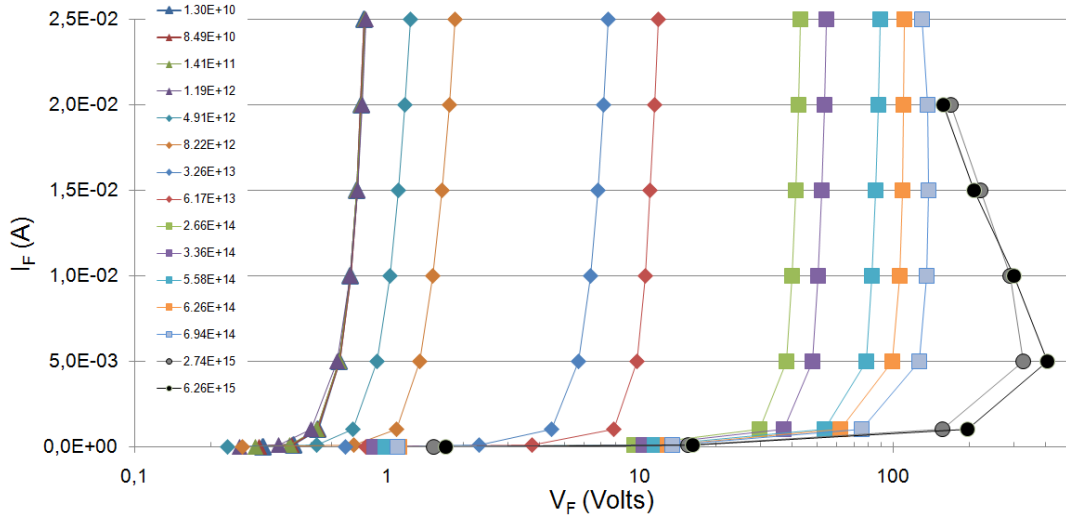


Figure 5.8: Forward current-voltage characteristics of the BPW34FS silicon PIN diodes after 24 GeV/c proton irradiations taken with the new readout protocol. Each curve represents a measurement done at different Φ_{eq} as indicated in the legend.

It can be observed that for $\Phi_{eq} > 2 \times 10^{12} \text{ n}_{eq}/\text{cm}^2$, the I-V characteristics of the PIN diode start to shift to the positive direction with increasing equivalent fluence.

At higher fluences, the forward voltage becomes very high as well as the power dissipated in the PIN diode which is equal to:

$$P = V_F \times I_F \quad (5.2)$$

From it, the energy deposition during a certain time (t) can be estimated using the following formula:

$$Q = P \times t \quad (5.3)$$

Where the unit of Q, P and t are Joules, Watts and seconds respectively.

Furthermore, the increase of temperature inside the PIN diode during measurement (i.e. the self-heating effect) is directly related to the power dissipated inside the device as:

$$\Delta T = \frac{Q}{c \times m} = \frac{P \times t}{c \times m} \quad (5.4)$$

Where c is the specific heat capacity for silicon and m is the mass of the diode.

Therefore, the increase of the power dissipated inside the silicon PIN diode can generate self-heating effect. It means that possible self-annealing can be induced by the rise of temperature during measurement, or even more that the device could be totally destructed. For this reason, the maximum readout current supplied to the BPW34FS silicon PIN diode was set to 20 mA for $\Phi_{eq} \geq 2.74 \times 10^{15} n_{eq}/cm^2$.

Moreover, it should be mentioned that equations presented above are consistent for bare detector measurements, which means for PIN diodes without any surrounding package. For packaged diode, the energy dissipated inside the device is influenced by the package, due to the reduced thermal exchange between the air and the diode. The calculation of the temperature variation has not been performed during this thesis work. However, this simplified approach allows understanding the relation between the temperature variation during measurement and the power dissipated inside the silicon PIN diode.

For $\Phi_{eq} \geq 6.94 \times 10^{14} n_{eq}/cm^2$, the forward voltage starts to bend back to lower values with increasing the readout current injection. Contrary to section 5.2.2, since the maximum injected current is of about 25 mA, this effect can only be observed at very high fluences.

From the previous study summarized in this chapter, Ravotti described that at such high irradiation levels, the silicon PIN diode tends to be thyristor-like. However self-heating effects cannot be ignored.

More precisely, because silicon has a negative temperature coefficient (NTC), when its temperature is increased, its resistivity is reduced. As a consequence, one of the hypothesis which should be considered here is that I-V curves bend back to lower V_F when the readout current is increased, due to the self-heating effect.

5.4.3 Self-heating effect

With the intention of validating this hypothesis, a test has been performed on diodes irradiated at $\Phi_{eq} = 6.94 \times 10^{14} n_{eq}/cm^2$ and $\Phi_{eq} = 2.74 \times 10^{15} n_{eq}/cm^2$.

It is based on the measurement of heavily irradiated PIN diodes with two different readout protocols: “the normal protocol” which is the protocol described in Figure 5.6 and another one established on the temperature stabilization inside the detector during measurement of I-V curves, as described in Figure 5.9. Results are shown in Figure 5.10.

As for the “normal readout protocol”, when the measurement is run, a 10 μ A forward readout current is applied to the device during 50 ms. Then the corresponding forward voltage (V_{F1}) is recorded. A 50 ms readout current pulse of value I_{Fn} (from 10 μ A to 25 mA) is afterwards injected into the PIN diode and the corresponding V_{Fn} is also recorded.

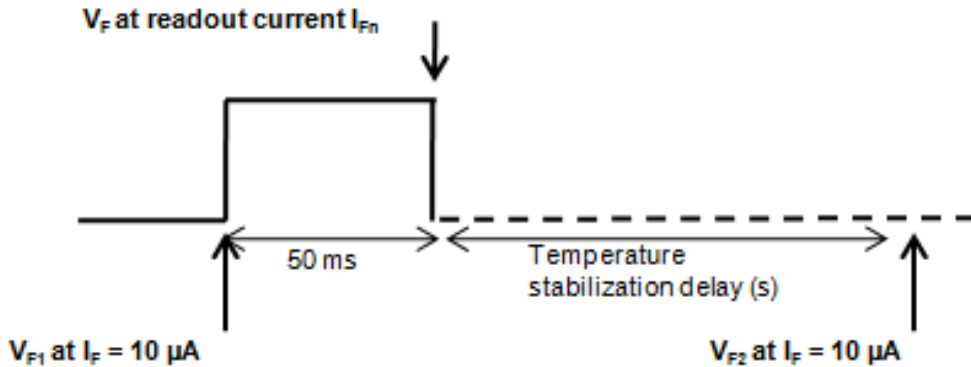
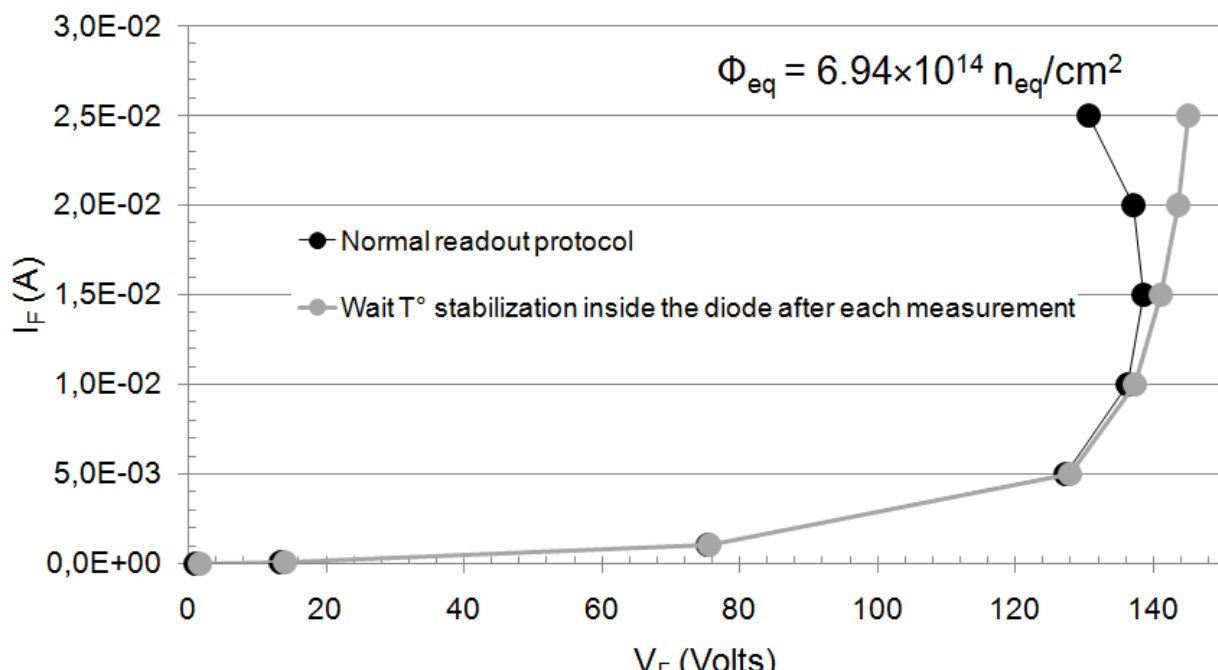


Figure 5.9: Schematic representation of the readout protocol developed for stabilizing the temperature inside the PIN diode between each measurement. In the figure, V_{F1} and V_{F2} represent the forward voltages measured with $I_F = 10 \mu\text{A}$ respectively before and after the higher current injection pulse. The temperature stabilization condition is confirmed when after a certain time delay $V_{F1} = V_{F2}$.

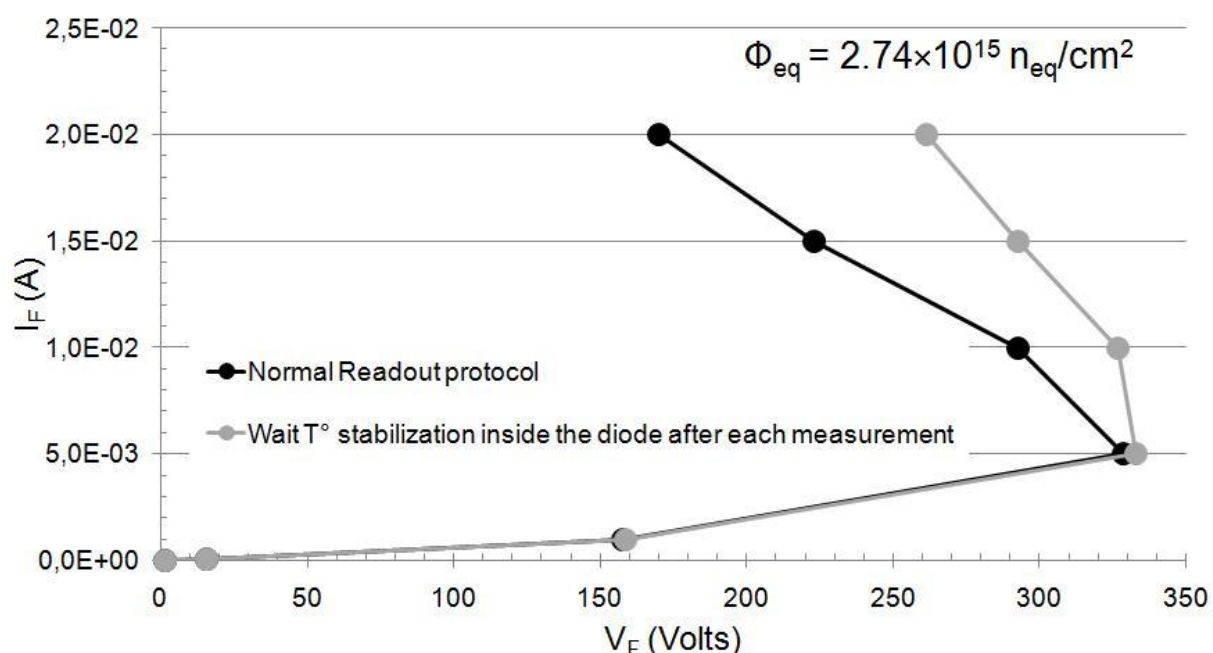
Subsequent to this measurement, a readout current of $10 \mu\text{A}$ is continuously applied to the diode in order to monitor the variation of the forward voltage V_{F2} versus time.

Since Silicon PIN diodes have a negative temperature coefficient, the forward voltage (V_{F2}) measured just after the current pulse is lower than (V_{F1}) even if both voltages were measured at $I_F = 10 \mu\text{A}$. As time increases, V_{F2} is approaching V_{F1} , since the temperature inside the diode decreases. It clearly indicates that during measurement, heavily irradiated diodes are self-heated by high current injection.

In order to avoid this effect, each PIN diode measurements were done after stabilizing the temperature inside the device, which means when V_{F2} became equal to V_{F1} . In order to give some orders of magnitude to the reader, two examples are given here. The time in which V_{F2} becomes equal to V_{F1} (within $\pm 1\%$) is around 2 minutes, after a $20 \text{ mA} \times 50\text{ms}$ (I_{Fn}) readout current injected in a diode irradiated at $6.94 \times 10^{14} \text{ n}_{\text{eq}}/\text{cm}^2$ (e.g. in Figure 5.10(a)). While this stabilization time is around 7 minutes (until V_{F2} becomes equal to V_{F1} within $\pm 1\%$ after being operated at $20\text{mA} \times 50\text{ms}$) for a diode irradiated at a fluence of $2.74 \times 10^{15} \text{ n}_{\text{eq}}/\text{cm}^2$ (e.g. in Figure 5.10(b)).



(a)



(b)

Figure 5.10: Forward current-voltage characteristics of the BPW34FS silicon PIN diode irradiated at (a) $\Phi_{\text{eq}} = 6.94 \times 10^{14} \text{ n}_{\text{eq}}/\text{cm}^2$ and (b) $2.74 \times 10^{15} \text{ n}_{\text{eq}}/\text{cm}^2$. Measurements were carried out after 24 GeV/c proton irradiations with the normal readout protocol (black curves) and by waiting temperature stabilization inside the BPW34FS Silicon PIN diode (grey curves).

It can be notified here, that the time for stabilizing the temperature inside the device after high current injection increases with fluence, which means that the power dissipated in the PIN diode is more important for the most heavily irradiated devices.

This readout procedure was repeated for the same readout currents as for the “normal protocol”. (100 µA, ..., 10 mA, ..., 20 mA ...). Results are presented in Figure 5.10.

The grey curves represent measurements performed by waiting for the temperature stabilization between each measurement, while the black curves represent measurements carried out with the “normal readout protocol”. By comparing both protocols, it can be observed in Figure 5.10(a) that the grey curve does not bend back to lower values with increasing the readout current, whereas the black curve does. This remark clearly demonstrates that in addition to the “thyristor-like” behavior (see section 5.2.2), there is a self-heating effect which also induces a modification of the BPW34FS PIN diode I-V characteristic.

The same observation can be made for Figure 5.10(b). Nevertheless in this case, even when the self-heating effect is reduced by temperature stabilization, the I-V curve still bends back to lower values. This phenomenon can be explained since as described in [Rav08b] when the radiation level is increased, the “thyristor-like” behavior of the silicon PIN diode is amplified.

Another reason could also be that at such irradiation level, the resistivity of the Silicon PIN diode becomes very high. As a consequence, the power dissipated inside the diode increases in such a way that 50 ms pulse duration becomes too long for avoiding self-heating effect.

Forward voltages versus Φ_{eq} are plotted in Figure 5.11. Each couple of points numbered (1;2), (3;4) and (5;6) were measured on the same irradiated PIN diode with both readout current protocols.

For the couple of points (1;2), a 10 mA readout current was applied to the BPW34FS silicon PIN diode irradiated at $\Phi_{eq} = 2.74 \times 10^{15} n_{eq}/cm^2$; (1) by waiting temperature stabilization inside the device and (2) with the normal readout protocol.

As it has been already observed in Figure 5.10, the value of the forward voltage is higher when the temperature inside the device is stabilized before running the next measurement.

Same observations can be done for the other couple of points. In the case of (5;6), instead of recording forward voltages with a 10 mA readout current, the PIN diode were operated at 20 mA. The difference between these two points is even more significant since by increasing the current level injection, the self-heating effect is amplified. For couple of points (3;4), the injected readout current was equal to 10 mA and the particle fluence was raised up to $2.74 \times 10^{15} n_{eq}/cm^2$. Same behavior can be observed.

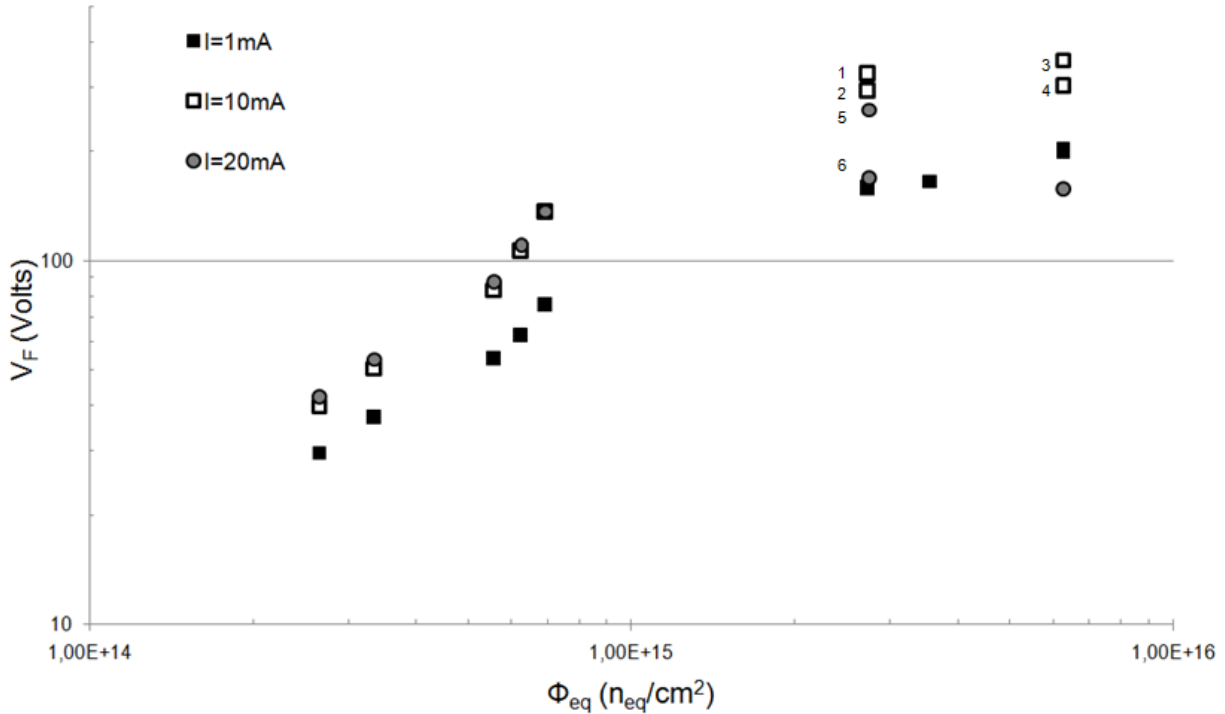


Figure 5.11: Radiation response of BPW34FS for $\Phi_{eq} \geq 1 \times 10^{14} n_{eq}/cm^2$. The diode's forward voltage at 1 mA, 10 mA and 20 mA readout currents are presented here. The points numbered 1, 3, 5 and 2, 4, 6 have been recorded when PIN diodes have been operated respectively, by waiting temperature stabilization and with the normal readout protocol as described in the text.

As a result, it can be stated that operating BPW34FS diodes at high readout current is not a good solution for monitoring very high fluences. The radiation response strongly depends on the current injection level and can be completely altered.

Since for the Super-LHC, detectors will be exposed to a fluences up to $1 \times 10^{16} n_{eq}/cm^2$, a new method for using the BPW34FS silicon PIN diode as radiation monitoring sensors have to be found. This method is discussed in the next section.

5.5 New approach in predicting the radiation response of PIN diodes up to very high fluences

In the previous section it was shown that Silicon PIN diode operated at high current injection condition should not be used for monitoring radiation levels as expected for the Super-

LHC. For this reason, a new method for characterizing the OSRAM BPW34FS Silicon PIN diode as radiation monitoring sensors has been developed in this thesis. It is based on the analysis of complete reverse and forward silicon PIN diode I-V curves, in order to verify if the PIN diode may be operated at low current injection level, for monitoring SLHC fluences (i.e. $\Phi_{eq} \geq 1 \times 10^{14} n_{eq}/cm^2$).

A new measurement setup for laboratory tests has been therefore developed for this purpose, which allows performing complete I-V characteristics from very low to high injected current.

5.5.1 Measurement method and equipment

All measurements presented in this section were carried out using a test bench based on a Keithley 2400 (or 2410 for voltages higher than 210 Volts) and a Keithley 485 picoamperemeter. From here they will be named Keithley 24XX, for a better readability.

Both devices are connected to a PC via GPIB bus interface and are driven by a new Labview software specifically developed for this study.

Since BPW34FS Silicon PIN diode is light sensitive, as presented in previous sections, measurements have been performed in a light-tight box. The temperature during measurement was recorded by placing a PT100 temperature sensor close to the diode. Figure 5.12 represents the new setup for characterizing the radiation response of the BPW34FS silicon PIN diode.

Reverse bias measurements were done using the Keithley 24XX as d.c voltage source, from -1 mV to -500 V. The reverse current was measured by the picoamperemeter and limited to a compliance of 1mA in order to avoid possible self-heating effect at high current.

In addition, forward bias measurements were carried out in several steps:

- For the lower current values ($I_F \leq 100nA$), the measurements were performed as for reverse bias, i.e. by sourcing voltages with the Keithley 24XX and by measuring the forward current with the picoamperemeter. This method was selected since for measurements of low current values, the Keithley 485 is more precise than the Keithley 24XX.
- From 100 nA to 1 mA, measurements were done only with the Keithley 24XX by injecting short current pulse of 50 ms pulse duration and by measuring the corresponding forward voltage. In order to avoid self-heating effect inside the detector, it is better to reduce the measurement time by taking only few points at high injection level. Thus, at $I_F > 1$ mA,

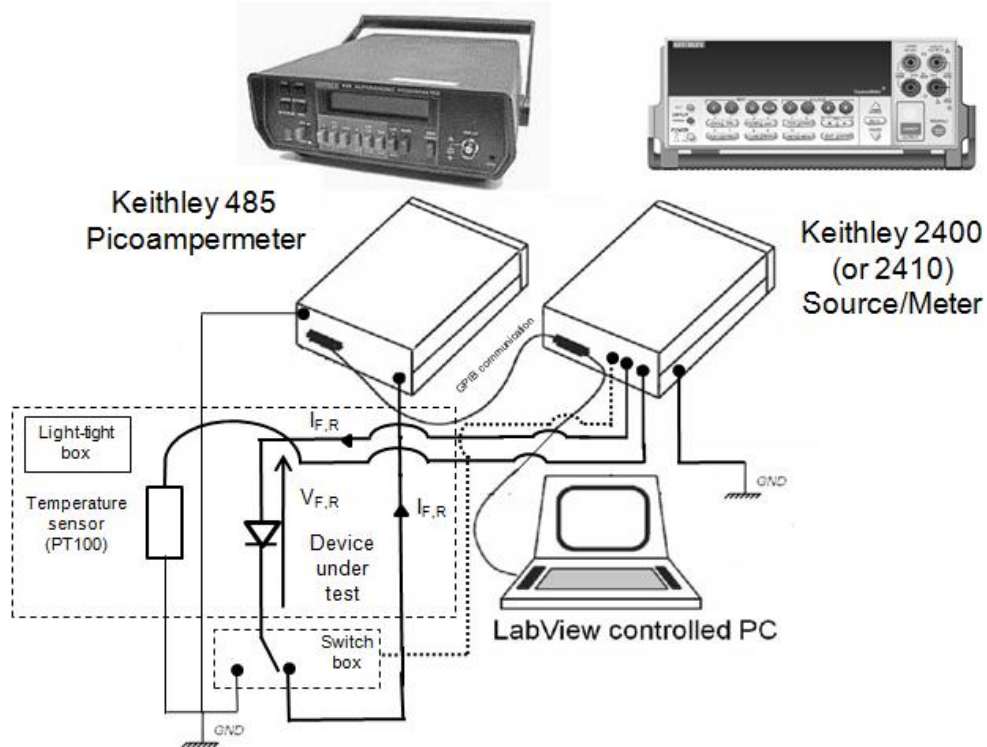


Figure 5.12: New setup for the OSRAM BPW34FS Silicon PIN diode's characterization using both instruments (Keithley 485 and Keithley 2400 (or 2410)). Due to light sensitivity, PIN diodes have been measured in a light-tight box. During measurement, temperature has been recorded using a PT100 temperature sensor. The switch box allows the commutation between measurements with or without the picoampermeter.

measurements were carried out by injecting only 8 current steps: 2 mA, 3mA, 4 mA, 5 mA, 10 mA, 15 mA, 20 mA and 25 mA).

Since forward I-V measurements have been performed with and without the Keithley 485 picoampermeter, a system for switching automatically between both options has been produced. As it is represented in Figure 5.12, a switch box is driven by the Labview Software via the digital output of the Keithley 24XX. It allows disconnection of the Keithley 485 picoampermeter during forward measurement from 100 nA to 1 mA and its connection to the setup at current injection below 100 nA. A more detailed scheme of the switch box is given in Figure 5.13.

It consists of two relays connected together; a semi-conductor switch ADG801 from Analog Devices and a reed relay DIL05-2C90-63L from Meder Electronic. The Digital I/O Port of

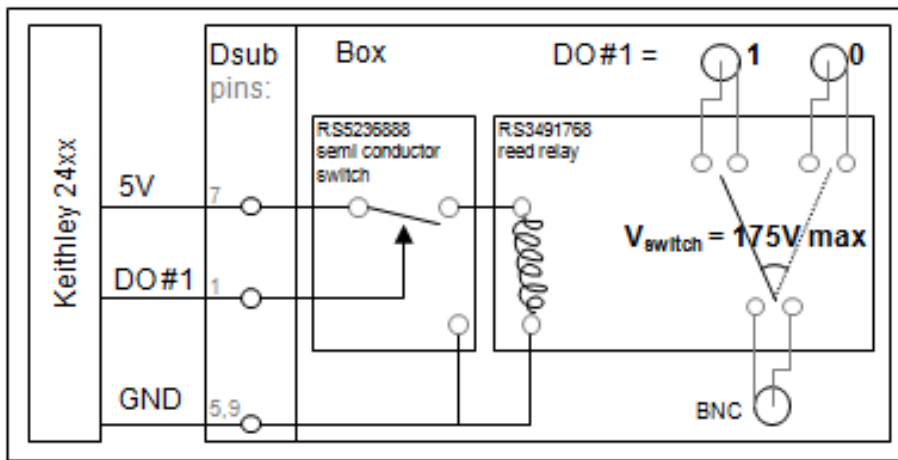


Figure 5.13: Block diagram of the switch box.

the Keithley 24XX is used for driving the switch box. It provides a +5V output (d. c.) with a maximum current output for this line of 300mA. In addition, each digital output line can source a current up to 2 mA and can be piloted by software. The semi-conductor switch is driven via its digital input by a digital output of the Keithley 24XX.

Commutation between the two measurement states is done by means of Meder reed relay DIL05-2C90-63L. It stands a switching voltage up to 175V and provides as mechanical switch best signal performance for low currents. Its solenoid has to be operated at a current of 300 mA that cannot be provided directly by the digital outputs of the Keithley 24XX. Thus, Analog Devices semiconductor switch ADG801 has been connected in between that switches the constant 5V (300mA) DC power output of the Keithley 24XX according to the digital output state.

5.5.2 Experimental results

Silicon PIN diodes were exposed to the 24 GeV/c proton beam of the IRRAD1 facility at CERN. As for the preliminary study presented in section 5.4, after irradiation exposure, the diodes were stored in a freezer at a temperature below -20°C.

Forward and reverse I-V characteristics of unirradiated and irradiated BPW34FS silicon PIN diodes have been performed at room temperature. Measurements were obtained from different irradiation exposures with various fluences ranging from 1.41×10^{11} to $6.3 \times 10^{15} n_{eq}/cm^2$. Irradiations were performed at room temperature within a fluence accuracy of $\pm 7\%$. The proton

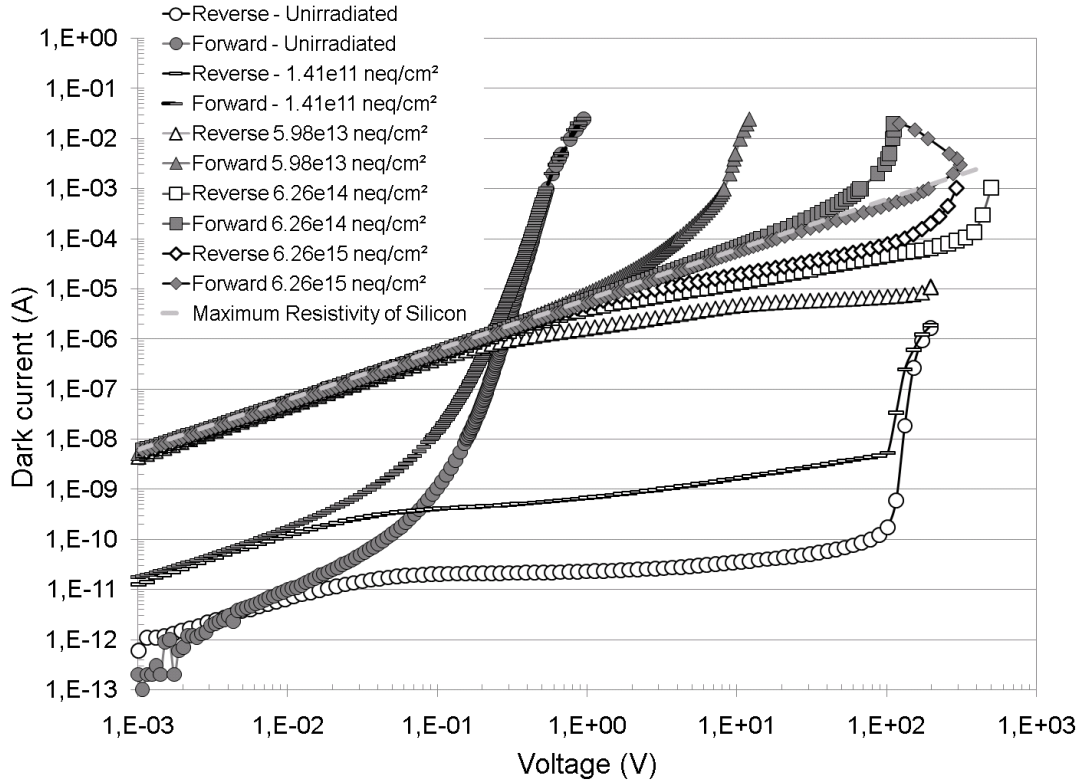


Figure 5.14: Forward and reverse I-V characteristics of non-irradiated and irradiated PIN diodes after 24 GeV/c proton irradiations. Results are presented in logarithmic scale. Measurements were performed at room temperature. The dashed line represents the maximum resistance of the diode at 300K. I_R values > 1 mA have not been plotted in this figure, since the reverse current was limited to a compliance of 1 mA.

fluence was converted into 1-MeV neutron equivalent fluence (Φ_{eq}) by the experimental hardness factor (k) of 0.62. Results are presented in log-log scale in Figure 5.14 and Figure 5.15 (forward I-V characteristics only). For a better visibility, only a few measurements are shown here.

Two different cases can be distinguished in the I-V characteristics.

In the first situation, for non-irradiated diode, at low voltages (up to around 20 mV), for both operation directions, a linear region can be observed. As the voltage increases, the curve shape changes. While for forward bias measurements there is a change from linear region to a sharp increase of the forward current, for reverse bias measurements a saturation of the reverse current appears. At even higher reverse voltages, the current starts to increase rapidly inducing that the device is approaching breakdown.

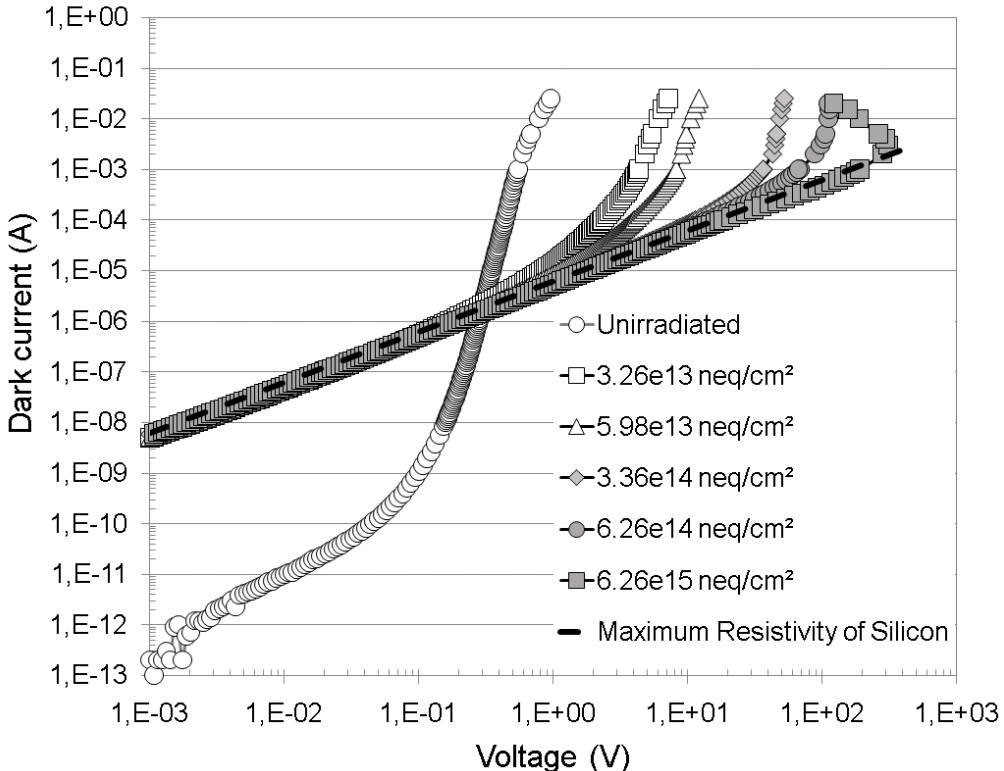


Figure 5.15: I-V characteristics for forward bias of non-irradiated and irradiated PIN diodes after 24 GeV/c proton irradiation and $\Phi_{eq} > 10^{13}$ n_{eq}/cm² with the corresponding maximum resistance line at 300K. Results presented here are taken from Figure 5.14 but for a better readability of the curves only forward measurements are illustrated and some radiation levels are added for completeness.

As the radiation level increases up to around 1×10^{13} n_{eq}/cm², a rise of both reverse and forward currents versus fluences can be observed.

For fluences above 1×10^{13} n_{eq}/cm², there is a linear region at low voltages. Because the current increased versus radiation damage, this linear region appears at higher currents than the one observed for unirradiated diode. With further increase of the radiation level, this linear behavior will extend to higher voltages.

5.5.3 Analysis of the Current-Voltage characteristics

In order to obtain a better understanding on how radiation damage changes properties in the BPW34FS diode, the following discussion is based on a comparison between irradiated silicon p-i-n diodes and relaxation materials which has been already studied in [McP97a], [McP97b], [San98], [Jon99], [McP04] and [Deh04].

In the first part of this section, the relaxation régime and the silicon PIN diode properties when the device assumes a “relaxation-like” behavior are summarized. Furthermore an analysis of the current-voltage characteristics established on this relaxation régime theory is performed here. From it, a new approach to use the OSRAM BPW34FS silicon PIN diode for monitoring SLHC fluences is presented.

5.5.3.1 Relaxation regime and diode properties

This section presents and discusses a not so well documented effect of radiation damage in silicon PIN diodes, which is the modification of high resistivity material into another class of semiconductor: the relaxation material. The semiconductor industry has mainly used silicon because of the valuable materials properties, made from such material. However, a few studies of relaxation semiconductors have been performed during the past but they are not usually mentioned in text books and semiconductor physicists are often not familiar with this concept. This phenomenon is not obvious and often neglected but it is an important issue as it suggests a new method for analyzing radiation response of irradiated silicon PIN diode.

The lattice destruction by protons or neutrons introduces deep levels defects which modify the electrical properties of the silicon material. These defects increase the resistivity of the semiconductor material and are responsible for its semi-insulating behavior, which from 1972 has been attributed to the relaxation-like properties in semiconductors as it is referenced in [Roo72], [Que73] , [Hae91].

From the relaxation material theory, a material becomes relaxation-like, if it has a high resistivity due to a low carrier density and a large density of generation recombination (g-r) centers. Such traps can be produced by radiation damage in silicon p-i-n diodes.

Relaxation material has characteristics which appears strange to physicists who are familiar to lifetime material. Contrary to lifetime material in which the resistivity is decreased by minority carrier injection, if minority carriers are injected into relaxation material, the resistivity increases since the concentration of both minority and majority carriers is reduced by recombination with the g-r centers.

The dielectric relaxation time τ_D , is the time in which a space charge is neutralized by the flow of free carriers that are drawn in by the excess charge but slowed down by the resistance of the material.

It is assumed to be the bulk equivalent of a RC time constant and is equal to:

$$\tau_D = \rho \epsilon_s \epsilon_0 \quad (5.5)$$

Where ρ is the material resistivity, ϵ_s is the relative dielectric constant and ϵ_0 is the permittivity of free space. In addition of this description, a more detailed definition of the dielectric relaxation time taken from [And05] is given here.

The dielectric relaxation time is also defined by the time needed to restore charge neutrality to a region when excess carriers of one polarity are suddenly introduced. When a PN junction is turned on and excess carriers are injected across the junction, at the instant of injection ($t = 0$), there will be an excess charge ($\Delta_{n,p}$) in the material.

For example, there will be an excess negative charge (Δ_n) if electrons are injected into the p-side of a PN junction. In this case, extra positive charges must be summoned from external circuit to re-establish charge neutrality in the p-material. This process takes a small but finite time named the “dielectric relaxation time” (τ_D). It is a measure of the time required to neutralize excess carriers injected in the material.

In the case of forward biased junction, minority carriers, for instance holes are injected in the n-material, and are dispersed by diffusion since the gradient of holes in the n-side is significant. However diffusion is a relative slow process.

Suppose that holes are injected into the n-side so that the field built up by the excess holes (Δ_p) acts on electrons.

At $t = 0$, there are excess holes but no excess electrons on the n-side. The electrons (majority carriers) are attracted into this region by drift because of the field induced by the excess holes, and (Δ_n) tends to neutralize (Δ_p). This neutralization occurs in a dielectric relaxation time (τ_D).

While electrical neutrality is normally quickly established (for unirradiated diode); excess holes diffuse slowly and recombine with electrons, in such a way that there are still excess carriers for a certain time. This time is called the carrier lifetime (τ_0).

In conventional lifetime material, neutrality is restored before excess carriers recombine, so that:

$$\tau_0 \gg \tau_D \quad (5.6)$$

Furthermore, while for most practical cases the material relaxation can be considered almost instantaneous, for irradiated diodes where deep levels are introduced by radiation

damage, the dielectric relaxation time is enhanced. The influence of the defects is based on their efficiency in trapping free carrier. As a consequence, since the material becomes highly recombinative due to a high density of recombination centers, the carrier density decreases and the bulk material resistivity increases which causes that:

$$\tau_0 \ll \tau_D \quad (5.7)$$

so that the enhancement of resistivity also increases the dielectric relaxation time.

Such a behavior can be observed if the carrier mobility is decreased, for instance when the temperature is low enough so that the free carrier are frozen out, or it can occurs for compensated semiconductors such as irradiated Silicon PIN diode. In this case the free carriers from thermally ionized shallow defects are trapped into deep levels which are not thermally ionized, and are immobilized or recombine with the free carrier of the opposite sign.

In addition, due to the rapid recombination that occurs through the g-r centers, when the diode is forward biased, injection of minority carrier lead to a depletion of majority carriers. As a consequence, the carrier equilibrium is rapidly reached through the g-r centers activity so that it is not possible to influence the carrier equilibrium by externally applied voltage.

For the lifetime régime, when carriers are injected into the diode by applying an external voltage (non steady-state condition), the np product becomes a function of V as referenced in [Sze81]:

$$np = n_i^2 \times \exp\left[\frac{qV}{kT}\right] = n_i^2 \times \exp\left[\frac{q(\phi_n - \phi_p)}{kT}\right] \quad (5.8)$$

where in this equation, n_i is the intrinsic carrier concentration, k is the Boltzmann constant, T is the temperature, q is the electron charge, V is the external applied voltage and Φ_n and Φ_p are the two quasi-Fermi levels [Sze81]. Contrary, for the relaxation case since any external disturbances do not affect the carrier equilibrium (as for the steady state condition of a lifetime material), the np product becomes equal to:

$$np = n_i^2 \quad (5.9)$$

In addition, as material becomes relaxation-like if it has a large density of defect g-r electronic levels near the middle of the energy gap (E_g) which can readily interact with both types of carriers, recombination pins the Fermi levels at the value of minimum conductivity [Roo72].

Both quasi-Fermi levels are equalized, pinned at the midgap level as:

$$\phi_R = \phi_n = \phi_p \quad (5.10)$$

Here Φ_R is the single relaxation potential.

With these considerations, the relaxation material is assumed to have minimum conductivity so that:

$$\frac{d\sigma}{dn} = \frac{d}{dn}(q \times (\mu_n n + \mu_p p)) = 0 \quad (5.11)$$

where μ_n and μ_p are the electron and hole mobilities respectively. From this equation, it is possible to obtain the expression of n :

$$n = \sqrt{\frac{\mu_p}{\mu_n}} \times n_i \quad (5.12)$$

The values of n and p can be also obtained by another method, since for steady state conditions, the electron and hole currents are continuous and identical so that [Sze01]:

$$n \times \mu_n \times \frac{dE_F}{dx} = p \times \mu_p \times \frac{dE_F}{dx} \quad (5.13)$$

where E_F represents the Fermi level.

Using this equation, since the np product is equal to n_i^2 , the values of n and p can be found equal to:

$$n = \sqrt{\frac{\mu_p}{\mu_n}} \times n_i$$

$$p = \sqrt{\frac{\mu_n}{\mu_p}} \times n_i \quad (5.14)$$

From this point the expression of the minimum conductivity and the maximum resistivity can be obtained, as expressed by the following equations:

$$\sigma_{\min} = 2 \times q \times n_i \times \sqrt{\mu_n \times \mu_p} \quad (5.15)$$

$$\rho_{\max} = \frac{1}{2 \times q \times n_i \times \sqrt{\mu_n \times \mu_p}} \quad (5.16)$$

For Silicon the value of the maximum resistivity at 300 K is around $3 \times 10^5 \Omega \cdot \text{cm}$.

This value is used to calculate the maximum resistance of the diode (R_{\max}) when the relaxation régime is established as:

$$R_{\max} = \frac{\rho_{\max} \times L}{A} \quad (5.17)$$

where L and A represent the diode's thickness and area in unit of cm.

5.5.3.2 Analysis of the I-V curves

First of all, the reverse bias measurements are discussed. As it is expected from the conventional lifetime theory [Sze01], for unirradiated diode, at voltage superior to $3kT/q$ (78 mV), a saturation of the current can be observed, since the diffusion current dominates in the diode. At higher reverse voltages, the current rises sharply which indicates the occurrence of the avalanche breakdown. For irradiated diodes, as radiation damage increases with fluences, more generation-recombination (g-r) centers are created in the silicon bulk. As a consequence, for low voltages (in the linear region) the reverse current versus Φ_{eq} increases until it reaches a maximum value. For higher voltages, it can be mentioned that the generation current dominates, as in reverse bias; traps alternately emit electrons and holes. In this case, this current dominates and gives the $V^{1/2}$ variation corresponding to the increase of the depletion width [Sze01].

In the forward bias regime, for $\Phi_{\text{eq}} < 10^{13} \text{ n}_{\text{eq}}/\text{cm}^2$, the PIN diode behaves as conventional lifetime diode, with high current flowing in the forward direction due to the diffusion current. At higher currents, the PIN diode may enter in high injection state i.e. the injected minority carrier density becomes comparable to the doping density in the n-substrate [Sze01].

With increasing fluences, a growth of the current at lower voltages can be observed, up to a maximum value which is the same than for reverse bias.

For both operation modes, at $\Phi_{\text{eq}} > 10^{13} \text{ n}_{\text{eq}}/\text{cm}^2$, the ohmic-like behavior appears and the I-V characteristics become parallel to the line of maximum resistivity as illustrated in Figure 5.14

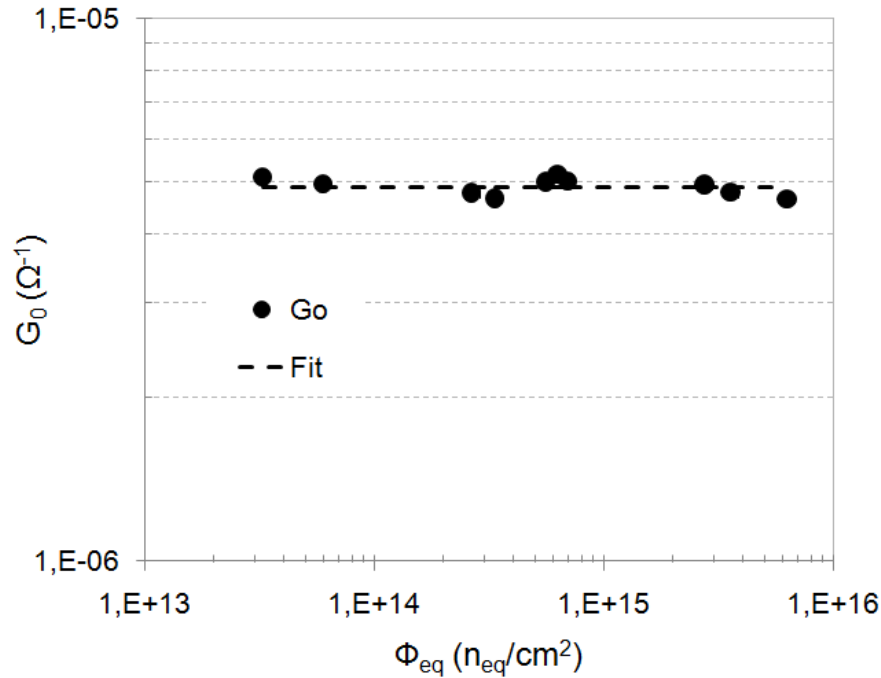


Figure 5.16: The value of the fitting parameter G_0 as a function of equivalent fluences.

and Figure 5.15, which indicates that the material is becoming relaxation-like when radiation damage increases. The line of maximum resistivity is expressed by:

$$R_{\max} = \frac{V}{I} \quad (5.18)$$

5.5.3.3 Characterization of the forward bias radiation response

In previous study [Wal69], I-V characteristics of relaxation materials were experimentally fitted with the following empirical expression:

$$I = G_0 V \exp\left(\frac{V}{V_0}\right) \quad (5.19)$$

where G_0 is the conductance in unit of Ω^{-1} , defined by the following formula:

$$G_0 = \left(\frac{1}{R_0} \right) = \left(\frac{A}{\rho \times L} \right) \quad (5.20)$$

In this study, as illustrated in Figure 5.16 the value of G_0 has been evaluated from I-V curves of diodes irradiated at $\Phi_{eq} > 1 \times 10^{13} n_{eq}/cm^2$ as $G_0 = (4.90 \times 10^{-6} \pm 6.43 \times 10^{-8}) \Omega^{-1}$. A and L

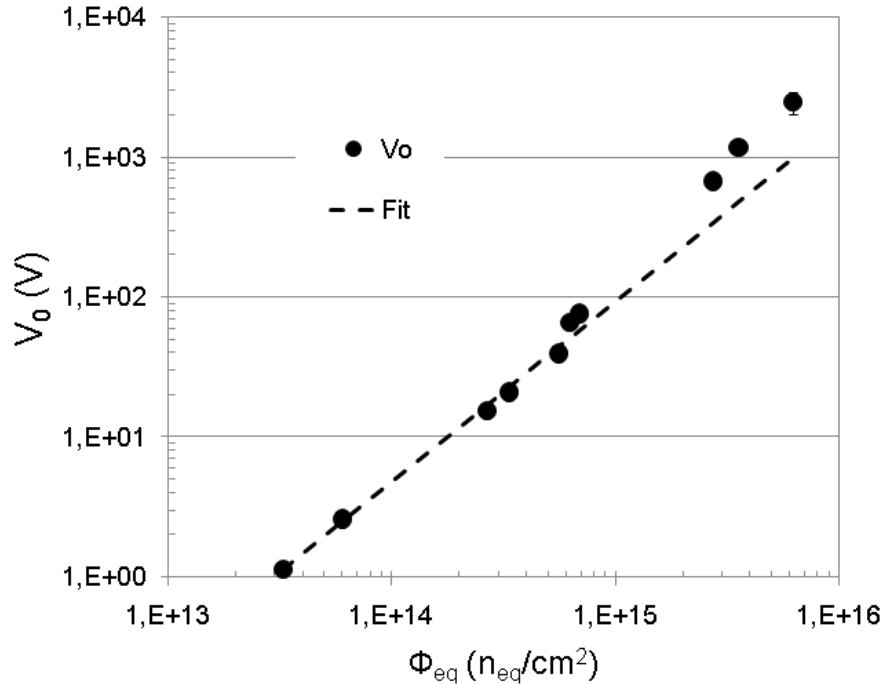


Figure 5.17: The value of the fitting parameter V_0 as a function of equivalent fluences.

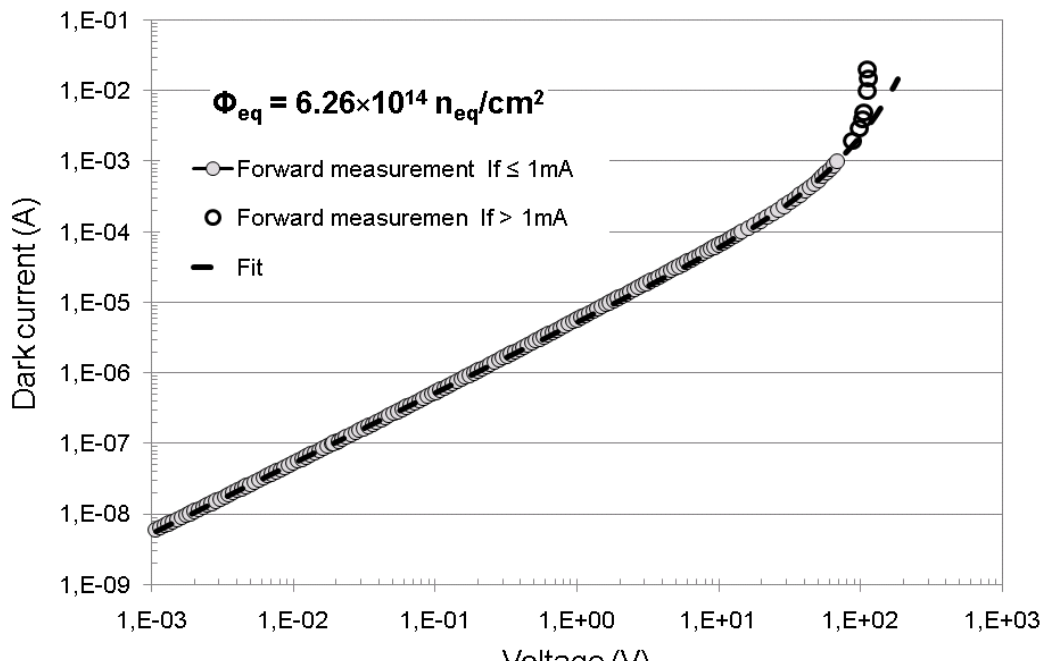
are the diode's active area and thickness which are equal to $70.225 \times 10^{-3} \text{ cm}^2$ and $3 \times 10^{-2} \text{ cm}$, respectively. As it can be observed here, the fitting parameter G_0 is not fluence dependent, contrary to [Jon99], where the G_0 values decrease versus fluence between $3.4 \times 10^{13} \text{ n}_{eq}/\text{cm}^2 \leq \Phi_{eq} \leq 2.5 \times 10^{14} \text{ n}_{eq}/\text{cm}^2$.

G_0 depends on the maximum resistivity of silicon (ρ). Since the latter one depends on carrier mobility and intrinsic carrier concentration as it is shown in Equation 5.16 temperature during measurement is stable enough, the value of ρ_{max} should be constant as it has been proven that the carrier mobilities in irradiated silicon do not vary versus fluences up to $2.4 \times 10^{14} \text{ n}_{eq}/\text{cm}^2$ [Bro02]. Contrary to G_0 , the fitting parameter V_0 is dependent on the radiation level as illustrated in Figure 5.17. The dependence of V_0 according to the equivalent fluence can be described by an empiric expression of the following form:

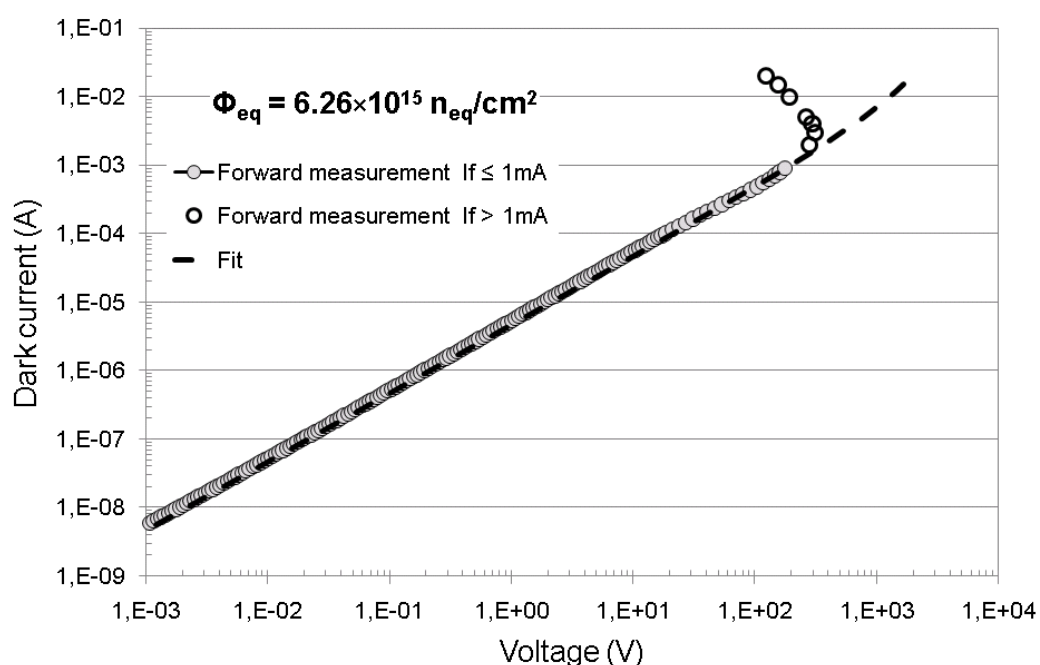
$$V_0 = \alpha \phi_{eq}^\beta \quad (5.21)$$

Here, the parameters α and β were found to be equal to $(4.27 \pm 0.37) \times 10^{-18} \text{ V.cm}^2$ and (1.289 ± 0.003) , respectively.

Forward I-V characteristics and fitting curves for $6.26 \times 10^{14} \text{ n}_{eq}/\text{cm}^2$ and $6.26 \times 10^{15} \text{ n}_{eq}/\text{cm}^2$ are presented in Figure 5.18.



(a)



(b)

Figure 5.18: Experimental forward characteristics and fitting curves (a) at $\Phi_{eq} = 6.26 \times 10^{14} n_{eq}/cm^2$ and (b) at $\Phi_{eq} = 6.26 \times 10^{15} n_{eq}/cm^2$ of BPW34FS diodes. Measurements were carried out at room temperature. Empty circles represent measurements at high injection levels where a deviation from the fitting curve can be observed.

As it is shown in this figure, the predicted I-V curves based on Equation (5.19) fit properly the experimental measurements. Nevertheless, at high injection levels ($I_F > 1\text{mA}$) experimental values deviate strongly from the fitting curves. A modification of the experimental I-V characteristics can be noted, since the voltage starts to bend back to lower values with increasing readout current injection. As described in previous sections, this phenomenon may occurs because at such high radiation levels, the PIN diode can exhibit a thyristor-like behavior and/or that it might be due to the self-heating effect. As a consequence, since silicon has a negative temperature coefficient, if the device is self heated by high current injection, the voltage would tend to lower values.

Taking into account Equation (5.19), when V is much lower than V_0 the exponential term tends towards 1; which means that the diode has an ohmic-like behavior since Equation (5.19) becomes equal to:

$$I = G_0 \times V = \frac{V}{R_0} \quad (5.22)$$

where R_0 is the maximum diode's resistance when the relaxation régime is established.

As the voltages increases and becomes higher than V_0 , the current grows exponentially.

For $\Phi_{eq} > 1 \times 10^{15} \text{n}_{eq}/\text{cm}^2$, and high injection current, voltages bend back to lower values and I-V curves are not govern anymore by the relaxation material equation. As a consequence, the value V_0 taken from the fitting curve of I-V characteristics (e.g. in Figure 5.18(b)) does not fit the data for very high fluences as it can be observed in Figure 5.17.

Since for such high radiation levels, this phenomenon appears at $I_F > 1 \text{ mA}$, one can assume that the prediction is not longer valuable for values in the discussed region (high injection level).

In addition it should be mentioned that for $\Phi_{eq} > 1 \times 10^{15} \text{n}_{eq}/\text{cm}^2$ and $I_F \leq 1 \text{ mA}$, the diode behaves like a resistor with maximum resistivity (see Equation 5.22). For this reason, it is not significant if the V_0 curve presented in Figure 5.17 does not fit properly with the data, since in this case the value V_0 has no influence on the forward response.

In the framework of the RadMON project [Rad], [Rav05a] at CERN, BPW34FS silicon PIN diodes are used as radiation monitoring sensors to follow on-line the evolution of the LHC fluence. For this reason, BPW34FS diodes are characterized and operated in forward bias. In this operation mode, it is more reliable to inject current and control voltage since in forward polarization, the current increases sharply versus voltage.

It is therefore convenient to have an expression of the forward voltage versus the readout current. From Equation (5.19), it can be obtained:

$$V = V_0 \times LambertW\left(\frac{I}{G_0 V_0}\right) \quad (5.23)$$

The *LambertW(x)* function [Cor96] is defined as the inverse function of:

$$f(x) = x \times \exp(x) \quad (5.24)$$

Finally, it can be stated that a new formulation for predicting the variation of the forward voltage versus Φ_{eq} based on the relaxation material theory when the diode is operated at readout current was obtain as:

$$V = \alpha \phi_{eq}^\beta \times LambertW\left(\frac{I}{G_0 \times \alpha \phi_{eq}^\beta}\right) \quad (5.25)$$

Thanks to this formulation, the radiation response of the OSRAM BPW34FS silicon p-i-n diode operated at constant readout current can be precisely predicted up to very high fluences with three parameters (G_0 , α and β). The *LambertW* function has previously been used to obtain the voltage-current dependence in Schottky barrier diode with inclusion of series resistance and shunt conductance as in solar cells [Ban00], [Hru06] and [Jun09].

However, to our best knowledge, in the work presented in this chapter, the formulation is used for the first time to predict the variation of the forward voltage versus fluence for irradiated silicon diodes. On the basis of the relaxation theory, it allows to predict OSRAM BPW34FS diode's radiation response for $\Phi_{eq} \geq 10^{13} n_{eq}/cm^2$ up to very high fluences and for all readout currents $I_F \leq 1mA$.

Figure 5.19 illustrates experimental and predicted values of the OSRAM BPW34FS silicon PIN diode versus Φ_{eq} , for all $\Phi_{eq} \geq 10^{13} n_{eq}/cm^2$ and for readout current $I_F \leq 1mA$. This current value is taken as the optimum maximum readout current before the device enters in unpredictable state.

5.5.4 Qualitative evaluation of the temperature dependence

The BPW34FS forward voltage versus equivalent fluence dependence for five different temperatures has been qualitatively evaluated in this study.

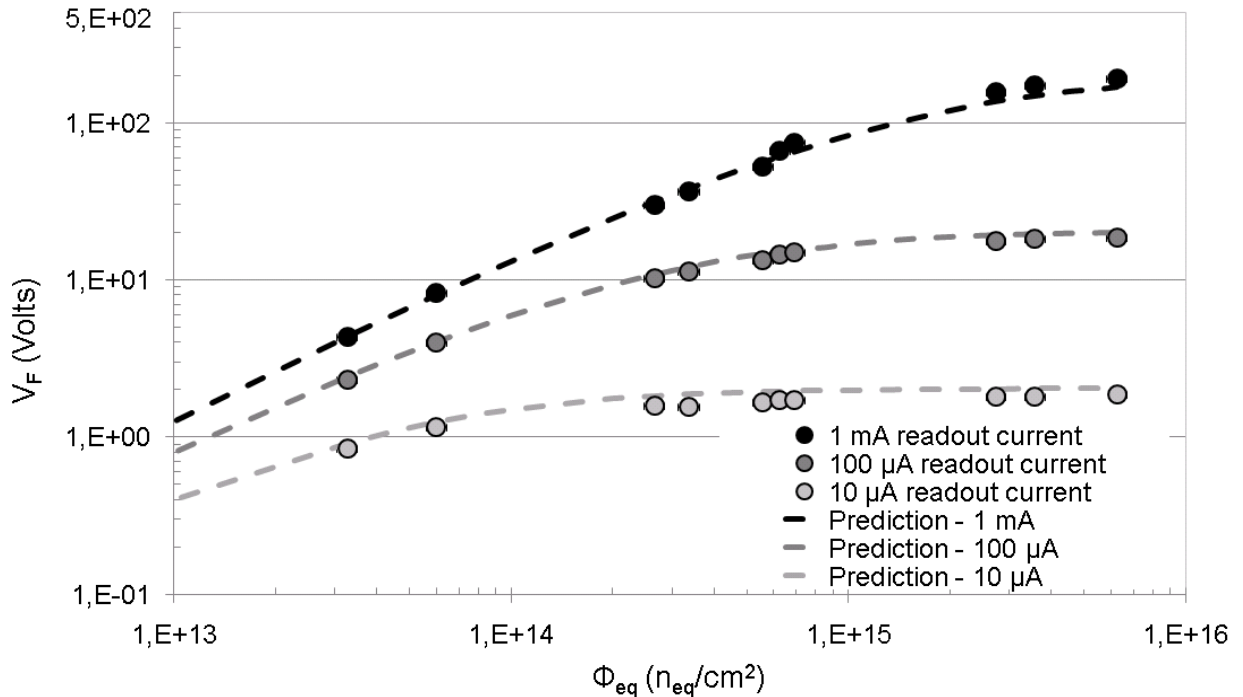


Figure 5.19: Experimental and predicted radiation responses of BPW34FS PIN diodes at room temperature for equivalent fluences higher than $10^{13} n_{eq}/cm^2$. The forward voltage was measured using different readout current of 50 ms duration.

The new approach to use BPW34FS Silicon PIN diodes as radiation monitoring sensors consists in operating the device with low readout current since at high injection level the diode radiation response is not stable enough. For this reason, an evaluation of the temperature dependence when BPW34FS diodes operated in high injection level would be not interesting for our application.

Moreover, measurements were carried out at low current injection level, since it has been shown that in this regime the irradiated BPW34FS PIN diode assumes a “relaxation-like” behavior that can be predicted.

The temperature dependence was studied operating the silicon PIN diode with 10 μ A and 100 μ A readout currents as it is illustrated in Figure 5.20 and Figure 5.21 respectively.

Since silicon PIN diode has a negative temperature coefficient, the forward voltage decreases as the temperature growth. Furthermore, it can be observed that at high irradiation levels the forward voltage becomes independent on radiation damage, since for different fluences V_F tends to saturate.

For example, as it is shown in Figure 5.20(b), measurements performed at -10 °C of irradiated diodes ($\Phi_{eq} > 1 \times 10^{14} n_{eq}/cm^2$) operated at $I_F = 10 \mu A$, reveal that the diode's forward response is fluence dependent since V_F increases versus equivalent fluences. Contrary, for measurement carried out at 30 °C, V_F remains constant.

This effect can be explained since at this temperature, the BPW34FS diode operated at 10 μA , is ohmic-like at already maximum silicon resistivity (see Figure 5.22). Therefore, for Φ_{eq} higher than around $10^{14} n_{eq}/cm^2$, the BPW34FS diode becomes no more sensitive to increasing radiation damage.

Results of the forward voltage measured at constant readout current versus equivalent fluence for different temperatures are shown in Figure 5.22.

As it can be seen in Figure 5.22(a), for $\Phi_{eq} > 1 \times 10^{14} n_{eq}/cm^2$ the forward voltage versus fluences remains constant or slightly increases. This observation indicates that in the temperature range from -10°C to 30°C at such injection level, the diode behaves like a resistance with a maximum resistivity near ρ_{max} .

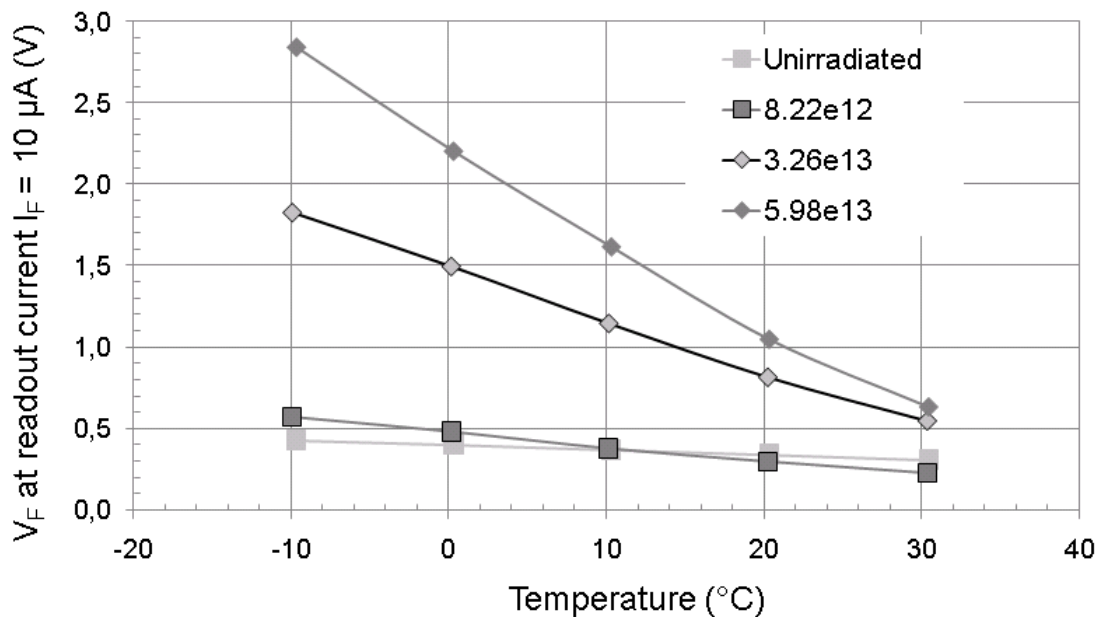
Nevertheless, it can be noticed that as the temperature decreases, V_F slightly rises up to higher fluences before saturating. It means that the maximum silicon resistivity increased at lower temperature.

The value of ρ_{max} changes with temperature since the intrinsic carrier concentration n_i is temperature dependent [Sze01].

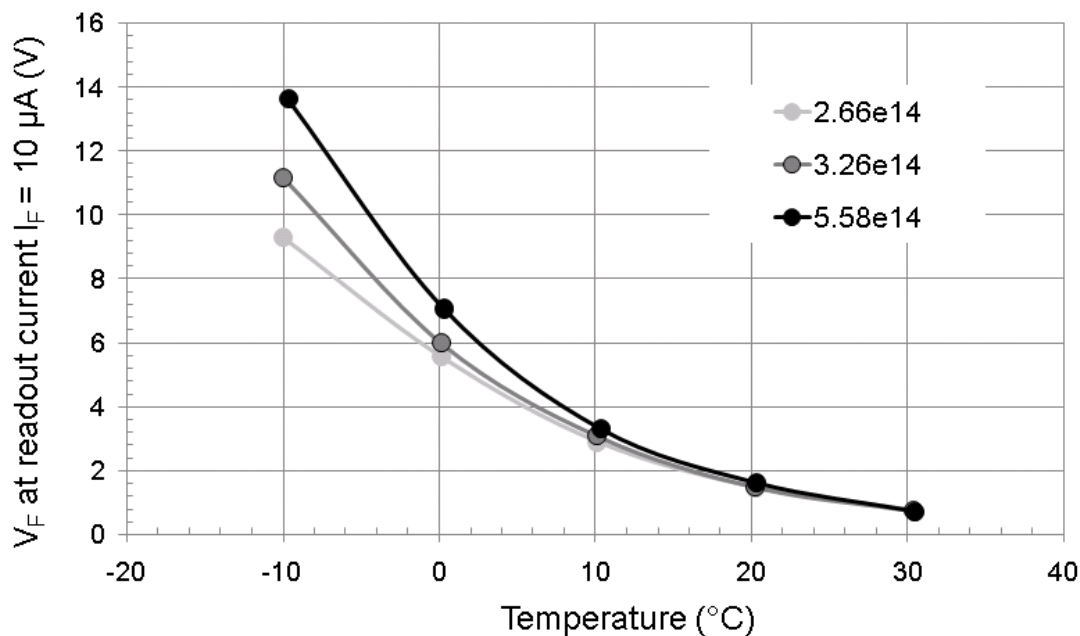
Therefore, at lower temperature, the maximum resistance of the BPW34FS will increase leading to an expanded upper-limit fluence range for the application of the diode as radiation monitor.

Same remarks can be made for Figure 5.22(b) when BPW34FS is operated at 100 μA . The major difference is that, at this readout current the Φ_{eq} at which the diode becomes not sensitive to radiation damage anymore (V_F saturation) is higher than the ones observed at $I_F = 10 \mu A$.

This means that the “ohmic-like” behavior of the relaxation regime extends to 100 μA at higher fluences (see discussion in section 5.5.2) and V_F saturates at higher fluences (when the diode is ohmic-like).



(a)



(b)

Figure 5.20: Temperature dependence on the BPW34FS diode forward voltage. Measurement have been performed at a readout current $I_F = 10 \mu\text{A}$ of 50 ms pulse duration for (a) $\Phi_{eq} \leq 5.98 \times 10^{13} \text{ n}_{eq}/\text{cm}^2$ and for (b) $\Phi_{eq} > 5.98 \times 10^{13} \text{ n}_{eq}/\text{cm}^2$. Each curve corresponds to a different Φ_{eq} as indicated in the legend.

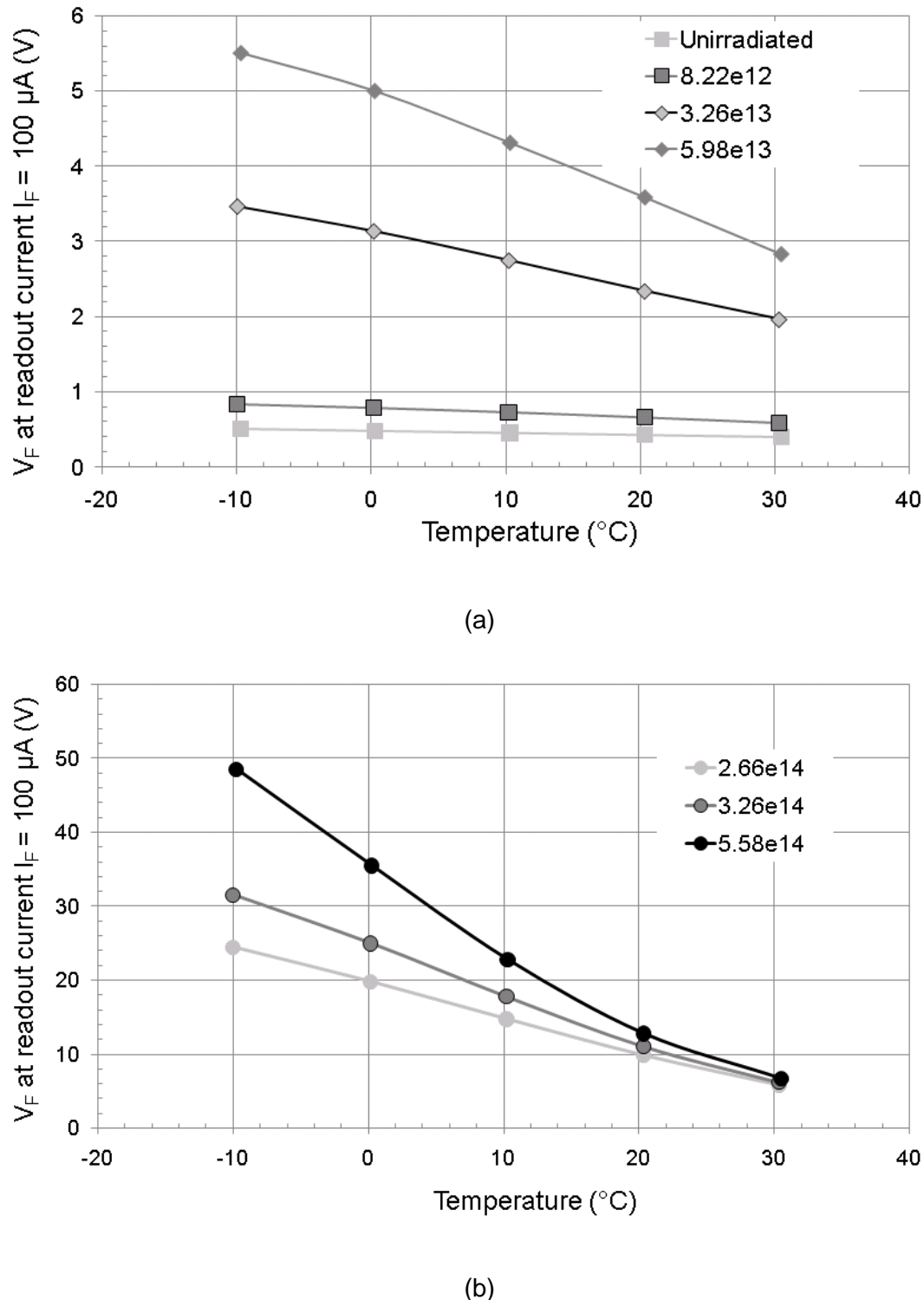
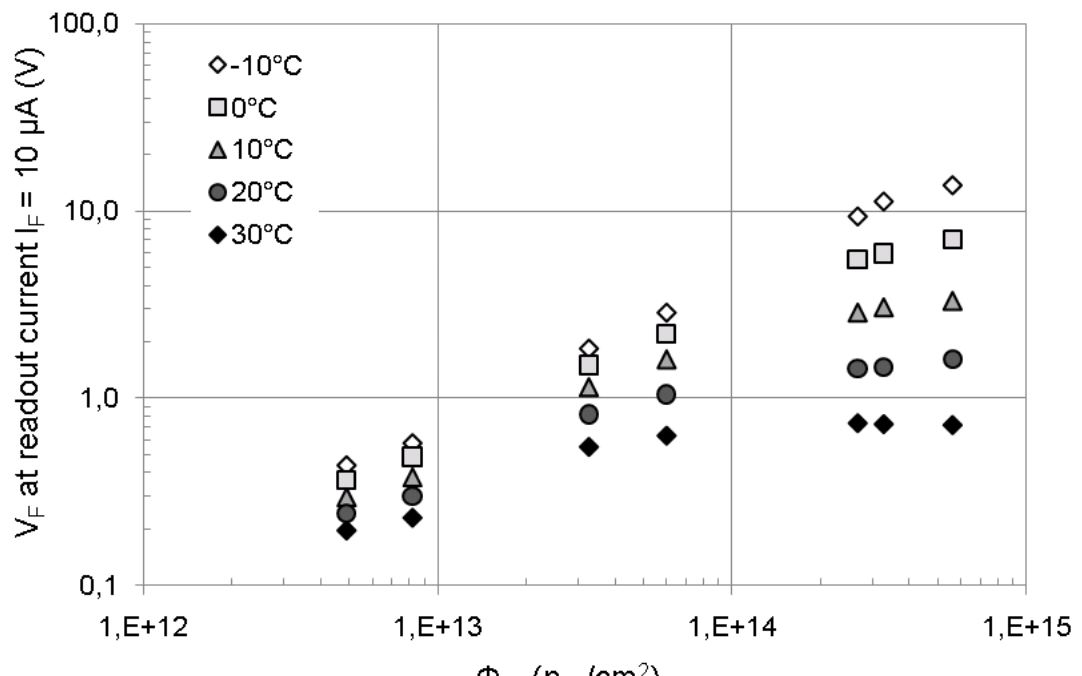
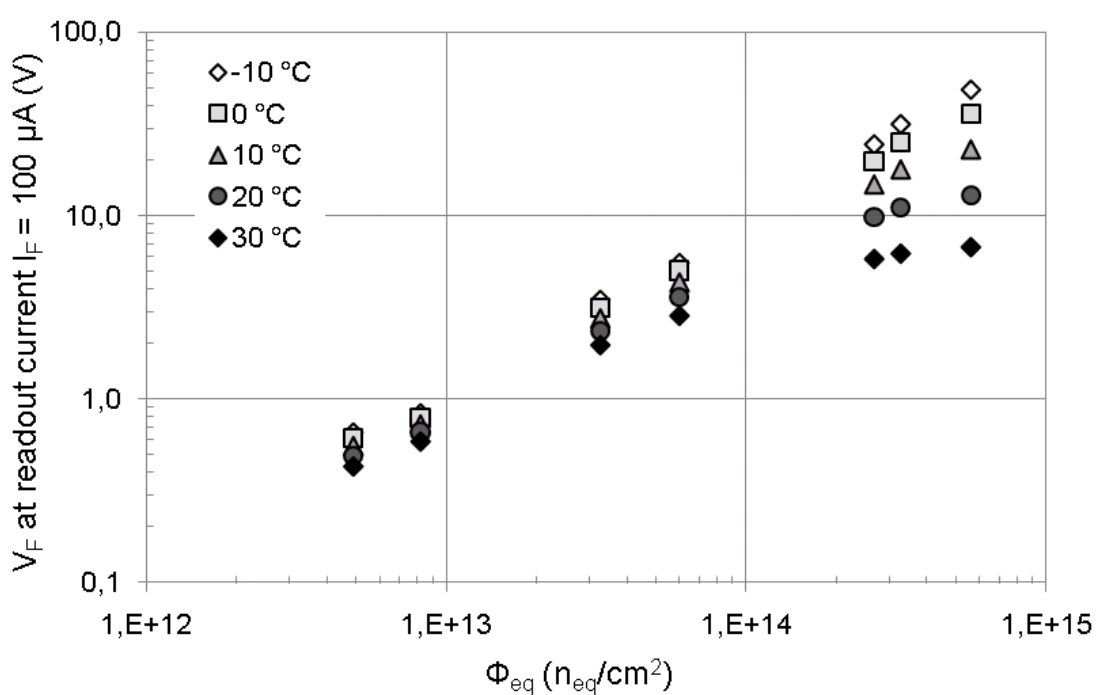


Figure 5.21: Temperature dependence on the BPW34FS diode forward current. Measurement have been performed at a readout current $I_F = 100 \mu\text{A}$ of 50 ms pulse duration for (a) $\Phi_{eq} \leq 5.98 \times 10^{13} \text{ n}_{\text{eq}}/\text{cm}^2$ and for (b) $\Phi_{eq} \geq 5.98 \times 10^{13} \text{ n}_{\text{eq}}/\text{cm}^2$. Each curve corresponds to a different Φ_{eq} as indicated in the legend.



(a)



(b)

Figure 5.22: Experimental response of BPW34FS PIN diodes at five different temperatures: -10°C , 0°C , 10°C , 20°C and 30°C . The forward voltage was measured at (a) $10 \mu\text{A}$ and (b) $100 \mu\text{A}$ readout current pulse of 50 ms duration.

In addition, it should be mentioned that an investigation of the temperature dependence on complete forward and reverse I-V characteristics, from -40°C to 20°C is still in progress. Since such time extensive study went beyond the timeframe of this thesis, this work will be addressed in a future dedicated paper.

5.6 Conclusion

In this chapter, effects of radiation damage up to $6.3 \times 10^{15} \text{ n}_{\text{eq}}/\text{cm}^2$ on the OSRAM BPW34FS commercial p-i-n diodes response have been studied.

BPW34FS silicon PIN diodes are already used as radiation sensors in LHC experiments, where detectors are exposed to radiation level up to few $10^{14} \text{ n}_{\text{eq}}/\text{cm}^2$. In order to use them for monitoring Super-LHC fluences, a new approach to characterize the diode's radiation response at high fluences has been presented.

From previous and preliminary studies it has been shown that the diode should be operated at low readout current, since it allows avoiding "thyristor-like" behavior and self-heating effect which occur at high fluences.

For a better understanding of the PIN diode's behavior, a comparison with relaxation material has been achieved since the silicon becomes semi-insulating with high-resistivity after radiation damage.

From this theory, it was possible to derive a function allowing to fit experimental I-V curves at room temperature for $\Phi_{\text{eq}} \geq 10^{13} \text{ n}_{\text{eq}}/\text{cm}^2$ at forward readout current $I_F \leq 1 \text{ mA}$. From the evaluation of the fits to the different I-V curves, a new formulation to predict the variation of the forward voltage versus equivalent fluence at room temperature has been developed.

In addition, its temperature dependence at constant readout current was qualitatively evaluated. It revealed that the upper limit of the fluence's measurement range can be expanded by measuring the p-i-n diodes at lower temperature. A more comprehensive investigation on the temperature dependence of I-V characteristics with the aim to integrate the temperature as a parameter into the parameterization of the diode voltage response is under way and will be subject to a later paper.

In summary, a new approach for characterizing and predicting the radiation response of the OSRAM BPW34FS silicon p-i-n diode has been developed. It is established on the relaxation material theory which allows a deep understanding of the physics principles underlying the radiation induced changes of the PIN diode characteristics. It allows to extend the existing readout protocol with only one readout current ($I_F = 1 \text{ mA}$), to a multitude of possibilities

depending on the user requirements and permits to predict diode's radiation response to monitor expected Super-LHC fluences.

Chapter 6

Perspectives and outlook on future studies

As discussed in Chapter 2, particle fluences over 10-years in LHC experiments will cover a wide range from 10^9 - 10^{10} to 10^{14} - 10^{15} n_{eq}/cm^2 (10^{16} n_{eq}/cm^2 for the Super-LHC). In Chapter 5 and in previous studies [Rav04], [Rav06], [Rav08b], it has been shown that OSRAM BPW34FS silicon PIN diodes can be used for monitoring LHC and Super-LHC fluences from 2×10^{12} n_{eq}/cm^2 to equivalent fluences higher than 1×10^{15} n_{eq}/cm^2 . Nevertheless, this type of diode is not sensitive to radiation damage for $\Phi_{eq} < 2 \times 10^{12}$ n_{eq}/cm^2 .

However, the BPW34FS silicon PIN diodes can be brought immediately to their operation point (where the device starts to be sensitive) by pre-irradiating them to a Φ_{eq} level of 2×10^{12} n_{eq}/cm^2 [Rav08b]. With this pre-irradiation method, the fluence measurement range can be extended starting from about 8×10^9 n_{eq}/cm^2 without altering the diode sensitivity for the higher fluence range [Rav05a]. Another type of diode which is manufactured from the *Center for Medical Physics* (CMRP) [Ros03] of the university of Wollongong, Australia, is already used at CERN for monitoring very low fluences which reveals a linear sensitivity dependence of 1.7×10^8 cm^{-2}/mV when Φ_{eq} is lower than 2×10^{12} n_{eq}/cm^2 [Rav06]. Nevertheless this device is quiet expensive as it cost around 120 CHF per piece.

For monitoring the full fluence range as it can be encountered in LHC experiments, other devices are needed. Moreover, with the intention to develop our specific dosimeter in terms of geometry and material, an investigation carried out on the radiation response of custom made devices has been performed during this thesis and is presented in this chapter.

In this work, the first batch of devices investigated is “silicon detector” made with a very high resistivity (several $k\Omega \cdot cm$) n-type bulk. These detectors are manufactured by different research institutes such as in our case; the Helsinki Institute of Physics (HIP), Finland, and the Centro National de Microelectronica (CNM), Barcelona, Spain.

The second type of devices evaluated consists of two Czechoslovak silicon PIN diodes used as dosimeters and made with different geometries, which are distributed by the Czech Metrology Institute of Praha, Czech Republic. This type of diodes are named “Long Base Silicon Diode” (LBSD) SI1 and SI2.

6.1 Silicon detectors

Different silicon detectors have been investigated for this study. They are made from two different research institutes, with different materials and geometries.

Radiation studies have been performed by exposing the detectors to the $24\text{GeV}/c$ proton beam of the IRRAD1 facility, with fluences ranging from about 2.9×10^9 up to $3.4 \times 10^{14} n_{eq}/cm^2$.

After a brief description of the different growth techniques for monocrystalline silicon (with the specific interest of the material used in this work), results for irradiated silicon detectors are presented and discussed.

6.1.1 Silicon growth method

The manufacturing of silicon detectors used for high energy physics experiments (HEP) required two main conditions: High resistivity and high minority carrier lifetime [Mol99].

The main techniques for growing silicon detector are the Float Zone (FZ) and the Czochralski (Cz) method (see the next sub-sections).

Together with the demand for a reasonable price and a homogeneous resistivity distribution, not only over a single wafer, but also over the whole ingot, Float Zone is the best choice of material and therefore mainly used for detector applications nowadays, as for instance in LHC experiments.

In the research field of “Radiation hardening” and in order to perform radiation test on different materials, other silicon growth techniques have been used. The Rose Collaboration [ROSE] proved that an elevated concentration of oxygen in the silicon bulk improve the radiation hardness of particle detectors with respect to the depletion voltage, when they are irradiated by charged particles [Bat06]. From this statement, Cz and Magnetic Cz (MCz) silicon are being

studied and characterized for HEP detectors since both have a higher concentration in oxygen than FZ silicon.

This work has been mainly performed by the RD50 collaboration [RD50] which studied the radiation hard detectors for very high luminosity colliders.

For a detailed description of these silicon growth techniques, the reader is referred to [Mol99] and [Lin94]. Only a short review of the two main methods is given in this section.

6.1.1.1 Float zone silicon (FZ)

Almost all the silicon detectors currently used in HEP experiments are made from silicon produced by the Float Zone growth method. It is based on the zone melting principle and was invented by Theurer in 1962 [The62].

This growth technique passes a radio frequency (RF) coil up a vertical rod of polysilicon under vacuum or in an inert gaseous atmosphere. The RF coil melts a section of the rod and any impurities are kept on the molten side of the solid/liquid phase transition as the region re-solidifies. The silicon re-solidifies as crystalline silicon. The typical oxygen concentration of FZ silicon is of the order of a few 10^{16} cm^{-3} [Bat06].

6.1.1.2 Magnetic Czochralski silicon (MCz)

The Czochralski method is named after J. Czochralski [Czo18], who determined the crystallization velocity of metals by pulling mono and polycrystals against gravity out of a melt which is held in a rotating quartz crucible.

The Magnetic Czochralski method is the same as the Cz method except that it is carried out within a strong horizontal or vertical magnetic field.

The presence of a magnetic field during the process of MCz silicon affects the melt flow in the crucible leading to different impurity (oxygen) distribution in the ingot and therefore can modify the properties of the resultant Cz silicon which becomes MCz. During this process, the quartz crucible dissolves into the melt giving an oxygen concentration up to the solid solubility of oxygen in Silicon [Bat06].

High resistivity MCz silicon has typically an oxygen concentration of $2\text{-}5 \times 10^{17} \text{ cm}^{-3}$. With such a high concentration, the radiation tolerance of MCz silicon detectors is expected to be improved compared to standard FZ silicon.

Since MCz silicon has higher oxygen concentration, care has to be taken to avoid thermal donor (TD) creation during the growth process as it affects the effective doping concentration [Har03]. Moreover, TD generation is strongly dependent on the oxygen concentration present in the material.

Producer	Series name	Material	Active area (mm ²)	Thickness (μm)
HIP	HIP-003-C42	MCz	2.5 × 2.5	300
HIP	HIP-002-C1	FZ	2.5 × 2.5	300
CNM	CNM-009-32	FZ	5 × 5	1000
CNM	CNM-009-S01	FZ	2.5 × 2.5	1000

Table 6.1: Investigated silicon detectors made from two different research institutes (HIP and CNM) with different geometries. FZ and MCz silicon detectors with different geometries have been studied here.

There is a real motivation for studying MCz silicon as another option for particle detectors in future HEP experiments. Nevertheless its fabrication procedure is more complicated, because it is difficult to control the TD production during the process.

6.1.2 Investigated silicon detectors

Tested devices are p⁺-n silicon detectors produced by CNM and HIP. The detectors investigated during this study were made from n-type FZ and MCz silicon wafers. The geometry dependence on the detector's radiation response has been evaluated from different silicon detectors.

CNM and HIP detectors have an active area of (2.5 × 2.5) mm² or (5 × 5) mm². The active area of each silicon detectors is surrounding by a p⁺ guard ring. Two detector thicknesses have been considered in this work: 300 μm and 1000 μm. Geometry and material for each detector are given in Table 6.1.

After 24 GeV/c proton irradiations performed in the IRRAD1 facility, silicon detectors have been measured at room temperature using the setup described in section 5.3 and have been operated with the readout protocol presented in section 5.4.1, which means by injecting forward current ranging from 10 μA to 25 mA with 50 ms pulse duration. In all figures presented in this section, for a better visibility, only few measurements performed at different currents are shown.

6.1.3 Comparison between MCz and FZ silicon detectors

Figure 6.1 shows the radiation response of the HIP-003-C42 and HIP-002-C1 silicon detectors, which are respectively MCz and FZ detectors with an identical geometry. Results for both silicon detectors operated at 1 mA and 25 mA are presented in Figure 6.1(a), while measurements performed at 100 µA and 1 mA readout current are illustrated in Figure 6.1(b).

As it can be observed in this figure, these types of detectors are not sensitive to radiation damage up to around $1 \times 10^{12} n_{eq}/cm^2$. In addition, it can be mentioned that both silicon detectors have almost the same geometry as the commercial OSRAM BPW34FS silicon PIN diode that is a 300 µm base thickness with an active area equal to $2.65 \times 2.65 mm^2$ for the BPW34FS diode and $2.5 \times 2.5 mm^2$ for both silicon detectors. For this reason, one can assume that the radiation response of these types of silicon detectors should not be totally different from the BPW34FS diode (see Chapter 5). On the other hand, the material from which the silicon detectors have been made is different and might influence their sensitivity.

As for the BPW34FS diode, the calibration factor $1/c$ which links the variation of the forward voltage with the equivalent fluence (see Equation 6.1) has been evaluated for both detector types at readout currents illustrated in Figure (6.1).

$$\Delta V_F = c \times k \times \phi = c \times \phi_{eq} \quad (6.1)$$

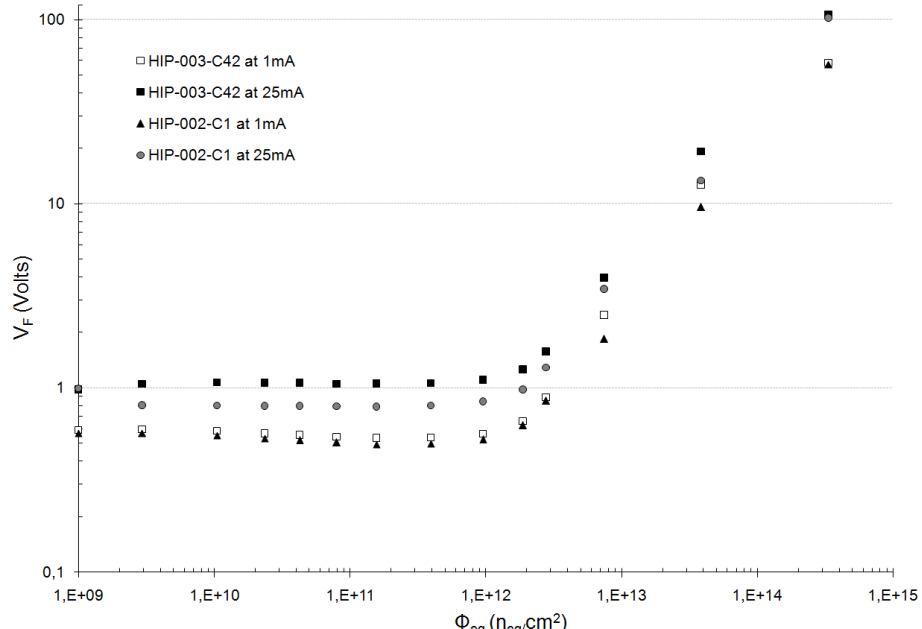
Results are summarized in Table 6.2.

From this table, data show that the sensitivity to radiation damage of both silicon materials is on the same order of magnitude and very close to each other. However, the MCz material reveals a highest sensitivity, since for 1 mA and 25 mA readout currents, its calibration factor ($1/c$) is slightly lower. Nevertheless, one can assume that the sensitivity to radiation damage is not considerably increased by using oxygenated material.

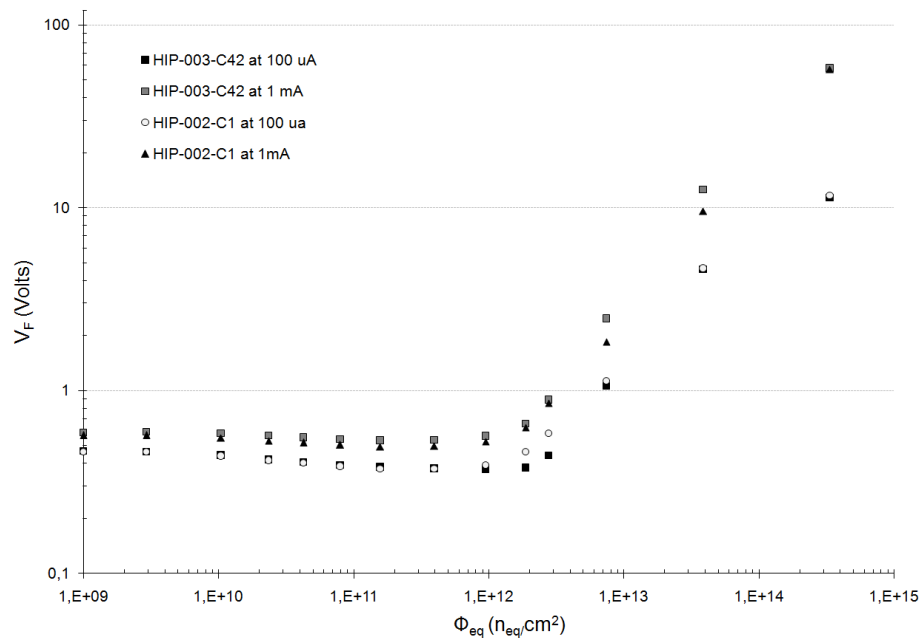
In addition, both sensitivities of silicon detectors and commercial BPW34FS silicon PIN diode are compared. Results show that their sensitivity is on the same order of magnitude. However, silicon detectors are slightly more sensitive than the commercial PIN diode.

As mentioned previously, both devices start to be sensitive to radiation damage at a $\Phi_{eq} \approx 1 \times 10^{12} n_{eq}/cm^2$.

From experimental curves, it is possible to estimate the upper limit of the fluence measurement range, where the detector response is still linear versus fluence.



(a)



(b)

Figure 6.1: Radiation response of the HIP-003-C42 (MCz) and HIP-002-C1 (FZ) after 24 GeV/c proton irradiations. The diode's forward voltages measured at (a) 1 mA and 25 mA and (b) 100 μ A and 1 mA are plotted versus Φ_{eq} . The width of the readout current pulse was set to 50 ms. Both devices have a 2.5×2.5 mm 2 active area, and a thickness of 300 μ m.

Readout current	1/c (MCz)	1/c (FZ)	1/c (BPW)
100 μ A	$9.1 \times 10^9 \text{ cm}^{-2}/\text{mV}$	$9.1 \times 10^9 \text{ cm}^{-2}/\text{mV}$	$1.7 \times 10^{10} \text{ cm}^{-2}/\text{mV}$
1 mA	$3.3 \times 10^9 \text{ cm}^{-2}/\text{mV}$	$4.2 \times 10^9 \text{ cm}^{-2}/\text{mV}$	$9.1 \times 10^9 \text{ cm}^{-2}/\text{mV}$
25 mA	$2 \times 10^9 \text{ cm}^{-2}/\text{mV}$	$2.3 \times 10^9 \text{ cm}^{-2}/\text{mV}$	$6.7 \times 10^9 \text{ cm}^{-2}/\text{mV}$

Table 6.2: Summary of the sensitivity to radiation damage for 300 μ m thick MCz, FZ silicon detectors and commercial BPW34FS silicon PIN diode which have been irradiated with 24 GeV/c proton beam. For both silicon detectors, the active area is of $2.5 \times 2.5 \text{ mm}^2$. The active area of the BPW34FS PIN diode is of about $2.65 \times 2.65 \text{ mm}^2$.

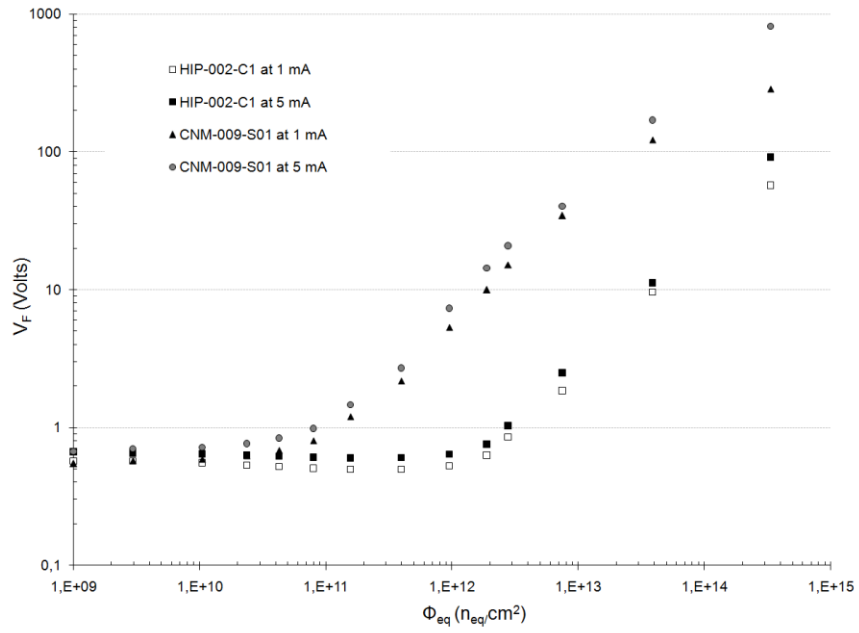
For both devices, it can be observed that the forward voltage saturates for an equivalent fluence of $3.4 \times 10^{14} \text{ n}_{\text{eq}}/\text{cm}^2$, when detectors are operated at 100 μ A readout current (see Figure 6.1(b)). Therefore a maximum Φ_{eq} range of few $10^{14} \text{ n}_{\text{eq}}/\text{cm}^2$ has been evaluated.

At such high fluences one can consider that for these types of detectors the relaxation regime is already established, since the V_F saturation indicates that the device is ohmic-like.

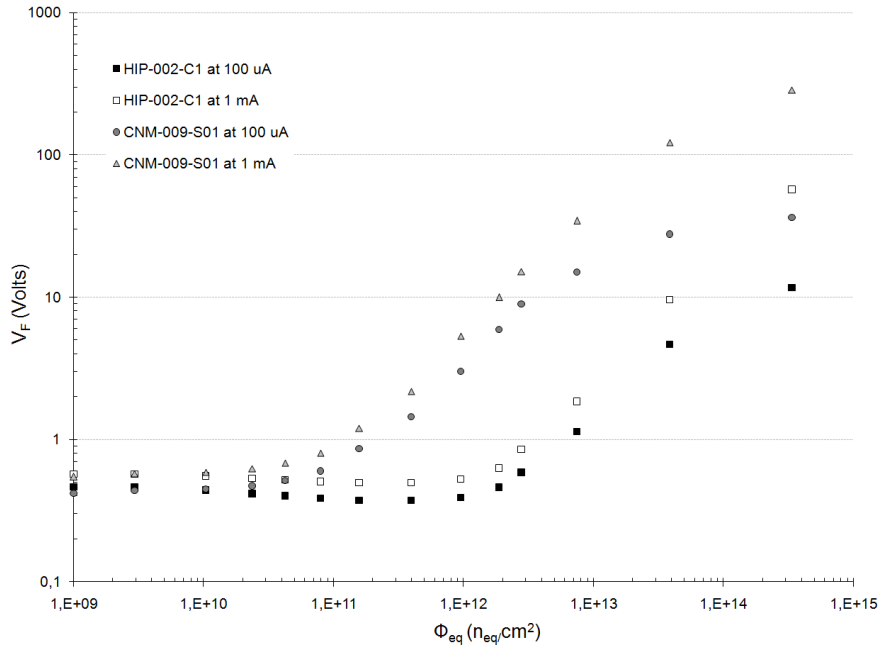
6.1.4 Influence of the detector thickness

In addition, an investigation of the thickness influence on the detector's radiation response has been carried out in this study. Two types of FZ silicon detectors from CNM and HIP have been compared. Detectors have an identical active area ($2.5 \times 2.5 \text{ mm}^2$) and different thicknesses. The variation of the forward voltage versus equivalent fluence for 1000 μ m (CNM-009-S01) and 300 μ m (HIP-002-C1) thick silicon detectors have been evaluated. Figure 6.2 shows the experimental data taken for both types of silicon detectors operated (a) at 5 mA and 1 mA, (b) at 100 μ A and 1 mA readout currents, after 24 GeV/c proton irradiations.

As remarked for HIP-002-C1 in previous section, at low fluence CNM-009-S01 is not sensitive to radiation damage since the forward voltage remains constant versus fluence.



(a)



(b)

Figure 6.2: Radiation response of the HIP-002-C1 ($300\ \mu m$) and CNM-009-32 ($1000\ \mu m$) after 24 GeV/c proton irradiations. The diode's forward voltages measured at (a) 1 mA and 5 mA and (b) $100\ \mu A$ and 1 mA are plotted versus Φ_{eq} . The width of the readout current was of 50 ms. Both devices are FZ silicon with an active area of $2.5 \times 2.5\ mm^2$.

Readout current	1/c (300 µm)	1/c (1000 µm)
100 µA	$9.1 \times 10^9 \text{ cm}^{-2}/\text{mV}$	$3.2 \times 10^8 \text{ cm}^{-2}/\text{mV}$
1 mA	$4.2 \times 10^9 \text{ cm}^{-2}/\text{mV}$	$1.9 \times 10^8 \text{ cm}^{-2}/\text{mV}$
5 mA	$3.3 \times 10^9 \text{ cm}^{-2}/\text{mV}$	$1.4 \times 10^8 \text{ cm}^{-2}/\text{mV}$

Table 6.3: Summary of the sensitivity to radiation damage for 300 µm and 1000 µm FZ silicon detectors which have been irradiated with 24 GeV/c proton beam. For both devices, the active area is identical ($2.5 \times 2.5 \text{ mm}^2$)

However, it can clearly be noted that contrary to the 300 µm thick detector, which is not sensitive up to around $1 \times 10^{12} \text{ n}_{\text{eq}}/\text{cm}^2$, the 1000 µm thick silicon detectors start to be sensitive to radiation damage at around $2 \times 10^{10} \text{ n}_{\text{eq}}/\text{cm}^2$.

As in the previous section, the calibration factor (1/c) has been evaluated from the experimental curves presented in Figure 6.2 and are presented in Table 6.3. The thicker detector reveals the highest sensitivity to radiation damage which is around 25 times greater than the one observed for the 300 µm thick detector.

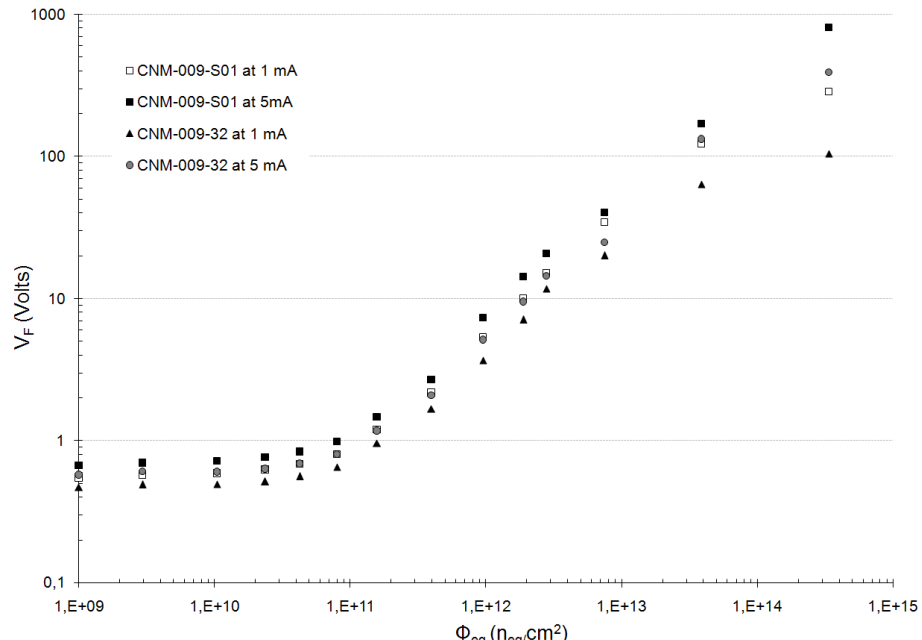
However, the maximum Φ_{eq} range observed for the 1000 µm thick detector is lower than for the 300 µm, since the forward voltage of the CNM-009-32 silicon detector starts to saturate at an equivalent fluence of few $10^{12} \text{ n}_{\text{eq}}/\text{cm}^2$.

Finally, in this work the influence of the detector active area have been evaluated and discussed in the next section.

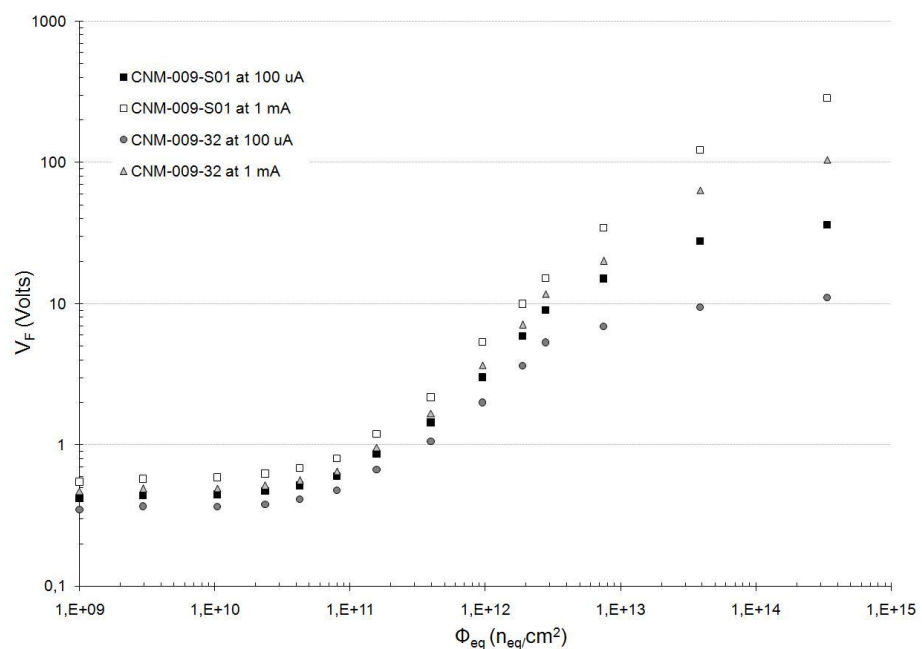
6.1.5 Influence of the active area

Comparison has been performed between 1000 µm thick FZ silicon detectors from CNM made with different active areas.

The investigated active areas were $5 \times 5 \text{ mm}^2$ and $2.5 \times 2.5 \text{ mm}^2$ for the CNM-009-32 and CNM-009-S01 silicon detectors respectively. Results are presented in Figure 6.3 for both devices operated at (a) 5 mA and 1 mA, (b) 1 mA and 100 µA readout currents.



(a)



(b)

Figure 6.3: Radiation response of CNM-009-S01 (active area = $2.5 \times 2.5 mm^2$) and CNM-009-32 (active area = $5 \times 5 mm^2$) after 24 GeV/c proton irradiations. The diode's forward voltages measured with a 50 ms readout current of (a) 1 mA and 25 mA and (b) 100 μ A and 1 mA are plotted versus Φ_{eq} . Both devices are 1000 μ m thick FZ silicon detectors.

Readout current	$1/c (2.5 \times 2.5 \text{ mm}^2)$	$1/c (5 \times 5 \text{ mm}^2)$
100 μA	$3.2 \times 10^8 \text{ cm}^{-2}/\text{mV}$	$5.6 \times 10^8 \text{ cm}^{-2}/\text{mV}$
1 mA	$1.9 \times 10^8 \text{ cm}^{-2}/\text{mV}$	$2.5 \times 10^8 \text{ cm}^{-2}/\text{mV}$
5 mA	$1.4 \times 10^8 \text{ cm}^{-2}/\text{mV}$	$2 \times 10^8 \text{ cm}^{-2}/\text{mV}$

Table 6.4: Summary of the sensitivity to radiation damage for ($2.5 \times 2.5 \text{ mm}^2$) and ($5 \times 5 \text{ mm}^2$) FZ silicon detectors which have been irradiated with 24 GeV/c proton beam. For both devices, the thicknesses are identical (1000 μm).

On the one hand, as discussed in previous section, increasing the detector thickness makes the device more sensitive at lower fluence. On the other hand, the variation of the active area does not modify the fluence range of measurement (where the detector response is linear versus Φ_{eq}). For both detector types, the radiation sensitivity starts around $\Phi_{\text{eq}} \approx 2 \times 10^{10} \text{ n}_{\text{eq}}/\text{cm}^2$ and the shape of the forward voltage change from a linear increase to a saturation versus Φ_{eq} around few $10^{12} \text{ n}_{\text{eq}}/\text{cm}^2$.

As for the previous section, the comparison between both detectors is based on the evaluation of their sensitivity at different readout currents. Results are presented in Table 6.4 for silicon detectors operated at 100 μA , 1 mA and 5 mA. From this, it can be notified that the sensitivity is increased by a factor of about 1.5 in average, when the active area is reduced by 4. Compare to the sensitivity variation observed when the device thickness is increased (see previous section), this slight sensitivity enhancement is negligible.

In summary, it has been clearly shown that the main parameter which influences the silicon detector's radiation response in terms of sensitivity and fluence measurement range is the thickness.

6.2 LBSD silicon PIN diodes

The LBSD silicon PIN diodes have been manufactured by the Institute for Research, Production and Application of Radioisotopes (IRPAR) in Prague [Pro89]. The type LBSD-SI1 is a 1.2 mm thick silicon PIN diode with an active area of about $1.8 \times 1.8 \text{ mm}^2$, while the type LBSD-

SI2 is a silicon PIN diode with a base length of 2.5 mm and an active area of about $2 \times 2 \text{ mm}^2$. These devices were prepared by ion implantation of boron and phosphorus into the n-type silicon single crystal using the Float Zone (FZ) growth technique. The initial resistivity of the diode is about $100 \Omega\cdot\text{cm}$. A complete list of technical parameters for both LBSD-SI1 and LBSD-SI2 devices is available in [Rav06].

As for the preliminary study performed on the detector's radiation response made with different geometries and materials, a comparison between the two device geometries has been carried out for the LBSD diodes. It is based on the evaluation of their radiation sensitivity and fluence measurement range. As for silicon detectors, diodes were operated at different readout currents ranging from $10 \mu\text{A}$ to 25 mA .

Figure 6.4 shows the radiation response of (a) LBSD-SI1 and (b) LBSD-SI2. Not all the measurements are shown in this figure, for a better visibility.

From data, it can be observed that, for both types of silicon PIN diodes, when devices are operated at $100 \mu\text{A}$ and $10 \mu\text{A}$ (not shown in Figure 6.4) readout currents, the devices are not sensitive to radiation damage, since the forward voltage does not vary versus equivalent fluence,

From the experimental curves presented in Figure 6.4, it is possible to evaluate the fluence measurement range for both devices which is the maximum Φ_{eq} at which the forward voltage response still follows a linear behavior versus fluence. From [Rav06], a Φ_{eq} range of about $1 \times 10^{12} \text{ n}_{\text{eq}}/\text{cm}^2$ and $2 \times 10^{11} \text{ n}_{\text{eq}}/\text{cm}^2$ has been determined for the type LBSD-SI1 and LBSD-SI2 diodes respectively. For LBSD-SI2 diode, this result is in good agreement with the maximum Φ_{eq} range evaluated from Figure 6.4(b), which is around $1 \times 10^{11} \text{ n}_{\text{eq}}/\text{cm}^2$. This value is an estimation based on the determination of the maximum Φ_{eq} range in [Rav06], which is more precise (since there is more measurements), and experimental data from this study, where there is no measurements between $8.4 \times 10^{10} \text{ n}_{\text{eq}}/\text{cm}^2 \leq \Phi_{\text{eq}} \leq 3.2 \times 10^{11} \text{ n}_{\text{eq}}/\text{cm}^2$.

From the evaluation of experimental data show in Figure 6.4(a), the variation of forward voltage versus Φ_{eq} of diode type SI1 is linear up to around $4 \times 10^{11} \text{ n}_{\text{eq}}/\text{cm}^2$. At Φ_{eq} higher than this value ($\Phi_{\text{eq}} = 8.1 \times 10^{11} \text{ n}_{\text{eq}}/\text{cm}^2$ from Figure 6.4(a)), the forward response versus fluence is not linear anymore. As mentioned above, from the study carried out by Ravotti, this value is expected to be at $\Phi_{\text{eq}} \approx 1 \times 10^{12} \text{ n}_{\text{eq}}/\text{cm}^2$. Therefore, taking into account both observations, the Φ_{eq} range will be considered smaller than $8 \times 10^{11} \text{ n}_{\text{eq}}/\text{cm}^2$ in this study.

On Figure 6.4, the radiation sensitivity where V_F versus Φ_{eq} still follows at linear behavior for both types of silicon PIN diodes operated at different readout currents from 1 mA to 25 mA have been evaluated and summarized in Table 6.5.

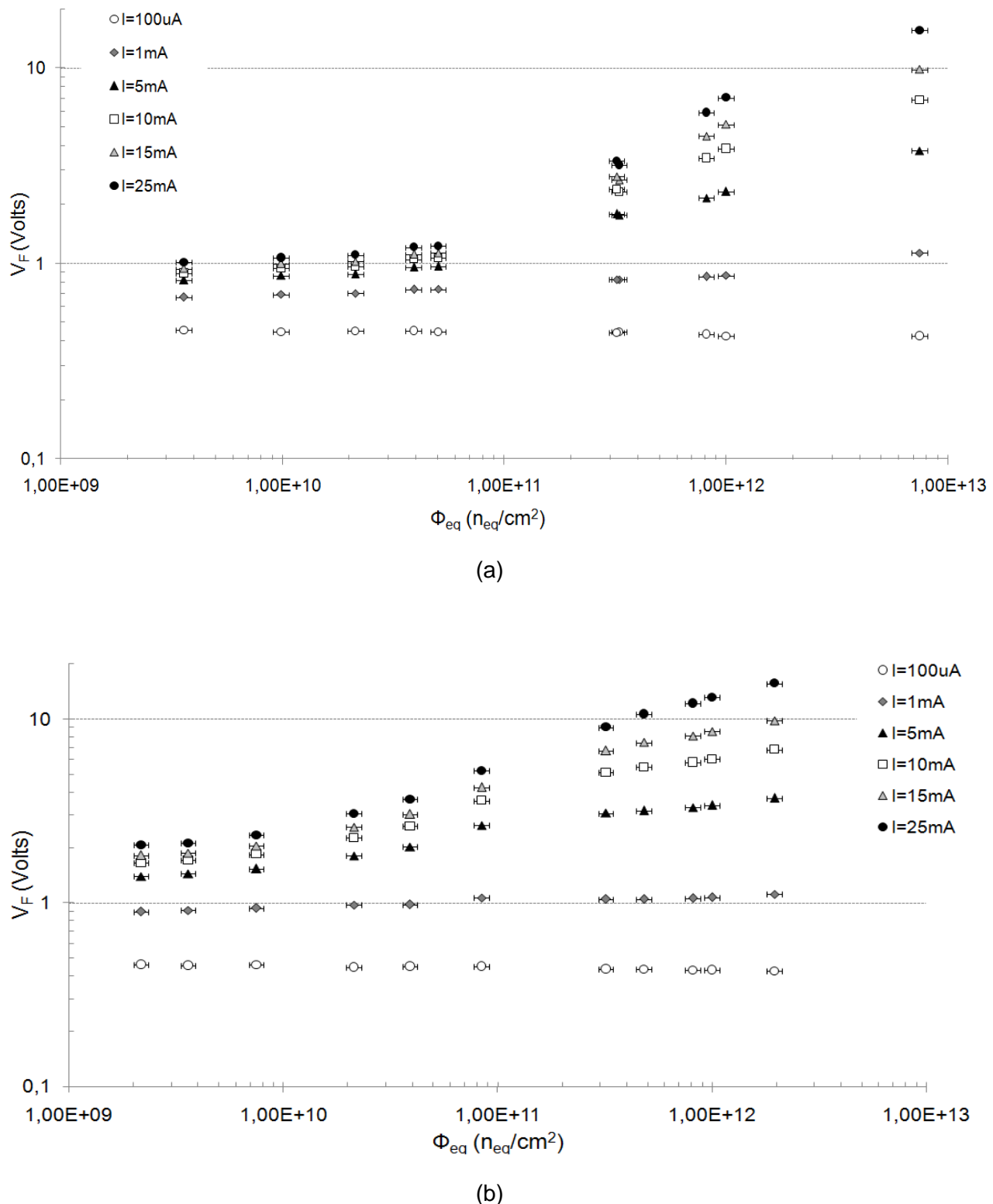


Figure 6.4: Radiation response of LBSD diodes (a) type SI1 and (b) type SI2 after 24 GeV/c proton irradiations. Diodes were operated at different readout currents from 10 μ A to 25 mA.

Readout current	1/c (SI1)	1/c (SI2)
1 mA	$(2.5 \pm 0.31) \times 10^9 \text{ cm}^{-2}/\text{mV}$	$(5.4 \pm 0.65) \times 10^8 \text{ cm}^{-2}/\text{mV}$
5 mA	$(3.4 \pm 0.069) \times 10^8 \text{ cm}^{-2}/\text{mV}$	$(6.7 \pm 0.32) \times 10^7 \text{ cm}^{-2}/\text{mV}$
10 mA	$(2.2 \pm 0.057) \times 10^8 \text{ cm}^{-2}/\text{mV}$	$(4.2 \pm 0.18) \times 10^7 \text{ cm}^{-2}/\text{mV}$
15 mA	$(1.8 \pm 0.053) \times 10^8 \text{ cm}^{-2}/\text{mV}$	$(3.4 \pm 0.14) \times 10^7 \text{ cm}^{-2}/\text{mV}$
20 mA	$(1.6 \pm 0.05) \times 10^8 \text{ cm}^{-2}/\text{mV}$	$(2.9 \pm 0.12) \times 10^7 \text{ cm}^{-2}/\text{mV}$
25 mA	$(1.4 \pm 0.048) \times 10^8 \text{ cm}^{-2}/\text{mV}$	$(2.6 \pm 0.11) \times 10^7 \text{ cm}^{-2}/\text{mV}$

Table 6.5: Summary of the sensitivity to radiation damage for silicon PIN diodes of types LBSD-SI1 and LBSD-SI2 which have been irradiated with 24 GeV/c proton beam. At $I_F = 10 \mu\text{A}$ and $100 \mu\text{A}$, both types of diodes do not reveal sensitivity to radiation damage.

Results show that the LBSD-SI2 silicon PIN diode is more sensitive to radiation damage than the diode type SI1. Furthermore, it reveals that the sensitivity is increased by operating the diode at higher readout current.

6.3 Conclusion

With the intention of monitoring $\Phi_{\text{eq}} < 2 \times 10^{12} \text{ n}_{\text{eq}}/\text{cm}^2$ for the LHC experiments and developing our specific particle fluence detectors, several devices have been investigated during this study.

In this chapter, the radiation response of silicon detectors and PIN diodes, made with different materials and geometries have been evaluated from low fluences ($\Phi_{\text{eq}} \approx 1 \times 10^9 \text{ n}_{\text{eq}}/\text{cm}^2$) to few $10^{14} \text{ n}_{\text{eq}}/\text{cm}^2$.

The outcome of the study carried out on different silicon detectors reveals that the device thickness is the main parameter which influences their radiation response. Thicker devices (1000 μm) start to be sensitive to radiation damage at lower equivalent fluence and show a

sensitivity which is around 25 greater than the one observed for thinner detectors (300 μm). This result allows to state that the use of thick silicon detectors for monitoring low LHC fluences is an option that should be considered in the future.

However, the response of this type of devices is limited to their utilization at medium and low fluences ($\Phi_{\text{eq}} < 1 \times 10^{14} \text{ n}_{\text{eq}}/\text{cm}^2$), since the forward voltage does not increase linearly up to very high fluences as observed for the 300 μm thick detectors operated at 100 μA .

A solution for using them as radiation monitoring sensors for expected Super-LHC fluences, is to characterize the device response with the new approach presented in Chapter 5. This study should be done in the future. From the study carried out on BPWFS silicon PIN diodes, it has been proven that the behavior of this device can be predicted up to $\Phi_{\text{eq}} = 6.3 \times 10^{15} \text{ n}_{\text{eq}}/\text{cm}^2$ (when the radiation response is not linear anymore), so that the upper limit of the Φ_{eq} measurement range can be expanded. This value is taken from the limitation of experimental measurements done in this thesis, but it should be higher since at such fluences the relaxation regime is well established, and that to our best knowledge there is no other regimes at even higher radiation levels.

The forward voltage for 1000 μm and 300 μm thick silicon detectors start to grow around $2 \times 10^{10} \text{ n}_{\text{eq}}/\text{cm}^2$ and $1 \times 10^{12} \text{ n}_{\text{eq}}/\text{cm}^2$ respectively. This result is in good agreement with the data obtained for the OSRAM BPW34FS diodes (presented in Chapter 5) where the 300 μm thick diode starts to be radiation sensitive at $\Phi_{\text{eq}} \approx 2 \times 10^{12} \text{ n}_{\text{eq}}/\text{cm}^2$. Furthermore, since both types of devices have a similar geometry, it can be stated that the initial material resistivity (which is higher for silicon detectors) does not affect the lower limit of the fluence measurement range.

Moreover, in this study the influence of the device's material and active area have also been considered. It shows that both parameters do not have a significant impact on the detector's radiation response compared to the thickness. Nevertheless, the detector response is somewhat influenced by them, since their sensitivity is increased by a factor around 1.5 when the active area is reduced by a factor of 4 and slightly enhanced for oxygenated material.

Finally, another type of silicon PIN diodes made with different geometries and resistivity than for OSRAM BPW34FS has been investigated here. LBSD-SI1 and LBSD-SI2 diodes reveal a highest sensitivity to radiation damage at low fluences than the one observed for the BPW34FS diode. The two LBSD devices start to be sensitive to radiation at $\Phi_{\text{eq}} > 1 \times 10^{10} \text{ n}_{\text{eq}}/\text{cm}^2$. Moreover it should be mentioned that the diode type LBSD-SI2 is the highest sensitive device of all the ones presented here. Nevertheless, both SI1 and SI2 diodes start to saturate at an equivalent fluence below $2 \times 10^{12} \text{ n}_{\text{eq}}/\text{cm}^2$ (value where the BPW34FS start to be sensitive).

For this reason, a solution for monitoring the full LHC fluence range is proposed here. It consists in the use of thick silicon detectors for monitoring low fluences and thin ones for high fluences. In this way, particle fluence can be monitored from $\Phi_{\text{eq}} \approx 1 \times 10^{10} \text{ n}_{\text{eq}}/\text{cm}^2$ to few $10^{14} \text{ n}_{\text{eq}}/\text{cm}^2$. In addition, a pre-irradiation can be performed on such devices to bring them directly to their operation point for monitoring very low fluences (as for instance fluences starting from about $8 \times 10^9 \text{ n}_{\text{eq}}/\text{cm}^2$ by using pre-irradiated BPW34FS silicon PIN diodes)

As discussed previously, for monitoring very high fluences as expected for the Super-LHC, a complete characterization of the devices should be done using the new approach based on the relaxation material theory (see Chapter 5). However, it would also be interesting to perform some irradiation tests on silicon detectors thinner than 300 μm to confirm that the expected SLHC fluence range can be monitored also by using very thin silicon detectors.

Chapter 7

Summary and Conclusions

At CERN, a new particle accelerator has been built for discovering the fundaments of the matter and universe, the “Large Hadron Collider”. With this new type of accelerator, it will be possible to collide heavy charged particles with a center mass energy of 14 TeV, and to reach unprecedent luminosity such as $10^{34} \text{ cm}^{-2}\text{s}^{-1}$ for LHC and $10^{35} \text{ cm}^{-2}\text{s}^{-1}$ for Super-LHC. Five experiments are included in the LHC collider, ATLAS, CMS, TOTEM, ALICE and LHCb. Inside each of them proton-proton or ion-ion collisions will produce a complex radiation field composed mainly of charged hadrons (π^\pm , proton, K^\pm , etc..), electrons, muons, photons and neutrons of energies up to hundred of GeV.

The detectors are composed by different layers of sub-detectors, which include electronic devices and systems. All this equipment can be affected by the radiation field generated inside each experiment. Particles can cause three different types of radiation damage inside electronic components, namely Total Ionizing Dose (TID), displacement damage and single event effects. In this thesis work, the two quantities of interest are the TID and the displacement damage effects measured in terms of 1-MeV equivalent neutron fluence (Φ_{eq}). Before LHC starts to run, an important task was to predict the radiation impact on electronic devices. For this reason Monte Carlo simulations have been performed for all the experiments and revealed that in the expected radiation fields, electronic devices are subjected to TID values from some Gy to 1×10^5 Gy and to equivalent fluences from 1×10^8 to $1 \times 10^{15} \text{ n}_{\text{eq}}/\text{cm}^2$, for LHC. For Super-LHC, the radiation environment will even be much higher in intensity since the radiation levels will be multiplied by a factor 10.

Radiations interact in many ways with matter, depending on the particle type and energy. Particles deposit a part or their total energy by interacting with atomic electrons and nuclei. For a deeper understanding on their effects on materials and components, a complete comprehensive review of their transport through matter has been given for the particles which are in major quantity inside the LHC. With the intention to monitor this field, in a previous study [Rav06] a complete radiation monitoring equipment has been developed. It is composed of two types of electronic devices used as radiation sensors; RadFETs sensors are used for measuring the TID effect and commercial silicon PIN diodes for monitoring the 1-MeV equivalent neutron fluence (Φ_{eq}). For this purpose, RadFET sensors have been characterized in different radiation fields during this previous study. Nevertheless, even if the particle spectrum is well predicted by Monte Carlo simulations, the question remains how much ionizing energy is deposited in the RadFET sensors under real experimental conditions. In addition, the packaging itself can alter the radiation response of RadFET sensors since particle passing through it may be completely stopped (e. g. for low energetic particles) and also because creation of secondary particles can enhance their radiation response. For both reasons, a study based on Geant4 simulations has been carried out by simulating the RadFET sensors with different packaging configurations with the aim to understand the effect of the main particles contained in the LHC radiation field. Once the influence of each particle type and energy has been evaluated, and their effects on the measured dose were understood, the TID have been calculated for two different packaging configurations in two specific locations in the ATLAS detector. This study revealed that the RadFET sensors covered with a 260 μ m Alumina cover (which has tentatively been defined as the cover to be used in LHC experiments) can enhance predicted measured dose by a factor of up to 25% depending on the location of the RadFET sensors in the LHC experiments. In the LHC radiation environment, this increase in measured dose is certainly smaller than the accuracy of RadFET dose measurements, however the dose enhancement caused by the package cannot be neglected and care has to be taken for selecting packaging configurations of dosimeters used in high energy physics experiments.

The second quantity that has to be monitored is the displacement damage which can be created by neutral and charged hadrons as well as by high energetic leptons. In previous studies, it was found that the solution for monitoring the 1-MeV equivalent neutron fluence can be done by the utilization of silicon PIN diodes. After being characterized in different radiation fields, the BPW34 commercial silicon PIN diodes were considered as to be a good choice for monitoring the high Φ_{eq} that will be integrated over 10-years of LHC runs in the inner sub-detector regions of the experiments. The principle of measurement is to measure the shift of

forward voltage versus Φ_{eq} , by injecting a constant forward current during a certain short pulse duration in the diode. Using this method, this device reveals a sensitivity to fast hadrons from $2 \times 10^{12} n_{eq}/cm^2$ to $4 \times 10^{14} n_{eq}/cm^2$ by applying a constant readout current pulse of $1mA \times 700ms$. In previous study and from the preliminary studies that have been carried out in this thesis, it has been shown that the operation of the diode at higher injection levels may be responsible of the occurrence of a thyristor-like behavior and/or can produce a self-heating effect in the diode at high fluences. For this reason, it is not recommended to operate the BPW34 silicon PIN diode at a readout current higher than 1 mA.

In view to use this device for monitoring the expected fluences of the Super-LHC, where the radiation level will be multiplied by a factor of 10 and where the equipment located in the innermost sub-detectors could be exposed to fluences up to $10^{16} n_{eq}/cm^2$, a new solution had to be found. For this purpose, a comparison between results obtained on irradiated silicon PIN diodes and relaxation materials theory has been carried out. It allows to obtain a better understanding on the physics principles underlying the radiation induced changes of the current-voltage PIN diode characteristics. This comparison led to the finding of a new formulation for predicting their radiation response for expected Super-LHC fluences, by operating the diode with readout current $I_F \leq 1mA$ at room temperature.

In addition, a qualitative evaluation of the temperature dependence has been carried out to give some suggestions about the optimum operational temperature in which the silicon PIN diode should be used for optimizing the measurement. It has been found that the upper limit of the fluence measurement range can be expanded to higher fluences and that their radiation sensitivity can be increased by measuring the device at lower temperature. A complete study with the aim to integrate the temperature parameter in the new formulation is still in progress and will be addressed in a later paper.

However, this type of diode is not sensitive to radiation levels lower than $2 \times 10^{12} n_{eq}/cm^2$. Even if some solutions already exist for monitoring fluence starting from $10^8 n_{eq}/cm^2$ to $2 \times 10^{12} n_{eq}/cm^2$, as for instance the use of CMRP diodes (expensive device) or the pre-irradiation of the BPW34 silicon diodes to bring them to their operation point, other directions have been taken during this thesis. With the intention to develop our specific dosimeter in the future, a first study has been carried out on the radiation response of custom made silicon detectors with different geometries and materials. In addition other types of silicon PIN diodes which are named “Long Base Silicon Diode” (LBSD) have been tested.

Finally, the outcome of this study was that the major parameter which influences the radiation response of the dosimeter in terms of sensitivity and lower limit of the fluence

measurement range is the thickness of the device. This study was carried out on 1000 µm and 300 µm thick silicon detectors as well as on 1.2 mm and 2.5 mm thick LBSD silicon PIN diodes.

For these types of silicon detectors, the study revealed that the thicker ones start to be sensitive at lower fluence values (around two orders of magnitude less than the thinner ones) and show a radiation sensitivity increased by a factor of around 25. Both material and active area reveal only a slight influence in comparison with the thickness. In addition, the two types of LBSD silicon PIN diodes are sensitive to radiation damage at equivalent fluences lower than $1 \times 10^{10} n_{eq}/cm^2$, but their radiation response saturates at values lower than $2 \times 10^{12} n_{eq}/cm^2$. As for silicon detectors, the thicker LBSD diode is the highest sensitive to radiation damage.

For the future and perspectives on the research field concerning the radiation monitoring of Φ_{eq} , for the next generation of high energy physics experiments with custom made sensors, two solutions have been proposed in the final chapter. The first one is the use of silicon detectors made with different thickness, so that the thinner one can monitor high fluences and the thicker ones can measure low radiation levels. The second one is to make a complete characterization based on the new approach presented in Chapter 5 for different silicon detectors geometries in order to optimize their operational conditions as far as possible.

Appendix A

Value specifications of the energy deposited in the RadFET sensors

As it has been shown in Chapter 4, the expected response of RadFETs dosimeters in the complex radiation fields of LHC experiments has been studied using the Geant4 toolkit. For this study, a Geant4 application was developed describing the geometry and material of the RadFET sensors and the surrounding package in great detail.

In this work, the average deposited energy on the RadFETs dosimeters covered and uncovered by a 260 μm Alumina lid was evaluated as a function of incident particle energies over energy bins corresponding to a realistic incident particle energy spectrum expected in the LHC experiments.

This appendix specifies the values of average energy deposited per incident particle presented in the different figures shown in Chapter 4.

Table A correspond to the simulation carried out on the dosimeters considering the four full RadFET sensors as sensitive volume and Table B correspond to the refined simulation performed assuming the oxide layer of the LAAS detector as sensitive volume.

Energy bins	Av. Edep/proton Without cover (keV)	Av. Edep/proton With cover (keV)
1 – 2.15 MeV	$9.02 \times 10^1 \pm 1.5 \times 10^0$	0
2.15 – 4.64 MeV	$2.81 \times 10^2 \pm 3.2 \times 10^0$	0
4.64 – 10 MeV	$4.14 \times 10^2 \pm 4.3 \times 10^0$	$1.04 \times 10^2 \pm 1.4 \times 10^0$
10 – 21.5 MeV	$2.03 \times 10^2 \pm 2.2 \times 10^0$	$2.68 \times 10^2 \pm 2.9 \times 10^0$
21.5 – 46.4 MeV	$1.05 \times 10^2 \pm 9.9 \times 10^{-1}$	$1.11 \times 10^2 \pm 1.1 \times 10^0$
46.4 – 100 MeV	$5.83 \times 10^1 \pm 2.8 \times 10^{-1}$	$5.85 \times 10^1 \pm 2.8 \times 10^{-1}$
100 – 215 MeV	$3.2 \times 10^1 \pm 1.5 \times 10^{-1}$	$3.28 \times 10^{-1} \pm 1.5 \times 10^{-1}$
215 – 464 MeV	$2.049 \times 10^1 \pm 9.1 \times 10^{-2}$	$2.133 \times 10^1 \pm 9.2 \times 10^{-2}$
464 – 1000 MeV	$1.4 \times 10^1 \pm 2.7 \times 10^{-1}$	$1.55 \times 10^1 \pm 3 \times 10^{-1}$
1 – 2.15 GeV	$1.23 \times 10^1 \pm 2.6 \times 10^{-1}$	$1.3 \times 10^1 \pm 1.3 \times 10^{-1}$
2.15 – 4.64 GeV	$1.08 \times 10^1 \pm 2.2 \times 10^{-1}$	$1.1 \times 10^1 \pm 0$
4.64 – 10 GeV	$1.01 \times 10^1 \pm 2 \times 10^{-1}$	$1.06 \times 10^1 \pm 2.1 \times 10^{-1}$
10 – 21.5 GeV	$9.5 \times 10^0 \pm 1.3 \times 10^{-1}$	$1.4 \times 10^1 \pm 1.4 \times 10^{-1}$

Table A.1: Summary of energy deposited by protons into the four full RadFET sensors uncovered and covered by a 260 μm thick Alumina cover.

Energy bins	Av. Edep/pion Without cover (keV)	Av. Edep/pion With cover (keV)
1 – 2.15 MeV	$1.312 \times 10^2 \pm 8.4 \times 10^{-1}$	0
2.15 – 4.64 MeV	$1.731 \times 10^2 \pm 8.3 \times 10^{-1}$	$6.5 \times 10^1 \pm 3.7 \times 10^{-1}$
4.64 – 10 MeV	$7.97 \times 10^1 \pm 4.8 \times 10^{-1}$	$1.076 \times 10^2 \pm 8.5 \times 10^{-1}$
10 – 21.5 MeV	$4.17 \times 10^1 \pm 2.4 \times 10^{-1}$	$4.38 \times 10^1 \pm 2.6 \times 10^{-1}$
21.5 – 46.4 MeV	$2.366 \times 10^1 \pm 9.4 \times 10^{-2}$	$2.48 \times 10^1 \pm 1 \times 10^{-1}$
46.4 – 100 MeV	$1.59 \times 10^1 \pm 2.5 \times 10^{-1}$	$1.75 \times 10^1 \pm 2.9 \times 10^{-1}$
100 – 215 MeV	$1.21 \times 10^1 \pm 1.2 \times 10^{-1}$	$1.38 \times 10^1 \pm 1.4 \times 10^{-1}$
215 – 464 MeV	$1.016 \times 10^1 \pm 8.4 \times 10^{-2}$	$1.16 \times 10^1 \pm 2 \times 10^{-1}$
464 – 1000 MeV	$1.02 \times 10^1 \pm 2 \times 10^{-1}$	$1.15 \times 10^1 \pm 2.3 \times 10^{-1}$
1 – 2.15 GeV	$1.06 \times 10^1 \pm 2.1 \times 10^{-1}$	$1.14 \times 10^1 \pm 2.2 \times 10^{-1}$
2.15 – 4.64 GeV	$1.06 \times 10^1 \pm 0$	$1.18 \times 10^1 \pm 0$
4.64 – 10 GeV	$1.03 \times 10^1 \pm 2 \times 10^{-1}$	$1.15 \times 10^1 \pm 2.2 \times 10^{-1}$
10 – 21.5 GeV	$9.8 \times 10^0 \pm 1.4 \times 10^{-1}$	$1.11 \times 10^1 \pm 1.5 \times 10^{-1}$
21.5 – 46.4 GeV	$1.012 \times 10^1 \pm 7.6 \times 10^{-2}$	$1.09 \times 10^1 \pm 1.6 \times 10^{-1}$
46.4 – 100 GeV	$1.02 \times 10^1 \pm 0$	$1.07 \times 10^1 \pm 2.3 \times 10^{-1}$

Table A.2: Summary of energy deposited by pions into the four full RadFET sensors uncovered and covered by a 260 μm thick Alumina cover.

Energy bins	Av. Edep/photon Without cover (keV)	Av. Edep/photon With cover (keV)
> 10 keV	$1.476 \pm 7.6 \times 10^{-3}$	$3.00 \times 10^{-2} \pm 7.9 \times 10^{-4}$
10 – 21.5 keV	$1.329 \pm 1.2 \times 10^{-2}$	$5.90 \times 10^{-1} \pm 3.7 \times 10^{-3}$
21.5 – 46.4 keV	$3.34 \times 10^{-1} \pm 3.3 \times 10^{-3}$	$2.66 \times 10^{-1} \pm 2.9 \times 10^{-3}$
46.4 – 100 keV	$1.32 \times 10^{-1} \pm 5.7 \times 10^{-3}$	$9.9 \times 10^{-2} \pm 1.4 \times 10^{-3}$
100 – 215 keV	$5.7 \times 10^{-2} \pm 2 \times 10^{-3}$	$5.52 \times 10^{-2} \pm 8.4 \times 10^{-4}$
215 – 464 keV	$5.7 \times 10^{-2} \pm 4.2 \times 10^{-3}$	$7.6 \times 10^{-2} \pm 2.4 \times 10^{-3}$
464 – 1000 keV	$6.2 \times 10^{-2} \pm 6.9 \times 10^{-3}$	$1.5 \times 10^{-1} \pm 1.1 \times 10^{-2}$
1 – 2.15 MeV	$4.1 \times 10^{-2} \pm 4.7 \times 10^{-3}$	$1.5 \times 10^{-1} \pm 1.1 \times 10^{-2}$
2.15 – 4.64 MeV	$2.3 \times 10^{-2} \pm 2.9 \times 10^{-3}$	$9.4 \times 10^{-2} \pm 3.9 \times 10^{-3}$
4.64 – 10 MeV	$1.8 \times 10^{-2} \pm 3.2 \times 10^{-3}$	$6.5 \times 10^{-2} \pm 3.3 \times 10^{-3}$
10 – 21.5 MeV	$1.3 \times 10^{-2} \pm 3 \times 10^{-3}$	$1.04 \times 10^{-1} \pm 9.2 \times 10^{-3}$
21.5 – 46.4 MeV	$1.5 \times 10^{-2} \pm 2.7 \times 10^{-3}$	$1.41 \times 10^{-1} \pm 9.6 \times 10^{-3}$
46.4 – 100 MeV	$2.0 \times 10^{-2} \pm 4.2 \times 10^{-3}$	$8.5 \times 10^{-2} \pm 1.1 \times 10^{-2}$
100 – 215 MeV	$2.2 \times 10^{-2} \pm 4.6 \times 10^{-3}$	$9.0 \times 10^{-2} \pm 1.1 \times 10^{-2}$
215 – 464 MeV	$2.3 \times 10^{-2} \pm 2.1 \times 10^{-3}$	$9.5 \times 10^{-2} \pm 9.9 \times 10^{-3}$
464 – 1000 MeV	$2.1 \times 10^{-2} \pm 4.1 \times 10^{-3}$	$1.7 \times 10^{-1} \pm 1.8 \times 10^{-2}$
1 – 2.15 GeV	$2.1 \times 10^{-2} \pm 4.6 \times 10^{-3}$	$1.77 \times 10^{-1} \pm 9.3 \times 10^{-3}$
2.15 – 4.64 GeV	$2.1 \times 10^{-2} \pm 4.2 \times 10^{-3}$	$1.8 \times 10^{-1} \pm 1.2 \times 10^{-2}$
4.64 – 10 GeV	$2.4 \times 10^{-2} \pm 4.6 \times 10^{-3}$	$7.8 \times 10^{-2} \pm 9.8 \times 10^{-3}$
10 – 21.5 GeV	$3.0 \times 10^{-2} \pm 3.5 \times 10^{-3}$	$9.2 \times 10^{-2} \pm 7.2 \times 10^{-3}$
21.5 – 46.4 GeV	$3.2 \times 10^{-2} \pm 4.1 \times 10^{-3}$	$9.3 \times 10^{-2} \pm 8.6 \times 10^{-3}$

Table A.3: Summary of energy deposited by photons into the four full RadFET sensors uncovered and covered by a 260 μm thick Alumina cover.

Energy bins	Av. Edep/electron Without cover (keV)	Av. Edep/electron With cover (keV)
21.5 – 46.4 keV	$1.7 \times 10^{-1} \pm 0$	$7.5 \times 10^{-6} \pm 3.5 \times 10^{-6}$
46.4 – 100 keV	$2.22 \times 10^{-1} \pm 3.3 \times 10^{-3}$	$1.7 \times 10^{-4} \pm 2.2 \times 10^{-5}$
100 – 215 keV	$9.52 \times 10^0 \pm 8.2 \times 10^{-2}$	$1 \times 10^{-3} \pm 7.4 \times 10^{-5}$
215 – 464 keV	$2 \times 10^1 \pm 1.4 \times 10^{-1}$	$1.38 \times 10^0 \pm 2.7 \times 10^{-2}$
464 – 1000 keV	$1.55 \times 10^1 \pm 1.9 \times 10^{-1}$	$1.58 \times 10^1 \pm 2 \times 10^{-2}$
1 – 2.15 MeV	$1.05 \times 10^1 \pm 1.3 \times 10^{-1}$	$1.97 \times 10^1 \pm 1.8 \times 10^{-1}$
2.15 – 4.64 MeV	$9.6 \times 10^0 \pm 8.2 \times 10^{-2}$	$1.258 \times 10^1 \pm 8.9 \times 10^{-2}$
4.64 – 10 MeV	$9.7 \times 10^0 \pm 1.9 \times 10^{-1}$	$1.08 \times 10^1 \pm 1.9 \times 10^{-1}$
10 – 21.5 MeV	$9.8 \times 10^0 \pm 2.1 \times 10^{-1}$	$1.06 \times 10^1 \pm 2.2 \times 10^{-1}$
21.5 – 46.4 MeV	$9.9 \times 10^0 \pm 8.9 \times 10^{-2}$	$1.074 \times 10^1 \pm 9.4 \times 10^{-2}$
46.4 – 100 MeV	$9.8 \times 10^0 \pm 2 \times 10^{-1}$	$1.07 \times 10^1 \pm 2.1 \times 10^{-1}$
100 – 215 MeV	$9.9 \times 10^0 \pm 2 \times 10^{-1}$	$1.09 \times 10^1 \pm 2.1 \times 10^{-1}$
215 – 464 MeV	$1.02 \times 10^1 \pm 1.7 \times 10^{-1}$	$1.114 \times 10^1 \pm 8.4 \times 10^{-2}$
464 – 1000 MeV	$1.02 \times 10^1 \pm 2.1 \times 10^{-1}$	$1.11 \times 10^1 \pm 2.2 \times 10^{-1}$
1 – 2.15 GeV	$1.01 \times 10^1 \pm 2.2 \times 10^{-1}$	$1.09 \times 10^1 \pm 2.3 \times 10^{-1}$
2.15 – 4.64 GeV	$1.01 \times 10^1 \pm 9 \times 10^{-2}$	$1.1 \times 10^1 \pm 2.1 \times 10^{-1}$
4.64 – 10 GeV	$1.03 \times 10^1 \pm 2.1 \times 10^{-1}$	$1.12 \times 10^1 \pm 2.2 \times 10^{-1}$
10 – 21.5 GeV	$1.05 \times 10^1 \pm 1.4 \times 10^{-1}$	$1.11 \times 10^1 \pm 1.5 \times 10^{-1}$

Table A.4: Summary of energy deposited by electrons into the four full RadFET sensors uncovered and covered by a 260 μm thick Alumina cover.

Energy bins	Av. Edep/neutron Without cover (keV)	Av. Edep/neutron With cover (keV)
> 10 keV	$5.1 \times 10^{-3} \pm 5 \times 10^{-4}$	$8.2 \times 10^{-4} \pm 2.6 \times 10^{-4}$
10 – 21.5 keV	$5.5 \times 10^{-3} \pm 5.5 \times 10^{-4}$	$2.5 \times 10^{-3} \pm 1.1 \times 10^{-3}$
21.5 – 46.4 keV	$5.4 \times 10^{-3} \pm 5.7 \times 10^{-4}$	$5.3 \times 10^{-3} \pm 9.8 \times 10^{-4}$
46.4 – 100 keV	$1.1 \times 10^{-2} \pm 1.1 \times 10^{-3}$	$1.1 \times 10^{-2} \pm 3.1 \times 10^{-3}$
100 – 215 keV	$2.7 \times 10^{-2} \pm 2.8 \times 10^{-3}$	$2.4 \times 10^{-2} \pm 8.4 \times 10^{-3}$
215 – 464 keV	$4.9 \times 10^{-2} \pm 4.9 \times 10^{-3}$	$3.5 \times 10^{-2} \pm 8.5 \times 10^{-3}$
464 – 1000 keV	$1.03 \times 10^{-1} \pm 7.6 \times 10^{-3}$	$9.7 \times 10^{-2} \pm 1.8 \times 10^{-2}$
1 – 2.15 MeV	$1.8 \times 10^{-1} \pm 1.7 \times 10^{-2}$	$1.8 \times 10^{-1} \pm 3.5 \times 10^{-2}$
2.15 – 4.64 MeV	$2.5 \times 10^{-1} \pm 2 \times 10^{-2}$	$2.6 \times 10^{-1} \pm 1.8 \times 10^{-2}$
4.64 – 10 MeV	$2.8 \times 10^{-1} \pm 2.1 \times 10^{-2}$	$2.5 \times 10^{-1} \pm 2.1 \times 10^{-2}$
10 – 21.5 MeV	$3.6 \times 10^{-1} \pm 2.6 \times 10^{-2}$	$4 \times 10^{-1} \pm 3.3 \times 10^{-2}$
21.5 – 46.4 MeV	$5.7 \times 10^{-1} \pm 4.7 \times 10^{-2}$	$7.4 \times 10^{-1} \pm 4.3 \times 10^{-2}$
46.4 – 100 MeV	$6.5 \times 10^{-1} \pm 6.2 \times 10^{-2}$	$9 \times 10^{-1} \pm 1.3 \times 10^{-1}$
100 – 215 MeV	$4.4 \times 10^{-1} \pm 4.8 \times 10^{-2}$	$9.5 \times 10^{-1} \pm 1.1 \times 10^{-1}$
215 – 464 MeV	$5.8 \times 10^{-1} \pm 7.6 \times 10^{-2}$	$9.3 \times 10^{-1} \pm 1.1 \times 10^{-1}$
464 – 1000 MeV	$5.4 \times 10^{-1} \pm 8.5 \times 10^{-2}$	$1.11 \times 10^0 \pm 7.8 \times 10^{-2}$
1 – 2.15 GeV	$7 \times 10^{-1} \pm 1.2 \times 10^{-1}$	$1.3 \times 10^0 \pm 1.2 \times 10^{-1}$
2.15 – 4.64 GeV	$5.6 \times 10^{-1} \pm 1 \times 10^{-1}$	$1.4 \times 10^0 \pm 1.3 \times 10^{-1}$
4.64 – 10 GeV	$4.9 \times 10^{-1} \pm 6.3 \times 10^{-2}$	$1.06 \times 10^0 \pm 6.1 \times 10^{-2}$
10 – 21.5 GeV	$1.6 \times 10^{-1} \pm 2 \times 10^{-2}$	$3.8 \times 10^{-1} \pm 4.4 \times 10^{-2}$

Table A.5: Summary of energy deposited by neutron into the four full RadFET sensors uncovered and covered by a 260 μm thick Alumina cover.

Energy bins	Av. Edep/muon Without cover (keV)	Av. Edep/muon With cover (keV)
1 – 2.15 MeV	$1.6 \times 10^2 \pm 1.6 \times 10^0$	$3.48 \times 10^0 \pm 8.1 \times 10^{-2}$
2.15 – 4.64 MeV	$1.48 \times 10^2 \pm 1.3 \times 10^0$	$1.07 \times 10^2 \pm 1.1 \times 10^0$
4.64 – 10 MeV	$6.7 \times 10^1 \pm 1.2 \times 10^0$	$7.83 \times 10^1 \pm 6.9 \times 10^{-1}$
10 – 21.5 MeV	$3.59 \times 10^1 \pm 6.5 \times 10^{-1}$	$3.76 \times 10^1 \pm 6.7 \times 10^{-1}$
21.5 – 46.4 MeV	$2.06 \times 10^1 \pm 3.9 \times 10^{-1}$	$2.11 \times 10^1 \pm 2.3 \times 10^{-1}$
46.4 – 100 MeV	$1.38 \times 10^1 \pm 2.8 \times 10^{-1}$	$1.42 \times 10^1 \pm 2.5 \times 10^{-1}$
100 – 215 MeV	$1.1 \times 10^1 \pm 2.2 \times 10^{-1}$	$1.16 \times 10^1 \pm 2.3 \times 10^{-1}$
215 – 464 MeV	$9.8 \times 10^0 \pm 2.1 \times 10^{-1}$	$1.03 \times 10^1 \pm 2.2 \times 10^{-1}$
464 – 1000 MeV	$9.5 \times 10^0 \pm 2.1 \times 10^{-1}$	$1.04 \times 10^1 \pm 2.2 \times 10^{-1}$
1 – 2.15 GeV	$9.5 \times 10^0 \pm 2.1 \times 10^{-1}$	$1.05 \times 10^1 \pm 2.2 \times 10^{-1}$
2.15 – 4.64 GeV	$9.5 \times 10^0 \pm 2.1 \times 10^{-1}$	$1.04 \times 10^1 \pm 2.2 \times 10^{-1}$
4.64 – 10 GeV	$9.8 \times 10^0 \pm 2.1 \times 10^{-1}$	$1.06 \times 10^1 \pm 2.2 \times 10^{-1}$

Table A.6: Summary of energy deposited by muons into the four full RadFET sensors uncovered and covered by a 260 μm thick Alumina cover.

Energy bins	Av. Edep/proton Without cover (keV)	Av. Edep/proton With cover (keV)
1 – 2.15 MeV	$1.63 \times 10^1 \pm 2.9 \times 10^{-1}$	0
2.15 – 4.64 MeV	$9 \times 10^0 \pm 1.6 \times 10^{-1}$	0
4.64 – 10 MeV	$4.5 \times 10^0 \pm 4.4 \times 10^{-2}$	$4.22 \times 10^0 \pm 3.1 \times 10^{-2}$
10 – 21.5 MeV	$2.4 \times 10^0 \pm 3.2 \times 10^{-2}$	$3.04 \times 10^0 \pm 3 \times 10^{-2}$
21.5 – 46.4 MeV	$1.3 \times 10^0 \pm 1.9 \times 10^{-2}$	$1.53 \times 10^0 \pm 2.6 \times 10^{-2}$
46.4 – 100 MeV	$6.99 \times 10^{-1} \pm 1.2 \times 10^{-2}$	$8.2 \times 10^{-1} \pm 1.4 \times 10^{-2}$
100 – 215 MeV	$3.97 \times 10^{-1} \pm 7.2 \times 10^{-3}$	$4.57 \times 10^{-1} \pm 7.9 \times 10^{-3}$
215 – 464 MeV	$2.43 \times 10^{-1} \pm 4.3 \times 10^{-3}$	$2.72 \times 10^{-1} \pm 4.9 \times 10^{-3}$
464 – 1000 MeV	$1.58 \times 10^{-1} \pm 3 \times 10^{-3}$	$2.04 \times 10^{-1} \pm 4.1 \times 10^{-3}$
1 – 2.15 GeV	$1.34 \times 10^{-1} \pm 2.7 \times 10^{-3}$	$1.68 \times 10^{-1} \pm 3.2 \times 10^{-3}$
2.15 – 4.64 GeV	$1.3 \times 10^{-1} \pm 2.7 \times 10^{-3}$	$1.5 \times 10^{-1} \pm 3 \times 10^{-3}$
4.64 – 10 GeV	$1.24 \times 10^{-1} \pm 2.5 \times 10^{-3}$	$1.47 \times 10^{-1} \pm 3 \times 10^{-3}$
10 – 21.5 GeV	$1.24 \times 10^{-1} \pm 2.5 \times 10^{-3}$	$1.4 \times 10^{-1} \pm 2.9 \times 10^{-3}$

Table B.1: Summary of energy deposited by protons into the LAAS detectors uncovered and covered by a 260 μm thick Alumina cover.

Energy bins	Av. Edep/pion Without cover (keV)	Av. Edep/pion With cover (keV)
1 – 2.15 MeV	$3.8 \times 10^0 \pm 5.9 \times 10^{-2}$	0
2.15 – 4.64 MeV	$1.8 \times 10^0 \pm 2.1 \times 10^{-2}$	$1.81 \times 10^0 \pm 1.8 \times 10^{-2}$
4.64 – 10 MeV	$9.7 \times 10^{-1} \pm 1.3 \times 10^{-2}$	$1.23 \times 10^0 \pm 1.4 \times 10^{-2}$
10 – 21.5 MeV	$5.09 \times 10^{-1} \pm 6.7 \times 10^{-3}$	$5.71 \times 10^{-1} \pm 7.6 \times 10^{-3}$
21.5 – 46.4 MeV	$2.87 \times 10^{-1} \pm 3 \times 10^{-3}$	$3.18 \times 10^{-1} \pm 3.3 \times 10^{-3}$
46.4 – 100 MeV	$2.07 \times 10^{-1} \pm 3 \times 10^{-3}$	$2.53 \times 10^{-1} \pm 3.6 \times 10^{-3}$
100 – 215 MeV	$1.59 \times 10^{-1} \pm 2.3 \times 10^{-3}$	$1.9 \times 10^{-1} \pm 2.7 \times 10^{-3}$
215 – 464 MeV	$1.32 \times 10^{-1} \pm 2 \times 10^{-3}$	$1.67 \times 10^{-1} \pm 2.4 \times 10^{-3}$
464 – 1000 MeV	$1.33 \times 10^{-1} \pm 1.9 \times 10^{-3}$	$1.46 \times 10^{-1} \pm 2.1 \times 10^{-3}$
1 – 2.15 GeV	$1.35 \times 10^{-1} \pm 2 \times 10^{-3}$	$1.48 \times 10^{-1} \pm 2.2 \times 10^{-3}$
2.15 – 4.64 GeV	$1.28 \times 10^{-1} \pm 1.9 \times 10^{-3}$	$1.51 \times 10^{-1} \pm 2.3 \times 10^{-3}$
4.64 – 10 GeV	$1.22 \times 10^{-1} \pm 1.8 \times 10^{-3}$	$1.46 \times 10^{-1} \pm 2.1 \times 10^{-3}$
10 – 21.5 GeV	$1.29 \times 10^{-1} \pm 1.9 \times 10^{-3}$	$1.42 \times 10^{-1} \pm 2.1 \times 10^{-3}$
21.5 – 46.4 GeV	$1.25 \times 10^{-1} \pm 1.8 \times 10^{-3}$	$1.42 \times 10^{-1} \pm 2.1 \times 10^{-3}$
46.4 – 100 GeV	$1.28 \times 10^{-1} \pm 1.9 \times 10^{-3}$	$1.44 \times 10^{-1} \pm 2.1 \times 10^{-3}$

Table B.2: Summary of energy deposited by pions into the LAAS detectors uncovered and covered by a 260 μm thick Alumina cover.

Energy bins	Av. Edep/photon Without cover (keV)	Av. Edep/photon With cover (keV)
> 10 keV	$3.43 \times 10^{-2} \pm 2.6 \times 10^{-4}$	$5.6 \times 10^{-4} \pm 4.1 \times 10^{-5}$
10 – 21.5 keV	$1.02 \times 10^{-2} \pm 3.7 \times 10^{-4}$	$5.3 \times 10^{-3} \pm 2.5 \times 10^{-4}$
21.5 – 46.4 keV	$4.6 \times 10^{-3} \pm 2.7 \times 10^{-4}$	$4 \times 10^{-3} \pm 1.8 \times 10^{-4}$
46.4 – 100 keV	$7.1 \times 10^{-4} \pm 9.9 \times 10^{-5}$	$9 \times 10^{-4} \pm 1.3 \times 10^{-4}$
100 – 215 keV	$2.8 \times 10^{-4} \pm 8.3 \times 10^{-5}$	$4.7 \times 10^{-4} \pm 6.6 \times 10^{-5}$
215 – 464 keV	$2.6 \times 10^{-4} \pm 5.1 \times 10^{-5}$	$9.8 \times 10^{-4} \pm 5.5 \times 10^{-5}$
464 – 1000 keV	$2.4 \times 10^{-4} \pm 5.1 \times 10^{-5}$	$1.7 \times 10^{-3} \pm 1.1 \times 10^{-4}$
1 – 2.15 MeV	$2.1 \times 10^{-4} \pm 3 \times 10^{-5}$	$1.55 \times 10^{-3} \pm 7.7 \times 10^{-5}$
2.15 – 4.64 MeV	$1.1 \times 10^{-4} \pm 1.7 \times 10^{-5}$	$9.1 \times 10^{-4} \pm 4.1 \times 10^{-5}$
4.64 – 10 MeV	$8 \times 10^{-5} \pm 1.9 \times 10^{-5}$	$5.7 \times 10^{-4} \pm 2.9 \times 10^{-5}$
10 – 21.5 MeV	$3.69 \times 10^{-5} \pm 9.9 \times 10^{-6}$	$8.6 \times 10^{-4} \pm 4.6 \times 10^{-5}$
21.5 – 46.4 MeV	$3.9 \times 10^{-5} \pm 1.2 \times 10^{-5}$	$7.8 \times 10^{-4} \pm 4.8 \times 10^{-5}$
46.4 – 100 MeV	$1.2 \times 10^{-4} \pm 4.3 \times 10^{-5}$	$6.3 \times 10^{-4} \pm 4.9 \times 10^{-5}$
100 – 215 MeV	$1.1 \times 10^{-4} \pm 4.1 \times 10^{-5}$	$7 \times 10^{-4} \pm 5.6 \times 10^{-5}$
215 – 464 MeV	$1.2 \times 10^{-4} \pm 4.5 \times 10^{-5}$	$1.9 \times 10^{-3} \pm 1.2 \times 10^{-4}$
464 – 1000 MeV	$5.3 \times 10^{-5} \pm 2.7 \times 10^{-5}$	$9.8 \times 10^{-4} \pm 6.4 \times 10^{-5}$
1 – 2.15 GeV	$5.2 \times 10^{-5} \pm 2.7 \times 10^{-5}$	$1.01 \times 10^{-3} \pm 5 \times 10^{-5}$
2.15 – 4.64 GeV	$2.8 \times 10^{-5} \pm 1.2 \times 10^{-5}$	$8.7 \times 10^{-4} \pm 4.5 \times 10^{-5}$
4.64 – 10 GeV	$9 \times 10^{-6} \pm 3.6 \times 10^{-6}$	$8.4 \times 10^{-4} \pm 5.5 \times 10^{-5}$
10 – 21.5 GeV	$2.1 \times 10^{-5} \pm 5 \times 10^{-6}$	$7.2 \times 10^{-4} \pm 3.5 \times 10^{-5}$
21.5 – 46.4 GeV	$1.4 \times 10^{-5} \pm 3.7 \times 10^{-6}$	$7 \times 10^{-4} \pm 3.6 \times 10^{-5}$

Table B.3: Summary of energy deposited by photons into the LAAS detectors uncovered and covered by a 260 μm thick Alumina cover.

Energy bins	Av. Edep/electron Without cover (keV)	Av. Edep/electron With cover (keV)
21.5 – 46.4 keV	$1.19 \times 10^{-1} \pm 3.2 \times 10^{-3}$	0
46.4 – 100 keV	$4.4 \times 10^{-1} \pm 3.4 \times 10^{-3}$	0
100 – 215 keV	$3.86 \times 10^{-1} \pm 2.7 \times 10^{-3}$	0
215 – 464 keV	$2.57 \times 10^{-1} \pm 1.1 \times 10^{-3}$	$5.18 \times 10^{-2} \pm 8.7 \times 10^{-4}$
464 – 1000 keV	$1.96 \times 10^{-1} \pm 1.7 \times 10^{-3}$	$3.18 \times 10^{-1} \pm 1.6 \times 10^{-3}$
1 – 2.15 MeV	$1.52 \times 10^{-1} \pm 1.3 \times 10^{-3}$	$2.57 \times 10^{-1} \pm 2.3 \times 10^{-3}$
2.15 – 4.64 MeV	$1.25 \times 10^{-1} \pm 1.3 \times 10^{-3}$	$1.6 \times 10^{-1} \pm 9.4 \times 10^{-4}$
4.64 – 10 MeV	$1.24 \times 10^{-1} \pm 9.8 \times 10^{-4}$	$1.42 \times 10^{-1} \pm 6.6 \times 10^{-4}$
10 – 21.5 MeV	$1.22 \times 10^{-1} \pm 1.3 \times 10^{-3}$	$1.4 \times 10^{-1} \pm 1.9 \times 10^{-3}$
21.5 – 46.4 MeV	$1.2 \times 10^{-1} \pm 1.3 \times 10^{-3}$	$1.43 \times 10^{-1} \pm 1.5 \times 10^{-3}$
46.4 – 100 MeV	$1.28 \times 10^{-1} \pm 1.3 \times 10^{-3}$	$1.43 \times 10^{-1} \pm 1.5 \times 10^{-3}$
100 – 215 MeV	$1.25 \times 10^{-1} \pm 1.3 \times 10^{-3}$	$1.44 \times 10^{-1} \pm 1.5 \times 10^{-3}$
215 – 464 MeV	$1.26 \times 10^{-1} \pm 1.4 \times 10^{-3}$	$1.44 \times 10^{-1} \pm 1.6 \times 10^{-3}$
464 – 1000 MeV	$1.29 \times 10^{-1} \pm 1.3 \times 10^{-3}$	$1.41 \times 10^{-1} \pm 1.4 \times 10^{-3}$
1 – 2.15 GeV	$1.27 \times 10^{-1} \pm 1.3 \times 10^{-3}$	$1.43 \times 10^{-1} \pm 2.7 \times 10^{-3}$
2.15 – 4.64 GeV	$1.23 \times 10^{-1} \pm 1.3 \times 10^{-3}$	$1.45 \times 10^{-1} \pm 2.1 \times 10^{-3}$
4.64 – 10 GeV	$1.23 \times 10^{-1} \pm 1.3 \times 10^{-3}$	$1.46 \times 10^{-1} \pm 1.5 \times 10^{-3}$
10 – 21.5 GeV	$1.24 \times 10^{-1} \pm 1.3 \times 10^{-3}$	$1.41 \times 10^{-1} \pm 1.4 \times 10^{-3}$

Table B.4: Summary of energy deposited by electrons into the LAAS detectors uncovered and covered by a 260 μm thick Alumina cover.

Energy bins	Av. Edep/neutron Without cover (keV)	Av. Edep/neutron With cover (keV)
> 10 keV	$2.59 \times 10^{-7} \pm 1.8 \times 10^{-7}$	0
10 – 21.5 keV	$7.12 \times 10^{-7} \pm 7.1 \times 10^{-7}$	0
21.5 – 46.4 keV	$1.26 \times 10^{-6} \pm 1.3 \times 10^{-6}$	0
46.4 – 100 keV	$5.61 \times 10^{-7} \pm 4.3 \times 10^{-7}$	0
100 – 215 keV	$1.8 \times 10^{-6} \pm 1.3 \times 10^{-6}$	0
215 – 464 keV	0	0
464 – 1000 keV	$6.42 \times 10^{-5} \pm 4.6 \times 10^{-5}$	$6.37 \times 10^{-5} \pm 3.7 \times 10^{-5}$
1 – 2.15 MeV	$4.38 \times 10^{-4} \pm 1.8 \times 10^{-4}$	$1.9 \times 10^{-4} \pm 1 \times 10^{-4}$
2.15 – 4.64 MeV	$1 \times 10^{-3} \pm 3 \times 10^{-4}$	$5.88 \times 10^{-4} \pm 2 \times 10^{-4}$
4.64 – 10 MeV	$1.01 \times 10^{-3} \pm 2.3 \times 10^{-4}$	$4.76 \times 10^{-4} \pm 8.7 \times 10^{-5}$
10 – 21.5 MeV	$4.96 \times 10^{-3} \pm 9.3 \times 10^{-4}$	$4.7 \times 10^{-3} \pm 4.8 \times 10^{-4}$
21.5 – 46.4 MeV	$6.26 \times 10^{-3} \pm 6.9 \times 10^{-4}$	$7.58 \times 10^{-3} \pm 4.4 \times 10^{-4}$
46.4 – 100 MeV	$8.83 \times 10^{-3} \pm 7.6 \times 10^{-4}$	$1.02 \times 10^{-2} \pm 4 \times 10^{-4}$
100 – 215 MeV	$6.44 \times 10^{-3} \pm 4.6 \times 10^{-4}$	$1.06 \times 10^{-2} \pm 4.6 \times 10^{-4}$
215 – 464 MeV	$1.16 \times 10^{-2} \pm 6.9 \times 10^{-4}$	$1.33 \times 10^{-2} \pm 4.3 \times 10^{-4}$
464 – 1000 MeV	$1.1 \times 10^{-2} \pm 5 \times 10^{-4}$	$2.04 \times 10^{-2} \pm 8.4 \times 10^{-4}$
1 – 2.15 GeV	$8.51 \times 10^{-3} \pm 3.6 \times 10^{-4}$	$1.72 \times 10^{-2} \pm 5.2 \times 10^{-4}$
2.15 – 4.64 GeV	$7.85 \times 10^{-3} \pm 2.8 \times 10^{-4}$	$1.81 \times 10^{-2} \pm 4.5 \times 10^{-4}$
4.64 – 10 GeV	$1.02 \times 10^{-2} \pm 3.1 \times 10^{-4}$	$1.36 \times 10^{-2} \pm 3.1 \times 10^{-4}$
10 – 21.5 GeV	$4.12 \times 10^{-3} \pm 2.3 \times 10^{-4}$	$6.49 \times 10^{-3} \pm 1.6 \times 10^{-4}$

Table B.5: Summary of energy deposited by neutrons into the LAAS detectors uncovered and covered by a 260 μm thick Alumina cover.

Energy bins	Av. Edep/muon Without cover (keV)	Av. Edep/muon With cover (keV)
1 – 2.15 MeV	$2.95 \times 10^0 \pm 3.2 \times 10^{-2}$	$1 \times 10^{-1} \pm 3.8 \times 10^{-3}$
2.15 – 4.64 MeV	$1.51 \times 10^0 \pm 1.6 \times 10^{-2}$	$1.98 \times 10^0 \pm 2 \times 10^{-2}$
4.64 – 10 MeV	$7.68 \times 10^{-1} \pm 1 \times 10^{-2}$	$9.24 \times 10^{-1} \pm 8.4 \times 10^{-3}$
10 – 21.5 MeV	$4.07 \times 10^{-1} \pm 5.5 \times 10^{-3}$	$4.53 \times 10^{-1} \pm 6 \times 10^{-3}$
21.5 – 46.4 MeV	$2.41 \times 10^{-1} \pm 3.4 \times 10^{-3}$	$2.73 \times 10^{-1} \pm 3.8 \times 10^{-3}$
46.4 – 100 MeV	$1.69 \times 10^{-1} \pm 2.4 \times 10^{-3}$	$1.91 \times 10^{-1} \pm 2.7 \times 10^{-3}$
100 – 215 MeV	$1.28 \times 10^{-1} \pm 1.9 \times 10^{-3}$	$1.5 \times 10^{-1} \pm 2.1 \times 10^{-3}$
215 – 464 MeV	$1.23 \times 10^{-1} \pm 1.9 \times 10^{-3}$	$1.41 \times 10^{-1} \pm 2.1 \times 10^{-3}$
464 – 1000 MeV	$1.21 \times 10^{-1} \pm 1.8 \times 10^{-3}$	$1.36 \times 10^{-1} \pm 2 \times 10^{-3}$
1 – 2.15 GeV	$1.18 \times 10^{-1} \pm 1.7 \times 10^{-3}$	$1.4 \times 10^{-1} \pm 2 \times 10^{-3}$
2.15 – 4.64 GeV	$1.24 \times 10^{-1} \pm 1.9 \times 10^{-3}$	$1.44 \times 10^{-1} \pm 2.2 \times 10^{-3}$
4.64 – 10 GeV	$1.33 \times 10^{-1} \pm 1.9 \times 10^{-3}$	$1.41 \times 10^{-1} \pm 2 \times 10^{-3}$

Table B.6: Summary of energy deposited by muons into the LAAS detectors uncovered and covered by a 260 μm thick Alumina cover.

List of Publications

Listed in reverse chronological order:

1. **J. Mekki**, M. Moll, M. Fahrer, M. Glaser, L. Dusseau.
“A new Approach in Predicting the Response of Silicon p-i-n Diodes used as Radiation Monitoring Sensors up to Very High Fluences”, *Paper presented at the 10th international conference on Radiation Effects on Components and System (Radecs 2009)*, Bruges, Belgium, 14-18 September, 2009. **Award for the best student paper of the conference (Jean Marie Palau Award)**. Submit to the scientific journal “*IEEE Transactions on Nuclear Science*” in September 2009.
2. **J. Mekki**, L. Dusseau, M. Glaser, S. Guatelli, M. Moll, M. G. Pia, F. Ravotti.
“Packaging Effects on RadFET sensors for High Energy Physics Experiments”, *Paper presented at the International workshop on Radiation Effects on Components and System (Radecs 2008)*, Jyvaskyla, Finland, 10-12 September, 2008. *IEEE Transactions on Nuclear Science*, vol. 56, no. 4, pp. 2061-2069, 2009.

Other contributions to conferences and workshops:

3. **J. Mekki**, M. Moll, M. Fahrer, M. Glaser.
“Forward I-V Characteristics of Silicon p-i-n diodes after Proton Irradiation ”, *14th RD50 Workshop on Radiation Hard Semiconductor Devices for Very High Luminosity Colliders*, Freiburg, Allemagne, 3-5 Juin 2009.

4. **J. Mekki, M. Fahrer, M. Glaser, M. Moll, F. Ravotti.**

“Development Studies on Radiation Monitoring Sensors for LHC & Super-LHC Experiments within the framework of the LHC Experiments RADMON working group”, EIRO School on Instrumentation (ESI 2009), Genève, Suisse, 11-15 may 2009.

Acknowledgements

First of all, I like to express my thanks to Prof. Laurent Dusseau from University of Montpellier 2 and to Dr. Michael Moll from CERN for supervising this thesis work and for their continuous support, advice and encouragements.

I am grateful to all the members of the “Physics Detector Technology” group of the “Physics” department for the good co-operation and the friendly and pleasant working atmosphere. In particular, I would like to thank the PH/DT group leader Dr. Christian Joram for hosted me within his team. In addition, I like to thanks Francoise, Antoine and Ian McGill from the CERN PH/DT Bonding Lab for their support and their daily good moon. It was a pleasure for me to work at CERN in such scientific, technical and friendly environment.

A very special thanks to Michael Moll, for being always confident on me and on the scientific directions that I have chosen to take during this thesis. Also for the many discussions about semiconductor physics, data analysis and for the patience he demonstrated in correcting my english manuscripts. *Vielen Dank Michael !*

I am also grateful to Maurice Glaser for technical skills he learned to me and the several discussions on the different possibilities for the research project. Furthermore, I would like to thanks Manuel Fahrer for his scientific and technical support, especially for the collaborative work carried out on the program that made my measurements not so easy, but almost.

There are many people without whom this work would not have been possible. I like to thanks Dr. Maria Grazia Pia for her strong support and help concerning the Geant4 study, especially for helping me to write my first publication. I also like to thanks Dr. Susanna Guatelli for her strong encouragement and many discussions allowing the success of this Geant4 project and Dr. Federico Ravotti for his friendly support.

Of course I like to thanks all my family and friends, especially my mother, Floriane Caupert, as my in-laws, Susanne and Jean-Bernard Chazan for being sure that I would manage to get my PhD thesis with honours. During moments of doubt, it was essential !

I would like to conclude this thesis by expressing my feelings to Anne-Laure, who follows me without hesitation from Montpellier to Annecy during these 3 years. She gave me the energy to

conclude this part of my life in the best possible way and to start another one by saying me "yes" and becoming my wife at the end of this thesis. *Comme une évidence ... Merci Anne-Laure !*

Bibliography

- [Ago03] S. Agostinelli, et al., “GEANT4 - A Simulation Toolkit”, *Nuclear Instrumentation & Methods in Physics Research*, A506:250-303, 2003.
- [ALI95] ALICE Collaboration. “Technical Proposal”. *CERN/LHCC 95-71 LHCC/P3*, 1995.
- [All06] J. Allison et al., “Geant4 Developments and Applications”, *IEEE Transactions on Nuclear Science*, 53(1):270-278, 2006.
- [Ama05] K Amako et al., “Comparison of Geant4 electromagnetic physics models against the NIST reference data”, *IEEE Transactions on Nuclear Science*, 52(4):910-918, 2005.
- [And77] H. H. Andersen and J. F. Ziegler, “The Stopping and Ranges of Ions in Matter”, *Edition Oxford: Pergamon Press*, 1977.
- [And05] B. L. Anderson and R. L. Anderson, “Fundamentals of Semiconductor Devices”, *published by McGraw-Hill Companies*, ISBN 0-07-236977-9, 2005.
- [Apo99] J. Apostolakis, S. Giani, M. Maire, P. Nieminen, M.G. Pia, L. Urban, “Geant4 low energy electromagnetic models for electrons and photons”, *INFN/AE-99/18*, 1999.
- [AST94] ASTM Committee. “Standard practice for characterizing neutron fluence spectra in terms of an equivalent monoenergetic neutron fluence for radiation hardness testing of electronics”. *ASTM E772-94 (revision)*, 1994.
- [ATL97] ATLAS. “ID Technical Design Report”. *CERN/LHCC/97-16 and 17*, 1997.

- [Ban00] T. C. Bandwell, A. Jayakumar, "Exact analytical solution for current flow through diode series resistance", *Electronics Letters*, vol. 36, no. 4, pp. 291-292, 2000.
- [Bar05] S. Baranov, M. Bosman, I. Dawson, V. Hedberg, A. Nisati and M. Shupe, "Estimation of Radiation Background, Impact on Detectors, Activation and Shielding Optimization in ATLAS", *Atlas Radiation Background Task Force Summary Document, ATL-GEN-2005-001*, 2005.
- [Bat06] A. G. Bates, "Czochralski silicon radiation detectors", *Nuclear Instrumentation & Methods in Physics Research*, A569:73-76, 2006.
- [Ber99] M. J. Berger, J. H. Hubbell, S. M. Seltzer, J. S. Coursey, and D. S. Zucker, "XCOM: Photon Cross Section Database", *National Institute of Standards and Technology*, 1999.
- [Bic06] H. Bichsel, D.E. Groom, S.R. Klein. Passage of particle through matter. W.-M. Yao *et al*, " Review No. 27 on Passage of particles through matter", *J. Phys. G33*, p. 258, 2006.
- [Bog06] A. G. Bogdanov, H. Burkhardt, V. N. Ivanchenko, S. R. Kelner, R. P. Kokoulin, M. Maire, A. M. Rybin, and L. Urban, "Geant4 simulation of production and interaction of muons", *IEEE Transactions on Nuclear Science*, 53(2):513-519, 2006.
- [Bpw] BPW34 silicon pin photodiode Datasheet. Available online from OSRAM Opto-Semiconductors: <http://www.osram-os.com>.
- [Bro02] T. J. Brodbeck, A. Chilingarov, T. Sloan, E. Fretwurst, M. Kuhnke, G. Lindstroem, "Carrier mobilities in irradiated silicon", *Nuclear Instrumentation & Methods in Physics Research*, A477:287-292, 2002.
- [Bru95] G.J. Brucker, S. Kronenberg and F. Gentner, "Effects of package geometry, materials and die design on energy dependence of pMOS dosimeters", *IEEE Transactions on Nuclear Science*, 42(1):33-40, 1995.
- [Bur05] H. Burkhardt V.M. Grichine, P. Gumplinger, V.N. Ivanchenko, R.P. Kokoulin, M. Maire, L. Urban, "Geant4 Standard Electromagnetic Package", *in Proceeding of Conference on Monte Carlo Method, American Nuclear Society*, 2005.
- [CER04] CERN. "The LHC Technical Design Report", Vol. 1-4. *CERN-2004-003*, 2004.

- [Cha01] S. Chauvie et al., “Geant4 Low Energy Electromagnetic Physics”, in *Proceedings of the Computing in High Energy and Nuclear Physics (CHEP) conference*, Beijing, pp. 337-340, China, 2001.
- [Cha04] S. Chauvie et al., “Geant4 Low Energy Electromagnetic Physics”, in *Conference Record IEEE Nuclear Science Symposium*, N33-165, 2004.
- [CMS94] CMS Collaboration. “Technical Proposal”. *CERN/LHCC/94-38*, 1994.
- [Col07] GEANT4 Collaboration, Geant4 User's Guide for Toolkit Developers, available on the website <http://geant4.cern.ch/>, 2007.
- [Cor96] R. M. Corless, G. H. Gonnet, D. E. G. Hare, D. J. Jeffrey and D. E. Knuth, “On the LambertW function”, in *Advances in Computational Mathematics*, ISSN 1572-9044, vol. 5, no. 1, pp. 329-359, 1996.
- [Cor03] G. Corti and L. Shekhtman, “Radiation background in the LHCb experiment”, *LHCb-Note-2003-083*, 2003.
- [Cul97] D. Cullen, J. H. Hubbell, L. Kissel, “EPDL97: The Evaluated Photon Data Library, 97 version”, *LLNL UCRL-50400*, vol. 6, rev. 5, 1997.
- [Czo18] J. Czochralski, “Metalle”, *Z. Phys. Chem.*, 92:219, 1918.
- [Daw00] I. Dawson and C. Buttar, “The radiation environment in the ATLAS inner detector”, *Nucl. Instr. & Meth. in Physics Research*, A453:461-467, 2000.
- [Deg00] P. V. Degtyarenko, M.V. Kossov and H. P. Wellisch, “Chiral invariant phase space event generator”, *The European Physical Journal A*, volume 9, no. 3, pp. 411-420, 2000.
- [Deh04] L. Dehimi, N. Sengouga, B. K. Jones, “Modelling of semi-conductor diodes made of high defect concentration, irradiated, high resistivity and semi-insulating material: the current-voltage characteristics”, *Nucl. Instr. & Meth. in Physics Research*, A519:532-544, 2004.
- [Dup02] S. A. Dupree and S. K. Fraley, “Monte Carlo Primer – A Practical Approach to Radiation Transport, Kluwer Academic/Plenum publisher, 2002.
- [Ebe69] P. J. Ebert, A.F. Lauzon, E. M. Lent. “Transmission and Backscattering of 4.0- to 12.0-MeV Electrons”. *Physical. Review.* vol.183, no. 2, pp. 422-430, 1969.
- [Ers04] T. Ersmark et al., “Status of the DESIRE Project: Geant4 Physics Validation Studies and First Results From Columbus/ISS Radiation Simulations”, *IEEE Transactions on Nuclear Science*, 51(4):1378-1384, 2004.

-
- [Fas90] A. Fassó, K. Goebel, Herwig Schopper, “Shielding against high energy radiation”, *Springer-Verlag edition*, ISBN 978-3-540-52125-9, 1990.
- [Fas03] A. Fassó et al., “The physics models of FLUKA: status and recent developments”, in *Proceedings of the Computing in High Energy and Nuclear Physics (CHEP) conference*, La Jolla, California, March 2003.
- [Fer05] A. Ferrari, P. R. Sala, A. Fassó, and J. Ranft, “Fluka: a multi-particle transport code”, *Report CERN-2005-010*, Geneva, Oct. 2005.
- [Fes85] H. S. Fesefeldt, “The simulation of hadronic showers: physics and applications”, *PITHA-85-02*, RWTH Aachen, September 1985.
- [Fol03] G. Folger and J. P. Wellisch, “String parton models in Geant4”, in *Proceedings of the Computing in High Energy and Nuclear Physics (CHEP) conference*, La Jolla, California, March 2003.
- [Fol04] G. Folger, V.N. Ivanchenko, and J.P. Wellisch, “The Binary Cascade”, *The European Physical Journal A*, volume 21, pp. 407-417, 2004.
- [Gea] Geant4 website : <http://geant4.cern.ch/>
- [Gia99] S. Giani, V.N. Ivanchenko, G. Mancinelli, P. Nieminen, M.G. Pia, L. Urban, “Geant4 simulation of energy losses of slow hadrons”, *INFN Report INFN/AE-99/20*, 1999.
- [Gia05] F. Gianotti et al, “Physics potential and experimental challenges of the LHC luminosity upgrade”, *The European Physical Journal C*, volume 39, pp. 293-333, 2005.
- [Gla06] M. Glaser, S. Guatelli, B. Mascialino, M. Moll, M.G. Pia, F. Ravotti., “Geant4 Simulation for LHC Radiation Monitoring”, in *Conf. Rec. 2006, IEEE Nuclear Science Symposium*, N35-4.
- [Gla08] M. Glaser, F. Ravotti, M. Moll, “Dosimetry Assessments in the Irradiation Facilities at the CERN-PS Accelerator”, *IEEE Transactions on Nuclear Science*, 53(4):2016-2022, 2008.
- [Gla61] S. L. Glashow, “Partial-Symmetries of Weak Interactions”, *Nuclear Physics*, vol. 22, pp. 579-588, 1961.
- [Gou95] J. P. Gourber, “The LEP2 and LHC Projects at CERN”, *CERN/AT/97-37, International Europhysics Conference on High Energy Physics*, Brussels, Belgium, 27 July – 2 August 1995.

- [Gou05] A. Gouldwell-Bates. “Developments in Silicon Detectors and their impact on LHCb Physics Measurements”, PhD thesis, University of Glasgow, 2005. CERN-THESIS-2006-003.
- [Gri96] P. Griffin et al. SAND92-0094 (Sandia National Laboratories, Nov.93), 1996. Neutron cross sections taken from ENDF/B-VI, ORNL. See also <http://sesam.desy.de/members/gunnar/Si-dfuncs.html>
- [Hae91] N. M. Haegel, “Relaxation semiconductors: in theory and in practice”, *Journal of Applied Physics*, A53:1-7, 1991
- [Haj02] W. Hajdas, F. Burri, Ch. Eggel, R. Harboe-Sorensen and R. de Marino. “Radiation Effects Testing Facilities in PSI during implementation of the Proscan Project”, in *Proc. 2002 IEEE Radiation Effects Data Workshop*, pp-160-164, 2002.
- [Har03] J. Häkkinen et al, “Processing of microstrip detectors on Czochralski grown high resistivity silicon substrates”, *Nucl. Instr. & Meth. in Physics Research*, A514:173-179, 2003.
- [Hen92] W. R. Hendee and E. R. Ritenour, “Medical imaging physics”, 3rd ed. St. Louis: Mosby-Year Book, 1992.
- [Her04] L. Fernandez Hernando, “Development of a Beam Condition Monitor system for the experimental areas of the LHC using CVD diamond”. PhD thesis, Ecole Polytechnique Federale de Lausanne, Switzerland, 2004. These 3122.
- [Hol02] A. G. Holmes-Siedle and L. Adams, “Handbook of Radiation Effects”, Oxford University Press, second edition, ISBN 0-19-850733-X, 2002.
- [Hru06] P. Hruska, Z. Chobola, L. Grmela, “Diode I-U curves Fitting with Lambert W function”, In *Proc. of the International Conference on Microelectronics (MIEL2006)*, Belgrade, Serbia and Montenegro, 14-17 May, 2006.
- [Huh93a] M. Huhtinen and P. Aarino, “Estimation of pion induced displacement damage in silicon”, *HU-SEFT R 1993-02*, 1993.
- [Huh93b] M. Huhtinen and P. Aarnio, “Pion induced displacement damage in silicon devices”, *Nucl. Instr. & Meth. in Physics Research*, A335:580, 1993.
- [Huh95] M. Huhtinen, “Radiation Environment Simulations for the CMS Detector”, *CERN CMS Tech. Note 95-19*, 1995.
- [Huh00] M. Huhtinen and F. Faccio, “Computational method to estimate Single Event Upset rates in an accelerator environment”, *Nucl. Instr. & Meth. in Physics Research*, A450:155-172, 2000.

- [Huh02] M. Huhtinen, 2002. "Radiation Environment in Experimental (CMS) area", *Presentation given at the Radiation Effects course*, 10 april 2000.
- [Icr93] International Commission on Radiation Units and Measurements, "ICRU Report 49, Stopping Powers and Ranges for Protons and Alpha Particles", 1993.
- [Iva03] V. Ivanchenko, G. Folger, J. P. Wellisch, T. Koi and D. H. Wright, "The Geant4 Hadronic Verification Suite for the Cascade Energy Range", in *Proceedings of the Computing in High Energy and Nuclear Physics (CHEP) conference*, La Jolla, California, March 2003.
- [Jak06] A. Jaksic, Y. Kimoto, A. Mohammadzadeh, and W. Hajdas. "RADFET Response to Proton Irradiation Under Different Biasing Configurations". *IEEE Transactions on nuclear science*, 53(4):2004_2007, 2006.
- [Jun09] W. Jung. M Guziewicz, "Schottky diode parameters extraction using Lambert W function", *Mater. Sci. Eng B*, 2009. Doi:0.1016/j.mseb.2009.02.013
- [Jon99] B. K. Jones, M. McPherson, "Radiation damaged silicon as a semi-insulating relaxation semiconductor: static electrical properties", *Semiconductor Science and Technology*, volume 14, pp. 667-678, 1999.
- [Kea03] A. B. Keating, A. Mohammadzadeh, R. Nickson, A. Jaksic and W. Hajdas, "Modelling packaging effects on proton irradiation response on NMRC RadFETs. New GEANT4 simulations and Co-60 irradiations", in proceeding of the *Radiation Effects in Components and Systems Conference (RADECS 03)*, Noordwijk, The Netherlands, September 15-19, pp. 457-463, 2003.
- [Kei] Keithley, "Model 2400 Source meter, User's manual", available on-line from Keithley Instruments Inc. page: <http://www.keithley.fr/products/currentvoltage/>
- [Kol33] A. N. Kolmogorov, "On the empirical determination of a distribution law", *Gior. Ist. Ital. Attuari*, vol. 4, pp. 83-91, 1933.
- [Kon92] A. Yu. Konobeyev et al, "Neutron displacement cross-sections for structural materials below 800 MeV", *J. Nucl. Mater.*, 186:117, 1992.
- [Kos02] M. Kossov, "Chiral-invariant phase space model", *The European Physical Journal A*, volume 14, no. 3, pp. 265-269, 2002.
- [Kra04] G. Kramberger. "Development of ATLAS Radiation Monitor", presentation given at the CERN RADMON meeting, 16 November 2004.

- [Lec08] A. Lechner and M. G. Pia, "Analysis of Geant4 physics models for the simulation of proton depth dose profiles in radiotherapeutic applications", in conference record of the *IEEE Nuclear Science Symposium*, Dresden, Germany, October 19-25, pp. 875-882, 2008.
- [Lec09] A. Lechner, M. G. Pia and M. Sudhakar, "Validation of Geant4 low energy electromagnetic processes against precision measurements of electron energy deposit", *IEEE Transactions on Nuclear Science*, 56(2):398-416, 2009.
- [Ler04] C. Leroy, P. G. Rancoita, "Principles of Radiation Interaction in Matter and Detection", *World scientific Publishing Co. Pte. Ltd*, ISBN 981-238-909-1, 2004.
- [LHC98] LHCb Collaboration. "Technical Proposal". CERN/LHCC/98-4. LHCC/P4, 1998.
- [Lin80] V. A. J. van Lint, T. M. Flanagan, R. E. Leadon, J. A. Naber, V. C. Rogers, "Mechanisms of Radiation Effects in Electronic Materials", *John Wiley & sons*, 1980.
- [Lin94] W. Lin, "Oxygen in Silicon", vol. 52 of *Semiconductors and Semimetals*, chapter "The incorporation of oxygen into silicon crystals", pp. 9-52. Academic Press Inc., Boston, San Diego, New York, London, Sydney, Tokyo, Toronto, 1994,. ISBN 0-12-752142-9.
- [Loh85] W. Lohmann, R. Kopp and R. Voss, "Energy Loss of Muons in the Energy Range 1-10000 GeV", *CERN 85-03, Experimental Physics Division*, 1985.
- [Mal92] L. Malfante, "Utilisation de dosimètres semi-conducteurs au Silicium autour des accélérateurs de particules à haute énergie". *CERN-TIS-CFM/IR/92-09*, 1992.
- [Man07] I. Mandic, V. Cindro, A. Gorisek, G. Kramberger and M. Mikuz, "Online Integration Radiation Monitoring System for the ATLAS Detector at the Large Hadron Collider", *IEEE Transactions on Nuclear Science*, 54(4):1143-1150, 2007.
- [McP97a] M. McPherson, B. K. Jones, T. Sloan, "Suppression of irradiation effects in gold-doped silicon detectors", *Journal of Physics-London-D: Applied Physics*, volume 30, pp. 3028-3035, 1997.
- [McP97b] M. McPherson, B. K. Jones, T. Sloan, "Effect of radiation damage in silicon p-i-n photodiodes", *Semiconductor Science and Technology*, volume 12, pp. 1187-1194, 1997.

- [McP04] M. McPherson, “The space charge relaxation behavior of silicon diodes irradiated with 1 MeV neutrons”, *Nucl. Instr. & Meth. in Physics Research*, A517:42-53, 2004.
- [Mol99] M. Moll. “Radiation damage in silicon particle detectors – Microscopic defects and Macroscopic properties”, *PhD thesis*, University of Hamburg, Germany, 1999. DESY-THESIS-1999-040, ISSN 1435-8085.
- [Mol02] M. Moll, E. Fretwurst, M. Kuhnke and G. Lindström, “Relation between microscopic defects and macroscopic changes in silicon detector properties after hadron irradiation”, *Nucl. Instr. & Meth. in Physics Research*, B186:100-110, 2002.
- [Mor99] F.F. Moreno, “Mechanisms of Radiation Interaction with Materials”, *RADECS Short Course*, 1999.
- [Mou94] I. Mouret, M. Allenspach, R. D. Schrimpf, J. R. Brews and K. F. Galloway, “Temperature and Angular Dependence of Substrate Response in SEGR”, *IEEE Transactions on Nuclear Science*, 41(6):2216-2221, 1994.
- [Nis09] National Institute of Standards and Technologies (NIST) Physical Reference Data [Online]. Available on: <http://physics.nist.gov/PhysRefData/>.
- [Pas02] B. Pastircák, 2002. Radiation Levels in ALICE – Presentation given at the CERN ALICE Forum, 20 March 2002.
- [Per97] S. T. Perkins, D. E. Cullen, S. M. Seltzer, “Tables and Graphs of Electron-Interaction Cross-Sections from 10 eV to 100 GeV Derived from the LLNL Evaluated Electron Data Library (EEDL)”, *LLNL UCRL-50400*, vol. 31, 1997.
- [Pey08] D. Peyre, Ch. Binois, R. Mangeret et al., “SEGR study on Power MOSFETs: Multiple impacts assumption”, *IEEE Transactions on Nuclear Science*, 55(4):2181-2187, 2008.
- [Pot95] K. Potter, M. Höfert and G. Stevenson. “Individual monitoring in high-energy stray radiation fields”. *CERN TIS-RP/IR/95-19*, 1995.
- [Pro89] Z. Prouza, O. Bratz, B. Sopko, F. Spurny, A. Skubal, J. Kits and F. Latal, “Dosimetric parameters of a new Czechoslovak neutron Si diode”, *Radiation Protection Dosimetry*, 28(4):277-281, 1989.
- [Que73] H. J. Queisser, “Semiconductors in the relaxation régime”, in *Proceeding of the European Solid-State Device Research Conference (ESSDERC'72)*, no.

- 15, ISSN 0305-4632, vol. 15, Lancaster, UK, 12-15 September, pp:145-188, 1973.
- [Rad] LHC Experiment Radiation Monitoring Working Group (RADMON). <http://lhcb-expt-radmon.web.cern.ch/lhc-expt-radmon>.
- [Rav03] Ravnik and R. Jeraj, "Research Reactor Benchmarks", *Nuclear Science and Engineering*, vol. 145, pp. 145-152, 2003.
- [Rav04] F. Ravotti, M. Glaser, M. Moll, K. Idri, J-R. Vaillé, H. Prevost and L. Dusseau, "Conception of an Integrated Sensor for the Radiation Monitoring of the CMS Experiment at the Large Hadron Collider", *IEEE Transactions on Nuclear Science*, 51(6):3642-3648, 2004.
- [Rav05a] F. Ravotti, M. Glaser and M. Moll, SENSOR CATALOGUE – Data compilation of solid-state sensors for radiation monitoring, *TS-Note-2005-002 (CERN EDMS No.590497)*, 13 May, 2005.
- [Rav05b] F. Ravotti, M. Glaser, M. Moll, Ch. Ilgner, B. Camanzi and A. G. Holmes-Siedle, "Response of RadFET Dosimeters to High Fluences of Fast Neutrons", *IEEE Transactions on Nuclear Science*, 52(4):959_965, 2005.
- [Rav06] F. Ravotti, "Development and Characterization of Radiation Monitoring Sensors for the High Energy Physics Experiments of the CERN LHC Accelerator (Thesis)", University Montpellier II, France, 2006. *Also in CERN-THESIS-2007-013*.
- [Rav07] F. Ravotti, M. Glaser, A.B. Rosenfeld, M.L.F. Lerch, A.G. Holmes-Sielde and G. Sarrabayrouse, "Radiation Monitoring in Hadron Environment at CERN: From the IRRAD6 Facility to the LHC Experiments", *IEEE Transactions on Nuclear Science*, 54(4):1170_1177, 2007.
- [Rav08a] F. Ravotti, "Technical and Functional Specification of the TOTEM on-line radiation monitoring system", *(CERN EDMS No.874945)*, 2008.
- [Rav08b] F. Ravotti, M. Glaser, M. Moll and F. Saigné, "BPW34 Commercial p-i-n Diodes for High-level 1-MeV Neutron Equivalent Fluence Monitoring", *IEEE Transactions on Nuclear Science*, 55(4):2133-2140, 2008.
- [RD50] RD50 collaboration. Available on <http://rd50.web.cern.ch/rd50/>.
- [Roh54] F. Rohrlich and B. C. Carlson, "Positron-Electron Differences in Energy Loss and Multiple Scattering", *Physical Review*, vol. 93, no. 1, pp. 38-44, 1954.

- [Roo72] W. V. Roosbroeck, H. C. Cassey, "Transport in relaxation semiconductors", *Physical. Review B.* vol. 5, no. 6, pp. 2154-2155, 1972.
- [ROSE] The ROSE Collaboration (R&D On Silicon for future Experiments) CERN-RD48 Collaboration, available on <http://rd48.web.cern.ch/RD48/>
- [Ros95] A.B Rosenfeld, M.G. Carolan, G.I Kaplan, B.J. Allen and V. Khivrich, "MOSFET dosimeters: the role of encapsulation on dosimetric characteristic in mixed-gamma neutron and megavoltage x-ray field", *IEEE Transactions on Nuclear Science*, 42(6):1870_1877, 1995.
- [Ros03] A. B. Rosenfeld et al., "Neutron dosimetry with planar Silicon p-i-n diodes", *IEEE Transactions on Nuclear Science*, 44(6):2001-2006, 1997.
- [Rug02] F. Ruggiero (Editor) et al. "LHC luminosity and energy upgrade: a feasibility study", *LHC Project Report 626, CERN*, 2002.
<http://cern.ch/lhc-proj-IR-upgrade/>.
- [San98] J. Santana, B. K. Jones, "Semi-insulating GaAs as a relaxation semiconductor", *Journal of Applied Physics*, 83(12):7699-7705, 1966.
- [Sex98] F. W. Sexton, D. M. Fleetwood, M. R. Shaneyfelt, P. E. Dodd, G. L. Hash, L. P. Schanwald and R. A. Loemker, "Precursor Ion Damage and Angular Dependence of Single Event Gate Rupture in thin Oxides", *IEEE Transactions on Nuclear Science*, 45(6):2509-2518, 1998.
- [She89] W. Q. Shen, B. WANG, J. FENG, W. L. ZHAN, Y. T ZHU and E. P. FENG, "Total reaction cross section for heavy-ion collisions and its relation to the neutron excess degree of freedom", *Nucl. Instr. & Meth. in Physics Research*, A491:130-146, 1989.
- [Shu03] M. Shupe, "Radiation Background Task Force. Results from GCALOR with the Baseline shielding layout of Jan03". Available on:
http://atlas.web.cern.ch/Atlas/GROUPS/PHYSICS/RADIATION/Radiation_Levels.html
- [Smi39] N. V. Smirnov, "On the estimation of the discrepancy between empirical curves of distributions for two independent samples", *Bull. Math. Univ. Moscow*, 1939.
- [Sop91] B. Sopko, J. Pavlu, I. Macha, Z. Prouza, F. Spurny, J. Kits, and F. Latal, "Dosimetric parameters and application of Czechoslovak Long Base Silicon Diode", in *Proceeding of the Radiation Effects in Components and Systems Conference (RADECS91)*, IEEE Catalogue 91THO400-2, Montpellier, France, September 9-12, pp:81-83, 1991.

- [Sum93] G. P. Summers et al., "Damage correlations in semiconductors exposed to gamma, electrons and proton radiations", *IEEE Transactions on Nuclear Science*, 40:1372, 1993.
- [Sva68] N. Svartholm, "Elementary Particle Theory", *Proceedings of Nobel Symposium*, 19-25 May, Aspenäsgården, Lerum, 1968.
- [Swa66] M. Swartz, M. Thurston, "Analysis of effect of fast-neutron bombardment on the current-voltage characteristic of conductivity modulated p-i-n diodes", *Journal of Applied Physics*, 37(2):745-755, 1966.
- [Sze81] S. M. Sze, "Physics of semiconductor devices", John Wiley and sons, 2nd edition, 1981.
- [Sze01] S. M. Sze, "Semiconductor Devices – Physics and Technology", John Wiley and sons, 2nd edition, 2001.
- [Tab72] T. Tabata, R. Ito. "Generalized Semiempirical equations for the Extrapolated Range Of Electrons". *Nucl. Instr. & Meth. in Physics Research*, 103(1):85-91, 1972.
- [Tab75] T. Tabata, R. Ito. "A Generalized Empirical Equation for the Transmission Coefficient of Electrons". *Nucl. Instr. & Meth. in Physics Research*, 127(3):429-434, 1975.
- [Tav91] M. Tavlet, M. E. Leon-Florián. "PSAIF: The PS-ACOL irradiation facility at CERN", in *Proceeding of the First European Conference on Radiation and its Effects on Components and Systems*, RADECS 91, La Grande-Motte, France, September 9-12, pp: 582-585, 1991.
- [Tav05] M. Tavlet, 2005. Presentation given at the CERN RADMON meeting, 22 March 2005. Available online: <http://www.cern.ch/lhc-expt-radmon>.
- [Tel97] Telefunken Semiconductors, 1997. Infrared emitters and detectors data book.
- [The62] H. C.. Theuerer. U. S. patent. 3,060,123, 1962.
- [Tit95] J. L. Titus, C. F. Wheatley, D. I. Burton, I. Mouret, M. Allenspach, J. Brews, R. Schrimpf, K. Galloway and R. L. Pease. "Impact of Oxide Thickness on SEGR Failure in Vertical Power MOSFETs; Development of a Semi-Empirical Expression", *IEEE Transactions on Nuclear Science*, 42(6):1928-1934, 1995.

- [Tit96] J. L. Titus, C. F. Wheatley, "Experimental Studies of Single-Event gate Rupture and Burnout in Vertical Power MOSFETs", *IEEE Transactions on Nuclear Science*, 43(2):533-545, 1996.
- [TOT99] TOTEM. "Total Cross Section, Elastic scattering and Diffractive Dissociation at the LHC". *CERN/LHC/99-7*, 1999.
- [Tri96] R. K. Tripathi, Francis A. Cucinotta and John W. Wilson, "Accurate universal parameterization of absorption cross sections", *Nucl. Instr. & Meth. in Physics Research*, B117:347-349, 1996.
- [Tri97] R. K. Tripathi, Francis A. Cucinotta and John W. Wilson, "Universal Parameterization of Absorption Cross Sections", *NASA Technical Paper 3621*, January 1997.
- [Tri99a] R. K. Tripathi, Francis A. Cucinotta and John W. Wilson, "Universal Parameterization of Absorption Cross Sections - Light Systems", *NASA Technical Paper 1999-209726*, 1999.
- [Tri99b] R. K. Tripathi, Francis A. Cucinotta and John W. Wilson, "Universal Parameterization of Absorption Cross Sections III - Light Systems", *Nucl. Instr. & Meth. in Physics Research*, B155:349-356, 1999.
- [Urb05] L. Urban, "A Model for multiple scattering in Geant4", in Proceeding of the *Monte Carlo Method* conference, *American Nuclear Society*, La Grange Park, IL, 2005.
- [Wal69] P. J. Walsh, R. Vogel, E. J. Evans, "Conduction and Electrical Switching in Amorphous Chalcogenide Semiconductor Films", *Physical. Review.* vol.178, no. 3, pp. 1274-1278, 1969.
- [Wel03] J.P. Wellisch, "Geant4 hadronic physics status and validation for large HEP detectors", in *Proceedings of the Computing in High Energy and Nuclear Physics (CHEP)* conference, La Jolla, California, March 2003.
- [Wei67] S. Weinberg, "A model of Leptons", *Physical Review Letters*, vol. 19, no. 21, pp. 1264-1266, 1967.
- [Wie07] D. Wiednerand and G. Corti, "LHCb Radiation monitors for detectors and detector electronics", *LHCb Eng. Note*, (CERN EDMS No.860046), 2007.
- [Wij05] T. Wijnands. "Interfacing with the LHC accelerator during physics operation", in *proceeding of the 11th LECC workshop*, Heideberg, Germany, TS-Note 2005-054, 2005.

-
- [Wri06] D. H. Wright, T. Koi, G. Folger, V. Ivantchenko, M. Kossov, N. Starkov, A. Heikkinen and H. P. Wellisch, “Recent Developments and Validations in Geant4 Hadronic Physic”, in *AIP Conf. Proc.*, vol. 867, pp. 479-486, Oct. 2006.
 - [Wro87] T. F. Wrobel, “On heavy ion induced hard-errors in dielectric ruptures”, *IEEE Transactions on Nuclear Science*, 34(6):1262-1268, 1987.
 - [Wro05] F. Wrobel, “Fundamentals on Radiation-Matter Interaction”, *RADECS Short Course*, 19 to 23 September, Cap d'agde, France, 2005.
 - [Zei94] C. Zeitnitz and T. A Gabriel, “The GEANT-CALOR interface and benchmark calculations of ZEUS test calorimeters”, *Nucl. Instr. & Meth. in Physics Research*, A349(1):106-111, 1994.
 - [Zie85] J. F. Ziegler, J. P. Biersack, and U. Littmark, “The Stopping and Ranges of Ions in Solids”, *Edition Oxford: Pergamon Press*, 1985.
 - [Zie04] J. F. Ziegler, “SRIM-2003”, *Nuclear Instrumentation & Methods in Physics Research*, B219-220:1027-1036, 2004.

RESUME en français :

Le collisionneur de hadrons du CERN « le LHC », a été construit dans le but d'étudier la nature et la constitution de la matière. A l'intérieur de l'accélérateur, les collisions d'hadrons chargés produiront un champ radiatif complexe et localement très intense qu'il est nécessaire de mesurer précisément et de contrôler. Pour cette raison, des détecteurs de rayonnement ont été installés dans les expériences du LHC. Dans une étude précédente, des dosimètres RadFETs et des diodes PIN pour la mesure respective de dose ionisante et de fluence équivalente ont été caractérisés pour la métrologie du rayonnement à l'intérieur de l'accélérateur de particules. Cependant, bien que les RadFETs aient été extensivement caractérisés et leurs performances déterminées, leur réponse peut être influencée par leur support et boîtier qui, selon le matériau et la géométrie, peuvent induire des erreurs dans la mesure de dose ionisante. Dans ce travail de thèse, une étude complète menée à l'aide de l'outil de simulation interaction particules-matière « Geant4 » a été réalisée afin d'évaluer cette influence. Concernant les diodes PIN utilisées, le protocole de mesure adapté à l'environnement du LHC, atteint ses limites pour le Super-LHC et ne permettra pas la mesure de la fluence équivalente prévue. Une étude complète sur la réponse aux radiations de ces diodes jusqu'à très hautes fluences a été réalisée. Ainsi, la gamme de mesure de ces diodes a pu être étendue à des fluences équivalentes dix fois plus élevées que celles du LHC en vue de leur utilisation pour le Super-LHC.

TITRE en anglais

Characterization and performance optimization of radiation monitoring sensors for high energy physics experiments at the CERN LHC and super-LHC.

RESUME en anglais

In order to study the matter originating from the universe, a new particle accelerator named the Large Hadron Collider (LHC) has been built at CERN. The radiation environment generated by the hadrons collisions in the high energy physics experiments of the LHC will be complex and locally very intense. For monitoring this complex radiation field, dosimeters have been installed in the LHC experiments. In previous study, RadFET dosimeters and PIN diodes have been characterized for their use in the particle accelerator. However, even if the RadFETs sensors have been already extensively characterized, their radiation response can be affected by their package. Depending on the material and the geometry, the package can induce errors in the dose measurement. In this thesis, a complete study has been carried out in order to evaluate its influence. Concerning the PIN diodes, the readout protocol used for the LHC is no longer valuable for the Super-LHC. Therefore, a complete study on their radiation response has been performed up to very high fluences ($\approx 6 \times 10^{15} n_{eq}/cm^2$) in view of their utilization as radiation monitoring sensors for the Super-LHC.

DISCIPLINE

Electronique, Composant et Systèmes

MOTS-CLES

CERN, LHC, Super-LHC, Radiations, Dosimétrie, diode PIN, RadFET, Geant 4.

INTITULE ET ADRESSE DE L'U.F.R. OU DU LABORATOIRE :

Institut d' Electronique de Sud (IES) ; Unité Mixte de Recherche UMR UM2-CNRS 5214
Groupe Radiac
Université Montpellier 2
Place Eugène Bataillon, Case Courrier 83
34095 Montpellier Cedex 05